AN ELECTRON ENERGY-LOSS SPECTROSCOPIC INVESTIGATION OF MOLECULAR INTERACTIONS AT HYDROXYAPATITE-COLLAGEN INTERFACES IN HEALTHY AND DISEASED (OSTEOGENESIS IMPERFECTA) HUMAN BONE AND BIOMINERALIZED TISSUE-ENGINEERED BONE

A Dissertation
Submitted to the Graduate Faculty
of the
North Dakota State University
of Agriculture and Applied Science

By

Scott Andrew Payne

In Partial Fulfillment of the Requirements
for the Degree of
DOCTOR OF PHILOSOPHY

Major Program:
Materials and Nanotechnology

April 2018

Fargo, North Dakota

North Dakota State University

Graduate School

Title

An Electron Energy-Loss Spectroscopic Investigation of Molecular Interactions at Hydroxyapatite-Collagen Interfaces in Healthy and Diseased (Osteogenesis Imperfecta) Human Bone and Biomineralized Tissue Engineered Bone.

By

Scott Andrew Payne

The Supervisory Committee certifies that this ***disquisition*** complies with North Dakota State University's regulations and meets the accepted standards for the degree of

DOCTOR OF PHILOSOPHY

SUPERVISORY COMMITTEE:

Dr. Kalpana S Katti

Co-Chair

Dr. Dinesh R Katti

Co-chair

Dr. Achintya Bezbaruah

Dr. Jane Schuh

Approved:

10/4/2018

Date

Dr. Erik Hobbie

Department Chair

ABSTRACT

At its primary level (nm scale) bone is a nanocomposite consisting of a mineral (hydroxyapatite) phase which gives bone its strength and an organic (type I collagen) phase giving bone its fracture toughness. Hydroxyapatite, (HAP) $Ca_{10}(PO_4)_6(OH)_2$, is the most abundant mineral in the human body. Bone tissue has a complex hierarchical structure spanning multiple length scales (cm to nm).

Characterization of mineral composition in biomineralized tissues such as bone at their primary level, is very challenging and requires instrumentation with nanometer-scale spatial resolution. Transmission electron microscopy (TEM) combines high spatial resolution with visual correlation of diffraction and elemental-composition data. Electron energy-loss spectroscopy (EELS) is a sensitive technique used to probe electronic structure at the molecular level. TEM-based EELS is the only available technique that can provide information about the chemical and coordination environment of minerals with nm scale spatial resolution.

Prior studies in our group has developed a method to create biomimetic HAP using biomineralization routes inside the clay galleries of montmorillonite clay modified with amino acids (in-situ HAPclay). Incorporation of in-situ HAPclay into polymer scaffolds and seeding with human mesenchymal stem cells has enabled the cells towards differentiation into osteoblastic lineages without differentiating media. Because of the importance of these materials for bioengineering applications, TEM-EELS was used to evaluate differences and similarities among HAP, biomimetic in-situ HAPclay, modified MMT clay, and β-tricalcium phosphate.

Osteogenesis imperfecta (OI), also known as brittle bone disease, is an inheritable disease characterized by increased bone fragility, low bone mass, and bone deformity caused primarily by mutation in collagen type I genes and is expressed as changes in structure and mechanics at

the macrostructural level of bone. Therefore the mineralization of HAP in OI bone and the molecular basis of OI bone disease makes this an interesting system for molecular-level investigations. Small changes in the valence band and outer electronic structures of the diseased bone have been revealed through EELS. These small changes observed in the electron energy-loss spectra of the OI bone appear to play important biological roles towards development of the disease.

ACKNOWLEDGEMENTS

The author wishes to give sincere thanks and acknowledgement to:

My advisor, University Distinguished Professor, Dr. Kalpana S. Katti, for encouraging me to undertake this journey, guidance, motivation, enthusiasm, support, patience and friendship. Also, my Co-advisor, Dr. Dinesh R. Katti, for his advice, helpful discussions, tireless patience, support and friendship. You both have set an example of excellence and integrity as a researcher, mentor, role model, and more importantly, human being. I am humbled and truly honored to have had the opportunity to participate and contribute to your research and research group projects.

My committee members, Dr. Jane Schuh and Dr. Achintya Bezbaruah for their time, interest, and support over the course of my study.

Dr. Jayma Moore for manuscript discussions and editorial suggestions as well as encouragement, support, and friendship on a daily basis.

Dr. Thomas Freeman for hiring a “chemist” and then changing his life by imparting upon him his knowledge, the art of electron microscopy, and creating in him an appreciation for all things small.

National Disease Interchange (NDRI) ndriresource.org, for supplying the donated human bone tissue.

The donors and their families for their unselfish donation of tissue, without their generosity this work could not have been undertaken.

My group members past and present: Avinash Ambre, Bedabibhas Mohanty, Anurag Sharma, Chunju Gu, Md. Molla, Keshab Thapa, Rohit Khanna, Shashindra Pradhan, Kristin Alstadt , Nicholas Peterka, Zillur Patwary, Muniyamuthu Raviprasad, Lakshmikanth

Srinivasamurthy, Sumanta Kar, Krishna Kundu, HM Nasrullah Faisal and Haneesh Jasuja for valuable research discussions and friendship.

Jan Lofberg and Milka Singha in the Civil and Environmental Engineering office for their invaluable support in helping me navigate the procedural aspects of graduate school.

National Science Foundation Major Research Instrumentation program for instrumentation funding. This material is based upon work supported by the National Science Foundation under Grant No(s). 0619098, 0821655, 0923354. Any opinions, findings, and conclusions or recommendations expressed in this material are those of the author(s) and do not necessarily reflect the views of the National Science Foundation.

North Dakota Established Program to Stimulate Competitive Research (ND-EPSCoR) for research funding.

Finally, but most importantly, I would like thank my wife Rebecca, son Gunnar and daughter McKenna, without their constant love, patience, and understanding I could not have completed this research endeavor.

DEDICATION

This dissertation is dedicated to my wife Becky, son Gunnar, and daughter McKenna.

You are my world! I love you!

THE ROAD NOT TAKEN

Two roads diverged in a yellow wood,
And sorry I could not travel both
And be one traveler, long I stood
and looked down one as far as I could
To where it bent in the undergrowth;

Then took the other, as just as fair,
And having perhaps the better claim,
Because it was grassy and wanted wear;
Though as for that, the passing there
Had worn them really about the same,
And both that morning equally lay

In leaves no step had trodden black.
Oh, I kept the first for another day!
Yet knowing how way leads on to way,
I doubted if I should ever come back.

I shall be telling this with a sigh
Somewhere ages and ages hence:
Two roads diverged in a wood, and I-
I took the one less traveled by,
And that has made all the difference.

-Robert Frost

TABLE OF CONTENTS

ABSTRACT iii

ACKNOWLEDGEMENTS v

DEDICATION vii

LIST OF TABLES xiii

LIST OF FIGURES xiv

LIST OF ABBREVIATIONS xvi

LIST OF APPENDIX TABLES xviii

LIST OF APPENDIX FIGURES xix

CHAPTER 1. INTRODUCTION 1

1.1. Scope of this dissertation 1

1.2. Bone 2

1.3. Background of the biomineralized hydroxyapatite inside clay galleries sample used for EELS studies 5

1.4. Background of the healthy and diseased human bone samples used for EELS studies 9

1.4.1. Normal human bone sample 12

1.4.2. Diseased human bone sample 12

1.5. Transmission electron microscopy and electron energy loss spectroscopy 13

1.6. Theory of EELS 15

1.7. References 18

CHAPTER 2. FLUENCE RATE CALCULATIONS FOR THE JEOL-JEM-2100 LaB_6 TRANSMISSION ELECTRON MICROSCOPE 23

2.1. Introduction 23

2.2. Experimental 25

2.3. Results 26

2.4. Conclusions 27

2.5. References 27

CHAPTER 3. PROBING ELECTRONIC STRUCTURE OF BIOMINERALIZED28
HYDROXYAPATITE INSIDE NANOCLAY GALLERIES 28

3.1. Introduction 28

3.2. Materials and methods 31

3.2.1. Materials 31

3.2.2. Methods 32

3.3. Results and discussion 34

3.3.1. Low-loss spectra 36

3.3.2. Kramers-Kronig analysis 39

3.3.3. P-$L_{2,3}$-edge spectra 42

3.4. Conclusions 44

3.5. References 45

CHAPTER 4. AN ELECTRON ENERGY-LOSS SPECTROSCOPIC STUDY OF
MOLECULAR INTERACTIONS IN NORMAL AND OSTEOGENESIS
IMPERFECTA DISEASED HUMAN BONE 49

4.1. Introduction 49

4.2. Materials and methods 52

4.2.1. Materials 52

4.2.2. Methods 53

4.3. Results and discussion 55

4.3.1. FESEM imaging 55

4.3.2. TEM imaging 57

4.3.3. Low-loss spectra 59

4.3.4. Kramers-Kronig analysis 61

4.3.5. P-$L_{2,3}$-edge spectra 64
4.4. Conclusions 66
4.5. References 68
CHAPTER 5. SUMMARY AND CONCLUSIONS 72
CHAPTER 6. MAJOR CONTRIBUTIONS 75
CHAPTER 7. FUTURE WORK 76
APPENDIX A. HUMAN BONE SAMPLE INFORMATION 78
A.1. NDSU internal review board compliance letter 78
A.2. Healthy human femur 79
A.3. Osteogenesis imperfecta diseased human tibia 81
APPENDIX B. PREPARATION OF BONE FOR TEM 83
B.1. Images of bone samples prior to TEM preparation 83
B.2. Schematic representation defining relation of direction of the incident TEM electron beam to bone sample. 84
B.3. Typical longitudinal and transverse bone surfaces 84
APPENDIX C. TEM PREPARATION EQUIPMENT AND PROCEDURES 86
C.1. Buehler isomet 1000 low speed diamond saw 86
C.1.1. Buehler isomet 1000 low speed diamond saw operating procedure 87
C.2. Gatan ultrasonic disc cutter model 601 88
C2.1. Gatan ultrasonic disc cutter model 601 operating procedure 89
C.3. Gatan disc grinder model 623 93
C.3.1. Gatan disc grinder model 623 operating procedure 94
C.4. Gatan dimple grinder model 656 98
C.4.1. Gatan dimple grinder model 656 operating procedure 99
C.5. Gatan precision ion polishing system (PIPS) model 691 103
C.5.1. Gatan precision ion polishing system (PIPS) model 691 operating procedure 103

APPENDIX D. PROCEDURES FOR OBTAINING EELS DATA USING THE GATAN ENFINA SPECTROMETER ATTACHED TO A JEOL JEM-2100 TEM 106

D.1. Preparing a gain reference for the ENFINA camera 106

D.2. ENFINA spectrometer lens alignment procedure 106

D.3. ENFINA spectrometer EELS data acquisition procedure 107

APPENDIX E. FESEM IMAGES OF HUMAN BONE 109

E.1. Comparison of healthy and osteogenesis imperfecta diseased human bone 109

E.1.1. Longitudinal section 109

E.1.2. Transverse section 122

APPENDIX F. SELECTED TEM IMAGES OF UNMODIFIED CLAY, MODIFIED CLAY, HAP, IN-SITU HAPCLAY AND β-TCP 132

F.1. Unmodified clay 132

F.2. Modified clay 135

F.3. HAP 139

F.4. In-situ HAPclay 144

F.5. β-TCP 149

APPENDIX G. COMPARISON OF REPRESENTATIVE TEM IMAGES OF THE ACQUISITION AREAS OF EELS SPECTRA FROM HUMAN BONE 155

G.1. TEM images of healthy and OI diseased human bone where EELS spectra were acquired, longitudinal sections 155

G.2. TEM images of healthy and OI diseased human bone where EELS spectra were acquired, transverse sections 162

APPENDIX H. TEM IMAGES SHOWING BANDING IN HUMAN BONE, LONGITUDINAL SECTION 167

H.1. TEM images of banding in healthy and osteogenesis imperfecta diseased human bone 167

APPENDIX I. SELECTED OVERLAYS OF EELS SPECTRA 171

I.1. Overlays of ε_1 spectra 171

I.2. Overlays of ε_2 spectra 172

I.3. Overlays of ELF spectra 173

I.4. Overlays of P-$L_{2,3}$ spectra 175

LIST OF TABLES

Table Page

1.1. Microscopy and related techniques for investigating the structural components of bone hierarchical levels. 4

2.1. Calculated electron dose rate and electron dose for JEOL-JEM-2100 LaB_6 TEM at North Dakota State University. 26

3.1. Energy loss function peak positions (eV). 38

3.2. Energy loss function A:B ratio and peak shift (eV). 38

3.3. Justifications of ε_2 single-electron transitions (eV). 40

3.4. P-$L_{2,3}$ edge position (eV) and electronic transition assignments. 43

3.5. P-$L_{2,3}$ shift values. 44

4.1. Energy loss function peak positions (eV). 59

4.2. ε_2 peak positions (eV). 62

4.3. P-$L_{2,3}$ edge feature electronic transition origins (eV). 66

LIST OF FIGURES

Figure Page

1.1. Schematic representation of the hierarchical structure of bone. 3

3.1. Crystal structure of (a)HAP, (b) β-TCP, (c) amino acid modified nanoclay and (d) modified nanoclay-HAP. 34

3.2. TEM images at low-magnification (left column) and high-magnification (right column). (a,b) in-situ HAPclay, (c,d) HAP, (e,f) β-TCP, and (g,h) modified MMT clay. 36

3.3. Energy Loss Function spectra of in-situ HAPclay, HAP, β-TCP, and modified clay. Peak A corresponds to the plasmon peak, and peaks B and B^* correspond to the calcium $M_{2,3}$ edge. The spectra are separated vertically for clarity and bars denote peak position. 37

3.4. The real (ε_1) part (a) and imaginary (ε_2) part (b) of the complex dielectric function obtained from Kramers-Kronig analysis of the EEL spectra for in-situ HAPclay, HAP, β-TCP, and modified MMT clay. Overlaid spectra are separated vertically for clarity. 39

3.5. Calculated high-frequency AC conductivity plots for in-situ HAPclay, HAP, β-TCP, and modified MMT clay. The overlaid spectra are separated vertically for clarity. 41

3.6. Overlay of the P-$L_{2,3}$ core loss region (135-210 eV) obtained from in-situ HAPclay, HAP, and β-TCP. The spectra are separated vertically for clarity. The peak positions (A, B, C, and D) are denoted by vertical lines and discussed in the text. 42

4.1. FESEM images at low (left column), intermediate (middle column), and high (right column) magnification. (a-c) NHB-L, (d-f) OIHB-L, (g-i) NHB-T, and (j-l) OIHB-T. 56

4.2. TEM images at low-magnification (left column) and high-magnification (right column). (a,b) NHB-L, (c,d) OIHB-L, (e,f) NHB-T, (g,h) OIHB-T, and (i,j) HAP. 58

4.3. Energy Loss Function spectra: (a) OIHB-L, NHB-L, OIHB-T, NHB-T and HAP; (b) overlay of OIHB-L, NHB-L, and HAP; (c) overlay of OIHB-T, NHB-T, and HAP. Bars denote peak position and the spectra separated vertically for clarity. 60

4.4. The real (ε_1) part (a) and imaginary (ε_2) part (b) of the complex dielectric function obtained from Kramers-Kronig analysis of the EELS spectra for OIHB-L, OIHB-T, NHB-L, NHB-T and HAP. (c) and (d) represent ε_2 spectra grouped into longitudinal and transverse orientation for comparison of single-electron transitions. Spectra vertically separated for clarity. 63

4.5. Overlays of the P-$L_{2,3}$ core loss region (135-210 eV) obtained from (a) NHB-T, OIHB-T, HAP, OIHB-L and NHB-L. (b) HAP, OIHB-L and NHB-L. (c) NHB-T, OIHB-L and HAP. The spectra separated vertically for clarity and the peak positions (A-D) are indicated by vertical lines. 64

LIST OF ABBREVIATIONS

AFM	Atomic Force Microscopy
β-TCP	β-tricalcium phosphate.
DM	DigitalMicrograph from Gatan
DOS	Density of States
ChiPga	Chitosan polygalacturonic acid
EELS	Electron Energy-Loss Spectroscopy
EFTEM	Energy-Filtered Transmission Electron Microscopy
ELF	Energy Loss Function
ELNES	Electron-Loss Near-Edge Structure
FESEM	Field-Emission Scanning Electron Microscope
FTIR	Fourier Transform Infra-red
HAP	Calcium hydroxyapatite
hMSC	Human Mesenchymal Stem Cells
in-situ HAPclay	HAP biomineralized in 5-aminovaleric acid modified montmorillonite clay galleries
JEOL	Japan Electron Optics Laboratory, Inc.
μ-CT	Micro-Computed Tomography
NDRI	National Disease Registry Incorporated
NEXAFS	Near-Edge X-ray Absorption Fine Structure
NHB	Normal (Healthy) Human Bone
NHB-L	Normal (Healthy) Human Bone Longitudinal
NHB-T	Normal (Healthy) Human Bone Transverse
OI	Osteogenesis imperfecta
OIHB	Osteogenesis imperfecta diseased human bone

OIHB-L .....Osteogenesis imperfecta diseased human bone Longitudinal

OIHB-T .....Osteogenesis imperfecta diseased human bone Transverse

Pa-FTIR.....Photoacoustic Fourier Transform Infra-red

PCN.....Polymer Clay Nanocomposite

MMT .....Montmorillonite

SSD .....Single-scattering distribution function

STEM.....Scanning Transmission Electron Microscopy

STXM .....Scanning Transmission X-ray Microscopy

TEM .....Transmission Electron Microscopy

XANES .....X-ray Absorption Near-Edge Spectra

XRD .....X-ray diffraction

ZLP .....Zero-loss peak

LIST OF APPENDIX TABLES

Table Page

C.1. Gatan disc grinding schedule for side #1. 96

C.2. Gatan disc grinding schedule for side #2. 97

LIST OF APPENDIX FIGURES

Figure Page

A.1. NDSU IRB letter outlining board decision exempt status. 78

A.2. Healthy human femur as received from NDRI. 79

A.3. Patient information sheet of healthy human femur obtained from NDRI. 80

A.4. Osteogenesis imperfecta diseased human tibia as received from NDRI. 81

A.5. Patient information sheet of Osteogenesis imperfecta diseased human tibia obtained from NDRI. 82

B.1. Portion of healthy human femur used for TEM sample preparation. 83

B.2. Portion of osteogenesis imperfecta human tibia used for TEM sample preparation. 83

B.3. Schematic representation of bone showing the direction of the TEM incident beam relative to longitudinal and transverse surfaces. 84

B.4. Longitudinal bone surface. 84

B.5. Transverse bone surface. 85

C.1. Buehler Isomet 1000 low-speed saw. 86

C.2. Buehler low-speed saw equipped with diamond blade used for cutting 500-700 μm longitudinal and transverse sections from the stock bone samples. 87

C.3. Buehler isomet 1000 low-speed saw cuts of transverse (large, curved) and longitudinal (square, small) bone. 88

C.4. Gatan ultrasonic cutting device model 601. 88

C.5. Gatan ultrasonic cutting device used to cut 3 mm circular discs from the 500-700 μm bone section. 89

C.6. Transverse section of bone showing 3 mm disc cuts. 92

C.7. Longitudinal bone section with corresponding 3 mm disc. 92

C.8. Gatan disc grinder model 623 (Note: Turning the micrometer adjustment knob counter clockwise (CCW) retracts sample mount. Turning the micrometer adjustment knob clockwise (CW) extends sample mount.). 93

C.9. Gatan disc grinder with sample holder. 94

C.10. SEM image showing the edge view of a disc thinned to approximately 100 μm using the Gatan disc grinder. 97

C.11. Gatan dimple grinder model 656. 98

C.12. Phosphor bronze grinding wheel and sample on the Gatan dimple grinder. 98

C.13. A 70 micron thick 3 mm disc after dimpling and polishing (<20 μm in depth) using the Gatan dimple grinder. 102

C.14. Gatan PIPS model 691 with argon tank. 103

C.15. Bone sample milled to less than 100 nm thick near the center perforation using Gatan PIPS ion mill. 105

E.1. FESEM secondary electron image of longitudinal sections of human bone (x50 original magnification). (A) healthy. (B) osteogenesis imperfecta. 109

E.2. FESEM secondary electron image of longitudinal sections of human bone (x70 original magnification). (A) healthy. (B) osteogenesis imperfecta. 110

E.3. FESEM secondary electron image of longitudinal sections of human bone (x10,000 original magnification). (A) healthy. (B) osteogenesis imperfecta. 111

E.4. FESEM secondary electron image of longitudinal sections of human bone (x20,000 original magnification). (A) healthy. (B) osteogenesis imperfecta. 112

E.5. FESEM secondary electron image of longitudinal sections of human bone (x40,000 original magnification). (A) healthy. (B) osteogenesis imperfecta. 113

E.6. FESEM secondary electron image of longitudinal sections of human bone (x40,000 original magnification). (A) healthy. (B) osteogenesis imperfecta. 114

E.7. FESEM secondary electron image of longitudinal sections of human bone (x80,000 original magnification). (A) healthy. (B) osteogenesis imperfecta. 115

E.8. Comparison of secondary and low-angle backscattered electron images for identical areas of healthy longitudinal bone (x20,000 original magnification). (A) secondary electron image. (B) low-angle backscattered electron image. 116

E.9. Comparison of secondary and low-angle backscattered electron images for identical areas of osteogenesis imperfecta longitudinal bone (x10,000 original magnification). (A) secondary electron image. (B) low-angle backscattered electron image. 117

E.10. Comparison of secondary and low-angle backscattered electron images for identical areas of healthy longitudinal bone (x40,000 original magnification). (A) secondary electron image. (B) low-angle backscattered electron image. 118

E.11. Comparison of secondary and low-angle backscattered electron images for identical areas of osteogenesis imperfecta longitudinal bone (x40,000 original magnification). (A) secondary electron image. (B) low-angle backscattered electron image. 119

E.12. Comparison of secondary and low-angle backscattered electron images for identical areas of osteogenesis imperfecta longitudinal bone (x3,500 original magnification). (A) secondary electron image. (B) low-angle backscattered electron image. 120

E.13. Comparison of secondary and low-angle backscattered electron images for identical areas of osteogenesis imperfecta longitudinal bone (x5,000 original magnification). (A) secondary electron image. (B) low-angle backscattered electron image. 121

E.14. FESEM secondary electron image of transverse sections of human bone (x50original magnification). (A) healthy. (B) osteogenesis imperfecta. 122

E.15. FESEM secondary electron image of transverse sections of human bone (x70 original magnification). (A) healthy. (B) osteogenesis imperfecta..... 123

E.16. FESEM secondary electron image of transverse sections of human bone (x250 original magnification). (A) healthy. (B) osteogenesis imperfecta..... 124

E.17. FESEM secondary electron image of transverse sections of human bone (x750 original magnification). (A) healthy. (B) osteogenesis imperfecta..... 125

E.18. FESEM secondary electron image of transverse sections of human bone (x10,000 original magnification). (A) healthy. (B) osteogenesis imperfecta..... 126

E.19. FESEM secondary electron image of transverse sections of human bone (x20,000 original magnification). (A) healthy. (B) osteogenesis imperfecta..... 127

E.20. FESEM secondary electron image of transverse sections of human bone (x40,000 original magnification). (A) healthy. (B) osteogenesis imperfecta..... 128

E.21. FESEM secondary electron image of transverse sections of human bone (x40,000 original magnification). (A) healthy. (B) osteogenesis imperfecta..... 129

E.22. FESEM secondary electron image of transverse sections of human bone (x80,000 original magnification). (A) healthy. (B) osteogenesis imperfecta..... 130

E.23. FESEM secondary electron image of transverse sections of human bone (x100,000 original magnification). (A) healthy. (B) osteogenesis imperfecta..... 131

F.1. TEM image of unmodified clay (x40,000 original magnification) showing clay sheets. 132

F.2. TEM image of unmodified clay (x100,000 original magnification). 132

F.3. TEM image of unmodified clay (x200,000 original magnification). 133

F.4. TEM image of unmodified clay (x12,000 original magnification). 133

F.5. TEM image of unmodified clay (x80,000 original magnification). 134

F.6. TEM image of unmodified clay (x200,000 original magnification). 134

F.7. TEM image of modified clay (x8,000 original magnification). 135

F.8. TEM image of modified clay (x12,000 original magnification). 135

F.9. TEM image of modified clay (x80,000 original magnification). 136

F.10. TEM image of modified clay (x200,000 original magnification). 136

F.11. TEM image of modified clay (x5,000 original magnification). 137

F.12. TEM image of modified clay (x200,000 original magnification). 137

F.13. TEM image of modified clay (x40,000 original magnification). 138

F.14. TEM image of modified clay (x200,000 original magnification). 138

F.15. TEM image of HAP (x15,000 original magnification). 139

F.16. TEM image of HAP (x15,000 original magnification). 139

F.17. TEM image of HAP showing lattice structure (x250,000 original magnification). 140

F.18. TEM image of HAP showing lattice structure (x300,000 original magnification). 140

F.19. TEM image of HAP (x15,000 original magnification). 141

F.20. TEM image of HAP showing lattice structure (x200,000 original magnification). 141

F.21. TEM image of HAP showing lattice structure (x200,000 original magnification). 142

F.22. TEM image of HAP (x30,000 original magnification). 142

F.23. TEM image of HAP showing lattice structure (x200,000 original magnification). 143

F.24. TEM image of HAP showing lattice structure (x200,000 original magnification). 143

F.25. TEM image of in-situ HAPclay (x15,000 original magnification)..... 144

F.26. TEM image of in-situ HAPclay (x80,000 original magnification)..... 144

F.27. TEM image of in-situ HAPclay showing lattice structure (x200,000 original magnification). 145

F.28. TEM image of in-situ HAPclay (x20,000 original magnification)..... 145

F.29. TEM image of in-situ HAPclay (x80,000 original magnification)..... 146

F.30. TEM image of in-situ HAPclay showing lattice structure (x200,000 original magnification). 146

F.31. TEM image of in-situ HAPclay showing lattice structure (x200,000 original magnification) 147

F.32. TEM image of in-situ HAPclay (x30,000 original magnification)..... 147

F.33. TEM image of in-situ HAPclay showing lattice structure (x200,000 original magnification). 148

F.34. TEM image of in-situ HAPclay showing lattice structure (x200,000 original magnification). 148

F.35. TEM image of β-TCP (x15,000 original magnification)..... 149

F.36. TEM image of β-TCP showing lattice structure (x200,000 original magnification). 149

F.37. TEM image of β-TCP (x10,000 original magnification)..... 150

F.38. TEM image of β-TCP showing lattice structure (x200,000 original magnification). 150

F.39. TEM image of β-TCP showing lattice structure (x200,000 original magnification). 151

F.40. TEM image of β-TCP showing lattice structure (x200,000 original magnification). 151

F.41. TEM image of β-TCP (x20,000 original magnification)..... 152

F.42. TEM image of β-TCP showing lattice structure (x200,000 original magnification). 152

F.43. TEM image of β-TCP (x80,000 original magnification)..... 153

F.44. TEM image of β-TCP showing lattice structure (x200,000 original magnification). 153

F.45. TEM image of β-TCP (x15,000 original magnification)..... 154

F.46. TEM image of β-TCP showing lattice structure (x200,000 original magnification). 154

G.1. TEM image of longitudinal section of human bone (x40,000 original magnification). (A) healthy and (B) osteogenesis imperfecta. Arrows denote collagen fibrils. 155

G.2. TEM image of longitudinal section of human bone (x200,000 original magnification). (A) healthy and (B) osteogenesis imperfecta. Arrows denote collagen fibrils and arrowheads denote HAP crystal lattice..... 156

G.3. TEM image of longitudinal section of human bone (x200,000 original magnification). (A) healthy and (B) osteogenesis imperfecta. Arrows denote collagen fibrils and arrowheads denote HAP crystal lattice..... 157

G.4. TEM image of longitudinal section of human bone (x200,000 original magnification). (A) healthy and (B) osteogenesis imperfecta. Arrows denote collagen fibrils and arrowheads denote HAP crystal lattice..... 158

G.5. TEM image of longitudinal section of human bone (x200,000 original magnification). (A) healthy and (B) osteogenesis imperfecta. Arrowheads denote HAP crystal lattice..... 159

G.6. TEM image of longitudinal section of human bone (x200,000 original magnification). (A) healthy and (B) osteogenesis imperfecta. Arrows denote collagen fibrils and arrowheads denote HAP crystal lattice..... 160

G.7. TEM image of longitudinal section of human bone (x200,000 original magnification). (A) healthy and (B) osteogenesis imperfecta. Arrowheads denote HAP crystal lattice..... 161

G.8. TEM image of transverse section of human bone (x40,000 original magnification). (A) healthy and (B) osteogenesis imperfecta. Arrows denote collagen fibrils. 162

G.9. TEM image of transverse section of human bone (x200,000 original magnification). (A) healthy and (B) osteogenesis imperfecta. Arrows denote collagen fibrils and arrowheads denote HAP crystal lattice. 163

G.10. TEM image of transverse section of human bone (x200,000 original magnification). (A) healthy and (B) osteogenesis imperfecta. Arrows denote collagen fibrils and arrowheads denote HAP crystal lattice..... 164

G.11. TEM image of transverse section of human bone (x200,000 original magnification). (A) healthy and (B) osteogenesis imperfecta. Arrowheads denote HAP crystal lattice..... 165

G.12. TEM image of transverse section of human bone (x200,000 original magnification). (A) healthy and (B) osteogenesis imperfecta..... 166

H.1. TEM images showing banding in longitudinal sections of human bone (x10,000 original magnification). (A) healthy. (B) osteogenesis imperfecta. 167

H.2. TEM images showing banding in longitudinal sections of human bone (x12,000 original magnification). (A) healthy. (B) osteogenesis imperfecta. 168

H.3. TEM images showing banding in longitudinal sections of human bone (x20,000 original magnification). (A) healthy. (B) osteogenesis imperfecta. 169

H.4. TEM images showing banding in longitudinal sections of human bone (x25,000 original magnification). (A) healthy. (B) osteogenesis imperfecta. 170

I.1. ε_1 spectra overlays of healthy human bone (longitudinal and transverse), osteogenesis imperfecta diseased human bone (longitudinal and transverse) and HAP. 171

I.2. ε_2 spectra overlays of healthy human bone (longitudinal and transverse), osteogenesis imperfecta diseased human bone (longitudinal and transverse) and HAP. 172

I.3. ε_2 spectra overlays of longitudinal healthy human bone, longitudinal osteogenesis imperfecta diseased human bone and HAP. 172

I.4. ε_2 spectra overlays of transverse healthy human bone, transverse osteogenesis imperfecta diseased human bone and HAP. 173

I.5. ELF spectra overlays of healthy human bone (longitudinal and transverse), osteogenesis imperfecta diseased human bone (longitudinal and transverse) and HAP. 173

I.6. ELF spectra overlays of longitudinal healthy human bone, longitudinal osteogenesis imperfecta diseased human bone and HAP. 174

I.7. ELF spectra overlays of transverse healthy human bone, transverse osteogenesis imperfecta diseased human bone and HAP. 174

I.8. P-$L_{2,3}$ spectra overlays of healthy human bone (longitudinal and transverse), osteogenesis imperfecta diseased human bone (longitudinal and transverse) and HAP. 175

I.9. P-$L_{2,3}$ spectra overlays of β-TCP, in-situ HAPclay, and HAP. 175

CHAPTER 1. INTRODUCTION

1.1. Scope of this dissertation

Electron energy-loss spectroscopy (EELS) is used to investigate natural and synthetic bone systems, specifically molecular-level differences in healthy and osteogenesis-imperfecta diseased bone as well as a biomimetic hydroxyapatite biomineralized inside clay galleries and used for tissue-engineering applications. This doctoral dissertation focuses on the use of EELS in TEM to compare the electronic structure of HAP mineral, specifically the low-loss Ca-$M_{2,3}$ edge and the P-$L_{2,3}$ core loss edge in two different systems; synthetic HAP with biomimetic HAP and healthy with diseased human bone. The first comparison is between synthetic HAP and HAP that has been biomineralized in clay galleries within a unique clay-polymer biomaterial developed by our group (in-situ HAPclay). The second comparison is between the HAP in normal healthy human bone (NHB) and human bone with osteogenesis imperfecta disease (OIHB). This work represents a unique experimental EELS probe into molecular interactions in healthy and osteogenesis-imperfecta-diseased human bone and biomineralized HAP.

This dissertation is organized in the following manner:

- Chapter 1: Introduction. This chapter presents a description of bone and its components, background information on the experimental lineage of the in-situ HAPclay biomaterial system that brought about this EELS investigation, and detailed background information on the healthy and diseased human bones as well as the implications of using a single sample for each experiment. The theory of EELS and the electronic information that can be acquired using this technique is also discussed.

- Chapter 2: This chapter presents the calculation of the fluence (electron dose) for each of the beam-probe sizes for the JEOL JEM-2100 LaB_6 TEM used to obtain the EELS data presented in this dissertation in an effort to ensure the dose threshold or critical dose is not exceeded for the samples, thereby causing sample damage.
- Chapter 3: This chapter presents the EELS comparison of low-loss Ca-$M_{2,3}$ edges and P-$L_{2,3}$ core loss edges between synthetic HAP and biomimetic in-situ HAPclay
- Chapter 4: This chapter presents the EELS comparison of HAP mineral in healthy human bone and osteogenesis-imperfecta-diseased human bone with respect to low-loss Ca-$M_{2,3}$ edges and P-$L_{2,3}$ core loss edges.
- Chapter 5: This chapter summarizes of the major contributions of this work.
- Chapter 6: This chapter discusses possible future directions for this work

1.2. Bone

Bone is an integral part of the human body and functions as both an organ and a tissue. As an organ, bone produces white and red blood cells, stores ions, and provides endocrine regulation of blood sugar. There are two main configurations of bone: cancellous and compact. Cancellous (or trabecular) bone is found at the ends of long bones and in vertebrae and flat bones and is very porous (50-90% porosity). Compact bone, also referred to as cortical bone, is more dense (5-10% porosity) than cancellous bone, and is found in the shafts of long bones and forming the shell around cancellous bone at joints and in vertebrae.

Bone as a tissue gives the body shape/support and protection of vital organs. Bone and other types of tissues are formed by living organisms through a complex process termed

biomineralization. Biomineralized tissues consist of mineral and organic phases. Bone comprises approximately 60% mineral, an organic portion of 20% collagen and 10% non-collagenous proteins, and 10% water. The core component of bone, and the most abundant mineral in the human body, is hydroxyapatite (HAP). Bone mineral [$Ca_{10}(PO_4)_6(OH)_2$] has similar composition to synthetic HAP, however, HAP in bone mineral is poorly crystallized, structurally disordered, and compositionally nonstoichiometric when compared to synthetic HAP [1, 2],

Bone tissue has a complex hierarchical structure spanning multiple length scales (cm to nm) [3-5]. The hierarchical structure for compact bone is outlined in Fig. 1.1.

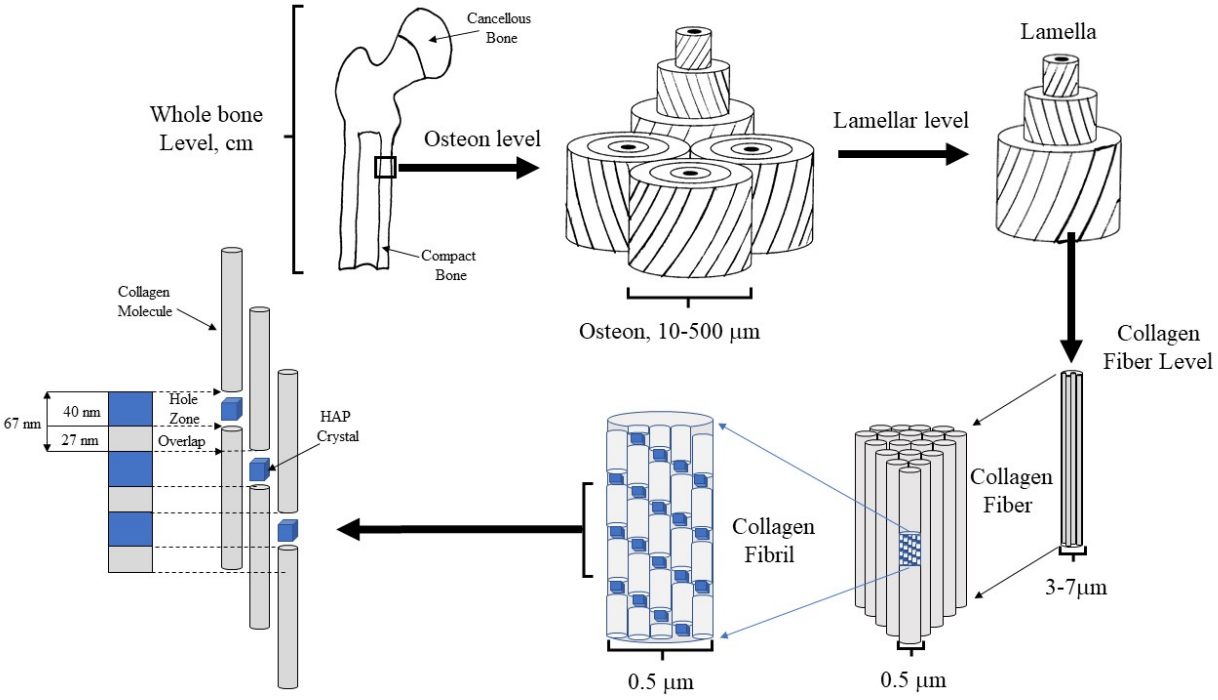

Figure 1.1. Schematic representation of the hierarchical structure of bone.

The structural unit of compact bone is the osteon. Osteons are small cylinders (diameter 10-500 μm) composed of concentric lamellae. Each lamella is made up of individual collagen fibers 3-7 μm in diameter. The collagen fibers are made up of fibrils approximately 500 nm in

width. Each collagen fibril contains a staggered arrangement of collagen molecules (1.5 nm wide x 300 nm long) and HAP crystals, which produces a periodicity of 67 nm [6, 7]. The HAP resides in the hole zone between the ends of the collagen molecules [3, 8, 9], where the c-axes of the mineral crystals are oriented along the long axis of the bone and well-aligned with the collagen fibril axis [5, 10]. Microscopy and related techniques currently available to investigate the component structure at each level of hierarchy can be found in Table 1.1.

Table 1.1. Microscopy and related techniques for investigating the structural components of bone hierarchical levels.

Hierarchical Level	Component Structures	Size Range	Techniques
Macrostructure	cortical bone cancellous bone	>500 μm	Light microscopy X-ray micro-computed tomography
Microstructure	Osteons	10-500 μm	Light microscopy X-ray micro-computed tomography Scanning electron microscopy
Sub-microstructure	Lamella	3-7 μm	Scanning electron microscopy Transmission electron microscopy
	Collagen fibers	1-2 μm	Scanning electron microscopy Transmission electron microscopy
	Collagen fibrils	<0.5 μm	Scanning electron microscopy Transmission electron microscopy
Nanostructure	Collagen fibrils/ molecules HAP mineral phase	<100 nm	High resolution transmission electron microscopy Scanning transmission electron microscopy (STEM) Atomic force microscopy (AFM)
Sub-nanostructure		<1 nm	Scanning transmission electron microscopy Atomic force microscopy (AFM) STEM-Electron energy-loss spectroscopy (EELS) Energy-filtered transmission electron microscopy (EFTEM) Scanning transmission x-ray microscopy (STXM) Synchrotron

Therefore, at its primary level (nm scale) bone is a nanocomposite of mineral and organic phases. The mechanical properties of bone are directly dependent on the individual properties of

the collagen and HAP [4, 11]. The mineral phase, HAP, gives bone its stiffness and strength. The organic matrix, comprising mainly type I collagen, gives bone its fracture toughness and ultimately determines its structural organization.

1.3. Background of the biomineralized hydroxyapatite inside clay galleries sample used for EELS studies

Bone-tissue engineering is the holy grail of regenerative medicine. Its focus is to address critical bone defects that cannot heal on their own due to events such as bone disease, trauma, infection, tumor removal, battlefield injuries, or hereditary bone abnormalities. This need for replacement or repair of damaged bone is the reason HAP and polymeric nanocomposites have been investigated as biomaterials for bone-tissue engineering. Recent work in our group has created a synthetic route to produce biomimetic HAP biomineralized inside amino-acid-modified clay galleries within a polymer scaffold system for use in bone-tissue engineering applications [12, 13].

In the early 1990s, Langer and Vacanti introduced tissue engineering as an interdisciplinary field applying principles of biology and engineering to development of functional biological substitutes for damaged tissues and organs [14]. Tissue engineering uses three-dimensional scaffolds seeded with cells as a "template" for tissue regeneration. Ideally, scaffold materials are biocompatible and biodegradable, with adequate mechanical properties as well as correct pore size and interconnected porosity so that they are suitable for seeded cells to proliferate and form the desired tissue.

Scaffolds made from synthetic polymeric materials have been studied extensively because their properties can be controlled through synthesis routes. Synthetic polymer systems have good mechanical and degradation properties but poor biocompatibility and toxic

degradation products. Bio-polymer-based scaffolds have excellent biocompatibility and nontoxic degradation products, but poor mechanical strength and uncontrolled degradation rates. To overcome the poor attributes of synthetic polymeric and bio-polymeric systems, polymeric composite scaffolds have been investigated. For example, HAP has been used to prepare polymeric composite scaffolds for bone-tissue-engineering studies due to its excellent osteoconductivity, nontoxicity, non-immunogenicity, and high biological affinity toward proteins.

HAP biomaterials have been used successfully as bone substitutes in the treatment of defects in human bone tissue because they are bioactive and non-allergenic, and they have excellent biocompatibility [15] [16]. The poor mechanical properties and resorption rates of HAP bioceramics, however, have limited their use for repair or total hard-tissue replacement [17-20].

Hydroxyapatite coatings have been used on surfaces of metal implants to improve bonding with bone [21]. Hydroxyapatite ceramics synthesized using standard sintering methods have been used as replacements for bone grafts but lack the interconnected porosity needed for osteoconductivity [22]. Foam-gel synthesis techniques have improved porosity of HAP ceramics for bone-tissue-engineering materials [23]. Still, despite its many favorable characteristics, poor mechanical properties limit the use of HAP as a scaffold material. However, polymer-HAP composites have been synthesized using biomimetic processes to provide bioactive porous scaffolds that are osteoconductive and osteoinductive [24].

Polymer clay nanocomposite (PCN) systems are created when small quantities of organically modified montmorillonite (MMT) clay are added to polymers [25, 26]. The resulting

PCNs show improved material properties compared to the initial polymer system, including improved mechanical properties, decreased flammability, and enhanced degradation.

Our group developed the “altered phase” model for PCNs based on experimental and simulation studies showing that molecular interactions among polymer, clay, and modifier components result in enhanced material properties of the polymer [27]. Localized interactions of polymer with intercalated nanoclay blocks alter the crystallization of the polymer. The modifier backbone chain length and functional groups also have an effect on the intercalation (d-spacing) and nanomechanical properties of the PCN [28].

Extending the application of PCNs to tissue engineering, MMT clay intercalated with unnatural amino acids was investigated [29]. Montmorillonite clay modified with 5-aminovaleric acid was found to be biocompatible in cell-culture experiments. Composite films of MMT clay modified with 5-aminovaleric acid and chitosan/polygalacturonic acid (ChiPgA) permitted rapid reproduction of human osteoblast cells in cell cultures, making them intriguing biomaterials for tissue-engineering applications. Fourier transform infra-red (FTIR) spectroscopic investigations and molecular modeling simulations of clay-polymer and clay-organic-modifier interactions in PCNs were used to evaluate the extent of molecular interactions [30].

To use amino-acid-modified clays for bone-tissue engineering applications, HAP must be incorporated into the system. Our group has reported a novel biomineralization route of HAP in MMT clay modified with 5-aminovaleric acid (in-situ HAPclay) [13]. Transmission FTIR used to investigate the molecular interactions between modifier, clay, and HAP in the in-situ HAPclay system confirmed the formation of HAP within the modified MMT galleries. Chelation of dissociated carboxylic groups of the modified clay with calcium ions was observed through peak shifts in the corresponding spectra, and mineralization is thought to occur at the functional

groups of the amino-acid modifier within the clay galleries. Studies using X-ray diffraction (XRD) showed the formation of apatite in modified MMT clay with subsequent shifts in the corresponding apatite peaks in the in-situ HAPclay, indicating that the apatite formed within the in-situ HAPclay has a different lattice structure than HAP. Films containing ChiPgA and in-situ HAPclay were used in cell-culture experiments with human osteoblast cells. Human osteoblast cells were found to adhere and cluster on the surface of the films, indicating good biocompatibility.

In related work, the response of human mesenchymal stem cells (hMSC) to films and scaffolds formed from a ChiPgA/in-situ HAPClay composite were studied using imaging and assay techniques [31]. The in-situ HAPclay mediated the osteoinductive and osteoconductive response from hMSCs, which adhered to scaffolds and formed mineralized bone nodules on the films.

In a recent study to investigate molecular interactions of PCN systems, molecular dynamics was used to construct representative models of 5-aminovaleric acid MMT clay and the corresponding in-situ HAPClay system [32]. Transmission electron microscopy, XRD, and FTIR were used to validate the models. Highly attractive and repulsive interactions were found between PO_4^{3-}, MMT clay, and aminovaleric molecules as well as large non-bonding interactions which indicate influence of the environment surrounding PO_4^{3-} in the in-situ HAPclay model. Considerable hydrogen bonding was found between the functional-group hydrogen atoms of the modifier and MMT clay in the in-situ HAPclay as compared to the 5-aminovaleric acid MMT clay indicating the HAP interaction with the clay was through the aminovaleric acid.

Molecular modeling studies of biological mineral-organic nanocomposite systems have shown that mineral proximity influences the mechanical properties of the organic phase [33].

Molecular interactions of ex-situ/in-situ HAP polymer composite interfaces have been studied using photoacoustic FTIR spectroscopy [34].

In in-situ HAPclay, the unique morphology, structure, and stoichiometry of the biomineralized HAP relates to the molecular interactions between the nanoclay, amino acid modifiers inside the clay galleries, and biomineralized HAP. Additional studies incorporating biomineralized in-situ HAPclay into polymer scaffold systems and seeding with human mesenchymal stem cells have resulted in the human mesenchymal stem cells being driven towards differentiation into osteoblastic lineages without the use of growth media. These demonstrated superior biological functions have indicated that this biomineralized in-situ HAPclay system is an effective component for tissue engineering bone-scaffold applications.

1.4. Background of the healthy and diseased human bone samples used for EELS studies

When the complex biomineralization process during bone formation is interrupted or the availability of components is limited by factors such as nutrition, age, or genetic mutation, diseases affecting bone structure occur. One such genetic disease is osteogenesis imperfecta (OI). Osteogenesis imperfecta (also known as brittle-bone disease) is an inheritable disease characterized by an increase in bone fragility, low bone mass, and bone deformity, and is caused primarily by mutation in collagen type I genes [35]. Sillence [36] and colleagues classified OI into four clinical types based on genetic, clinical and radiographic criteria, with type I (mild) being the least severe, type IV moderate, type III severe, and type II lethal. Approximately 90% of OI cases result from a variant in one of the two structural genes (COL1A1 and COL1A2) for type I procollagens. There is no known cure for OI. Patients are treated with various supplements in an attempt to manage the effects of the disease and increase quality of life. Osteogenesis imperfecta bone provides an interesting system for molecular-level investigations because the

abnormality is initiated by a variant at the molecular level within the structural genes and then expressed as changes in structure and mechanics at the whole-bone level.

A series of PA-FTIR experiments performed in our group on healthy and OI-diseased human bone revealed information about the stoichiometry of HAP with respect to longitudinal and transverse directionality within the bone. In the earliest reported study [37], directionality of the molecular interactions was probed using PA-FTIR spectroscopy by testing NHB (healthy) bone in the longitudinal and transverse directions. Comparison of those PA-FTIR spectra indicated that the mineral in the longitudinal surface is more stoichiometric than its transverse counterpart and the surface area of the longitudinal section of bone appears to have more organic matter exposed with higher stoichiometry. Further PA-FTIR experiments comparing NHB and OIHB sample spectrum revealed a slightly altered mineral structure in OIHB [38]. These spectra also show that the OIHB mineral is more attachable to water and more non-stoichiometric than NHB, which is related to the altered mineral environment. Additionally, it was found that OIHB has the same HAP orientational stoichiometry as NHB, i.e. the longitudinal direction is more stoichiometric than transverse. The NHB and OIHB samples used in the EELS studies reported in this dissertation were from the same bone samples previously used in the PA-FTIR studies reported by our group in [37,38].

PA-FTIR spectroscopy can detect changes at the molecular level in the form of shifting of the frequency of functional groups specific to the strength or weakness of the corresponding bond. This spectroscopic technique is limited in resolution from hundreds of nanometers into the micron range, which is essentially from the bulk of the sample. In contrast, EELS in the TEM can provide information about the electronic structure of the material with high spatial resolution from a specific area.

Heathy human bone samples are relatively easy to obtain from tissue banks, while diseased bone such as those with OI are immensely more difficult to obtain. There is a need for a more proactive effort to encourage patients with rare bone diseases to consider tissue donation. Donated OIHB tissue is in high demand and therefore in short supply in tissue banks. Availability of NHB and OIHB samples to non-medical researchers is very limited and, perfectly matched samples are next to impossible to obtain. For this study, we were not able to procure perfectly matched NHB and OIHB samples from the available national tissue banks. Therefore, the bone samples used in study were selected to meet certain criteria which would help eliminate many of the factors that could potentially affect the formation of bone. The NHB and OIHB samples we obtained from NDRI were consistent in race (Caucasian), and gender (female), and similar in age (22 and 27 years old). This age range was targeted to eliminate the role of post-menopausal osteoporosis and other age related changes. Availability of donated tissue played a large role in how the samples were chosen. Gender and race were easy to match, while finding a similar age was a little more difficult. We acquired the healthy human femur early in the study and later we were not able to find the same bone type for the OIHB, as only the tibia was available. The samples were matched according to the best available samples that closely fit the criteria. See Appendix A for a detailed description of each bone.

The NHB and OIHB samples used in this study were obtained from National Disease Research Interchange (NDRI, Philadelphia, PA; www.ndriresource.org) on separate dates. Prior to obtaining the bone samples, our research protocol summary "Multi-scale Modeling of Mechanics of Bone: Experimental and Modeling Studies" was submitted to NDRI and the North Dakota State University Institutional Review Board (NDSU-IRB) for approval. On 05/26/2009, the NDSU-IRB determined that our protocol did not require approval or certification of exempt

status as it did not fit the regulatory definition of “research involving human subjects” because the bone samples were collected from deceased individuals. The letter summarizing the decision is included as Fig A.1.

We acknowledge that the sample size (n=1 for NHB and OIHB) may not be adequate for addressing a host of important questions that arise and is insufficient for a statistical study. For statistical reasons, increased numbers of OIHB samples and more closely controlled (matched) samples are required. In future work, a statistical study of multiple matched samples of NHB and OIHB can be performed if the samples are available.

This dissertation represents an initial study using an EELS technique that has not been applied to OIHB and NHB for comparison of the electronic structure of the HAP mineral and we feel this is an important starting point. The results of this study are valuable because they provide new information about this disease as well as previously unreported information about the HAP mineral in healthy human bone. Specifically, changes to mineralization in OIHB have not been reported earlier and disclose a novel characteristic of the OI disease that needs to be addressed in therapies.

1.4.1. Normal human bone sample

On 08/05/2009 we obtained from NDRI a 22-cm proximal portion of a human femur (Fig A.2) from a 27-year-old Caucasian female whose cause of death was trauma due to a motor-vehicle accident on 06/30/2006. NDRI harvested the tissue and stored it frozen at -80C until our procurement. The NDRI donor summary is found in Fig A.2.1.

1.4.2. Diseased human bone sample

On 11/05/2012 we obtained a 21-cm distal portion of an osteogenesis-imperfecta diseased human tibia from NDRI (Fig A.3). The tibia from a 22-year-old Caucasian female

whose cause of death was an accidental overdose of methadone on 12/30/2005. NDRI harvested the tissue and stored it at -80C until our procurement. The NDRI donor summary is found in Fig A.3.1.

1.5. Transmission electron microscopy and electron energy loss spectroscopy

Characterization of mineral composition at the primary level of biomineralized tissues such as bone is challenging and requires instrumentation with nanometer-scale spatial resolution. Transmission electron microscopy (TEM) combines high spatial resolution with visual correlation of diffraction and elemental-composition data.

Electron energy-loss spectroscopy (EELS) is a sensitive technique used to probe electronic structure at the molecular level [39]. The high-energy (>100 keV) electrons of a TEM pass through thin foil samples (<100 nm) and can be used to produce transmitted electron images and spectroscopic data from extremely small volumes of sample. Therefore, TEM-based EELS is the only technique available that can provide information about the chemical and coordination environment of minerals with nm scale resolution. It has been used to measure the dielectric functions of semiconductors, superconductors, metals, and ceramics [40-43].

The EELS spectrum represents the result of the disturbance created by the electrostatic interactions of the incident electron with the sample electrons, the spectrum consists of three unique regions: zero loss peak (ZLP), low loss (0-50 eV), and core loss (> 50 eV).

The ZLP represents the elastically scattered electrons which have undergone no energy loss and or have an energy loss that is too small to measure. The ZLP is the most dominant feature and used as a reference (0 eV). The width of the ZLP relates to the energy distribution of the emission source of the TEM and generally has a range from 0.2 -2 eV.

The low-loss region of the EELS spectrum (0-50 eV) represents the interaction of the incident electrons with the outer shell (valence) electrons of the sample atoms and reflects the solid-state character of the sample. This interaction produces single-electron and collective electron excitations. Single-electron excitations occur when a process in which an electron in the valence band of an insulator or a semiconductor material is excited into a low-energy unoccupied states above the Fermi level; these transitions are referred to as inter-band transitions. The dominant feature of the low-loss region results from excitation of collective resonances of valence electrons by the primary electron, known as a plasma resonance and taking the form of a longitudinal traveling wave [39]. The primary electron typically loses 5-30 eV when exciting a plasma resonance. Energy of the plasmon peak is directly related to the density of valence electrons.

Features in the core-loss region (>50 eV) of the EELS spectrum are called ionization edges. These arise from excitation of a core electron into unoccupied electron states through interaction with the incident electron beam. Ionization-edge values indicate an energy-loss value equivalent to the critical ionization of that particular core electron from a specific element. The relative edge intensity can be used to measure the composition quantitatively.

Fine spectral details that are routinely found 0-50 eV beyond the ionization edge are called electron loss near-edge structure (ELNES). While ionization edges are due to electron transitions into unoccupied electronic states, ELNES is a reflection of the energy distribution of those unoccupied states (referred to as unoccupied density of states, DOS). Conditions of the local atomic environment (e.g., element-specific coordination, valency, and anisotropic density of states) affect ELNES and are used to elucidate electronic structure of materials [34].

1.6. Theory of EELS

Incident electrons passing through a sample in a TEM are scattered when they interact with the atomic nucleus or electrons of the material. This interaction is governed by electrostatic (Coulomb) forces due to the charged nature of the particles involved. These interactions can be either elastic, where the incident electron responds to the field of the nucleus; or inelastic, where the incident electron interacts with surrounding electrons. Interaction of an incident electron with an atomic nucleus results in an elastic scattering event. This interaction usually produces an immeasurably small because the nuclear mass greatly exceeds the rest mass of an electron, causing very little energy to be exchanged. Inelastic scattering is a result of the Coulomb interaction between the incident electron and atomic electrons. Unlike the elastic scattering event, the mass of the incident electron and atomic electron are similar, allowing a measurable energy loss to be observed. A typical inelastic scattering event results in energy losses ranging from a few electron volts to hundreds of electron volts.

Plasmon excitation is the predominant form of inelastic scattering in solids, occurring when outer-shell electrons such as valence electrons in a semiconductor or insulator or conduction electrons in a metal are coupled together through electrostatic forces but are weakly bound to the atoms of the material. As a result, their quantum states are delocalized, forming an energy band.

A fast-moving electron passing through a solid displaces nearby atomic electrons by Coulomb repulsion, which in turn creates a region of positive potential that trails behind the electron and is called a correlation hole. When the speed of the interacting electron exceeds the Fermi velocity, the response by the atomic electrons is oscillatory and results in regions of alternating positive and negative space charge along the electron path, a *plasmon wake*. The

wake periodicity in the direction of the electron trajectory is $\lambda_\omega = v/f_p$, where f_p is a plasma frequency (Hz) given by

$$2\pi f_p = \omega_p = \left[\frac{ne^2}{\varepsilon_0 m}\right]^{1/2} \quad (1)$$

where *n* is the density of the conduction or valence electrons and *m* is their effective mass. The plasma frequency is on the order of 10^{16} Hz, which corresponds to the ultraviolet region within the electromagnetic spectrum [44].

The movement of the electron through the solid results in energy loss due to the backward attractive force of the positive correlation hole and is described by the creation of pseudoparticles (plasmons) with the energy quantum expressed as

$$E_p = hf_p = \left(\frac{h}{2\pi}\right)\omega_p \quad (2)$$

where h is Planck's constant and f_p is the plasmon frequency. Inelastic scattering of the transmitted electron can be considered a creation of a plasmon at each scattering occurrence and produces peaks in the low loss spectrum equivalent to the E_p and multiples of that energy. Plasmon energy values for most materials fall in the range of 5-30 eV energy loss and are generally greater than the band gap.

The interaction of the electromagnetic wave property of the incident electron with the electrons of the sample allows the dielectric properties of the specimen to be elucidated through features in the energy-loss spectrum. The dielectric function is an intrinsic property of a material representing the response from the disturbance created through the interaction of the entire sample with the incident electron beam in the TEM. The dielectric function is a complex quantity dependent on both angular momentum, q, and frequency, ω, [$\boldsymbol{\varepsilon}(q,\omega)$]. This is the same response function that describes the interaction of photons with a solid and it allows correlation of energy

loss data with optical measurements in the visible/ultra-violet regions of the electromagnetic spectrum to properties such as refractive index, absorption, and reflection coefficients. The complete material response to the fast incident electron is known as the dielectric response function, represented by the imaginary part of the inverse dielectric function, Im[-1/ $\boldsymbol{\varepsilon}$(q,E)]; it describes the form of the low loss EELS spectrum corrected for thickness. The energy loss function (ELF) is represented by

$$Im\left[\frac{-1}{\varepsilon(E)}\right] = \frac{\varepsilon_2}{\varepsilon_1^2+\varepsilon_2^2} \tag{3}$$

where ε(E) is a complex permittivity consisting of a real part (ε_1) and an imaginary part (ε_2) in the form $\varepsilon = \varepsilon_1 + i\varepsilon_2$.

The dielectric response function is related to the double-differential cross section which gives the exact form of the EELS spectrum as

$$\frac{d^2\sigma}{d\Omega dE} \approx \frac{Im\left[-\frac{1}{\varepsilon(q,E)}\right]}{\pi^2 a_0 m_0 v^2 n}\left(\frac{1}{\theta^2+\theta_E^2}\right) \tag{4}$$

where $d^2\sigma/d\Omega dE$ represents the total electron scattering cross section, a_0 is the Bohr radius ($\varepsilon_0 h/(\pi m_0 e^2 t)$), ν is velocity, m_0 is rest mass, n is density of free electrons, e is electron charge, θ is scattering angle, θ_E is characteristic scattering angle ($E/(\gamma m_0 v^2)$), and γ is relativisitic correction ($(1-v^2/c^2)^{-1/2}$).

After using Fourier log deconvolution to remove the multiple scattering effects from the low loss spectrum, the single scattering distribution function (SSD) can be obtained by integrating Eq. (4)

$$SSD = \frac{2I_0}{\pi a_0 m_0 v^2}\, Im\left[\frac{-1}{\varepsilon(\omega)}\right] \int_0^\beta \frac{\theta\, d\theta}{\theta^2+\theta_E^2} \tag{5}$$

where I_0 is zero-loss intensity, t is sample thickness, and β is collection semi-angle of the spectrometer entrance aperture. Because the dielectric response function is a causal quantity, the

real part of the response function (Re[1/ **ε**(E)]) can be calculated from the imaginary part (Im[-1/ **ε**(E)]) by using Kramer's-Kronig relations

$$Re\left(\frac{1}{\varepsilon(E)}\right) = 1 - \frac{2}{\pi} P \int Im\left[\frac{-1}{\varepsilon(E')}\right] \frac{E' dE'}{E'^2 - E^2} \quad (6)$$

where P is the Cauchy part of the integral and the dielectric function is $\varepsilon = \varepsilon_1 + i\varepsilon_2$.

Using experimentally obtained values of Im(-1/ **ε**) and the value of Re(1/ε), ε_1 and ε_2 can then be calculated from Eqs. (4) and (6)

$$\varepsilon_1 = \frac{Re\left(\frac{1}{\varepsilon}\right)}{\left[Re\left(\frac{1}{\varepsilon}\right)\right]^2 + \left[Im\left(\frac{-1}{\varepsilon}\right)\right]^2} \quad (7)$$

$$\varepsilon_2 = \frac{Im\left(\frac{-1}{\varepsilon}\right)}{\left[Re\left(\frac{1}{\varepsilon}\right)\right]^2 + \left[Im\left(\frac{-1}{\varepsilon}\right)\right]^2} \quad (8)$$

Material properties such as AC conductivity provide insight into the electronic nature of materials [45]; AC conductivity (κ) can be calculated from the dielectric functions ε_1 and ε_2 as

$$\kappa = \frac{E\varepsilon_2}{2\hbar} \quad (9)$$

Collective electron excitations are represented by ε_1 while the fine structure on ε_2 plots indicates single-electron transitions.

1.7. References

[1] A. Sobczak, Z. Kowalski, and Z. Wzorek, "Preparation of hydroxyapatite from animal bones," (in eng), *Acta of bioengineering and biomechanics,* vol. 11, no. 4, pp. 23-28, 2009.

[2] A. B. Barry, A. A. Baig, S. C. Miller, and W. I. Higuchi, "Effect of age on rat bone solubility and crystallinity," *Calcified Tissue International,* journal article vol. 71, no. 2, pp. 167-171, August 01 2002.

[3] W. J. Landis, K. J. Hodgens, J. Arena, M. J. Song, and B. F. McEwen, "Structural relations between collagen and mineral in bone as determined by high voltage electron microscopic tomography," *Microscopy research and technique,* vol. 33, no. 2, pp. 192-202, 1996.

[4] S. Weiner and H. D. Wagner, "The material bone: Structure mechanical function relations," *Annual Review of Materials Science,* vol. 28, pp. 271-298, 1998.

[5] N. Reznikov, R. Shahar, and S. Weiner, "Bone hierarchical structure in three dimensions," *Acta biomaterialia,* vol. 10, no. 9, pp. 3815-3826, 2014.

[6] A. J. Hodge, J. A. Petruska, and A. J. Bailey, "The subunit structure of the tropocollagen macromolecule and its relation to various ordered aggregation states," *Structure and function of connective and skeletal tissue. Butterworths, London,* pp. 31-41, 1965.

[7] P. Fratzl, H. S. Gupta, E. P. Paschalis, and P. Roschger, "Structure and mechanical quality of the collagen-mineral nano-composite in bone," *Journal of Materials Chemistry,* vol. 14, no. 14, pp. 2115-2123, 2004.

[8] W. J. Landis *et al.*, "Mineralization of collagen may occur on fibril surfaces: evidence from conventional and high-voltage electron microscopy and three-dimensional imaging," *Journal of structural biology,* vol. 117, no. 1, pp. 24-35, 1996.

[9] S. Weiner and W. Traub, "Bone structure - from angstroms to microns," *Faseb Journal,* vol. 6, no. 3, pp. 879-885, Feb 1992.

[10] T. Nakano *et al.*, "Unique alignment and texture of biological apatite crystallites in typical calcified tissues analyzed by microbeam X-ray diffractometer system," *Bone,* vol. 31, no. 4, pp. 479-487, 2002.

[11] S. Lees and C. L. Davidson, "The role of collagen in the elastic properties of calcified tissues," *Journal of Biomechanics,* vol. 10, no. 8, pp. 473477-475486, 1977.

[12] A. H. Ambre, K. S. Katti, and D. R. Katti, "Nanoclay based composite scaffolds for Bone tissue engineering applications," *Journal of Nanotechnology in Engineering and Medicine,* vol. 1, no. 3, pp. 031013-031013, 2010.

[13] A. Ambre, K. S. Katti, and D. R. Katti, "In situ mineralized hydroxyapatite on amino acid modified nanoclays as novel bone biomaterials," *Materials Science and Engineering: C,* vol. 31, no. 5, pp. 1017-1029, 2011.

[14] R. Langer and J. P. Vacanti, "Tissue engineering," *Science,* vol. 260, no. 5110, pp. 920-926, 1993.

[15] M. Vallet-Regi, "Ceramics for medical applications," *Journal of the Chemical Society, Dalton Transactions,* no. 2, pp. 97-108, 2001.

[16] L. L. Hench, "Bioceramics: from concept to clinic," *Journal of the American Ceramic Society,* vol. 74, no. 7, pp. 1487-1510, 1991.

[17] W. Suchanek and M. Yoshimura, "Processing and properties of hydroxyapatite-based biomaterials for use as hard tissue replacement implants," *Journal of Materials Research*, vol. 13, no. 01, pp. 94-117, 1998.

[18] K. S. Katti, "Biomaterials in total joint replacement," *Colloids and Surfaces B-Biointerfaces*, vol. 39, no. 3, pp. 133-142, Dec 2004.

[19] S. M. Best, A. E. Porter, E. S. Thian, and J. Huang, "Bioceramics: Past, present and for the future," *Journal of the European Ceramic Society*, vol. 28, no. 7, pp. 1319-1327, 2008.

[20] S. Bose, M. Roy, and A. Bandyopadhyay, "Recent advances in bone tissue engineering scaffolds," *Trends in Biotechnology*, vol. 30, no. 10, pp. 546-554, 2012.

[21] R. A. Surmenev, M. A. Surmeneva, and A. A. Ivanova, "Significance of calcium phosphate coatings for the enhancement of new bone osteogenesis – A review," *Acta Biomaterialia*, vol. 10, no. 2, pp. 557-579, 2014.

[22] H. Zhou and J. Lee, "Nanoscale hydroxyapatite particles for bone tissue engineering," *Acta Biomaterialia*, vol. 7, no. 7, pp. 2769-2781, 2011.

[23] H. Yoshikawa, N. Tamai, T. Murase, and A. Myoui, "Interconnected porous hydroxyapatite ceramics for bone tissue engineering," *Journal of The Royal Society Interface*, 2008.

[24] D. Lickorish, J. A. Ramshaw, J. A. Werkmeister, V. Glattauer, and C. R. Howlett, "Collagen–hydroxyapatite composite prepared by biomimetic process," *Journal of Biomedical Materials Research Part A*, vol. 68, no. 1, pp. 19-27, 2004.

[25] M. Alexandre and P. Dubois, "Polymer-layered silicate nanocomposites: preparation, properties and uses of a new class of materials," *Materials Science and Engineering: R: Reports*, vol. 28, no. 1–2, pp. 1-63, 2000.

[26] S. Pavlidou and C. D. Papaspyrides, "A review on polymer–layered silicate nanocomposites," *Progress in Polymer Science*, vol. 33, no. 12, pp. 1119-1198, 2008.

[27] D. Sikdar, S. M. Pradhan, D. R. Katti, K. S. Katti, and B. Mohanty, "Altered phase model for polymer clay nanocomposites," *Langmuir*, vol. 24, no. 10, pp. 5599-5607, May 2008.

[28] D. Sikdar, D. R. Katti, K. S. Katti, and B. Mohanty, "Influence of backbone chain length and functional groups of organic modifiers on crystallinity and nanomechanical properties of intercalated clay-polycaprolactam nanocomposites," *International Journal of Nanotechnology*, vol. 6, no. 5-6, pp. 468-492, 2009.

[29] K. S. Katti, A. H. Ambre, N. Peterka, and D. R. Katti, "Use of unnatural amino acids for design of novel organomodified clays as components of nanocomposite biomaterials,"

Philosophical Transactions of the Royal Society A: Mathematical, Physical and Engineering Sciences, vol. 368, no. 1917, pp. 1963-1980, 2010.

[30] D. Sikdar, D. R. Katti, K. S. Katti, and R. Bhowmik, "Insight into molecular interactions between constituents in polymer clay nanocomposites," *Polymer,* vol. 47, no. 14, pp. 5196-5205, Jun 2006.

[31] A. H. Ambre, D. R. Katti, and K. S. Katti, "Nanoclays mediate stem cell differentiation and mineralized ECM formation on biopolymer scaffolds," *Journal of Biomedical Materials Research Part A,* vol. 101, no. 9, pp. 2644-2660, 2013.

[32] D. R. Katti, A. Sharma, A. H. Ambre, and K. S. Katti, "Molecular interactions in biomineralized hydroxyapatite amino acid modified nanoclay: In silico design of bone biomaterials," *Materials Science and Engineering: C,* vol. 46, no. 0, pp. 207-217, 2015.

[33] P. Ghosh, D. R. Katti, and K. S. Katti, "Mineral proximity influences mechanical response of proteins in biological mineral-protein hybrid systems," *Biomacromolecules,* vol. 8, no. 3, pp. 851-856, Mar 2007.

[34] K. S. Katti, D. Sikdar, D. R. Katti, P. Ghosh, and D. Verma, "Molecular interactions in intercalated organically modified clay and clay–polycaprolactam nanocomposites: Experiments and modeling," *Polymer,* vol. 47, no. 1, pp. 403-414, 2006.

[35] F. Rauch and F. H. Glorieux, "Osteogenesis imperfecta," *The Lancet,* vol. 363, no. 9418, pp. 1377-1385, 2004.

[36] D. Sillence, A. Senn, and D. Danks, "Genetic heterogeneity in osteogenesis imperfecta," *Journal of medical genetics,* vol. 16, no. 2, pp. 101-116, 1979.

[37] C. Gu, D. R. Katti, and K. S. Katti, "Photoacoustic FTIR spectroscopic study of undisturbed human cortical bone," *Spectrochimica Acta Part A: Molecular and Biomolecular Spectroscopy,* vol. 103, no. 0, pp. 25-37, 2013.

[38] C. Gu, D. R. Katti, and K. S. Katti, "Microstructural and photoacoustic infrared spectroscopic studies of human cortical bone with osteogenesis imperfecta," *JOM,* vol. 68, no. 4, p. 1116, 2016.

[39] R. Egerton, *Electron energy-loss spectroscopy in the electron microscope*. Springer Science & Business Media, 2011.

[40] G. Brockt and H. Lakner, "Nanoscale EELS analysis of dielectric function and bandgap properties in GaN and related materials," *Micron,* vol. 31, no. 4, pp. 435-440, 2000.

[41] K. S. Virdi *et al.*, "Electronic structure of $KCa_2Nb_3O_{10}$as envisaged by density functional theory and valence electron energy loss spectroscopy," *Physical Review B,* vol. 87, no. 11, p. 115108, 2013.

[42] B. J. Murdoch, D. G. McCulloch. and J. G. Partridge, "Structural and dielectric properties of energetically deposited hafnium oxide films," *Semiconductor Science and Technology*, vol. 29, no. 12, p. 125014, 2014.

[43] K. S. Katti, M. X. Qian, F. Dogan, and M. Sarikaya, "Dopant effect on local dielectric properties in barium titanate based electroceramics determined by transmission EELS," *Journal of the American Ceramic Society*, vol. 85, no. 9, pp. 2236-2243, Sep 2002.

[44] R. F. Egerton, "Electron energy-loss spectroscopy in the TEM," *Reports on Progress in Physics*, vol. 72, no. 1, p. 016502, 2009.

[45] H. Raether, *Excitation of Plasmons and Interband Transitions by Electrons*. Springer Berlin Heidelberg, 2013.

CHAPTER 2. FLUENCE RATE CALCULATIONS FOR THE JEOL-JEM-2100 LAB_6 TRANSMISSION ELECTRON MICROSCOPE

2.1. Introduction

The TEM electron beam can cause radiation damage to the bulk structure or surface of the sample depending on the nature of the sample, the electron source, and acquisition parameters of the TEM. The numerous electron-beam/sample interactions related to damage in the TEM and scanning transmission electron microscope have been studied extensively [1-3]. In short, mechanisms of electron-beam damage are complex and vary greatly with the sample material. Electron-beam damage is caused through two scattering mechanisms, elastic and inelastic.

Elastic scattering represents electrostatic deflection of the incident electrons by the Coulomb field of each atomic nucleus in the sample. Production of electron-diffraction patterns along with diffraction and phase-contrast images in the TEM are examples of useful functions of elastic scattering. When incident electrons transfer kinetic energy and momentum to the sample displacing atoms, this elastic scattering is termed knock-on damage. Knock-on damage occurs at high radiation doses in metallic and semi-metallic samples at a threshold incident energy above 200 keV for medium to heavy Z elements. However, electron-beam sputtering (displacement of surface electrons) has a lower threshold and is more common [4]. Electron sputtering occurs rapidly with use of a focused aberration-corrected electron probe is used where the current density routinely exceeds 10^6 A cm^{-2}.

Inelastic scattering represents Coulomb interaction of incident electrons with the atomic electrons that surround each nucleus in the sample. It produces secondary electrons for TEM imaging, the emission of x-rays used for chemical analysis in energy dispersive x-ray

acquisitions, and electron-energy loss spectroscopy. Electron-beam damage caused by inelastic scattering of the incident beam is called radiolysis or ionization damage and results from the breaking of chemical bonds in polymers and organic and inorganic materials. Under certain conditions beam damage can be observed visually; however, this is not always the case. Having knowledge of the electron dose delivered at each illumination condition for the particular TEM being used is critical for the accuracy of the data required. Field-emission TEM with or without aberration correction can easily produce current densities exceeding 10^6 A cm^{-2} which drastically increases the possibility of electron-beam damage occurring and ultimately changing the sample. With these high-resolution instruments "low-dose" techniques or direct-electron detection cameras are used to reduce the amount of electron dose the sample receives.

Transmission electron microscopes with LaB_6 emitters produce less beam-current density compared to the field-emission TEMs. However, the possibility of damage still exists. The electron dose and electron dose rate is unique to each instrument and the conditions used for imaging or data acquisition, e.g. EELS experiments. Therefore, it is in our best interest to determine if the dose rate exceeds the critical dose threshold of 100 x 10^6 electrons nm^{-2} for HAP [5]. The method of calculation of the electron dose and electron dose rate for each spot size available on the JEOL 2100-LaB_6 TEM at North Dakota State University is reported in this chapter.

In techniques such as x-ray micro-computed tomography, radiation damage is dependent on the energy absorbed by the sample and its mass. Due to the required thinness (< 100 nm) of the samples for TEM/STEM experiments, almost all of the incident electrons pass through the sample. The sample ionization cross-sectional area is extremely small; only a negligible portion of the electrons will be scattered laterally and eventually absorbed after multiple scattering

events. Therefore, the energy from inelastic scattering represents only a small portion of the total energy from the incident electron beam. The electron dose (fluence) is the number of incident electrons impinging on the sample during an exposure. It represents the strength of irradiation in the TEM/STEM experiment and is defined as the product of dose rate (fluence rate or current density) and exposure (illumination) time.

For each beam-sensitive sample there is thought to be a "dose threshold" or "critical dose" at or below which beam damage is negligible [6]. Eddisford et al. [5] reported a critical dose threshold of 100 x 10^6 electrons nm^{-2} for hydroxyapatite. They identified a radiolytic damage process loss of phosphorus and oxygen in HAP by monitoring the Ca/P ratio using EDS or EELS which occurred at fluences above 100 x 10^6 electrons nm^{-2} at 200 kV in a field emission or LaB_6 TEM.

In this chapter, we calculate the fluence of the JEOL JEM-2100 LaB_6 at all available beam probe sizes (spot sizes) to determine if any exceed the critical dose threshold of 100 x 10^6 electrons nm^{-2} determined by Eddisford et al. [5] This is a critical value to obtain before we proceed with the subsequent EELS experiments in chapters 2 and 3 in order to establish that the beam conditions are not producing sample damage/alteration.

2.2. Experimental

These experiments were carried out using a JEOL JEM-2100 LaB_6 TEM with the accelerating voltage set to 200 kV. The TEM was operated in energy-dispersive x-ray mode and diffraction mode with a 2-cm camera length at 200,000x magnification, the same conditions used to acquire EELS data for the samples in Chapters 3 and 4. The beam-current density at the specimen was obtained from the read-out of the current density on the viewing screen without a sample inserted. The dose rate for each spot size condition was calculated using Equation 2.1.

$$\left(\frac{pA}{CM^2}\right)\left(\frac{(magnification)CM}{cm}\right)^2\left(\frac{1\,x\,10^{-12}\,A}{pA}\right)\left(\frac{cm^2}{1\,x\,10^{14}nm^2}\right)\left(\frac{6.25\,x10^{18}\,e^-/_s}{1\,A}\right) \quad (2.1)$$

Where CM is the distance (cm) at the sample, cm is distance (cm) at the viewing screen, $\left(\frac{pA}{CM^2}\right)$ is the read-out of the current density at the viewing screen, $\left(\frac{(Magnification)CM}{cm}\right)^2$ is the magnification setting of the microscope and used as conversion factor to bring the screen distance (cm) to the sample distance (cm). The remaining terms are known conversion factors.

2.3. Results

The calculated electron dose rate and electron dose per 100-second acquisition at each spot size setting on the JEOL JEM-2100 LaB_6 TEM is listed in Table 2.1.

Table 2.1. Calculated electron dose rate and electron dose for JEOL-JEM-2100 LaB_6 TEM at North Dakota State University.

Spot Size (nm)	Current Density $\left(\frac{pA}{CM^2}\right)$	Dose Rate $\left(\frac{e^-/_s}{nm^2}\right)$	Dose/100s $\left(e^-/_{nm^2}\right)$
0.5	0.4	1×10^3	1×10^5
1.0	0.8	2×10^3	2×10^5
2.0	1.6	4×10^3	4×10^5
3.0	6.4	1.6×10^4	1.6×10^6
5.0	16.0	4×10^4	4×10^6
10	80	2×10^5	2×10^7
15	188	4.7×10^5	4.7×10^7
25	508	1.3×10^6	1.3×10^8

2.4. Conclusions

The calculated dose rate for the JEOL JEM-2100 LaB_6 operating under the conditions (10-nm spot size) set for EELS acquisition for the proceeding experiments was 2×10^5 $e^-/s/nm^2$. The electron dose for the a 100s acquisition was 2×10^7 e^-/nm^2. This value is an order of magnitude less than the critical dose threshold for HAP (100×10^6 e^-/nm^2) reported previously [5]. Using a spot size of 15 nm or smaller under these conditions should place the electron dose below the critical dose threshold of 100×10^6 e^-/nm^2. Increasing the spot size to 25 nm increases the electron dose into the 10^8 range where the possibility exists for radiolytic damage and it is recommended to use damage-reduction methods such as low-dose technique, specimen cooling, reduction of the incident intensity, or reduced incident beam diameter [7].

2.5. References

[1] R. F. Egerton, P. Li, and M. Malac, "Radiation damage in the TEM and SEM," *Micron,* vol. 35, no. 6, pp. 399-409, 2004.

[2] R. F. Egerton, "Electron energy-loss spectroscopy in the TEM," *Reports on Progress in Physics,* vol. 72, no. 1, p. 016502, 2009.

[3] N. Jiang and J. C. H. Spence, "On the dose-rate threshold of beam damage in TEM," *Ultramicroscopy,* vol. 113, pp. 77-82, 2012.

[4] R. F. Egerton, R. McLeod, F. Wang, and M. Malac, "Basic questions related to electron-induced sputtering in the TEM," *Ultramicroscopy,* vol. 110, no. 8, pp. 991-997, 2010.

[5] P. Eddisford, A. Brown, and R. Brydson, "Identifying and quantifying the mechanism of electronbeam induced damage and recovery in hydroxyapatite," *Journal of Physics: Conference Series,* vol. 126, no. 1, pp. 1-4, 012008, 2008.

[6] R. F. Egerton, P. A. Crozier, and P. Rice, "Electron energy-loss spectroscopy and chemical change," *Ultramicroscopy,* vol. 23, no. 3, pp. 305-312, 1987.

[7] R. F. Egerton, "Control of radiation damage in the TEM," *Ultramicroscopy,* vol. 127, pp.100-108, 2013.

CHAPTER 3. PROBING ELECTRONIC STRUCTURE OF BIOMINERALIZED HYDROXYAPATITE INSIDE NANOCLAY GALLERIES

This chapter presents a unique experimental probe into molecular interactions in complex biomineralized hydroxyapatite structures using EELS. Here we find that the small changes observed in the electron energy loss spectra appear to play important biological roles in biomineralized hydroxyapatite. The content of this chapter has been published in Payne, S. A.; Katti, K. S.; Katti, D. R.; Probing electronic structure of biomineralized hydroxyapatite inside nanoclay galleries. *Micron*, 103, 25-37, 2016.

3.1. Introduction

Through a complex process called biomineralization, living organisms form mineralized tissues for structural support and protection. These mineralized tissues can be considered a nanocomposite consisting of a mineral and an organic phase. Bone is one such mineralized tissue, comprising hydroxyapatite ($Ca_{10}(PO_4)_6(OH)_2$) (HAP) and collagen. The need for replacement or repair of damaged bone has given researchers reason to investigate HAP and polymeric nanocomposites as biomaterials for tissue regeneration in bone tissue engineering.

A novel mineralization route of HAP in montmorillonite (MMT) clay galleries modified with 5-aminovaleric acid has been reported [13]. Characterization of the 5-aminovaleric-acid-modified MMT clay with mineralized HAP (in-situ HAPclay) by Fourier transform infra-red spectroscopy (FTIR) indicated formation of HAP within the modified MMT clay galleries. Further, x-ray diffraction (XRD) demonstrated that the lattice structure of the HAP in modified MMT clay differed from that of synthetically made HAP. The in-situ HAPclay system was then incorporated into chitosan/polygalacturonic acid (ChiPgA) scaffolds and films for bone-tissue engineering studies [31]. When human mesenchymal stem cells (MSCs) were seeded on these

ChiPgA/in-situ HAPclay scaffolds and films, they produced mineralized nodules even without the osteogenic supplements normally needed for differentiation to osteoblasts. The ChiPgA/in-situ HAPclay nanocomposite elicits an osteoconductive and osteoinductive response from MSCs, indicating that this biomaterial system is promising for bone-tissue engineering applications. In a related study, when polycaprolactone (PCL)/in-situ HAPclay composite films were seeded with MSCs, scanning electron microscopy (SEM) showed formation of matrix vesicles [52]. Subsequent high-resolution transmission electron microscopy (TEM) studies showed vesicles containing highly crystalline minerals indicating that this system is favorable for bone mineral formation. Molecular dynamic (MD) simulations were carried out on the HAP/5-aminovaleric acid/MMT system to determine the extent of the molecular interactions among the different components [32]. High attractive and high repulsive interactions were found between PO_4^{3-} and MMT clay. The large non-bonded interaction in the in-situ HAPclay indicates the influence of the neighboring environment on PO_4^{3-}. These computational studies provide a framework for materials design and selection for biomaterials to be used in tissue engineering.

Identification of mineral composition is challenging in elucidating biomineralization processes because mineralization occurs on a level requiring instrumentation with nanometer-scale spatial resolution. The only technique available to directly provide information about the chemical and coordination environment of minerals at nm scale spatial resolution is TEM-based electron energy-loss spectroscopy (EELS). Transmission electron microscopy provides high spatial resolution while allowing visual correlation to diffraction and elemental-composition data. Electron energy-loss spectroscopy is a sensitive technique for probing electronic structure at the molecular level for a variety of materials [40, 43, 53, 54]. The EELS spectrum, created by electrostatic interactions of the incident electron with the sample electrons, consists of three

unique regions: zero loss peak (ZLP), low loss (0-50 eV), and core loss (> 50 eV). Egerton (2011) provides a detailed description of the electron scattering phenomenon and applications to materials characterization. The ZLP represents elastically scattered electrons that have undergone immeasurably small or no energy loss, used as a reference (0 eV), and is the most dominant feature of the EELS spectrum. The width of the ZLP generally 0.2 – 2 eV, is related to energy distribution of the emission source of the TEM. The low-loss region (0-50 eV) represents the interaction of the incident electrons with the outer shell (valence) electrons of the sample atoms. The dominant feature of the low-loss region, resulting from excitation of the collective resonances of valence electrons, is called a plasma resonance and it takes the form of a longitudinal traveling wave [39] Features in the core-loss region (>50 eV) of the EEL spectrum are called ionization edges. These arise from the excitation of a core electron into the unoccupied electron states through interaction with the incident electron beam. Ionization edges are located at an energy loss value equivalent to the critical ionization of that particular core electron from a specific element. The relative edge intensity can be used to evaluate material composition quantitatively. Fine spectral details routinely found 0-50 eV beyond the ionization edge are called electron loss near-edge structure (ELNES) and reflect the energy distribution of those unoccupied states (unoccupied density of states, DOS). Electron loss near-edge structure depends on the local atomic environment such as element-specific coordination, valence, and anisotropic density of states, which are used to elucidate electronic structure of materials. Analytical TEM-EELS has been used to investigate synthetic HAP systems and some types of mineralized tissue, e.g., natural apatite [55, 56] and carbonate from minerals of biological origin [57]. However, low-loss EELS with detailed interpretation of corresponding edges has seldom been employed. High angular annular dark field/TEM-EELS was used to investigate mineral-collagen

interactions in elephant-ivory dentin, which has a structure similar to bone, but detailed interpretation of the corresponding edges was not attempted [58]. Human enamel, peritubular dentin and intertubular dentin have been characterized using EELS/ELNES [59] and near-edge structures have been compared for synthetic and biological bone specimens containing an anti-osteoporotic drug [60].

Because of the importance of these materials for bioengineering applications, TEM-EELS was used to evaluate differences and similarities among HAP, biomimetic in-situ HAPclay, modified MMT clay and β-TCP. In particular, EELS low-loss transitions and ELNES of P-$L_{2,3}$ edges were compared to determine if there are electronic structural differences. Here we report detailed experimental analysis of electron energy-loss spectra from synthetic HAP, biomimetic HAP created using biomineralization routes inside clay galleries (in-situ HAPclay), MMT clay and β-TCP systems.

3.2. Materials and methods

3.2.1. Materials

Sodium montmorillonite (Na-MMT) clay (SWy-2, Crook County, Wyoming USA) with a cation exchange capacity of 76.4 meq/100g was obtained from the Clay Minerals Repository at the University of Missouri, Columbia. The modifier 5-aminovaleric acid and β-TCP were purchased from Sigma-Aldrich. For the preparation of HAP and in-situ HAPclay, sodium phosphate (Na_2HPO_4) was supplied by JT Baker and calcium chloride ($CaCl_2$) by Electron Microscopy Sciences. Lacey carbon on 300 mesh copper grids were purchased from Ted Pella, Inc.

3.2.2. Methods

Hydroxyapatite, modified MMT clay, and in-situ HAPclay previously prepared for use in other studies [13] were used for the current investigations. Preparation of these materials has been described in detail [29, 31, 61, 62] and is summarized here.

3.2.2.1. Preparation of HAP

Hydroxyapatite was prepared using the wet precipitation method [63]: a 39.8 mmol solution of $CaCl_2$ was added dropwise to a 23.8 mmol $NaHPO_4$ solution in distilled water and stirred. The resulting slurry was centrifuged, decanted, washed with distilled water, dried, and sieved to produce HAP powder.

3.2.2.2. Preparation of modified MMT clay

To prepare modified MMT clay, Na-MMT clay was suspended in distilled water heated to 60°C. While stirring, 5-aminovaleric acid was added and the solution was stirred at 60°C for 1 hour. The resulting mixture was centrifuged and the liquid decanted. The remaining slurry was washed with distilled water, centrifuged, decanted, dried at 70°C, and sieved to yield modified MMT clay powder.

3.2.2.3. Preparation of in-situ HAPclay

Modified MMT clay was stirred with a 23.8 mmol solution of $NaHPO_4$ for 2 hours to ensure dispersion. A 39.8 mmol solution of $CaCl_2$ in distilled water was then added dropwise to the suspension and stirred for 8 hours while maintaining a pH of 7.4 by adding NaOH. The solution was allowed to settle for 24 hours and the liquid was decanted. The precipitate was centrifuged to remove excess water and dried at 70°C. The dried precipitate was then sieved and ground to yield in-situ HAPclay.

3.2.2.4. Sample preparation for TEM-EELS experiments

Small amounts of HAP, in-situ HAPclay, β-TCP, and modified MMT clay were placed in separate test tubes. One to two milliliters of absolute ethanol was added to each and the test tubes were placed in a sonication bath for five minutes to disperse the particles. Approximately one microliter of each sample was transferred to a 300-mesh copper TEM grid with a lacey carbon support film. Torn filter paper was used to remove the excess liquid and the grids were air-dried prior to characterization by TEM-EELS.

3.2.2.5. TEM-EELS characterization

Brightfield images and EELS data from each sample were acquired using a JEOL JEM-2100 LaB_6 TEM equipped with a Gatan Orius SC1000 CCD camera and a Gatan ENFINA 1000 electron energy loss spectrometer. All EELS spectra were recorded in diffraction mode with a 10 nm probe size. The convergence angle (α) was 12.53 mrad and the collection semi-angle (β) was 14.43 mrad. Low-loss and core-loss spectra were collected using a 1 mm entrance aperture and a 0.1 eV/channel dispersion. Refer to Appendix D for concise procedures for acquiring EELS data. All spectral data processing was completed using Gatan Microscopy Suite with DigitalMicrograph Software (DM) (ver. 1.85 1535). Background contribution of the ZLP signal was removed from each core-loss spectrum by subtraction of a power-law fit to a window approximately 10 eV wide before the P-$L_{2,3}$ edge. The x-axis window was situated so the background-subtracted spectrum did not intersect the energy-loss axis in the DM preview. Deconvolution of each P-$L_{2,3}$ core loss spectrum was accomplished using the Fourier-ratio method to remove any effects of plural scattering. The P-$L_{2,3}$ core loss spectra then were normalized to the intensity of the 138 eV peak and smoothed using a Savitzky-Golay function. Background subtraction and deconvolution of each low-loss spectrum was done in a single step

using the Fourier-log method. Kramers-Kronig analysis was used to calculate the ε_1 and ε_2 plots and energy loss function (ELF) from each deconvolved low-loss spectrum using a refractive index of 1.63 with 100 iterations. The low-loss spectra were normalized for intensity using the first major peak (~10 eV for ε_1 and ε_2, ~20 eV for ELF) and smoothed using a Savitzky-Golay function. Energy positions for the peaks were determined by superimposing the calculated second derivative spectrum onto the original spectrum.

3.3. Results and discussion

Crystal structures of HAP (Fig 3.1a), β-TCP (Fig 3.1b), organically modified clay (Fig 3.1c) and in-situ HAPclay (Fig 3.1d) are shown in Fig 3.1.

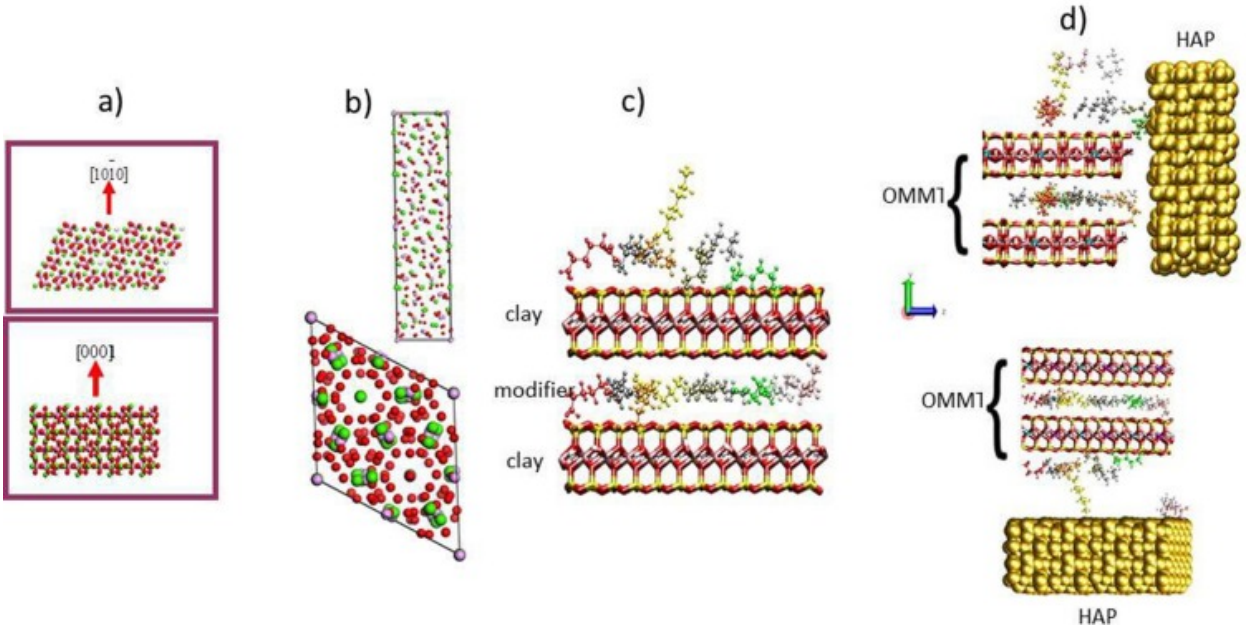

Figure 3.1. Crystal structure of (a)HAP, (b) β-TCP, (c) amino acid modified nanoclay and (d) modified nanoclay-HAP.

Representative TEM images of in-situ HAPclay, HAP, β-TCP, and modified MMT clay are shown in Fig. 3.2(a-h). The low-magnification image of in-situ HAPclay (Fig. 3.2a) shows clusters of grains. The higher-magnification image (Fig. 3.2b) reveals the lattice structure and

biomimetic rounded shapes interspersed within the clay sheets. At low magnification, HAP (Fig. 3.2c) appears similar to in-situ HAPclay (Fig. 3.2a); however, the rounded structures are not present (Fig. 3.2d). Elongated needle-like crystals of β-TCP (Fig. 3.2e) show lattice structure parallel to their long axis at higher magnification (Fig. 3.2f). Modified MMT clay is entirely different from the other samples, with its agglomerated individual clay sheets (Fig. 3.2g); at higher magnification, the lattice pattern of the clay sheets is apparent (Fig. 3.2h). Additional TEM images of in-situ HAPclay, HAP, β-TCP, and modified MMT clay can be found in Appendix F.

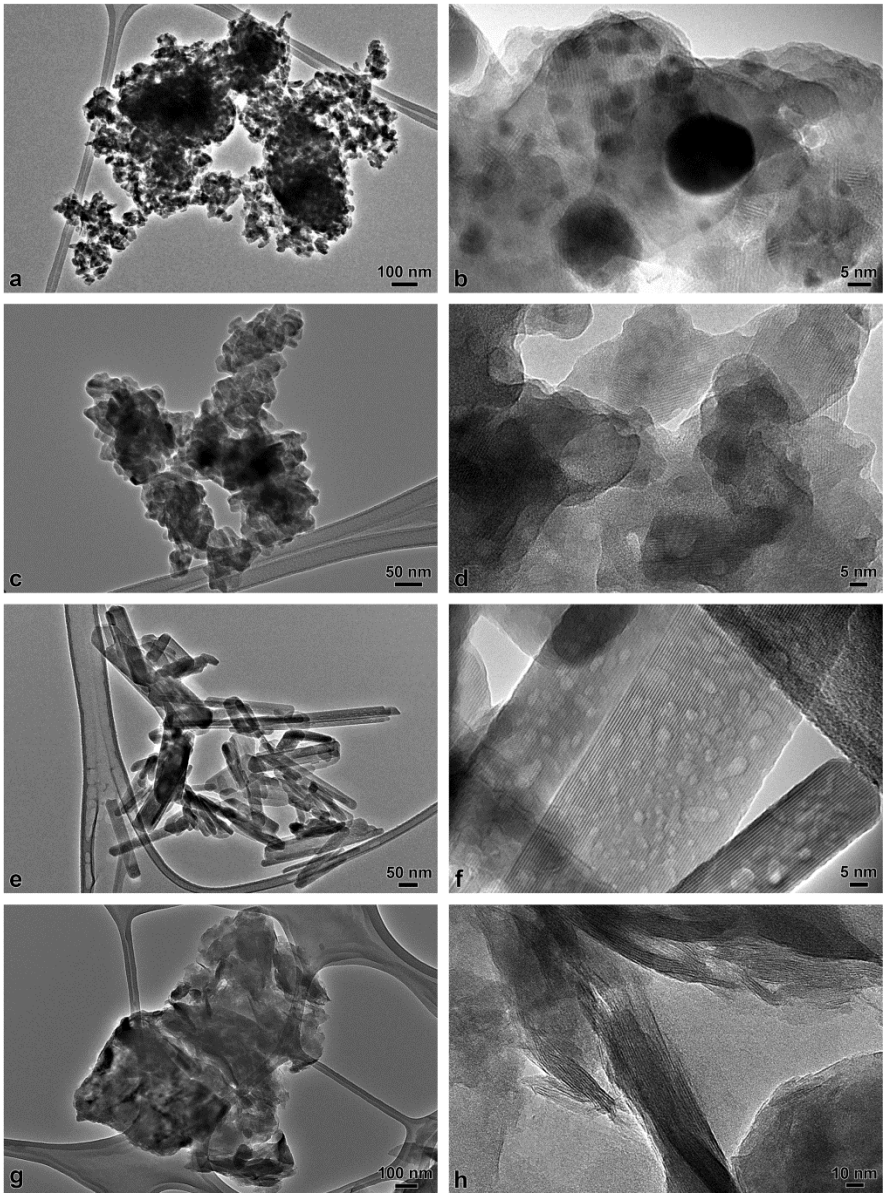

Figure 3.2. TEM images at low-magnification (left column) and high-magnification (right column). (a,b) in-situ HAPclay, (c,d) HAP, (e,f) β-TCP, and (g,h) modified MMT clay.

3.3.1. Low-loss spectra

Electron energy-loss spectroscopy analysis was performed on β-TCP, synthetic HAP, in-situ HAPclay, and modified MMT clay. Two energy-loss ranges were chosen for analysis: (I) the low-loss region from 0-65 eV containing the Ca-$M_{2,3}$ edge (Figs. 3.3-3.4) and (II) the core-loss region from 130-210 eV including the P-L_1 and P-$L_{2,3}$ ionization edges (Fig. 3.6).

Deconvolution by the Fourier-log method subtracted the ZLP and removed contributions from plural scattering for each of the low-loss spectra. The resulting energy loss function (ELF) plots for β-TCP, HAP, and in-situ HAPclay represent single scattering distribution (SSD) functions (Fig. 3.3).

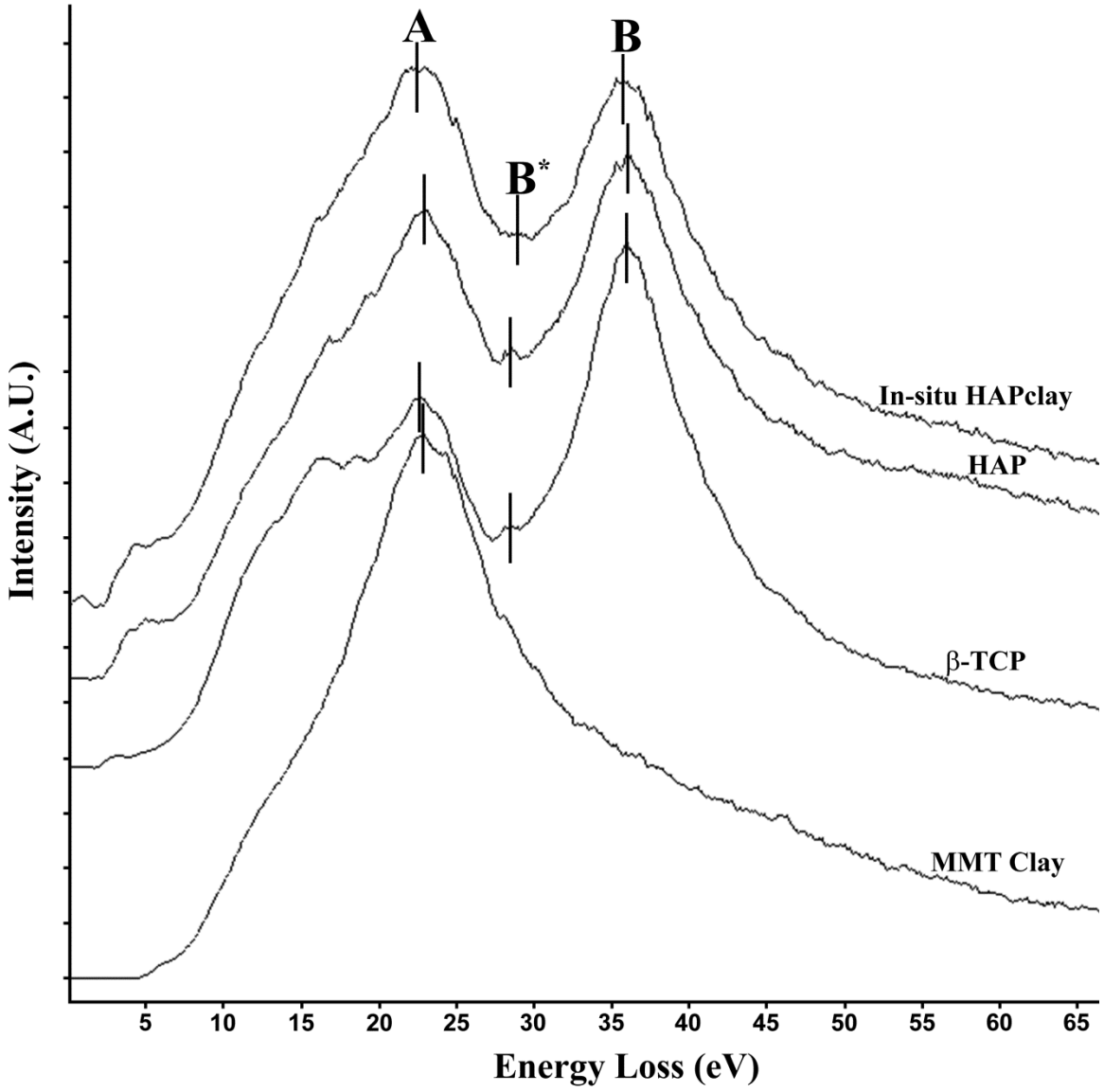

Figure 3.3. Energy Loss Function spectra of in-situ HAPclay, HAP, β-TCP, and modified clay. Peak A corresponds to the plasmon peak, and peaks B and B^* correspond to the calcium $M_{2,3}$ edge. The spectra are separated vertically for clarity and bars denote peak position.

These spectra consistently show two main peaks located at approximately 23 eV and 36 eV, labeled A and B respectively. Modified MMT clay spectra show a single peak at 23 eV. Corresponding peak positions from the energy loss function plots in Fig. 3.2 are summarized in Table 3.1.

Table 3.1. Energy loss function peak positions (eV).

	In-situ HAPclay	HAP	β-TCP	Modified MMT Clay
Peak A	22.7	22.9	22.7	23.0
Peak B*	29.8	28.7	28.5	--
Peak B	35.7	36.4	36.2	--

Peak A is attributed to the bulk plasmon as determined through ε_1- ε_2 comparison (Fig. 3.4). A weak feature (B^*) around 28 eV is present between peaks A and B. Peaks B and B^* correspond to the Ca-$M_{2,3}$ ionization edge [64]. The modified MMT clay spectrum does not exhibit the peaks B and B^* because calcium is absent. Low-loss spectra among samples differ in the presence or absence of fine structure on the low-energy side of peak A. Table 3.2 summarizes peak shifts and peak A:B ratios in the ELF.

Table 3.2. Energy loss function A:B ratio and peak shift (eV).

	In-situ HAPclay	HAP	β-TCP
A:B Ratio	~1	<1	<1
Peak B	-0.7	0	-0.2
Peak B*	+1.3	+0.2	0

Since peak B intensity varies, the A/B peak ratio of the in-situ HAPclay spectrum is close to one, while A/B peak ratios of HAP and β-TCP are less than one. Peak B of in-situ HAPclay is shifted (-0.5 eV) from β-TCP and (-0.7 eV) from HAP. Peak B^* of in-situ HAPclay is shifted

(+1.3 eV) from β-TCP and (+1.1 eV) from HAP. The spectra of β-TCP and HAP are similar to one another, but they differ markedly from the spectrum of in-situ HAPclay.

3.3.2. Kramers-Kronig analysis

Kramers-Kronig analysis was used to calculate ε_1 and ε_2 from the SSD spectrum of each sample: ε_1 represents collective electron excitations (bulk plasmon) (Fig. 3.4a); ε_2 represents single-electron transitions (Fig. 3.4b).

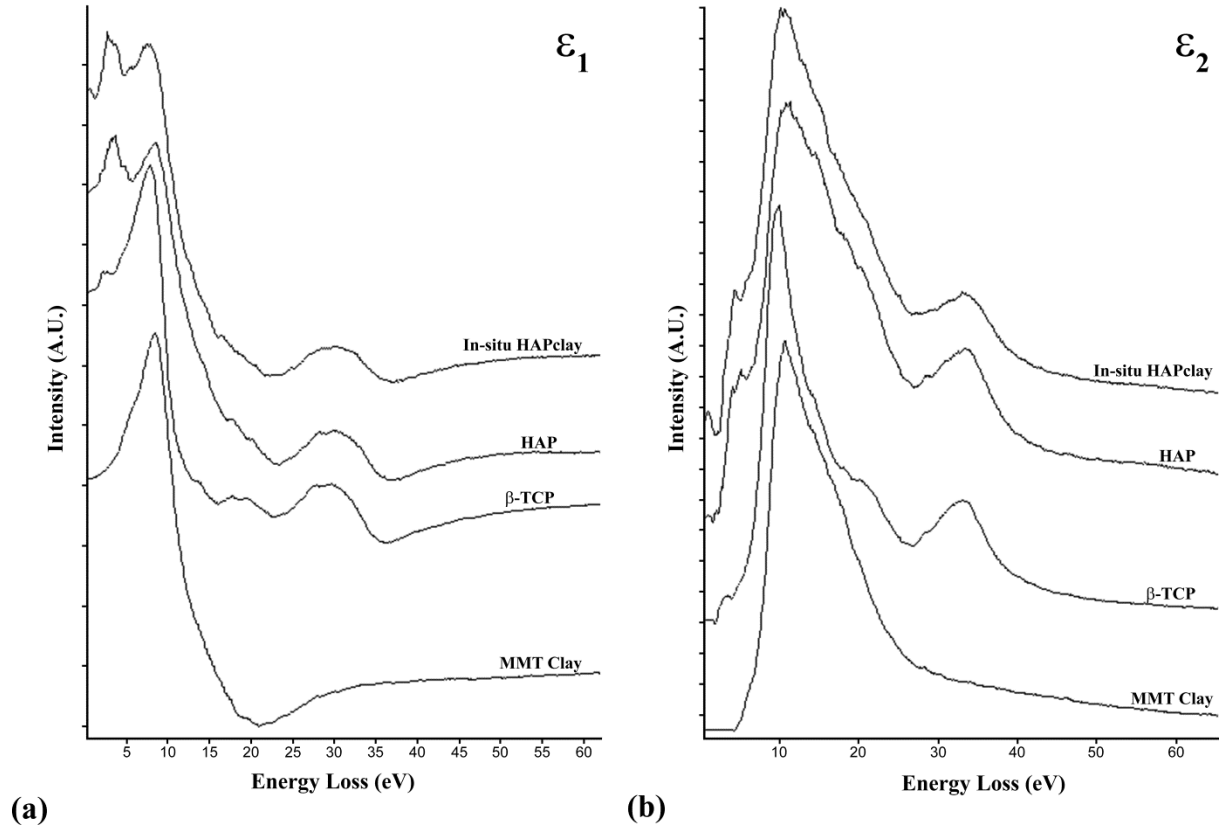

Figure 3.4. The real (ε_1) part (a) and imaginary (ε_2) part (b) of the complex dielectric function obtained from Kramers-Kronig analysis of the EEL spectra for in-situ HAPclay, HAP, β-TCP, and modified MMT clay. Overlaid spectra are separated vertically for clarity.

The ε_1 and ε_2 plots for each sample were compared to determine which features of the low-loss spectra were single transitions and which were due to bulk plasmon resonance. The bulk plasmon resides around 23 eV. The fine structure of the ε_2 plots represents single-electron

transitions related to electronic structure (Fig. 3.4b). Additional representative overlays of ε_2 spectra can be found in Appendix I. Single-electron transitions from the ε_2 plots are summarized in Table 3.3.

Table 3.3. Justifications of ε_2 single-electron transitions (eV).

In-situ HAPclay	HAP	β-TCP	Mod. MMT Clay	Assignment of Electron Transition Origin[Ref]
1.0	--	--	--	
--	--	3.0	--	
4.1	3.9	--	--	
5.8	--	--	--	
9.7	9.8	9.4	10.5	Exciton state [65, 66]
13.3	12.5	--	--	Valence band at -12.9 eV to conduction band edge [67, 68]
15.2	14.8	14.8	--	Valence band to exciton [67, 69]
17.6	--	--	17.4	Valence band to exciton [67, 69]
--	18.5	18.3	--	
19.5	--	--	--	
21.1	20.7	20.5	--	Valence band to exciton [69]
--	22.0	--	--	Valence band to exciton [68, 69]
25.1	--	--	--	O 2s, P 3s to exciton[70-72]
28.8	28.4	28.3	--	O 2s to exciton [69]
30.9	30.6	--	--	
33.3	33.8	33.8	--	O 2s to conduction band [69]

The modified MMT clay ε_2 spectrum shows a major peak at 10.5 eV and a minor peak located at 17.4 eV. No fine structure is seen on the low-energy side of the major peak. The β-TCP ε_2 spectrum is dominated by a narrow and very intense transition at 9.4 eV. There is very little fine structure on the low-energy side of this peak, with a weak transition at 3.0 eV being the only discernible feature. The ε_2 spectra of HAP and in-situ HAPclay are similar, with β-TCP transitions around 9.8, 14.8, 20.5, 28.3 and 33.3 eV. There is more fine structure on the low-energy side of the peak at 9.8 eV for HAP and in-situ HAPclay than for β-TCP. This 9.8 eV peak is broadened by the amount of fine structure located on the high-energy side. While there are

some overlapping transitions between HAP and in-situ HAPclay (3.9, 30.6 eV) that do not overlap with β-TCP, in-situ HAPclay has more unique transitions (1.0, 5.8, 13.3, 17.6, 19.5 and 25.1 eV) than either of the other materials.

The ε_2 plots were used to calculate the high-frequency AC conductivity plots for in-situ HAPclay, HAP, β-TCP, and modified MMT clay (Fig. 3.5). The plots of in-situ HAPclay and HAP are similar to each other and quite different from β-TCP and modified MMT clay.

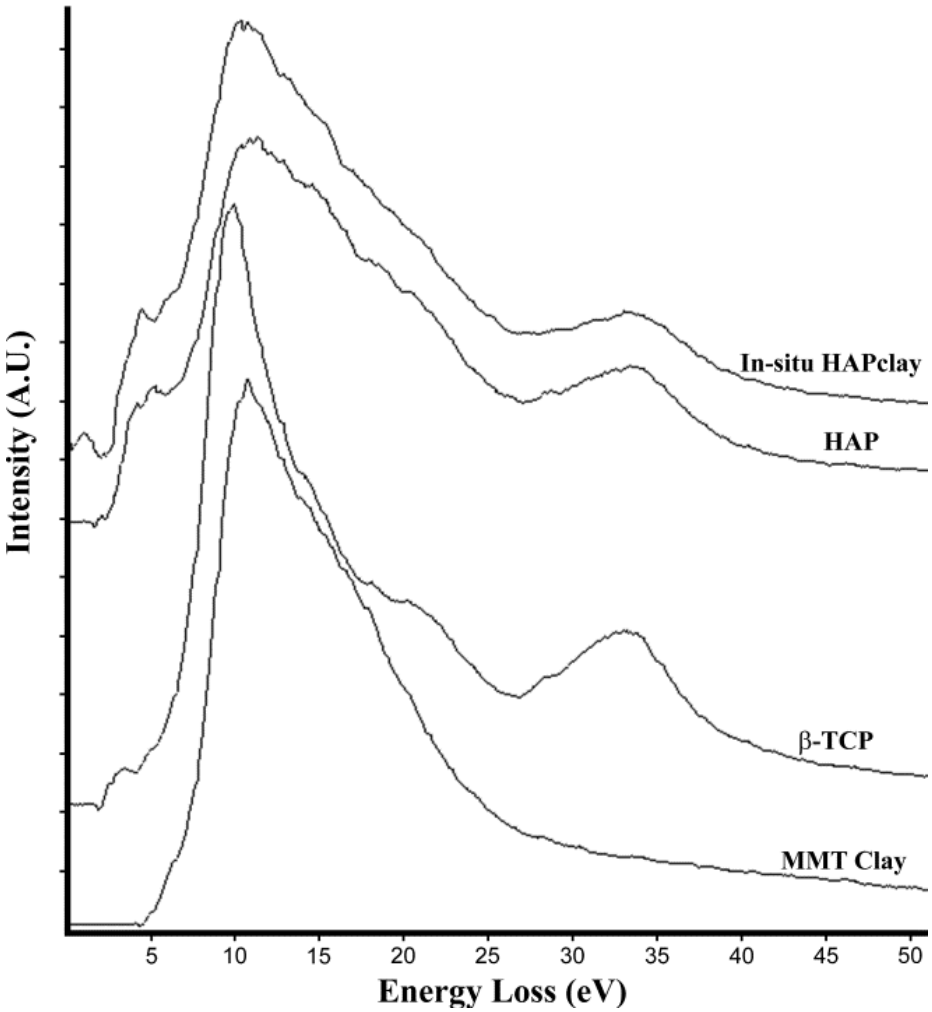

Figure 3.5. Calculated high-frequency AC conductivity plots for in-situ HAPclay, HAP, β-TCP, and modified MMT clay. The overlaid spectra are separated vertically for clarity.

3.3.3. P-$L_{2,3}$-edge spectra

The P-$L_{2,3}$-edge EELS spectra of β-TCP, HAP, and in-situ HAPclay express features in five energy-loss regions (Fig. 3.6), characterized by two sharp peaks located at 138-139 eV (A) and 146-147 eV (B), followed by a broader, more intense peak starting around 153 eV (C). Additional P-$L_{2,3}$ edge overlays can be found in Appendix I.

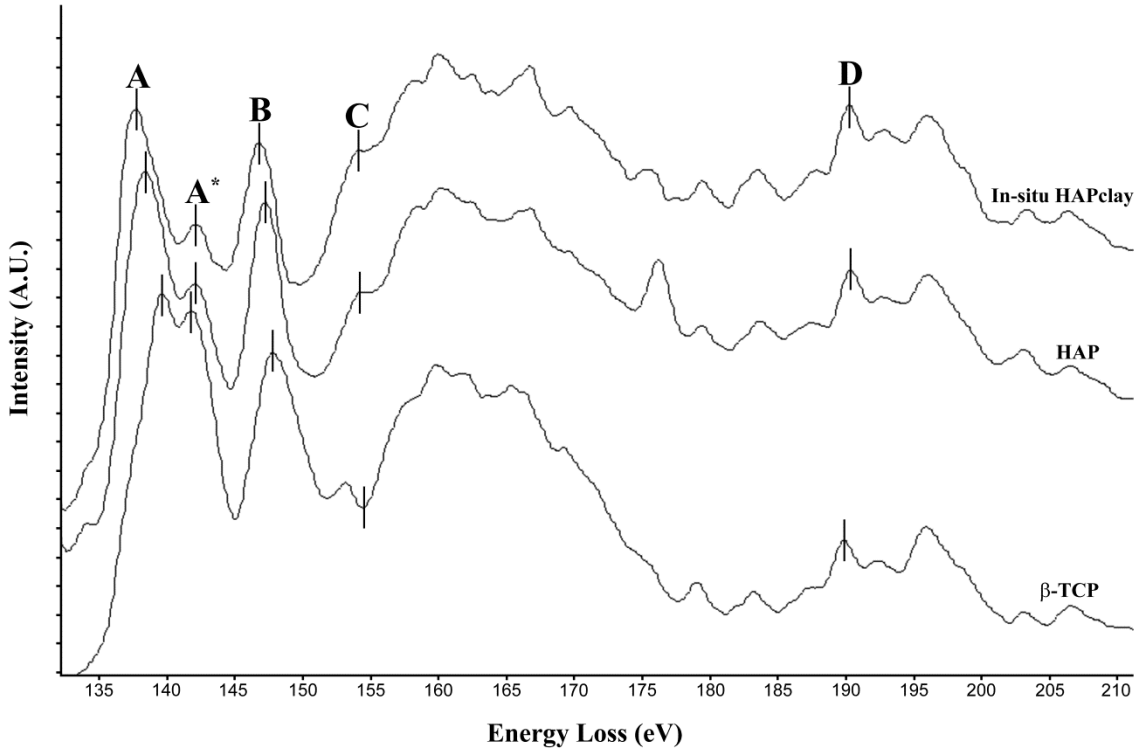

Figure 3.6. Overlay of the P-$L_{2,3}$ core loss region (135-210 eV) obtained from in-situ HAPclay, HAP, and β-TCP. The spectra are separated vertically for clarity. The peak positions (A, B, C, and D) are denoted by vertical lines and discussed in the text.

A weaker feature (A^*) is often located as a shoulder on the high-energy side (+2-3 eV) of peak A. The P-L_1 ionization edge (D) is present around 189 eV. The P-$L_{2,3}$ edge is represented by two peaks, one at 136 eV (P-L_3) and another peak within ~1 eV (P-L_2) due to the transitions from spin-orbit split 2p electrons (2p_{3/2} and 2p_{1/2}) into the first unoccupied 3s-antibonding state [73]. These peaks, while generally difficult to resolve, are most likely located

within the low-energy shoulder of peak A according to synchrotron-based X-ray absorption near-edge structure (XANES) data reported for phosphorus reference compounds [73, 74]. Peak A, located in the 138-139 eV energy-loss region, has been attributed to transitions to the 3p-like antibonding state in the Si L-edge spectrum of SiO_2, which is isoelectronic with PO_4^{3-} [75]. These transitions to dipole-forbidden 3p orbitals are made possible by the mixing of characters from other elements such as oxygen. Peak A^*, located ~142 eV on the high-energy side of peak A, is a broad peak that is unique to calcium phosphates and due to transition of the phosphorus 2p electron to calcium 3d empty orbitals [73], but also may be due to multiple scattering of the outgoing electron [76]. Peak B, located ~147 eV, is known as the d-state resonance or "shape resonance" peak; the energy position of this peak is sensitive to the molecular symmetry and to the local environment of the phosphorus [73, 77]. This peak is followed by a broad peak (C) starting at ~150 eV that corresponds to the position of the atomic cross-section maximum for the phosphorus 2p level relative to its respective 2p ionization edges [76, 78]. The P-$L_{2,3}$ core loss region spectral features for β-TCP, HAP, and in-situ HAPclay as well as transition origins are summarized in Table 3.4.

Table 3.4. P-$L_{2,3}$ edge position (eV) and electronic transition assignments.

Peak	β-TCP	HAP	In-situ HAPclay	Transition Origin [Ref]
Peak A	139.7	138.4	137.8	Transitions to 3p-like anti-bonding state, allowable to dipole forbidden 3p orbitals due to mixed characters from oxygen [75]
Peak A*	141.8	142.0	142.1	Phosphorus 2p to Ca 3d empty orbitals [73, 76]
Peak B	147.8	147.2	146.9	d-state shape resonance peak [73, 77]
Peak C	153.1	154.3	154.1	Atomic cross-section maximum for the P 2p level [76, 78]
Peak D	189.9	190.4	190.3	P L_1 peak [64]

Table 3.5 compares the peak shift values for the sample materials. Peak A*, the P 2p to Ca 3d empty orbital transition, shows small differences in energy values among the three samples.

Table 3.5. P-$L_{2,3}$ shift values.

	In-situ HAPclay shift (eV)		HAP shift (eV)	
	β-TCP	HAP	β-TCP	In-situ HAPclay
Peak A	-1.9	-0.6	-1.3	+0.6
Peak A*	+0.3	+0.1	+0.2	-0.1
Peak B	-0.9	-0.3	-0.6	+0.3
Peak C	+1.0	-0.2	+1.2	+0.2
Peak D	+0.4	-0.1	+0.5	+0.1

The d-state shape resonance peak, labeled Peak B, shows a shift (-0.9 eV) when comparing in-situ HAPclay to β-TCP. There is very small change (-0.3 eV) in the Peak B energy position between in-situ HAPclay and HAP. For the 2p level (peak C) in-situ HAPclay and HAP are shifted +1.0 eV and +1.2 eV respectively from β-TCP. The P-L_1 peak (D) of in-situ HAPclay and HAP show similar energy values while the P-L_1 peak for β-TCP is shifted -0.4 to -0.5 eV from in-situ HAPclay/HAP.

3.4. Conclusions

Clearly the HAP biomineralized inside clay galleries (in-situ HAPclay) is different morphologically from non-biomimetic HAP (Fig. 3.2). The rounded shapes seen in mineralized HAP with amino acid modified nanoclays resemble biogenic HAP in human bone. Shifts in the Ca-$M_{2,3}$ ionization edge in the in-situ HAPclay and HAP in the ELF are indicative of changes to the Ca outer shell interactions providing support for molecular dynamics simulations that predicted large interaction energies with Ca [32, 79]. Further, changes to the valence band of the

in-situ HAPclay are observed compared to the non-biomimetic HAP. Experimentally observed changes in the ε_2 spectra (Fig. 3.4) reflect subtle outer shell changes in the electronic structure as suggested through simulations; they result from biomineralization guided by weak non-bonded interactions between Ca and P from HAP and amino acid groups inside clay galleries. Further, ε_2 was used to calculate the high-frequency AC conductivity plots for in-situ HAPclay, HAP, β-TCP, and modified MMT clay (Fig. 3.5.). Again subtle differences in the valence bands of Ca and P in the in-situ HAPclay are observed. The near-edge structure of the P-$L_{2,3}$ edge was also analyzed. Extremely subtle changes resulting from transitions to the 3p-like anti-bonding state, allowable to dipole-forbidden 3p orbitals due to mixed characters from oxygen [75] (Table 3.3). Thus these EELS studies elucidate the small changes that occur in the valence band and outer electronic structures of HAP mineralized inside clay galleries (in-situ HAPclay). It is interesting to note the biological implications of these differences are significant. The biomineralized in-situ HAPclay used in scaffold systems exhibits superior biological functions, driving human mesenchymal stem cells towards differentiation into osteoblastic lineages without the use of differentiating media [31, 80].

3.5. References

[1] A. Ambre, K. S. Katti, and D. R. Katti, "In situ mineralized hydroxyapatite on amino acid modified nanoclays as novel bone biomaterials," *Materials Science and Engineering: C*, vol. 31, no. 5, pp. 1017-1029, 2011.

[2] A. H. Ambre, D. R. Katti, and K. S. Katti, "Nanoclays mediate stem cell differentiation and mineralized ECM formation on biopolymer scaffolds," *Journal of Biomedical Materials Research Part A*, vol. 101, no. 9, pp. 2644-2660, 2013.

[3] K. S. Katti, A. H. Ambre, S. Payne, and D. R. Katti, "Vesicular delivery of crystalline calcium minerals to ECM in biomineralized nanoclay composites," *Materials Research Express*, vol. 2, no. 4, p. 045401, 2015.

[4] D. R. Katti, A. Sharma, A. H. Ambre, and K. S. Katti, "Molecular interactions in biomineralized hydroxyapatite amino acid modified nanoclay: In silico design of bone biomaterials," *Materials Science and Engineering: C*, vol. 46, no. 0, pp. 207-217, 2015.

[5] G. Brockt and H. Lakner, "Nanoscale EELS analysis of dielectric function and bandgap properties in GaN and related materials," *Micron,* vol. 31, no. 4, pp. 435-440, 2000.

[6] K. S. Katti, M. X. Qian, F. Dogan, and M. Sarikaya, "Dopant effect on local dielectric properties in barium titanate based electroceramics determined by transmission EELS," *Journal of the American Ceramic Society,* vol. 85, no. 9, pp. 2236-2243, Sep 2002.

[7] B. Murdoch, D. McCulloch, and J. Partridge, "Structural and dielectric properties of energetically deposited hafnium oxide films," *Semiconductor Science and Technology,* vol. 29, no. 12, p. 125014, 2014.

[8] K. S. Virdi *et al.*, "Electronic structure of KCa 2 Nb 3 O 10 as envisaged by density functional theory and valence electron energy loss spectroscopy," *Physical Review B,* vol. 87, no. 11, p. 115108, 2013.

[9] R. Egerton, *Electron energy-loss spectroscopy in the electron microscope*. Springer Science & Business Media, 2011.

[10] G. Gregori, H. J. Kleebe, H. Mayr, and G. Ziegler, "EELS characterisation of beta-tricalcium phosphate and hydroxyapatite," *Journal of the European Ceramic Society,* vol. 26, no. 8, pp. 1473-1479, 2006.

[11] S.-C. Liou, S.-Y. Chen, H.-Y. Lee, and J.-S. Bow, "Structural characterization of nano-sized calcium deficient apatite powders," *Biomaterials,* vol. 25, no. 2, pp. 189-196, 2004.

[12] M. M. Kłosowski *et al.*, "Probing carbonate in bone forming minerals on the nanometre scale," *Acta biomaterialia,* vol. 20, pp. 129-139, 2015.

[13] V. Jantou-Morris, M. A. Horton, and D. W. McComb, "The nano-morphological relationships between apatite crystals and collagen fibrils in ivory dentine," *Biomaterials,* vol. 31, no. 19, pp. 5275-5286, Jul 2010.

[14] V. Srot, B. Bussmann, U. Salzberger, C. T. Koch, and P. A. van Aken, "Linking Microstructure and Nanochemistry in Human Dental Tissues," *Microscopy and Microanalysis,* vol. 18, no. 3, pp. 509-523, Jun 2012.

[15] A. L. Rossi *et al.*, "Effect of strontium ranelate on bone mineral: Analysis of nanoscale compositional changes," *Micron,* vol. 56, pp. 29-36, Jan 2014.

[16] K. S. Katti, A. H. Ambre, N. Peterka, and D. R. Katti, "Use of unnatural amino acids for design of novel organomodified clays as components of nanocomposite biomaterials," *Philosophical Transactions of the Royal Society A: Mathematical, Physical and Engineering Sciences,* vol. 368, no. 1917, pp. 1963-1980, 2010.

[17] A. Ambre, K. S. Katti, and D. R. Katti, "In situ mineralized hydroxyapatite on amino acid modified nanoclays as novel bone biomaterials," *Materials Science & Engineering C-Materials for Biological Applications,* vol. 31, no. 5, pp. 1017-1029, Jul 2011.

[18] A. H. Ambre, K. S. Katti, and D. R. Katti, "Nanoclay Based Composite Scaffolds for Bone Tissue Engineering Applications," *Journal of Nanotechnology in Engineering and Medicine,* vol. 1, no. 3, pp. 031013-9, 2010.

[19] D. Verma, K. Katti, and D. Katti, "Bioactivity in in situ hydroxyapatite–polycaprolactone composites," *Journal of Biomedical Materials Research Part A,* vol. 78A, no. 4, pp. 772-780, 2006.

[20] C. C. Ahn and O. L. Krivanek, *EELS Atlas: A Reference Collection of Electron Energy Loss Spectra Covering All Stable Elements*. Gatan, 1983.

[21] Y. M. Alexandrov, V. M. Vishnjakov, V. N. Makhov, K. K. Sidorin, A. N. Trukhin, and M. N. Yakimenko, "Electronic properties of crystalline quartz excited by photons in the 5–25 eV range," *Nuclear Instruments and Methods in Physics Research Section A: Accelerators, Spectrometers, Detectors and Associated Equipment,* vol. 282, no. 2–3, pp. 580-582, 1989.

[22] H. Philipp, "Optical properties of non-crystalline Si, SiO, SiO x and SiO 2," *Journal of Physics and Chemistry of Solids,* vol. 32, no. 8, pp. 1935-1945, 1971.

[23] H. R. Philipp, "Optical and bonding model for non-crystalline SiO x and SiO x N y materials," *Journal of Non-Crystalline Solids,* vol. 8, pp. 627-632, 1972.

[24] H. Ibach and J. Rowe, "Electron orbital energies of oxygen adsorbed on silicon surfaces and of silicon dioxide," *Physical Review B,* vol. 10, no. 2, p. 710, 1974.

[25] D. Griscom, "The electronic structure of SiO 2: a review of recent spectroscopic and theoretical advances," *Journal of Non-Crystalline Solids,* vol. 24, no. 2, pp. 155-234, 1977.

[26] J. A. Rotole and P. M. Sherwood, "Aluminum phosphate by XPS," *Surface Science Spectra,* vol. 5, no. 1, pp. 60-66, 1998.

[27] J. A. Rotole and P. M. Sherwood, "Oxide-free phosphate surface films on metals studied by core and valence band X-ray photoelectron spectroscopy," *Chemistry of materials,* vol. 13, no. 11, pp. 3933-3942, 2001.

[28] I. D. Welsh and P. M. A. Sherwood, "Valence band photoemission studies of corrosion inhibitor action on iron surfaces: effect of etidronate," *Chemistry of Materials,* vol. 4, no. 1, pp. 133-140, 1992.

[29] J. Kruse, P. Leinweber, K.-U. Eckhardt, F. Godlinski, Y. Hu, and L. Zuin, "Phosphorus L2,3-edge XANES: overview of reference compounds," *Journal of Synchrotron Radiation,* vol. 16, no. 2, pp. 247-259, 2009.

[30] J. Cosmidis, K. Benzerara, N. Nassif, T. Tyliszczak, and F. Bourdelle, "Characterization of Ca-phosphate biological materials by scanning transmission X-ray microscopy

(STXM) at the Ca L2,3-, P L2,3- and C K-edges," *Acta Biomaterialia,* vol. 12, no. 0, pp. 260-269, 2015.

[31] G. R. Harp, Z. L. Han, and B. P. Tonner, "X-ray absorption near edge structures of intermediate oxidation states of silicon in silicon oxides during thermal desorption," *Journal of Vacuum Science & Technology A,* vol. 8, no. 3, pp. 2566-2569, 1990.

[32] D. Sutherland, M. Kasrai, G. Bancroft, Z. Liu, and K. Tan, "Si L-and K-edge x-ray-absorption near-edge spectroscopy of gas-phase Si (CH 3) x (OCH 3) 4− x: Models for solid-state analogs," *Physical Review B,* vol. 48, no. 20, p. 14989, 1993.

[33] D. Li, G. M. Bancroft, M. E. Fleet, and X. H. Feng, "Silicon K-edge XANES spectra of silicate minerals," (in English), *Physics and Chemistry of Minerals,* vol. 22, no. 2, pp. 115-122, 1995.

[34] J. J. Yeh and I. Lindau, "Atomic subshell photoionization cross sections and asymmetry parameters: $1 \leqslant Z \leqslant 103$," *Atomic Data and Nuclear Data Tables,* vol. 32, no. 1, pp. 1-155, 1985.

[35] A. Sharma, S. Payne, K. Katti, and D. Katti, "Evaluating Molecular Interactions in Polycaprolactone-Biomineralized Hydroxyapatite Nanocomposites using Steered Molecular Dynamics," (in English), *JOM,* vol. 67, no. 4, pp. 733-743, 2015.

[36] A. H. Ambre, D. R. Katti, and K. S. Katti, "Biomineralized hydroxyapatite nanoclay composite scaffolds with polycaprolactone for stem cell-based bone tissue engineering," *Journal of Biomedical Materials Research Part A,* pp. n/a-n/a, 2014.

CHAPTER 4. AN ELECTRON ENERGY-LOSS SPECTROSCOPIC STUDY OF MOLECULAR INTERACTIONS IN NORMAL AND OSTEOGENESIS IMPERFECTA DISEASED HUMAN BONE

This chapter presents a unique experimental probe into molecular interactions in normal and osteogenesis imperfecta diseased human bone using EELS. Here we find that the small changes observed in the electron energy loss spectra appear to play important biological roles when comparing the normal and diseased bone. Small changes in the valence band and outer electronic structures of the diseased bone have been revealed through EELS. These subtle changes in the electronic structure of the OI diseased bone are caused through a genetic mutation within the collagen which affects HAP mineralization and results in the fragility of bone at the macroscale.

4.1. Introduction

Bone tissue has a complex hierarchical structure spanning multiple length scales (cm to nm). At its primary level, bone is a nanocomposite of mineral and organic phases. The mineral phase is hydroxyapatite [HAP, $Ca_{10}(PO_4)_6(OH)_2$], which gives bone its stiffness and strength. The organic matrix comprises mainly type I collagen, giving bone its fracture toughness and ultimately determining its structural organization. The mechanical properties of bone are directly dependent on the individual properties of the collagen and the HAP [1-3].

Osteogenesis imperfecta (OI), also known as brittle bone disease, is an inheritable disease characterized by increased bone fragility, low bone mass and bone deformity caused primarily by mutation in collagen type I genes. The mineralization of HAP in OI bone and the molecular basis of OI bone disease has generated extensive research interest [4]. Approximately 90% of OI cases result from a variant in one of the two structural genes (COL1A1 or COL1A2) for type I

procollagens, expressed as changes in structure and mechanics at the whole-bone level, making OI an interesting system for molecular-level investigations.

Recent photoacoustic Fourier transform infra-red (Pa-FTIR) spectroscopic investigations of healthy human bone in the longitudinal and transverse directions have shown that bone mineral in longitudinal section is more stoichiometric than in transverse section [5]. Bone mineral was also found to be more structurally disordered and compositionally non-stoichiometric compared to synthetic HAP. Additional Pa-FTIR experiments showed that OI bone mineral overall is more stoichiometric than in healthy human bone; OI bone has orientational stoichiometry of HAP similar to healthy human bone, with the longitudinal direction being more stoichiometric than the transverse direction [6].

Investigation of healthy and diseased bone at the primary mineral-collagen level requires nm-scale spatial resolution. Transmission electron microscopy-based electron energy-loss spectroscopy (TEM-EELS) is the only technique available to provide direct information about the chemical and coordination environment of the HAP in the collagen matrix, combining visual correlation of elemental composition and diffraction data with high spatial resolution. This sensitive technique has been used for molecular-level investigation of a variety of materials including minerals [7] [8]. A recent study reported the use of EELS to investigate the electronic structure of a biomimetic HAP synthesized using biomineralization routes inside the clay galleries of montmorillonite clay [9]. In this complex biomineralized HAP system, small changes identifiable in the EELS spectrum appeared to play an important role in the observed biological activity of the biomineralized HAP.

The EELS spectrum is produced when the TEM incident electron beam interacts with electrons of the sample. A detailed description of EELS technique and its applications to

materials characterization is provided by Egerton [10]; a brief summary follows. Three distinct regions define the EELS spectrum: zero loss peak (ZLP), low-loss region (0-50 eV) and core loss region (>50 eV).

The ZLP (0 kV) is the most prominent feature of the EELS spectrum, used as the reference, and represents elastically scattered electrons that have experienced no measureable energy loss. The width of the ZLP, generally in the range of 0.2-2 eV, is related to energy distribution of the TEM emission source and reflects the energy resolution of the EELS detector.

Interaction of incident electrons with the valence (outer-shell) electrons of sample atoms is represented in the low-loss region and is seen as both plasma oscillations and single electron transitions. Plasma resonance, the dominant feature of the low-loss region, results from excitation of the collective resonances of valence electrons and takes the form of a longitudinal traveling wave [10]. Single-electron transitions are more subdued and reveal subtle changes in electronic structure.

The core-loss region of the EELS spectrum is dominated by features termed ionization edges, attributed to excitation of a core electron into unoccupied electron states through beam-sample interaction. The location of an ionization edge corresponds to the energy-loss value of the critical ionization of a particular core electron from a specific element. Material composition can be evaluated quantitatively using the relative intensity of the ionization edge. Additional ionization-edge features give insight into the molecular make-up of the material. Electron energy-loss near-edge structure (ELNES) is fine spectral detail routinely found 0-50 eV beyond the ionization edge and reflects the energy distribution of those unoccupied orbitals. Electronic structure of materials can be elucidated from ELNES, which depends on the local atomic environment such as valence, anisotropic density of states, and element-specific coordination.

Investigations of normal and diseased bone ultrastructure using TEM have been extensively reported [11-14]. Analytical TEM-EELS has been used to investigate natural apatite systems [15, 16] [17], the effect of strontium on bone mineral composition [18], and the distribution of iron and calcium in bone cells [19, 20]. However, there are few reports of low-loss EELS with detailed interpretation of the corresponding edges for natural healthy or diseased bone or for bone-like systems such as ivory dentin. Mineral-collagen interactions in elephant-ivory dentin were studied using high angle annular darkfield/TEM-EELS by Jantou-Morris [21], but a detailed interpretation of the corresponding low-loss spectra was not provided. Recently, TEM-EELS ELNES was used to characterize human enamel [22], and near-edge structures were compared for synthetic and biological bone specimens treated with an anti-osteoporotic drug [18].

This work characterizes and compares normal human bone (NHB) and osteogenesis imperfecta human bone (OIHB) using TEM imaging, EELS, ELNES, and field-emission scanning electron microscopy (FESEM). Specifically, EELS low-loss transitions of Ca-$M_{2,3}$ and ELNES of P-$L_{2,3}$ edges were used to evaluate electronic structure differences among the following: synthetic HAP, NHB and OIHB. Normal and OI bone were evaluated in both longitudinal and transverse orientations. Imaging with FESEM and TEM was used to compare structure.

4.2. Materials and methods

4.2.1. Materials

Normal human cortical bone and OI human cortical bone were obtained from the National Disease Research Interchange (NDRI, Philadelphia, PA) having been stored in a -70°C freezer until acquisition. The NHB was a femur of a 27-year-old female with no history of

metabolic disease. The OIHB was from the tibia of a 22-year-old female, with patient height (170 cm) and weight (82 Kg) suggesting that the OI was type I (mild). The diagnosis of OI was based on genetic testing. (Refer to Appendix A and B for additional information concerning NHB and OIHB obtained from NDRI)

Calcium chloride ($CaCl_2$) and sodium phosphate (Na_2HPO_4) used in the preparation of hydroxyapatite were supplied by Electron Microscopy Sciences (Hatfield, PA) and JT Baker (Phillipsburg, NJ), respectively. For SEM sample processing, sodium phosphate buffer and 2.5% glutaraldehyde in sodium phosphate buffer were purchased from Tousimis (Rockville, MD), and osmium tetroxide was purchased from Electron Microscopy Sciences (Hatfield, PA). Lacey carbon on 300 mesh copper TEM grids were purchased from Ted Pella, Inc. (Redding, CA).

4.2.2. Methods

4.2.2.1. SEM sample preparation

A diamond wafering blade (Buehler, Isomet 1000, Lake Bluff, IL) was used to cut transverse and longitudinal bone sections approximately 1000 microns thick from the mid-diaphysis. Samples for SEM were fixed in 2.5% glutaraldehyde overnight, washed with sodium phosphate buffer, and post-fixed with 1% osmium tetroxide for 2 h, then were rinsed with buffer and dehydrated through a graded ethanol series, critical-point dried, and fractured in liquid nitrogen. Fractured samples were attached to aluminum mounts using silver paste, coated with carbon (Cressington 208C, Ted Pella, Inc., Redding, CA), and examined using a JSM-7600F field emission scanning electron microscope (JEOL-USA, Peabody, MA).

4.2.2.2. TEM EELS sample preparation

4.2.2.2.1. Hydroxyapatite preparation

HAP was prepared using the wet precipitation method [23, 24] was sonicated in absolute ethanol to disperse the particles. These particles were then collected on a TEM grid.

4.2.2.2.2. NHB and OIHB bone preparation

Mid-diaphyseal transverse (NHB-T and OIHB-T) and longitudinal (NHB-L and OIHB-L) sections ~500-600 μm thick were cut using a low-speed saw with a diamond wafering blade. An ultrasonic disc cutter with boron-carbide slurry (Model 601, Gatan, Inc., Pleasanton, CA) was used to cut a 3-mm diameter disc from the center of each of the transverse and longitudinal sections (bone images and schematic representation of transverse and longitudinal directions found in Appendix B). The discs were thinned manually to approximately half their original thickness using a disc grinder (Model 623, Gatan, Inc., Pleasanton, CA) with successively finer grit diamond paper (40, 15, 6, 3, 1 and 0.5 μm) and water. The disc thickness was measured using a scanning electron microscope (JSM-6490LV, JEOL USA, Peabody, MA) and then the disc was ground from the opposite side to a thickness of approximately 20 μm. A dimple approximately 15 μm deep was created using a dimple grinder (Model 656, Gatan, Inc., Pleasanton, CA) equipped with a phosphor bronze wheel and slurry of 2-4 μm diamond paste. The dimpled area was then polished with a felt wheel saturated with a 0.05 μm alumina polishing slurry. The polished disc was placed in a precision ion polishing system (PIPS) dual-beam ion mill (Model 691, Gatan, Inc., Pleasanton, CA) and milled until a perforation formed. Additional information for TEM sample preparation procedures can be found in Appendix C.

4.2.2.3. TEM-EELS characterization

Bright-field images and EELS data were obtained from with a JEOL JEM-2100 LaB_6 TEM with Gatan Orius SC1000 CCD camera and Gatan ENFINA 1000 electron energy loss spectrometer (refer to Appendix D for acquisition procedures). All EELS spectra were collected in diffraction mode with probe size 10 nm. The microscope convergence angle (α) was 12.53 mrad and the collection semi-angle (β) was 14.43 mrad. Low-loss and core-loss spectra were recorded using a 1 mm entrance aperture and 0.1 eV/channel dispersion. Spectral processing was completed using Gatan DigitalMicrograph (DM) (ver. 1.85 1535). Background subtraction and deconvolution of core-loss spectra and low-loss spectra, along with the subsequent Kramers-Kronig analysis of low-loss spectra used to calculate the energy loss function (ELF) (Fig. 4.3) and the ε_1, ε_2 (Fig. 4.4) plots and was performed as described previously [9]. The ZLP was subtracted and contributions from plural scattering were removed from each of the low-loss spectra through Fourier-log deconvolution. The resultant ELF plots represent single scattering distribution (SSD) functions (Fig. 4.3). For samples of NHB-T, OIHB-T, NHB-L, OIHB-L, and synthetic HAP, two energy-loss regions of each spectrum were selected for investigation: (I) the low-loss region (0-65 eV) containing the Ca-$M_{2,3}$ edge (Figs. 4.3-4.4) and (II) the core loss region (130-210 eV) which includes the P-L_1 and P-$L_{2,3}$ ionization edges (Fig 4.5).

4.3. Results and discussion

4.3.1. FESEM imaging

FESEM images (Fig. 4.1a-l) of the longitudinal and transverse surfaces of NHB and OIHB samples exposed through liquid nitrogen fracture, show distinct morphological differences. Compared to NHB (4.1a,g), OIHB (4.1d,j) is rougher and has more longitudinal sections of Haversian canals (more osteons) Higher magnification images of the transverse

surface of OIHB demonstrate a separation of fibrils from the mineral matrix (Figs. 4.1k,l) compared to the corresponding transverse NHB surface (Figs. 4.1h, i). This reflects a weaker interaction between bone constituents, which relates to the altered collagen structure of the OI diseased bone and results in brittle bones that fracture easily. Additional FESEM images of OIHB and NHB can be found in Appendix E.

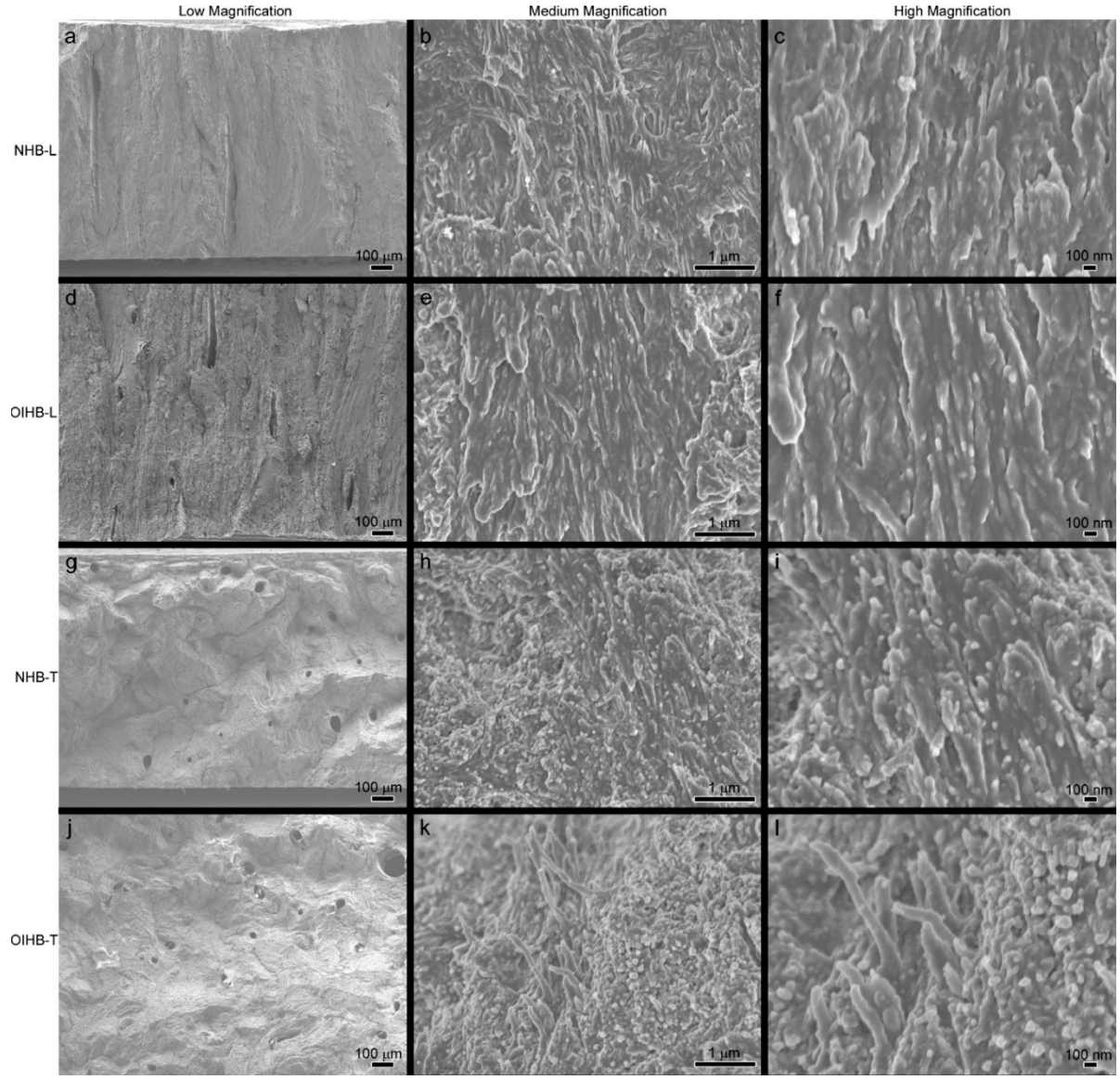

Figure 4.1. FESEM images at low (left column), intermediate (middle column), and high (right column) magnification. (a-c) NHB-L, (d-f) OIHB-L, (g-i) NHB-T, and (j-l) OIHB-T.

4.3.2. TEM imaging

Low magnification TEM images of NHB (Figs. 4.2a,e) and OIHB (Figs. 4.2c,g) show banding (additional TEM images of banding found in OIHB and NHB can be found in Appendix H) and fibril orientation in both longitudinal and transverse views. Mineral atomic lattice patterns are seen in the higher magnification images (Figs. 4.2b,d,f,h) with the lattice being more prevalent in the longitudinal view (Figs. 4.2b,d). In contrast to bone, synthetic HAP shows no banding and only mineral lattice (Figs 4.2i, j). Additional TEM images of OIHB (T,L) and NHB (T,L) can be found in Appendix G.

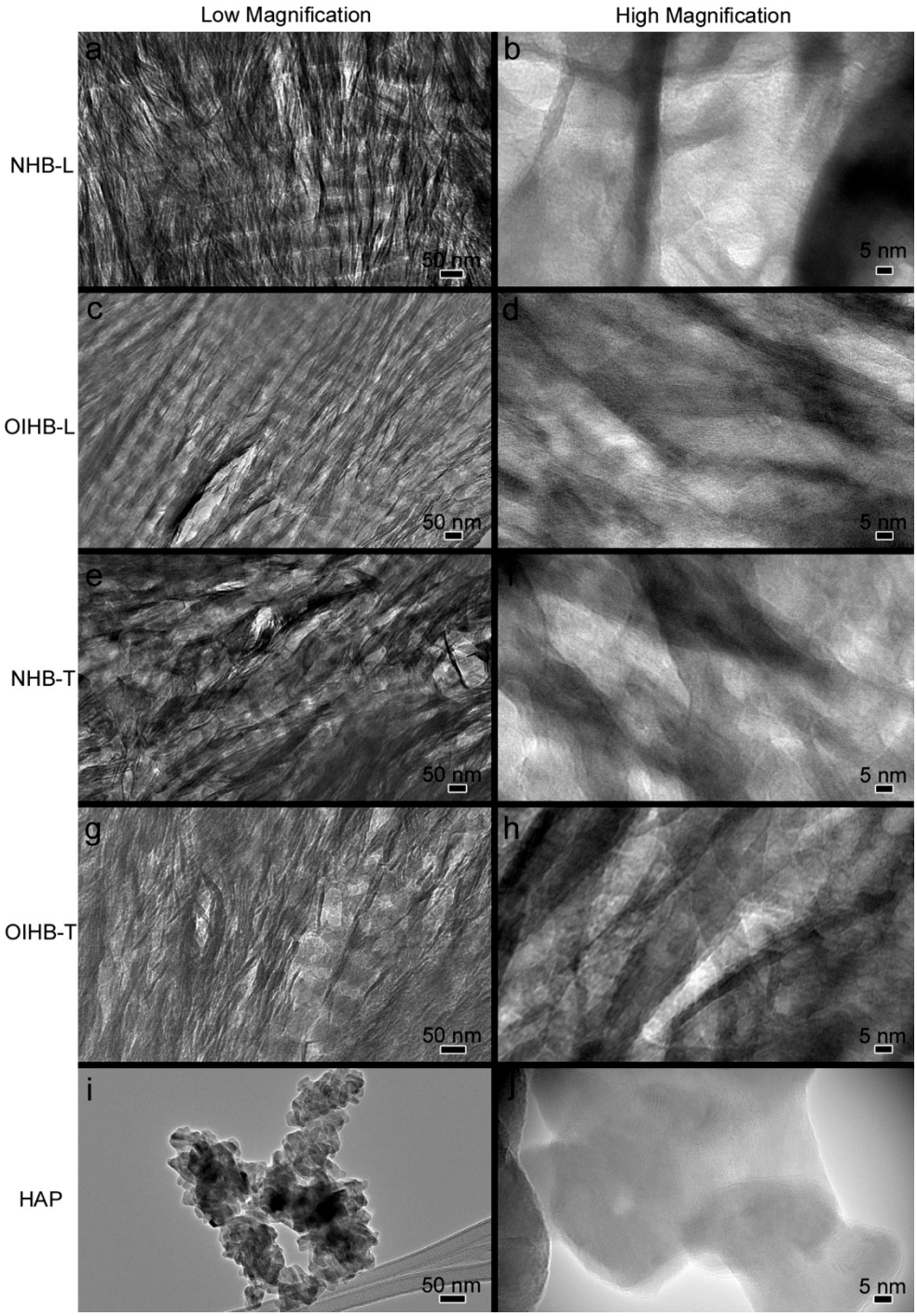

Figure 4.2. TEM images at low-magnification (left column) and high-magnification (right column). (a,b) NHB-L, (c,d) OIHB-L, (e,f) NHB-T, (g,h) OIHB-T, and (i,j) HAP.

4.3.3. Low-loss spectra

ELF spectrum (Fig. 4.3) consistently display two main peaks around 23 eV (A) and 36 eV (B); a weak feature (B^*) is located between A and B near 28 eV. Peak A corresponds to the bulk plasmon, while peaks B and B^* correspond to the Ca-$M_{2,3}$ ionization edge [25]. The presence or absence of fine structure on the low-energy side of peak A differentiates the low-loss spectrum among samples. Table 4.1 summarizes the peak positions for each of the ELF plots in Fig. 4.3. Peak B^* of OIHB-T and OIHB-L is shifted +0.6 eV from NHB-T, and NHB-L is shifted +0.5 eV from HAP. Peak B of OIHB-T is shifted -0.6 eV from HAP, OIHB-L is shifted -0.4 eV from HAP, NHB-T is shifted -0.5 eV from HAP, and NHB-L is shifted -0.7 eV from HAP. The spectra appear similar for all bone samples but differ from the spectrum of HAP. Additional selected overlays of ELF spectra can be found in Appendix I.

Table 4.1. Energy loss function peak positions (eV).

Peak	NHB-T	NHB-L	OIHB-T	OIHBL	HAP
A	22.9	22.8	22.9	22.9	22.9
B^*	28.5	28.5	29.1	29.1	28.6
B	35.9	35.7	35.8	36.0	36.4

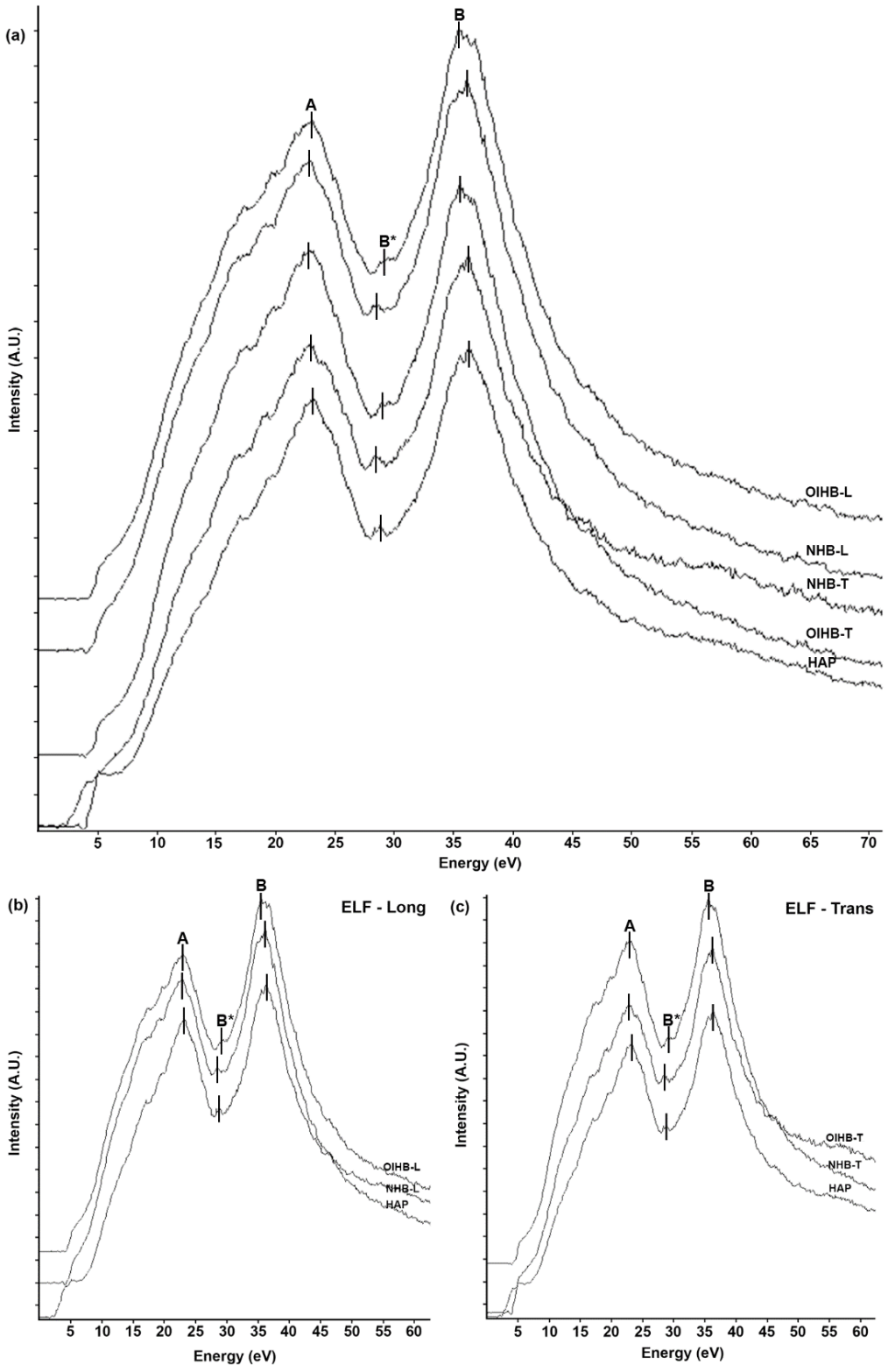

Figure 4.3. Energy Loss Function spectra: (a) OIHB-L, NHB-L, OIHB-T, NHB-T and HAP; (b) overlay of OIHB-L, NHB-L, and HAP; (c) overlay of OIHB-T, NHB-T, and HAP. Bars denote peak position and the spectra separated vertically for clarity.

4.3.4. Kramers-Kronig analysis

Kramers-Kronig analysis was used to calculate ε_1 (Fig. 4.4a) and ε_2 (Figs. 4.4b-d) from the SSD spectrum of each sample, where ε_1 represents collective electron excitations and ε_2 represents single-electron transitions. The bulk plasmon resonance was found to reside around 23 eV. Single-electron transitions related to electronic structure of the sample are represented by the fine structure of the ε_2 spectra and are summarized in Table 4.2 with transition origins identified [26-33]. The ε_2 spectra of NHB-L and OIHB-L (Fig. 4.4c) appear similar, while HAP shows more fine structure on the high-energy side of 10 eV. The ε_2 spectra of NHB-T and HAP are similar (Fig. 4.4d), while OIHB-T has less fine structure on the high energy side of 10 eV. Therefore, OIHB-T and OIHB-L are more like NHB-L than HAP; NHB-T is more similar to HAP. Additional overlays of select ε_1 and ε_2 spectra can be found in Appendix I.

Table 4.2. ε_2 peak positions (eV).

NHB-T	NHB-L	OIHB-T	OIHB-L	HAP	Transition Origin [Reference]
	1.1	1.7		1.0	
2.0	2.4	1.9	1.9	1.8	O 2p and P 3d with small contribution from P 3p and P 4d states [26]
3.1	3.5	3.0	2.9	3.8	
4.9	5.4	5.3	5.3	5.0	O 2p and P 3p states with some P 4p, P 3d and O 2s contribution [26]
6.3				6.3	
7.0	6.9	7.7	7.6	7.2	O 2p and P 3s states with O 2s contributions [26]
8.5	8.7				
9.7	9.4	9.6	9.2	9.0	Exciton state [27,28]
10.9	10.6	10.0	10.0	10.0	
				11.1	
		11.4	11.7	11.8	
12.2	12.2			12.1	Valence band at -12.9 eV to conduction band edge [29,30]
12.8		13.1	13.1	12.8	
14.5	14.6	15.3	15.2	14.7	Valence band to exciton [29,31]
16.1	15.9			16.2	Valence band to exciton [29,31] and O 2s contribution [26]
		16.7	16.9		
18.2	18.4	18.6	18.4	18.6	Ca 3p contribution [26]
20.2	20.2	20.2	19.2	20.5	Valence band to exciton [31]
21.5	21.5	21.0	21.0	21.6	Valence band to exciton [31]
22.3	22.2	22.3	22.4	22.2	Valence band to exciton [30,31]
		22.8	22.7		
24.0	24.2			24.5	
25.1		25.0	25.0		O 2s, P 3s to exciton [32,33]
25.8	25.9	26.4	26.7	26.1	
28.0	28.1	28.7	28.6	28.4	O 2s to exciton [31]
	30.4	30.7		30.6	
31.8	31.9		31.1		
33.2	33.0	32.8	32.9	32.2	O 2s to conduction band [31]
34.1		33.7	33.9	33.8	O 2s to conduction band [31]

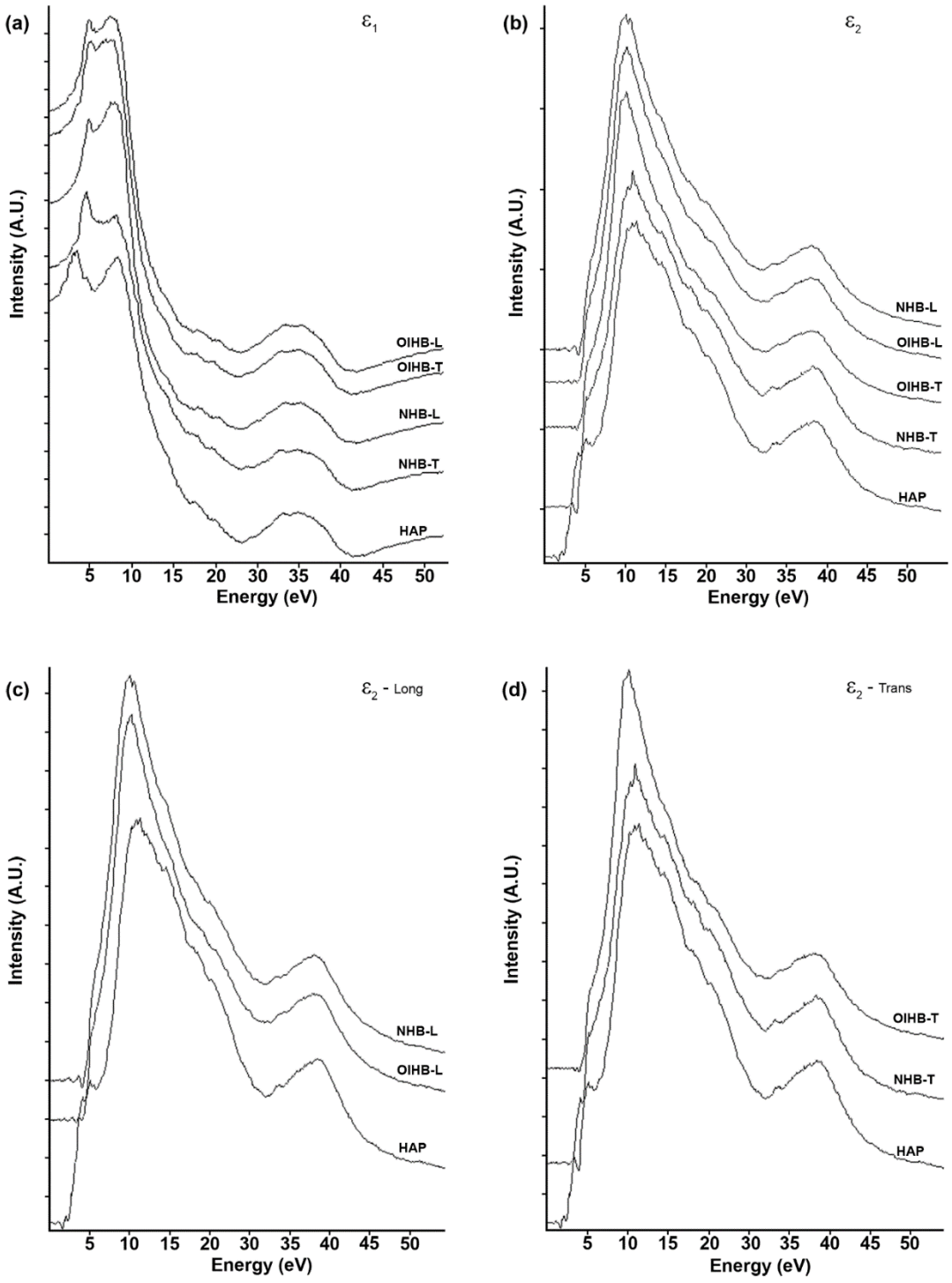

Figure 4.4. The real (ε_1) part (a) and imaginary (ε_2) part (b) of the complex dielectric function obtained from Kramers-Kronig analysis of the EELS spectra for OIHB-L, OIHB-T, NHB-L, NHB-T and HAP. (c) and (d) represent ε_2 spectra grouped into longitudinal and transverse orientation for comparison of single-electron transitions. Spectra vertically separated for clarity.

4.3.5. P-$L_{2,3}$-edge spectra

All core loss P-$L_{2,3}$-edge spectra (Fig. 4.5a-c) have five energy-loss regions with major features characterized by two sharp peaks located at 138-139 eV (A) and 146-147 eV (B). A broader more intense peak follows around 153 eV (C). Peak A often has a weaker feature (A^*) found as a shoulder approximately +2-3 eV from its high energy side. The P-L_1 peak (D) is located around 189 eV. Additional overlays of select P-$L_{2,3}$-edge spectra can be found in Appendix I.

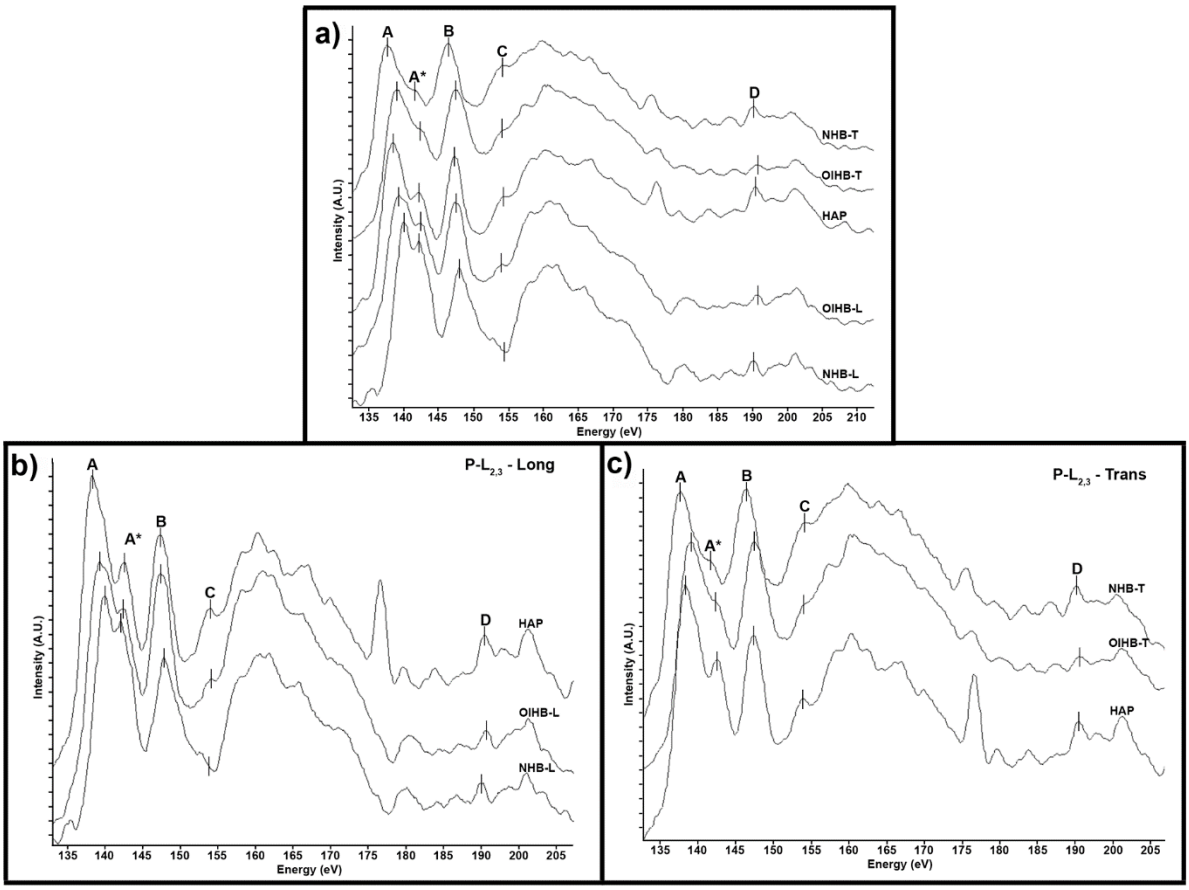

Figure 4.5. Overlays of the P-$L_{2,3}$ core loss region (135-210 eV) obtained from (a) NHB-T, OIHB-T, HAP, OIHB-L and NHB-L. (b) HAP, OIHB-L and NHB-L. (c) NHB-T, OIHB-L and HAP. The spectra separated vertically for clarity and the peak positions (A-D) are indicated by vertical lines.

Two peaks, one at 136 eV (P-L_3) and the other within ~1 eV (P-L_2), comprise the P-$L_{2,3}$ ionization edge; they result from the transitions from spin-orbit split 2p electrons (2p{3/2}) and (2p_{1/2}) into the first unoccupied 3s antibonding state[34]. These ionization edges are difficult to resolve but synchrotron-based x-ray absorption near-edge structure (XANES) data reported for phosphorus reference compounds indicate that they are most likely located within the low-energy shoulder of peak A [35, 36]. Peak A (138-139 eV), has been attributed to transitions to the 3p-like antibonding state in the Si L-edge spectrum of SiO_2, which is isoelectronic with PO_4^{3-}, with these transitions to dipole-forbidden 3p orbitals made possible through mixing of characters from other elements such as oxygen [37]. Peak A*, located ~142 eV on the high-energy side of peak A, is a broadened peak unique to calcium phosphates, and is due to transition of the P-2p electron to Ca-3d empty orbitals [36]. Sutherland et al [38] report it may be due to multiple scattering of the outgoing. Peak B, positioned ~147 eV, is well-known as the d-state resonance or "shape resonance" peak [36, 39], the energy position of this peak is sensitive to the local environment and molecular symmetry of phosphorus. Following is a broad peak (C) starting around 150 eV, which corresponds to the position of the atomic cross-section maximum for the phosphorus 2p level relative to its respective 2p ionization edges [38, 40]. The P-$L_{2,3}$ core loss region spectral features for NHB-T, OIHB-T, NHB-L, OIHB-L and HAP as well as their corresponding electron transition origins are summarized in Table 4.3.

Table 4.3. P-$L_{2,3}$ edge feature electronic transition origins (eV).

Peak	NHB-T	OIHB-T	NHB-L	OIHB-L	HAP	Transition Origin [Reference]
A	137.0	138.4	139.7	138.7	138.4	Transitions to 3p-like anti-bonding state, allowable to dipole forbidden 3p orbitals due to mixed characters from oxygen [37]
A*	141.9	142.8	142.2	142.7	142.1	Phosphorus 2p to Ca 3d empty orbitals [36,38]
B	146.4	147.2	147.8	147.2	147.3	d-state shape resonance peak [36,39]
C	153.9	153.8	152.8	153.8	154.1	Atomic cross section maximum for the 2p level [38,40]
D	190.0	190.5	190.0	190.6	190.1	P L_1 peak [25]

Comparison of the edge values for Peak A show that OIHB-T and OIHB-L have similar energy values to HAP, while NHB-L is shifted +1.3 eV from HAP, and NHB-T has a lower energy shift (-1.4 eV) from HAP. The NHB-T and NHB-L edge values for $A^*$are similar to HAP, while OIHB-T and OIHB-L are shifted to higher energy (+0.7 and +0.6 eV, respectively). The d-shape resonance peak, labeled Peak B, shows that OIHB-T and OIHB-L agree closely with HAP, while NHB-T is shifted -0.8 eV and NHB-L is shifted +0.6 eV. For the 2p level (Peak C), NHB-L is shifted from NHB-T (-1.1 eV), OIHB-T (-1.0 eV), OIHB-L (-1.0 eV), and HAP (-1.3 eV). Peak D (P-L_1) values are similar for OIHB-T and OIHB-L, which differ from NHB-T, NHB-L, and HAP (+0.5 eV to +0.6 eV).

4.4. Conclusions

FESEM and HRTEM imaging revealed morphological differences between normal human bone and OI human bone, with the transverse-direction differences being more distinct and longitudinal-direction differences more subtle. Areas of normal bone are still present within the OI sample.

Observed peak shifts of the Ca-$M_{2,3}$ ionization edges in the ELF plots of OIHB (T,L) and NHB (T,L) indicate changes to Ca outer shell interactions. Valence band changes within OIHB (T,L) are observed when compared to NHB (T,L) and HAP (Fig. 4.3 and Table 4.1).

Changes in the ε_2 spectra (Fig. 4.4) reflect single-electron transitions related to electronic structure, and subtle outer shell changes in electronic structure of Ca and P are observed. The ε_2 spectra of OIHB (T,L) more closely resemble NHB-L than HAP, whereas NHB-T is more like HAP.

Subtle changes/shifting were observed in the electronic near-edge structure of the P-$L_{2,3}$ edge of NHB (T,L), OIHB (T,L), and HAP (Fig. 4.5). The P-$L_{2,3}$ edge of OIHB (T,L) more closely resembles HAP than NHB(T,L). Inner-core P excitation of OIHB (T,L) is more similar to stoichiometric HAP than NHB (T,L), therefore, the electronic structure of the P-$L_{2,3}$ edge in OIHB (T,L) is different than NHB(T,L) and more like that of stoichiometric HAP. These near-edge structure shift changes are attributed to transitions to the 3p-like antibonding state, allowable to dipole-forbidden 3p orbitals due to mixed characters from oxygen [37]. The energy position of the d-shape resonance peaks is sensitive to the local environment and molecular symmetry of phosphorus; OIHB (T,L) resemble HAP more than does NHB (T,L).

EELS studies elucidate the small changes in the valence band and outer electronic structure within the OIHB and NHB samples. Ca-$M_{2,3}$ ionization edge shifts in the ELF between OIHB and NHB indicate the Ca outer-shell interaction differences of the diseased bone. Single-electron transitions related to electronic structure are represented through the fine structure of the ε_2 plots. The observed fine-structure changes between OIHB (T,L) and NHB(T,L) in the in ε_2 plots reflect subtle outer-shell interactions of the Ca and P. Changes in the EELS spectra directly reflect changes to the Ca and P environments within the samples. Small changes in the valence

band and outer electronic structures of the diseased bone have been revealed through EELS. These subtle changes in the electronic structure of the OI diseased bone are caused through a genetic mutation within the collagen which affects HAP mineralization and results in the fragility of bone at the macroscale.

4.6. References

[1] J. D. Currey, "The structure and mechanics of bone," *Journal of Materials Science,* vol. 47, no. 1, pp. 41-54, 2012.

[2] M. E. Launey, M. J. Buehler, and R. O. Ritchie, "On the mechanistic origins of toughness in bone," *Annual review of materials research,* vol. 40, pp. 25-53, 2010.

[3] W. Landis, "The strength of a calcified tissue depends in part on the molecular structure and organization of its constituent mineral crystals in their organic matrix," *Bone,* vol. 16, no. 5, pp. 533-544, 1995.

[4] A. Forlino and J. C. Marini, "Osteogenesis imperfecta," *The Lancet,* vol. 387, no. 10028, pp. 1657-1671, 2016.

[5] C. Gu, D. R. Katti, and K. S. Katti, "Photoacoustic FTIR spectroscopic study of undisturbed human cortical bone," *Spectrochimica Acta Part A: Molecular and Biomolecular Spectroscopy,* vol. 103, no. 0, pp. 25-37, 2013.

[6] C. Gu, D. R. Katti, and K. S. Katti, "Microstructural and Photoacoustic Infrared Spectroscopic Studies of Human Cortical Bone with Osteogenesis Imperfecta," *JOM,* vol. 68, no. 4, p. 1116, 2016.

[7] K. S. Katti, M. X. Qian, F. Dogan, and M. Sarikaya, "Dopant effect on local dielectric properties in barium titanate based electroceramics determined by transmission EELS," *Journal of the American Ceramic Society,* vol. 85, no. 9, pp. 2236-2243, Sep 2002.

[8] N. Bnvoso, "Use of electron–energy loss near–edge fine structure in the study of minerals," *Am. Mineral,* vol. 79, pp. 411-425, 1994.

[9] S. A. Payne, D. R. Katti, and K. S. Katti, "Probing electronic structure of biomineralized hydroxyapatite inside nanoclay galleries," *Micron,* vol. 90, pp. 78-86, 2016.

[10] R. Egerton, *Electron energy-loss spectroscopy in the electron microscope*. Springer Science & Business Media, 2011.

[11] E. A. McNally, H. P. Schwarcz, G. A. Botton, and A. L. Arsenault, "A model for the ultrastructure of bone based on electron microscopy of ion-milled sections," *PLoS One,* vol. 7, no. 1, p. e29258, 2012.

[12] J. Cassella, T. C. Stamp, and S. Ali, "A morphological and ultrastructural study of bone in osteogenesis imperfecta," *Calcified tissue international,* vol. 58, no. 3, pp. 155-165, 1996.

[13] M. A. Rubin and I. Jasiuk, "The TEM characterization of the lamellar structure of osteoporotic human trabecular bone," *Micron,* vol. 36, no. 7-8, pp. 653-664, 2005.

[14] X. Su, K. Sun, F. Z. Cui, and W. J. Landis, "Organization of apatite crystals in human woven bone," *Bone,* vol. 32, no. 2, pp. 150-162, Feb 2003.

[15] G. Gregori, H. J. Kleebe, H. Mayr, and G. Ziegler, "EELS characterisation of beta-tricalcium phosphate and hydroxyapatite," *Journal of the European Ceramic Society,* vol. 26, no. 8, pp. 1473-1479, 2006.

[16] S.-C. Liou, S.-Y. Chen, H.-Y. Lee, and J.-S. Bow, "Structural characterization of nano-sized calcium deficient apatite powders," *Biomaterials,* vol. 25, no. 2, pp. 189-196, 2004.

[17] M. M. Kłosowski *et al.*, "Probing carbonate in bone forming minerals on the nanometre scale," *Acta biomaterialia,* vol. 20, pp. 129-139, 2015.

[18] A. L. Rossi *et al.*, "Effect of strontium ranelate on bone mineral: Analysis of nanoscale compositional changes," *Micron,* vol. 56, pp. 29-36, Jan 2014.

[19] C. Bordat *et al.*, "Iron-distrubution in thalassemic bone by energy-loss spectroscopy and electron spectroscopic imaging," *Calcified Tissue International,* vol. 53, no. 1, pp. 29-37, Jul 1993.

[20] C. Bordat, O. Bouet, and G. Cournot, "Calcium distribution in high-pressure frozen bone cells by electron energy loss spectroscopy and electron spectroscopic imaging," *Histochemistry and cell biology,* vol. 109, no. 2, pp. 167-174, 1998.

[21] V. Jantou-Morris, M. A. Horton, and D. W. McComb, "The nano-morphological relationships between apatite crystals and collagen fibrils in ivory dentine," *Biomaterials,* vol. 31, no. 19, pp. 5275-5286, Jul 2010.

[22] V. Srot, B. Bussmann, U. Salzberger, C. T. Koch, and P. A. van Aken, "Linking Microstructure and Nanochemistry in Human Dental Tissues," *Microscopy and Microanalysis,* vol. 18, no. 3, pp. 509-523, Jun 2012.

[23] D. Verma, K. Katti, and D. Katti, "Bioactivity in in situ hydroxyapatite–polycaprolactone composites," *Journal of Biomedical Materials Research Part A,* vol. 78A, no. 4, pp. 772-780, 2006.

[24] A. Ambre, K. S. Katti, and D. R. Katti, "In situ mineralized hydroxyapatite on amino acid modified nanoclays as novel bone biomaterials," *Materials Science and Engineering: C,* vol. 31, no. 5, pp. 1017-1029, 2011.

[25] C. C. Ahn and O. L. Krivanek, *EELS Atlas: A Reference Collection of Electron Energy Loss Spectra Covering All Stable Elements*. Gatan, 1983.

[26] P. Rulis, L. Ouyang, and W. Y. Ching, "Electronic structure and bonding in calcium apatite crystals: Hydroxyapatite, fluorapatite, chlorapatite, and bromapatite," *Physical Review B,* vol. 70, no. 15, p. 155104, 2004.

[27] Y. M. Alexandrov, V. M. Vishnjakov, V. N. Makhov, K. K. Sidorin, A. N. Trukhin, and M. N. Yakimenko, "Electronic properties of crystalline quartz excited by photons in the 5–25 eV range," *Nuclear Instruments and Methods in Physics Research Section A: Accelerators, Spectrometers, Detectors and Associated Equipment,* vol. 282, no. 2–3, pp. 580-582, 1989.

[28] H. R. Philipp, "Optical properties of non-crystalline Si, SiO, SiO_x and SiO_2," *Journal of Physics and Chemistry of Solids,* vol. 32, no. 8, pp. 1935-1945, 1971.

[29] H. R. Philipp, "Optical and bonding model for non-crystalline SiO_x and $SiO_x N_y$ materials," *Journal of Non-Crystalline Solids,* vol. 8, pp. 627-632, 1972.

[30] H. Ibach and J. Rowe, "Electron orbital energies of oxygen adsorbed on silicon surfaces and of silicon dioxide," *Physical Review B,* vol. 10, no. 2, p. 710, 1974.

[31] D. Griscom, "The electronic structure of SiO_2: a review of recent spectroscopic and theoretical advances," *Journal of Non-Crystalline Solids,* vol. 24, no. 2, pp. 155-234, 1977.

[32] J. A. Rotole and P. M. Sherwood, "Oxide-free phosphate surface films on metals studied by core and valence band X-ray photoelectron spectroscopy," *Chemistry of materials,* vol. 13, no. 11, pp. 3933-3942, 2001.

[33] I. D. Welsh and P. M. A. Sherwood, "Valence band photoemission studies of corrosion inhibitor action on iron surfaces: effect of etidronate," *Chemistry of Materials,* vol. 4, no. 1, pp. 133-140, 1992.

[34] W. J. Landis, K. J. Hodgens, J. Arena, M. J. Song, and B. F. McEwen, "Structural relations between collagen and mineral in bone as determined by high voltage electron microscopic tomography," *Microscopy research and technique,* vol. 33, no. 2, pp. 192-202, 1996.

[35] J. Cosmidis, K. Benzerara, N. Nassif, T. Tyliszczak, and F. Bourdelle, "Characterization of Ca-phosphate biological materials by scanning transmission X-ray microscopy (STXM) at the Ca L2,3-, P L2,3- and C K-edges," *Acta Biomaterialia,* vol. 12, no. 0, pp. 260-269, 2015.

[36] J. Kruse, P. Leinweber, K.-U. Eckhardt, F. Godlinski, Y. Hu, and L. Zuin, "Phosphorus L2,3-edge XANES: overview of reference compounds," *Journal of Synchrotron Radiation,* vol. 16, no. 2, pp. 247-259, 2009.

[37] G. R. Harp, Z. L. Han, and B. P. Tonner, "X-ray absorption near edge structures of intermediate oxidation states of silicon in silicon oxides during thermal desorption," *Journal of Vacuum Science & Technology A,* vol. 8, no. 3, pp. 2566-2569, 1990.

[38] D. Sutherland, M. Kasrai, G. Bancroft, Z. Liu, and K. Tan, "Si L-and K-edge x-ray-absorption near-edge spectroscopy of gas-phase Si (CH 3) x (OCH 3) 4− x: Models for solid-state analogs," *Physical Review B,* vol. 48, no. 20, p. 14989, 1993.

[39] D. Li, G. M. Bancroft, M. E. Fleet, and X. H. Feng, "Silicon K-edge XANES spectra of silicate minerals," (in English), *Physics and Chemistry of Minerals,* vol. 22, no. 2, pp. 115-122, 1995.

[40] J. J. Yeh and I. Lindau, "Atomic subshell photoionization cross sections and asymmetry parameters: $1 \leqslant Z \leqslant 103$," *Atomic Data and Nuclear Data Tables,* vol. 32, no. 1, pp. 1-155, 1985.

CHAPTER 5. SUMMARY AND CONCLUSIONS

Electron energy-loss spectroscopy (EELS) was used to investigate the electronic structure and molecular interactions of biomimetic HAP that was prepared using biomineralization routes inside 5-aminovaleric modified clay galleries (in-situ HAPclay). The morphology of in-situ HAPclay is different from the morphology of non-biomimetic mineralized HAP as seen through SEM and TEM imaging. The rounded morphology of biogenic HAP in human bone is mimicked by mineralization of HAP within amino-acid-modified nanoclays. Shifts of the Ca-$M_{2,3}$ ionization edge in the in-situ HAPclay and HAP in the ELF are indicative of changes to the Ca outer-shell interactions, and changes to the valence band of the in-situ HAPclay are observed in comparison with the non-biomimetic HAP. Thus subtle changes to the outer-shell electronic structure enabled through biomineralization which was guided by weak nonbonded interactions between Ca and P from HAP and amino acid groups inside clay galleries (as suggested by simulations) are experimentally observed in the ε_2 spectra.

Further, ε_2 was used to calculate the high-frequency AC conductivity plots for in-situ HAPclay, HAP, β-TCP, and modified MMT clay. Again, subtle differences in the valence bands of Ca and P in the in-situ HAPclay are observed. The near-edge structure of the P-$L_{2,3}$ edge was also analyzed. Extremely subtle changes resulting from transitions to the 3p-like anti-bonding state, allowable to dipole forbidden 3P orbitals due to mixed characters from oxygen, are observed. These electron energy-loss spectroscopic studies elucidate the small changes that occur in the valence band and outer electronic structures of HAP when mineralized inside clay galleries. It is interesting to note the biological implications of these differences are significant as this biomineralized HAP used in scaffold systems has been shown to exhibit superior biological

functions resulting in mediation of human stem cells to differentiate into osteoblastic lineages without the use of differentiating media.

EELS was used to probe the electronic structure of Ca and P in the HAP of normal (NHB) and osteogenesis-imperfecta-diseased human bone (OIHB) samples in the transverse (T) and longitudinal (L) directions. Imaging with FESEM and TEM was used to determine morphological differences of the NHB (T,L) and OIHB (T,L).

Observed peak shifts of the Ca-$M_{2,3}$ ionization edges in the ELF plots of OIHB (T,L) and NHB (T,L) indicate changes to Ca outer-shell interactions. Valence band changes within OIHB (T,L) are observed when compared to NHB (T,L) and HAP. Changes in the ε_2 spectra reflect single-electron transitions related to electronic structure, and subtle outer shell changes in electronic structure of Ca and P are observed. The ε_2 spectra of OIHB (T,L) more closely resemble NHB-L than HAP, whereas NHB-T is more like HAP.

Subtle changes/shifting were observed in the electronic near-edge structure of the P-$L_{2,3}$ edge of NHB (L,T), OIHB (L,T), and HAP. The P-$L_{2,3}$ edge of OIHB (L,T) more closely resembles HAP than NHB (L,T). Inner-core P excitation of OIHB (L,T) is more similar to stoichiometric HAP than NHB (L,T), therefore, the electronic structure of the P-$L_{2,3}$ edge in OIHB (L,T) is different than NHB (L,T) and more like that of stoichiometric HAP. The energy position of the d-shape resonance peaks is sensitive to the local environment and molecular symmetry of phosphorus; OIHB (L,T) resembles HAP more than does NHB(L,T).

EELS studies elucidate the small changes in the valence band and outer electronic structure of the OIHB and NHB samples. Ca-$M_{2,3}$-ionization edge shifts in the ELF between OIHB and NHB indicate Ca outer-shell interaction differences in the diseased bone. Single-electron transitions related to electronic structure are represented through the fine structure of the

ε_2 plots. The observed fine-structure changes between OIHB (L,T) and NHB (L,T) in the ε_2 plots reflect subtle outer-shell interactions of the Ca and P. Changes in the EELS spectra directly reflect changes to the Ca and P environments within the samples that were created during biomineralization of HAP. The subtle changes in the electronic structure of the osteogenesis-imperfecta-diseased bone are caused by a genetic mutation within the collagen which affects HAP mineralization and results in the bone fragility at the macroscale.

CHAPTER 6. MAJOR CONTRIBUTIONS

EELS studies showed significant differences in valence band electronic structure of both Ca and P in-situ HAPclay (biomimetic) and HAP (synthetic). These experimental results are consistent with and validate molecular dynamic simulations which indicated the presence of significant non-bonded interaction of Ca and P in the in-situ HAPclay. The observed changes in the EELS spectra are experimental observations of the changes to the Ca and PO_4^{3-} environments that were predicted through simulations. Therefore, small changes occurring in the valence band and outer electronic structure of in-situ HAPclay, shown exclusively by EELS, are significant because of the demonstrated superior biological functions of polymer scaffolds containing in-situ HAPclay.

For healthy and OI-diseased bone, we compared the microstructure of healthy and osteogenesis-imperfecta-diseased human bone (using SEM and TEM) and the electronic structure of the two (using EELS), contributing to the understanding of the molecular basis of osteogenesis-imperfecta disease. Studies using EELS on healthy human bone and osteogenesis-imperfecta-human bone show small changes in valence and outer-shell electronic structure within the diseased bone. Changes in the EELS spectra directly reflect changes to the Ca and P electronic environments during the biomineralization process within the bone. The P electronic environment in OIHB (T,L) more closely resemble the stoichiometric HAP than non-stoichiometric NHB (T,L). Therefore, subtle changes in the electronic structure of osteogenesis-imperfecta-diseased bone are likely caused through biomineralization of HAP in the presence of the genetically mutated collagen molecules, disrupting the bone nanocomposite and forming the fragile bone that exemplifies this disease.

CHAPTER 7. FUTURE WORK

The following are possible directions for future investigations of molecular interactions of healthy bone, OI diseased bone, and biomineralized tissue-engineered bone systems:

- Use a focused-ion beam (FIB) or dual-beam system to mill bone samples and provide a more uniform sample thickness of bone for EELS analysis and TEM imaging.
- Investigate normal human bone, diseased human bone, and biomineralized tissure-engineered bone systems with energy-filtered transmisson electron microscopy (EFTEM), which will provide element/chemical mapping at the nanometer scale and allow extraction of the corresponding edge data from selected areas.
- Perform synchrotron scanning transmission x-ray microscopy (STXM) along with near-edge x-ray absorption fine structure (NEXAFS) which will provide increased resolution of the P-$L_{2,3}$ and Ca-$M_{2,3}$ edges of the HAP in healthy bone, OI diseased bone and biomineralized tissue-engineered bone systems.
- Conduct EELS investigations of metastatic biomineralized collagen in tissue-engineered bone systems for comparison to the healthy human bone and in-situ HAPclay data obtained in this study.
- Design a device that could biopsy a sample of bone 100 nm in thickness and 3 mm in diameter that could then be used in the TEM for EELS studies. This type of device would address tissue donation issues for the rare bone diseases. It also would be able to provide samples for statistical studies. Another use would be to biopsy cancerous bone tumors for EELS investigations.

- Collaborate with a medical school or medical foundation that specializes in the treatment of osteogenesis imperfecta to obtain matched samples of healthy and diseseased human bone for statistical EELS studies.

APPENDIX A. HUMAN BONE SAMPLE INFORMATION

A.1. NDSU internal review board compliance letter

NDSU NORTH DAKOTA STATE UNIVERSITY

March 16, 2018

Dr. Kalpana Katti
Dept. of Civil Engineering

Re: Your submission to the IRB: "Multi-Scale Modeling of Mechanics of Bone: Experimental and Modeling studies"

Research Team Members: Scott Payne

Thank you for your inquiry regarding your project. At this time, the IRB office has determined that the above-referenced protocol does not require Institutional Review Board approval or certification of exempt status because it does not fit the regulatory definition of 'research involving human subjects'.

Dept. of Health & Human Services regulations governing human subjects research (45CFR46, Protection of Human Subjects), defines 'research' as "…a systematic investigation, research development, testing and evaluation, designed to contribute to generalizable knowledge." These regulations also define a 'human subject' as "…a living individual about whom an investigator conducting research obtains (1) data through intervention or interaction with the individual, or (2) identifiable private information."

It was determined that your project does not require IRB approval (or a determination of exemption) because the bone specimens were collected from deceased individuals. This determination was made initially on information received via email on May 21, 2009 with original determination letter issued May 26. 2009.

We appreciate your intention to abide by NDSU IRB policies and procedures, and thank you for your patience as the IRB Office has reviewed your study. Best wishes!

Sincerely,

Kristy Shirley

Kristy Shirley, CIP; Research Compliance Administrator

For more information regarding IRB Office submissions and guidelines, please consult www.ndsu.edu/irb. This Institution has an approved FederalWide Assurance with the Department of Health and Human Services: FWA00002439.

INSTITUTIONAL REVIEW BOARD
NDSU Dept 4000 | PO Box 6050 | Fargo ND 58108-6050 | 701.231.8995 | Fax 701.231.8098 | ndsu.edu/irb

Shipping address: Research 1, 1735 NDSU Research Park Drive, Fargo ND 58102

Figure A.1. NDSU IRB letter outlining board decision exempt status.

A.2. Healthy human femur

Figure A.2. Healthy human femur as received from NDRI.

National Disease Research Interchange (NDRI)
8 Penn Center, 8th Floor
1628 JFK Blvd
Philadelphia, PA 19103
800-222-6374
www.ndriresource.org

HTOR Donor Information Form

Researcher: Katti
NDRI # 0058139
Procurement Date: 8/28/2006
I.D. # DTB 060349
Shipping Date: 8/5/2009

Qty	Size/Weight	Tissue	Normal/Diseased	Preservation Method	Hours Post	Recovery Time
1	whole	BONE/FEM/PART	NORMAL	FRZN	17.6	

Accepted by: Scott Payne
Comments: proximal

Donor Information

A/R/S: 27 / C / F
Cause of Death: Trauma
Second To: MVA
(Eastern Standard Time)
Date/Time of Death: 6/30/2006 17:24
Date/Time Recovery Complete: 7/1/2006 11:00

Medical History
Height: 61 "
Weight: 115 LB's

Medications:
birth control

Diabetes: N

Chemo/Rad: N
Alcohol: Y vodka on weekends
Tobacco: N
Drugs: Y smoked marijuana
Sepsis: N
WBC
Vent: N

Figure A.3. Patient information sheet of healthy human femur obtained from NDRI.

A.3. Osteogenesis imperfecta diseased human tibia

Figure A.4. Osteogenesis imperfecta diseased human tibia as received from NDRI.

NDRI
National Disease Research Interchange
THE NATIONAL RESOURCE CENTER
(800) 222-NDRI (6374)
1628 JFK Blvd. 8 Penn Center
Philadelphia, PA 19103
Fax: (215) 557-7154

HTOR Donor Information Form

Department: OBC- HTOR
Policy: Autopsy Donor Info
Version: 3
Effective Date: 10/27/10

NDRI #: 0056817-08 **Procurement Date:** 2/6/2006 **Shipping Date:**
Tracking Info: -

Source Ref#: OTB050554

Researcher:
Researcher Code:

Qty	Size/Weight	Tissue	Normal/Diseased	Pres Meth	Tissue ID	Hours Post	Recovery Time
2	distal	BONE/TIBIA/PART		FRZN	08	24.0	

Accepted by:

Donor Information

A/R/S: 22 / C / F
(Eastern Standard Time)
Date/Time of Death: 12/30/1899

Cause of Death: Accidental OD of Meth & Diphen
Second To:
Date/Time Recovery Complete: 12/30/1899

Medical History

Height: 67 " **Weight:** 180 LB's

Accidental overdose of methadone & diphenhydramine, broken bones (arms and ankles) second to osteogenesis imperfecta, asthma, c-section, portion of lung removed, second to congenital lobar emphysema (at time of birth)
Med Codes: Asthma; Emphysema; Osteogenesis imperfecta~
Meds: Antidepressives, vitamins, prenatals during pregnancy
Diabetes: N

Chemo/Rad: N
Alcohol: N
Tobacco: N
Drugs: Y History of methadone abuse; no IV drug use
Sepsis: N
WBC
Vent: N

Infectious Disease Testing Performed? Y **Results Received?** Y

HIV 1 Ab Test Performed?	Y	**Result: Nonreactive**	**HCV Ab Test Performed?**	Y	**Result: Nonreactive**
HIV 2 Ab Test Performed?	Y	**Result: Nonreactive**	**HBc Ab Test Performed?**	Y	**Result: Nonreactive**
RPR Syphilis Test Performed?	Y	**Results: Nonreactive**	**HBs Ag Test Performed?**	Y	**Result: Nonreactive**
HTLV Test Performed?	Y	**Results: Nonreactive**			

T:\QA-QC Docs\OBC\HTOR Autopsy Donor Information OBCa.rpt

Figure A.5. Patient information sheet of Osteogenesis imperfecta diseased human tibia obtained from NDRI.

APPENDIX B. PREPARATION OF BONE FOR TEM

B.1. Images of bone samples prior to TEM preparation

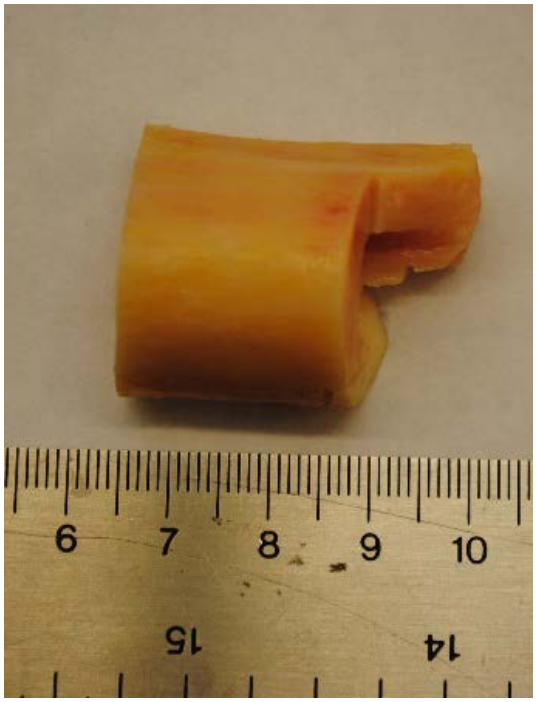

Figure B.1. Portion of healthy human femur used for TEM sample preparation.

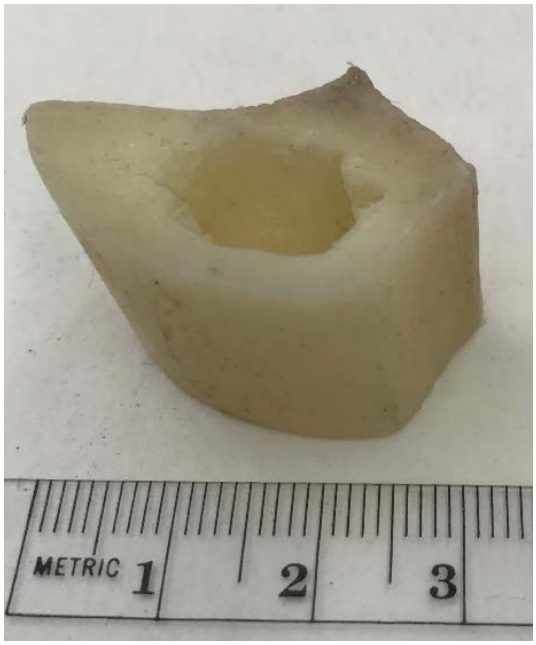

Figure B.2. Portion of osteogenesis imperfecta human tibia used for TEM sample preparation.

B.2. Schematic representation defining relation of direction of the incident TEM electron beam to bone sample.

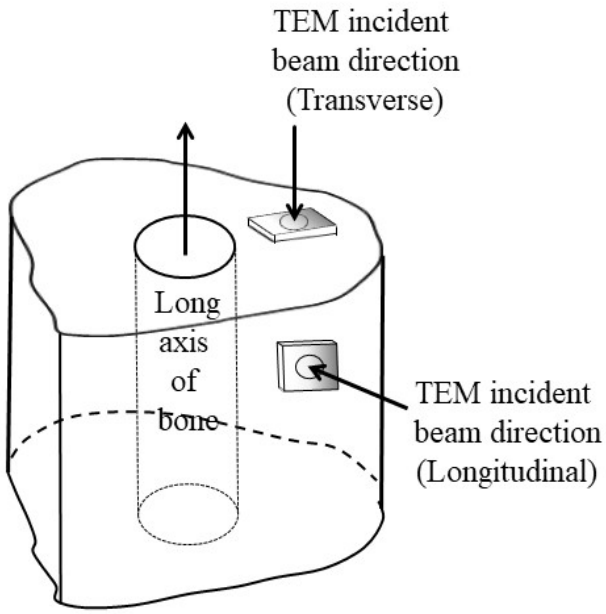

Figure B.3. Schematic representation of bone showing the direction of the TEM incident beam relative to longitudinal and transverse surfaces.

B.3. Typical longitudinal and transverse bone surfaces

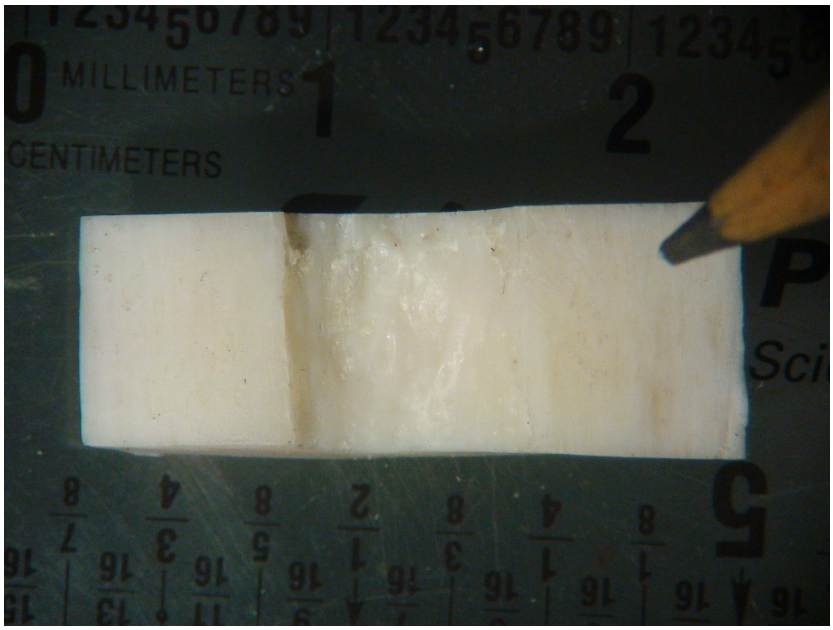

Figure B.4. Longitudinal bone surface.

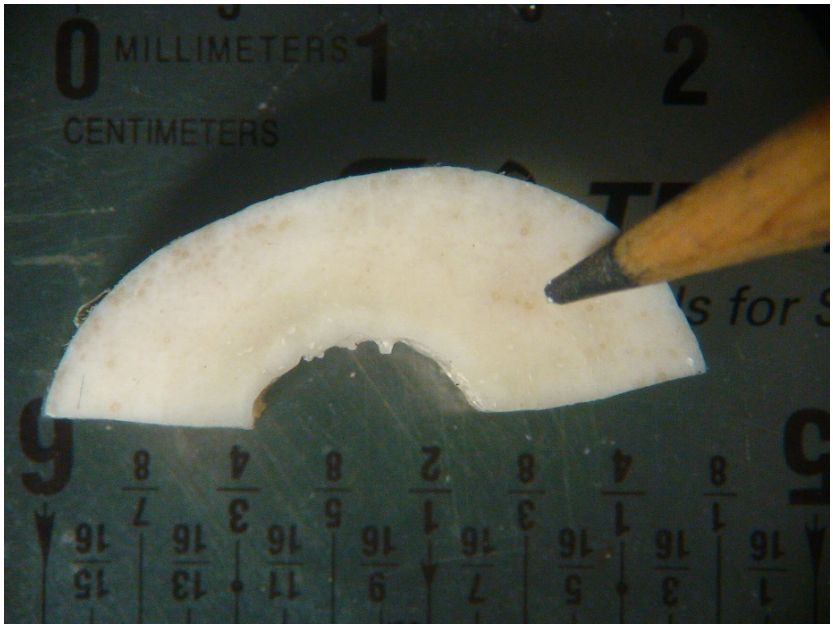

Figure B.5. Transverse bone surface.

APPENDIX C. TEM PREPARATION EQUIPMENT AND PROCEDURES

Each of the procedures contained in this appendix was compiled exclusively by the author using thorough research, conversations with manufacturer representatives and sometimes trial and error.

C.1. Buehler isomet 1000 low speed diamond saw

Figure C.1. Buehler Isomet 1000 low-speed saw.

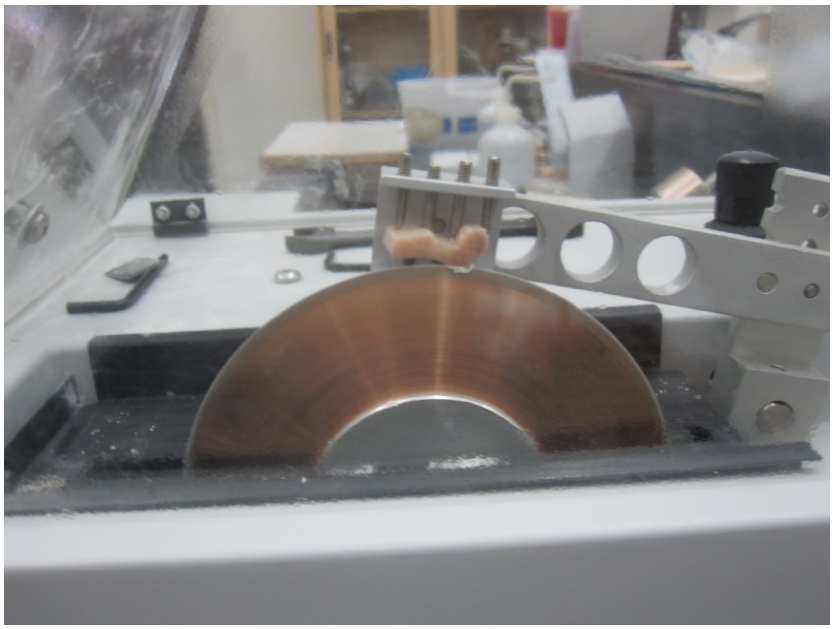

Figure C.2. Buehler low-speed saw equipped with diamond blade used for cutting 500-700 μm longitudinal and transverse sections from the stock bone samples.

C.1.1. Buehler isomet 1000 low speed diamond saw operating procedure

1. Secure diamond blade with collars and secure with set screw.
2. Insert throat plate.
3. Secure sample into holder that is appropriate for the sample size and shape.
4. Secure sample holder onto the cutting arm and rotate until cut area is aligned with the diamond blade.
5. Set tension weight to the 150 mark.
6. Set speed to 125.
7. Use dressing bar to clean the diamond blade (2-3 cuts).
8. Lower the bone onto the diamond blade.
9. Set the thickness (500-700 μm) of the section using the micrometer, adding 0.5 mm to account for the blade kerf.
10. Start the blade motor.

11. Allow the blade to cut through the sample, if cutting is slow, increase speed and/or weight.

Figure C.3. Buehler isomet 1000 low-speed saw cuts of transverse (large, curved) and longitudinal (square, small) bone.

C.2. Gatan ultrasonic disc cutter model 601

Figure C.4. Gatan ultrasonic cutting device model 601.

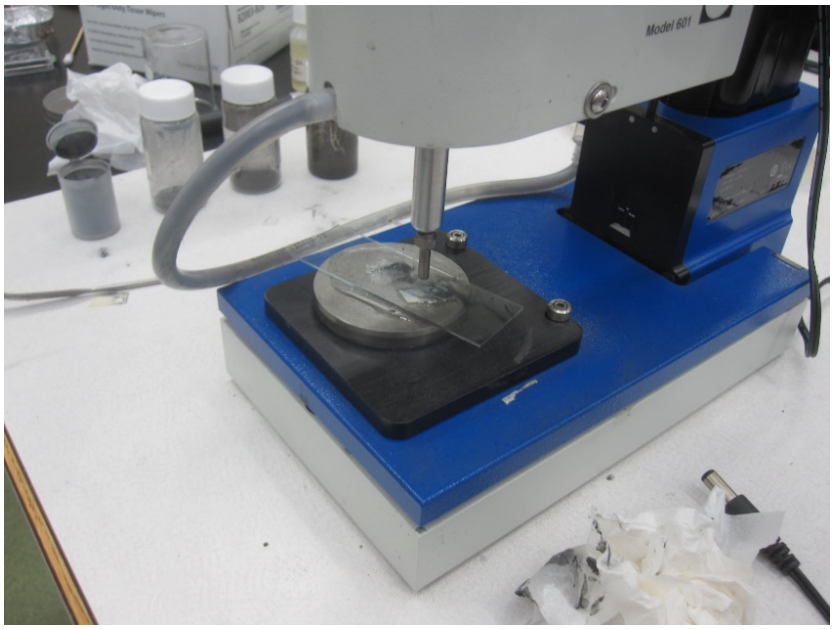

Figure C.5. Gatan ultrasonic cutting device used to cut 3 mm circular discs from the 500-700 μm bone section.

C2.1. Gatan ultrasonic disc cutter model 601 operating procedure

1. **Assemble Tool.** Choose cutting tool desired and screw on to threaded insert of TPC tool, being sure to incorporate the copper washer. Tighten carefully with circular wrench.
2. **Mount specimen.** Attach specimen to be cut to a portion of a glass microscope slide using Crystal Bond wax: heat glass slide and aluminum weigh boat containing a small amount of wax on the hot plate at 130C. Apply a bit of wax to slide with toothpick, and carefully but firmly press specimen into melted wax, rotating slightly for good wax coverage.
3. Place the metal specimen table disc on the hot plate at 130C for about 5 minutes. [Do not heat with the slurry ring in place as its O-ring will be damaged.] Use a small amount of Crystal Bond to attach the glass slide with the specimen to the specimen table: press carefully and move in small circles to get thin film of wax under entire

glass. Remove from hot plate with forceps etc. and allow to cool. If desired, slurry ring may be placed around specimen table and pressed in place. Put the specimen table onto the magnetic base (no wax needed.)

4. **Zero the Dial Indicator.** Set the magnetic base on the TPC so that the glass slide (not the specimen) is beneath the cutting tool; the notches need not be aligned with the posts. Lower the cutting tool onto the slide using either of the large knobs at right or left until the dial indicator stops changing and the horizontal indicator is aligned. Rotate the outer ring of the dial indicator to align the 0 µm mark with the dial needle. Note the reading on the small "coarse" dial; it should be 1, indicating the 1-mm thickness of the slide. Raise the cutting tool and remove the magnetic plate.
5. **Center the specimen.** Plug the cord of the binocular into the TPC. Place the magnetic plate on the binocular microscope, pressing the notches to the posts. Center the specimen table/area of interest. The center of the microscope crosshairs indicates the center of the cutting tool, with an accuracy of $\pm$ 0.2 mm; the field of view is about 4 mm diameter.
6. Without moving the specimen table on the magnetic plate, transfer the magnetic base to the TPC platform, pressing the notches to the posts.
7. **Cut.** Using a spatula, place a small conical mound of cutting grit on the area of the specimen directly under the cutting tool. Add 1-2 drops of water or slurry with pipette.
8. Lower the cutting tool into the grit until the horizontal reference indicator is aligned. The dial displays the thickness of the specimen plus wax layer.
9. Switch on the power and adjust the cutting rate using the tuning knob. Watch the dial indicator and listen to the sound to assess effectiveness of cutting. The dial should

move quickly—usually when the sound is noisiest. Add more water/slurry if the specimen begins to "smoke." If your specimen is much thicker than 1 mm, you may need to lower the cutting tool so that the horizontal reference indicator stays just below the lateral lines. As you go through the specimen and contact the wax, cutting speed increases. Cutting is complete when the dial movement slows or stops and the tone changes as the cutter contacts the glass slide. You may notice the slurry suddenly drain away. Cutting through a 1-mm specimen (other than glass) usually takes just a few seconds.

10. Move to a new location and repeat steps 8-10 as desired. Once all cuts are made, switch off the power. Remove the specimen table, wash off the slurry, and remove the cut sample. Sometimes samples migrate inside the cutting tool: use a pipette to flush out carefully over a container.
11. Detach the slurry ring (if used) and place the specimen table on the hot plate at 130C. Remove the remaining sample from the slide and the slide from the specimen table. Cool, then wipe with acetone to remove traces of wax. Don't get acetone on plastic or painted surfaces. Use a new area or a fresh glass slide for additional samples.
12. **Clean.** If you are done using the TPC, remove the cutting tool with the circular wrench and flush it in running water. Wipe off and be very careful not to lose the copper washer! Dry and store the cutting tool and washer. Thoroughly rinse and dry the specimen table and slurry ring. Wipe down the TPC platform, dials, etc. Turn off the hot plate.

Figure C.6. Transverse section of bone showing 3 mm disc cuts.

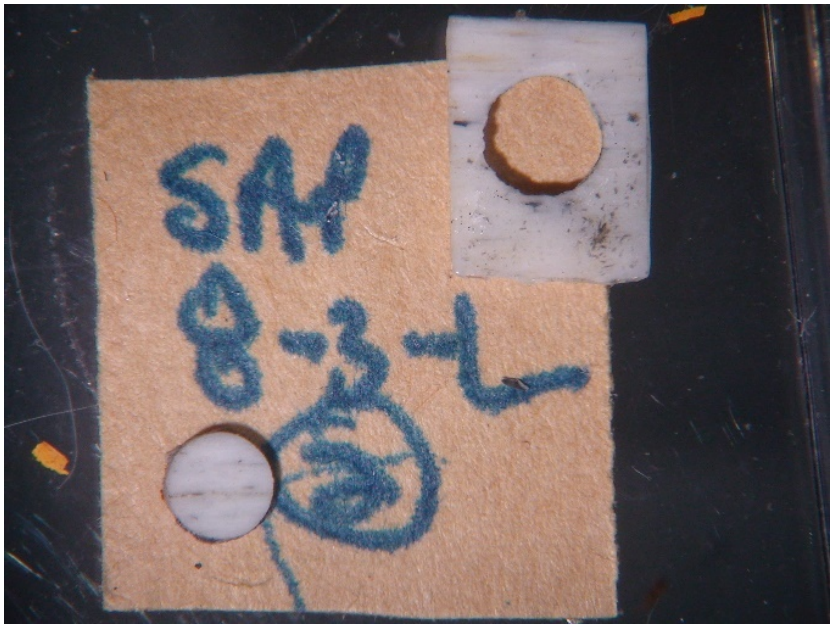

Figure C.7. Longitudinal bone section with corresponding 3 mm disc.

C.3. Gatan disc grinder model 623

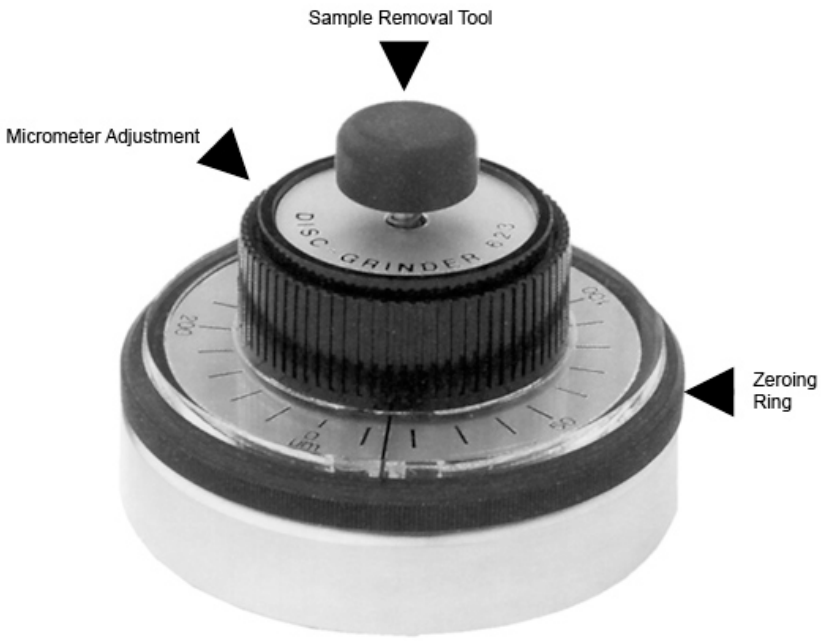

Figure C.8. Gatan disc grinder model 623 (Note: Turning the micrometer adjustment knob counter clockwise (CCW) retracts sample mount. Turning the micrometer adjustment knob clockwise (CW) extends sample mount.).

Figure C.9. Gatan disc grinder with sample holder.

C.3.1. Gatan disc grinder model 623 operating procedure

1. Zero the Disc Grinder for the mount you intend to use.

    a. place mount in Disc Grinder so that beveled edge goes in first and turn micrometer adjustment knob until flush to your eye.

    b. place a small drop of water around the opening and then cover with a glass slide.

    c. adjust the mount in or out with the micrometer adjustment knob to make the meniscus appear.

    d. an additional check is to use the glass slide on edge and run it across the surface to see if it “catches” on the mount, this will tell you if it is out too far.

e. Set scale to zero using the zeroing ring.

d. Use sample removal tool to eject mount from the disc grinder.

2. Determine thickness of ultrasonically cut disc with the SEM.

3. Attach disc to metal mount cylinder with crystal bond.

a. place mount on 130°C hot plate.

b. touch small amount of crystal bond to surface.

c. place disc onto crystal bond and move in circular fashion to thin out wax(note: use cocktail stick to manipulate sample).

d. remove from hot plate and allow to cool.

e. remove excess wax using small amount of acetone and cotton applicator.

4. Place mount with sample into disc grinder and zero the sample by rotating the micrometer adjustment knob counter clockwise until the thickness of the sample as determined by SEM is achieved. It may be necessary to gently push mount into grinder to firmly seat.

CAUTION: Damage from any abrasive paper can extend up to 3 times the micron size of the abrasive.

Initial thickness should be around 500 µm. Target thickness for first side should be approximately 300 µm.

Grinding Schedule for the First Side

5. Use 40 µm abrasive paper to remove enough of the sample to make it flat. (50-100 µm) Use 20 – 25 µm increments.

Rinse away any residual abrasive material with a stream of distilled water from the sample and the abrasive paper or diamond lapping film before proceeding to the next step. This is extremely important as any residual abrasive will make it impossible complete the next step.

6. Use 15 µm abrasive paper to remove 75 µm in 25 µm increments.

7. Use 6 µm diamond lapping film to remove 50 µm in 10 µm increments.

8. Use 3 µm diamond lapping film to remove 15 µm in 5 µm increments.

9. Use 1 µm diamond lapping film to remove 10 µm in 2.5 µm increments.

10. Use 0.5 µm diamond lapping film to remove 3 µm.

Table C.1. Gatan disc grinding schedule for side #1.

Paper	Increments	Remove	Total Removed
40 μm	20-25 μm	50-100 μm or Flat	
15 μm	25 μm	75 μm	
5 μm	10 μm	50 μm	
3 μm	5 μm	15 μm	
1 μm	2.5 μm	10 μm	
0.5 μm	1 μm	3 μm	

11. Remove sample from metal stub by placing on 130°C hot plate and teasing it off with a cocktail stick.

12. Using a self-closing forceps, dip the sample into 100% acetone to remove any crystal bond. Take note of the polished side under a dissecting microscope.

13. Measure thickness with SEM.

14. Remount sample with the first side against the metal stub using the procedure from step 3.

If initial thickness was 500 μm, the thickness of the disc should now be around 300 μm.

Grinding Schedule for Second Side

15. Use 40 μm abrasive paper until thickness is 215 μm. (20 μm increments)

Rinse away any residual abrasive material with a stream of distilled water from the sample and the abrasive paper or diamond lapping film before proceeding to the next step. This is extremely important, as any residual abrasive will make it impossible complete the fine grinding.

16. Use 15 μm abrasive paper until thickness is 155 μm (remove 60 μm using 20 μm increments).

17. Use 6 μm diamond lapping sheet until thickness is 105 μm (remove 50 μm using 10 μm increments).

18. Use 3 μm diamond lapping sheet until thickness is 85 μm (remove 20 μm using 5 μm increments).

19. Use 1 μm diamond lapping sheet until thickness is 75 μm (remove 10 μm using 2.5 μm increments).

20. Use 0.5 μm diamond lapping sheet until thickness is 70 μm (remove 5 μm using 1-2 μm increments)

Table C.2. Gatan disc grinding schedule for side #2.

Paper	Increments	Remove	Total Removed
40 μm	20-25 μm	Until 215 μm	
15 μm	20 μm	60 μm (155 μm)	
5 μm	10 μm	50 μm (105 μm)	
3 μm	5 μm	20 μm (85 μm)	
1 μm	2.5 μm	10 μm (75 μm)	
0.5 μm	1 μm	5 μm (70 μm)	

Remove sample from metal stub as before and clean with 100% acetone, sample should be ready for dimple grinding.

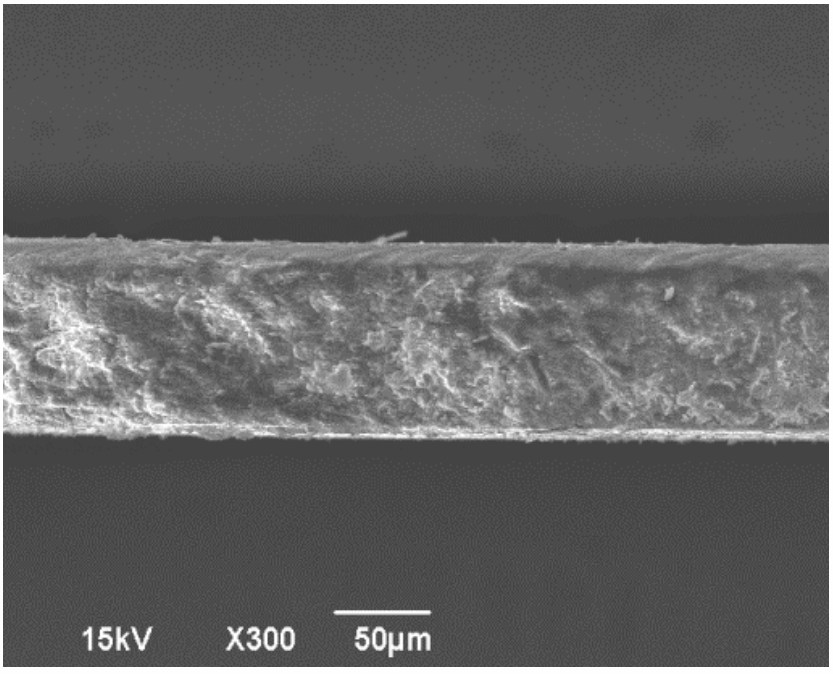

Figure C.10. SEM image showing the edge view of a disc thinned to approximately 100 μm using the Gatan disc grinder.

C.4. Gatan dimple grinder model 656

Figure C.11. Gatan dimple grinder model 656.

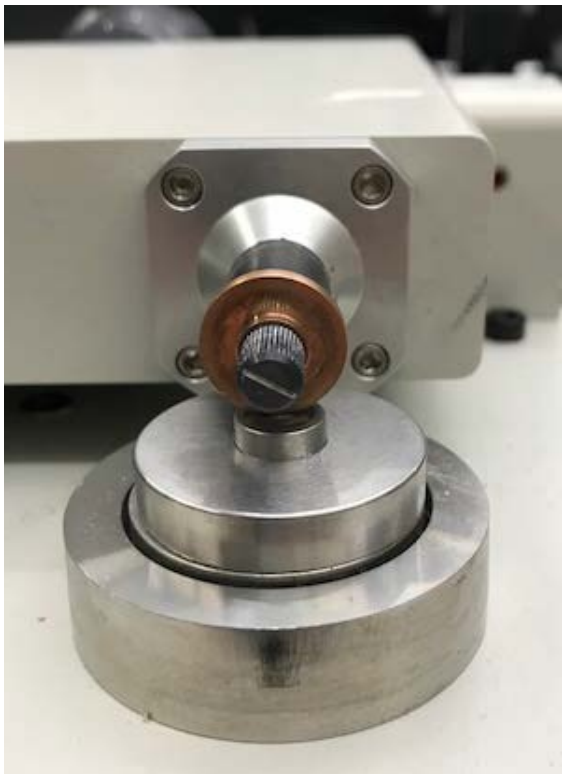

Figure C.12. Phosphor bronze grinding wheel and sample on the Gatan dimple grinder.

C.4.1. Gatan dimple grinder model 656 operating procedure

Prior to dimpling, the zero of the Dial Indicator should always be checked. If the zero is not accurately set, the accuracy of the dimple will be affected.

1. Adjust Zero of Dial Indicator.

    a. Raise the platform to the upright position.

        Remove the specimen mount from the magnetic turntable.

        Check that both TABLE and ARM motors are turned off.

    b. Set a load of 20 g on the Counterweight.

    c. Lower the platform onto the raise/lower cam stop.

        Make sure the Cam stop is in the “rear” position.

    d. Lower the micrometer end face by rotating the Micrometer Drive (clockwise, CW) until it bottoms against the base.

    e. Raise the micrometer end face by rotating the micrometer Drive counter-clockwise (CCW).

        Rotate (several revolutions may be necessary) until the Dial Indicator needle registers and rotates one complete turn coming to rest at or near the 12 o’clock position.

    f. Verify the Digital Display Reading.

        Rotate the Micrometer Drive (CW) to position the needle on “100” and see that the Digital Display reads 0.100 µm. Return the needle to zero.

<u>Mounting Specimen</u>

2. After disc grinding to 40-70 µm, attach disc to metal mount cylinder with crystal bond.

    a. place mount on 130°C hot plate.

    b. touch small amount of crystal bond to surface.

    c. place disc onto crystal bond and move in circular fashion to thin out wax(note: use cocktail stick to manipulate sample).

    d. remove from hot plate and allow to cool.

    e. remove excess wax using small amount of acetone and cotton applicator.

3. Positioning of Specimen

a. Place specimen mount and centering ring onto the magnetic turn-table.

Make sure the specimen mount, centering ring and magnetic turn-table are wiped down prior to use

b. Gently position the microscope onto its mount and plug in the light.

c. Move specimen mount/centering ring until the desired feature is centered in the cross-hairs.

d. Check to see if the feature stays centered when the sample is rotating by turning on the Turn Table motor. If it does not stay centered, adjust with the motor off and check again.

4. Set Grinding by Dimple Depth

a. Place 15 mm Phosphor bronze grinding wheel on shaft.

b. Set the Counterweight load to 20 g and select a mid-range grinding speed.

c. Determine initial specimen thickness.

d. Check that both the Table and Arm motors are turned off.

e. Lower the micrometer end face by rotating the Micrometer Drive CW.

f. Carefully lower the grinding wheel onto the specimen face with the Cam.

Cam in the back position is “raised” and Cam in the front position is “lowered”.

g. Raise the micrometer end face by rotating the Micrometer Drive until the dial indicator needle has rotated one complete turn and just reaches zero. Do not go past zero.

h. Press Zero button to zero the Dimple Depth digital display.

i. Lower the micrometer end face (CW rotation) until the Digital Display reads the required dimple depth. Ex. If the initial thickness is 70 µm and you would like to have a final thickness of 20 µm, set the Digital Display to 50 µm.

Note: The Dial Indicator will show the amount of material remaining to be removed.

5. Coarse Dimple Grinding of Sample

Coarse dimple grind the sample with the 15 mm phosphor bronze wheel to a thickness of 20-25 µm using 2-4 µm diamond paste, 15-20 g load and low to medium speed.

a. After step 3 and 4, place a small amount of diamond compound onto the wheel and the specimen using a cocktail stick, then moisten with distilled water.

b. Turn on both the Table and Arm motors.

Note: The specimen surface and grinding wheel must always remain wet with a dilute solution of diamond paste and water. Maintain through addition of small amounts of diamond paste using a cocktail stick and water using a pipette. Approximately half way through the grind, clean wheel and sample and rewet with diamond paste and distilled water.

c. When the Dial Indicator reaches zero, then stop motors and remove grinding disc and wash with distilled water to remove excess paste. Also, wash sample thoroughly with copious amounts of distilled water.

6. Dimple polish using 2-4 µm diamond paste.

a. Following coarse dimple grinding, change to a felt wheel, wet the felt wheel with distilled water and create slurry with 2-4 µm diamond paste. As before, do not allow to dry out, monitor closely and add distilled water or diamond paste as needed.

b. Dimple polish with the felt wheel for 3-5 min using 2-4 µm diamond paste, 20-25 g load and low to medium speed. This polish is to bring the thickness down to approximately 10 µm, which can be determined with transmitted light for most samples

c. When finished thoroughly clean felt wheel and collar, dry out felt wheel and place back into labeled zip lock bag.

7. Dimple polish using 0-2 mm diamond paste.

Note: To avoid contamination, use different felt wheels for each diamond paste and the Alumina suspension. The felt wheels for each diamond paste and Alumina suspension are stored in labeled zip lock bags.

a. Following dimple polishing using 2-4 µm diamond paste, change to a **new** felt wheel, wet with distilled water and create slurry with 2-4 µm diamond paste. As before, do not allow to dry out, monitor closely and add distilled water or diamond paste as needed.

b. Dimple polish with the **new** felt wheel for 5-6 min(or a thickness of 6-8 µm) using 0-2 µm diamond paste, 20-25 g load and medium speed.

c. When finished thoroughly clean felt wheel and collar, dry out felt wheel and place back into labeled zip lock bag.

8. Dimple polish using 0.05 Alumina suspension

a. Following dimple polishing using 0-2 μm diamond paste, change to a **new** felt wheel, wet wheel and sample with Alumina suspension. As before, do not allow to dry out, monitor closely and more Alumina suspension as needed.

b. Dimple polish with the **new** felt wheel for 8-10 min(or a thickness of 5 μm) using the Alumina suspension, 20-25 g load and medium speed.

c. When finished thoroughly clean felt wheel and collar, dry out felt wheel and place back into labeled zip lock bag.

Figure C.13. A 70 micron thick 3 mm disc after dimpling and polishing (<20 μm in depth) using the Gatan dimple grinder.

C.5. Gatan precision ion polishing system (PIPS) model 691

Figure C.14. Gatan PIPS model 691 with argon tank.

C.5.1. Gatan precision ion polishing system (PIPS) model 691 operating procedure

1. Turn on Argon Tank.
2. Remove sample holder/clamp by pressing and holding VENT button.
3. Evacuate empty chamber by holding down VAC button until green light appears.
4. Purge Guns.

   This needs to be done when the system has been off or after the chamber has been opened.

   a. Make sure HV is off to guns.
   b. Switch OFF the RIGHT gas control switch.
   c. Switch ON the LEFT gas control switch.
   d. Adjust gas flow to 1 x 10^{-4} torr.
   e. Turn OFF the LEFT gas control switch.
   f. Turn ON the RIGHT gas control switch.
   g. Adjust gas flow to 1 x 10^{-4} torr.
   h. Turn BOTH on gas control switches on and allow to purge for 15 min.
   i. Turn OFF LEFT and RIGHT gas switches and then turn HV ON. Confirm maximum beam current of <5 μa is obtained for each gun at 5.0 KeV

5. Adjust Gas Flow.
   Remove specimen holder or screen before adjusting gas flow.

a. Turn OFF LEFT gas switch and leave RIGHT gas switch on.
b. Set rotation speed to 3.
c. Turn off BEAM MODULATOR.
d. Press VAC button to evacuate airlock chamber.
e. Toggle AIRLOCK control button to lower.
f. Set HV Timer to 30 min and START.
g. Adjust voltage to 5.0
h. Adjust RIGHT needle valve CCW until pressure enters 1 x 10^{-4} torr range. Then slowly rotate needle valve CW until peak current is obtained. Make note of peak current value.
i. Set operating range by rotating needle back CCW to a value of 85-90% peak value obtained in step h. Example: peak current is 90 operating range should be set to 76.5.
j. Repeat step h and i for the LEFT gun.
k. Turn both LEFT and RIGHT guns back on when finished.

6. Ion-beam Milling
    a. Mount pre-thinned sample disc on a sample holder either clamp or glue type.
    b. Check beam alignment if necessary.
    c. Raise sample mount and VENT airlock chamber.
    d. Load sample holder into the sample mount inside the airlock chamber and lower it to the working position.
    e. Set the gun angles for each gun
    f. Set the rpm using the rotation speed control.
    g. Set the desired time interval on the digital process timer.
    h. Toggle the beam modulation switch to “Single”, “Double”, or “Off”.
    i. Press the START button on the HV Timer.
    j. Adjust the ion beam energy (keV) using the beam energy knob and watching the digital display readout.
    k. After milling is complete, unload the sample holder from the airlock chamber.

Note: The loads and speeds are suggested and work best for Si and Si based materials. Lower speeds and loads are necessary for brittle materials. For most metals and alloys, slightly higher loads and speeds work better.

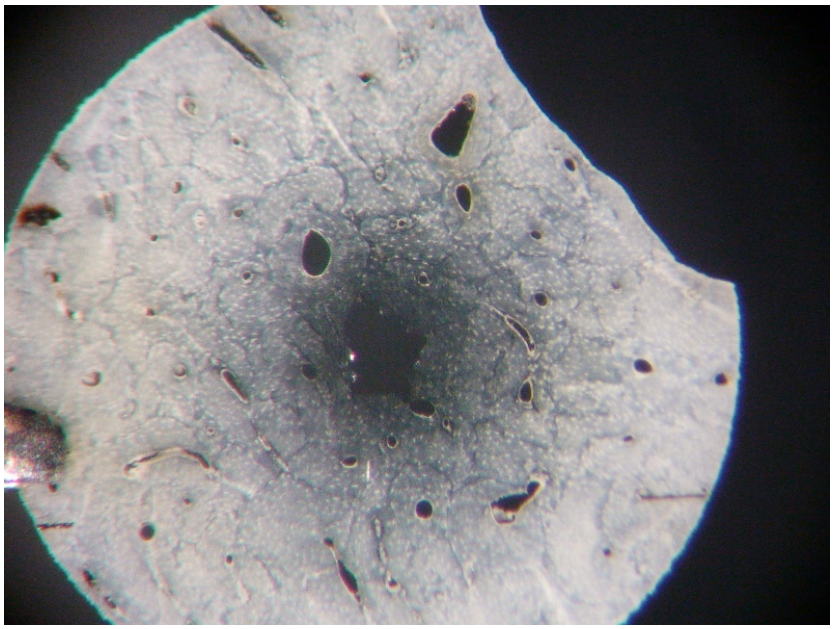

Figure C.15. Bone sample milled to less than 100 nm thick near the center perforation using Gatan PIPS ion mill.

APPENDIX D. PROCEDURES FOR OBTAINING EELS DATA USING THE GATAN ENFINA SPECTROMETER ATTACHED TO A JEOL JEM-2100 TEM

Each of the procedures contained in this appendix were compiled exclusively by the author using careful research and consultation with Gatan and JEOL applications personnel.

D.1. Preparing a gain reference for the ENFINA camera

1. Retract Orius Camera
2. With TEM in IMAGING mode find a hole in the sample
3. Setup even illumination across ENFINA CCD
4. Go to EELS Acquisition and set dispersion to 0.0 eV/ch, start energy to 0.0 and aperture size 1
5. Under EELS Acquistion options make sure Vertical binning set to 1x and Show Original Image for View is checked
6. Set Exposure to 0.1 and hit View. Intensity in the 2D spectrum should be centered, if not, adjust with start energy
7. Illuminate the whole of the detector by increasing aperture (use 5 mm) you will need to center the beam with the SHIFTS (X,Y) to center on the aperture and bring the counts up to 20K using Condenser. Allow to illuminate for 5 minutes to anneal the detector and remove any history.
8. Stop SPECTRUM VIEW and check the temperature of the ENFINA
9. Prepare GAIN REF using Target Intensity = 30000 and 100 Frames
10. Acquire GAIN REF and wait until finished

D.2. ENFINA spectrometer lens alignment procedure

1. Set JEOL 2100-LaB_6 conditions to 200kV and condenser aperture - 3 (Ap-3).

2. Retract Orius camera.

3. Three alignments: Condenser/Voltage center/Beam Center.

4. Condense Beam.

5. Switch to EDS mode and α-5, 10 nm spot size.

6. Read in 2 cm camera length condition.

7. PLA to center onto the entrance aperture (EA).

8. Switch back to EDS mode to view then back to TEM mode.

9. Find area of no sample in TEM mode.

10. Use the following conditions for the TEM: 10,000X magnification, Ap-2, TEM mode, and no sample.

11. Use the following conditions for the ENFINA: 3 mm EA, 0.3 ev/channel, 0.1 s exposure.

12. Use brightness knob to remove saturation and if done correctly there should be a thin line near zero.

13. Align focus using Fx, Fy, Sx, Sy, AccompA, AccompB. Value change for each axis should be within 0.5 eV of the previous value.

14. Use ENFINA Filter Control panel to touch up focus if needed.

15. Move to sample area.

16. This procedure should only need to be done at the beginning of a session.

D.3. ENFINA spectrometer EELS data acquisition procedure

1. Set TEM conditions to: TEM mode, condenser Ap-3 and set eucentric sample height.

2. Make sure Orius camera is retracted.

3. Three alignments: Condenser/Voltage Center/Beam Center.

4. Find area of interest.

5. Change to EDS mode and back to TEM mode. Cycle multiple times. (This removes lens hysteresis).

6. Set to EDS mode, α-5, 10 nm spot size. (Do not realign aperture).

7. Change brightness to condense beam and then change to SA Diffraction mode (SA-Diff) and Standard Focus.

8. Read in 2 cm camera length settings. (The diffraction pattern should be near the center)

9. Set EFINA parameters to 0.1 s exposure, 0.3 eV/channel, and 1 mm EA.

10. Check zero-loss peak (ZLP) and align if necessary. Touch up Fy and Sx.

11. Adjust PLA to center beam onto the EA of ENFINA.

12. Acquire 100 frames at 0.1 s exposure for low loss spectrum acquisition.

13. For core loss spectrum acquisition the exposure range can be up to 1.5 s.

14. PLA must be used to adjust the beam onto the EA and increase the acquired counts. If the counts go over 30,000 the spectrum appears red and the exposure must be decreased.

APPENDIX E. FESEM IMAGES OF HUMAN BONE

E.1. Comparison of healthy and osteogenesis imperfecta diseased human bone

E.1.1. Longitudinal section

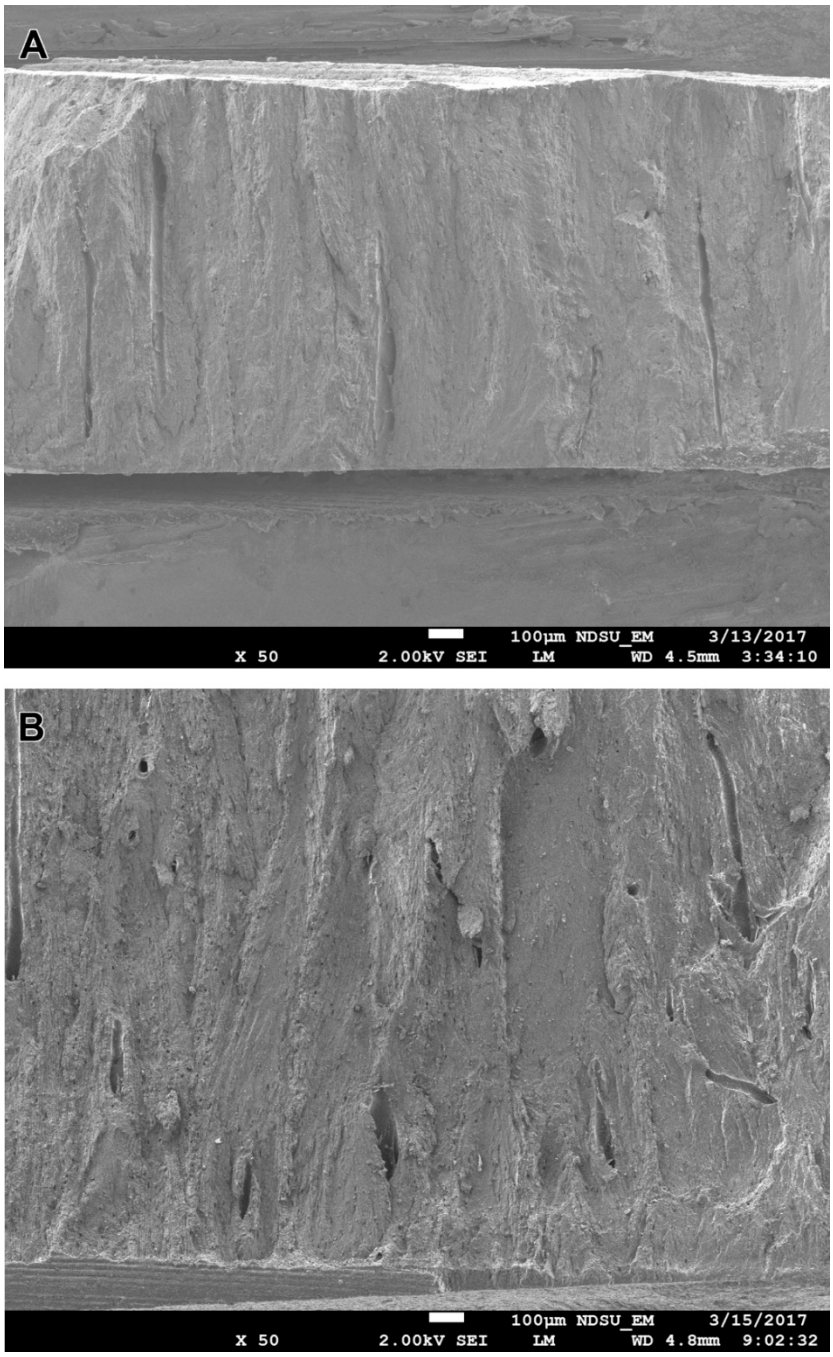

Figure E.1. FESEM secondary electron image of longitudinal sections of human bone (x50 original magnification). (A) healthy. (B) osteogenesis imperfecta.

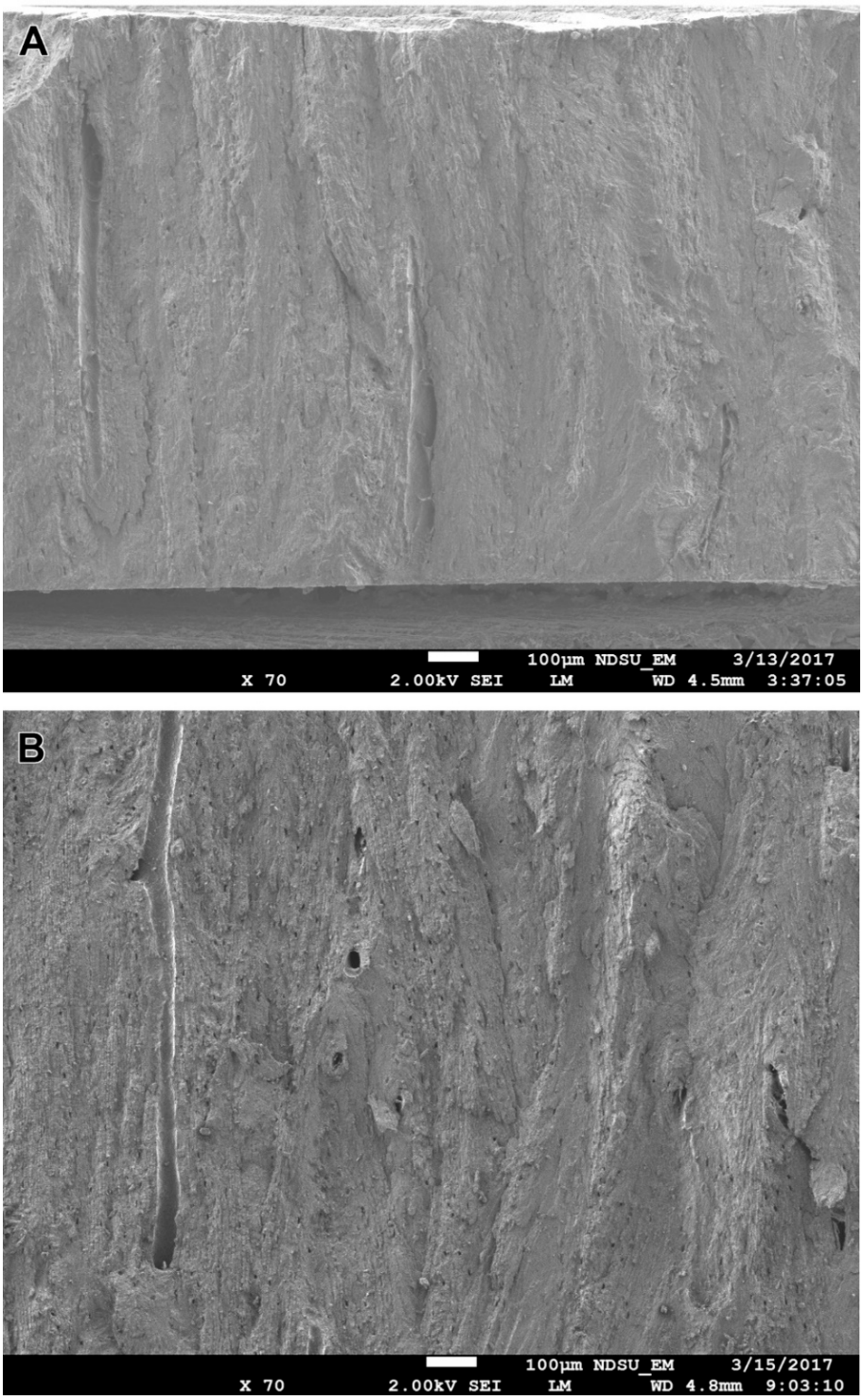

Figure E.2. FESEM secondary electron image of longitudinal sections of human bone (x70 original magnification). (A) healthy. (B) osteogenesis imperfecta.

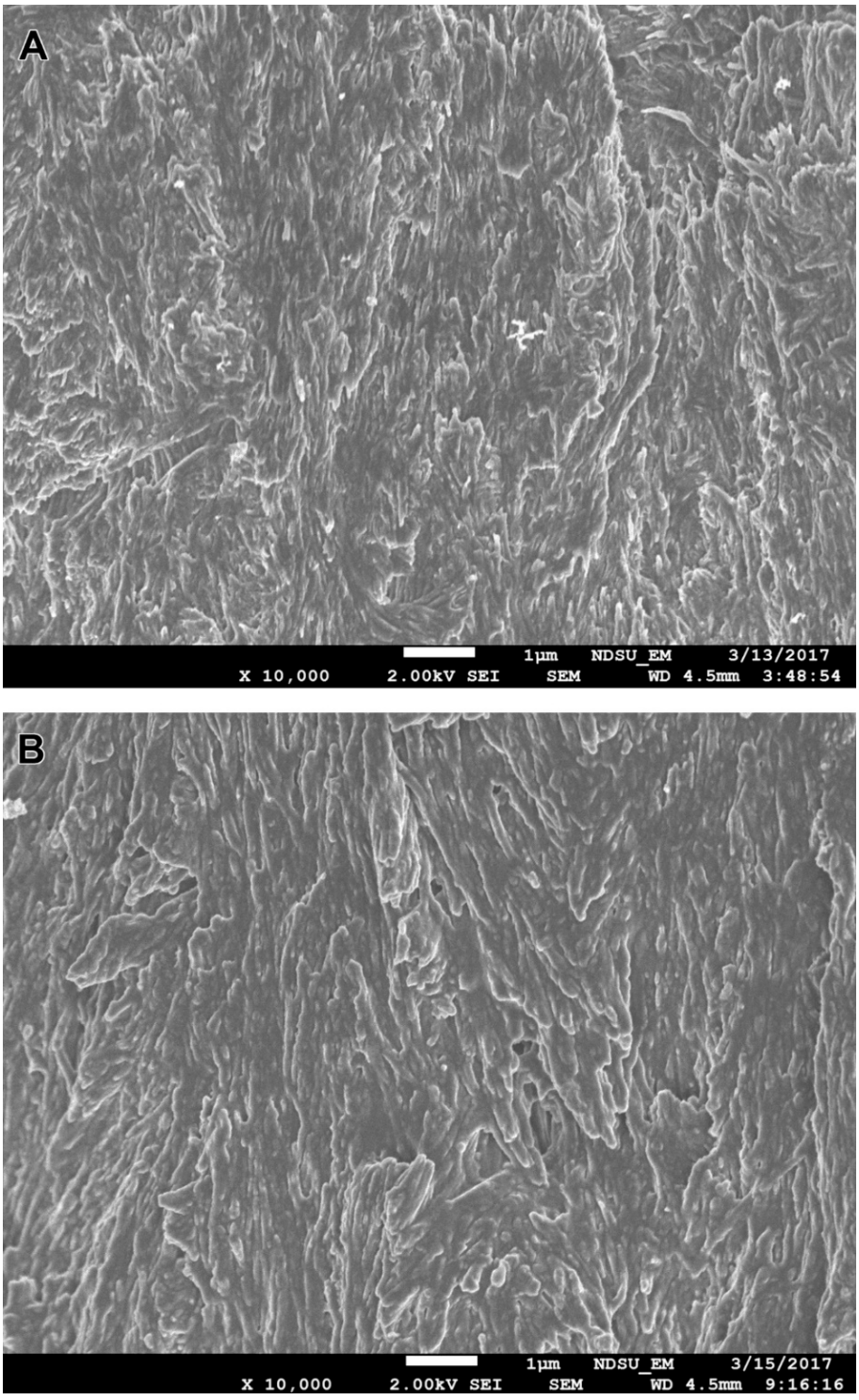

Figure E.3. FESEM secondary electron image of longitudinal sections of human bone (x10,000 original magnification). (A) healthy. (B) osteogenesis imperfecta.

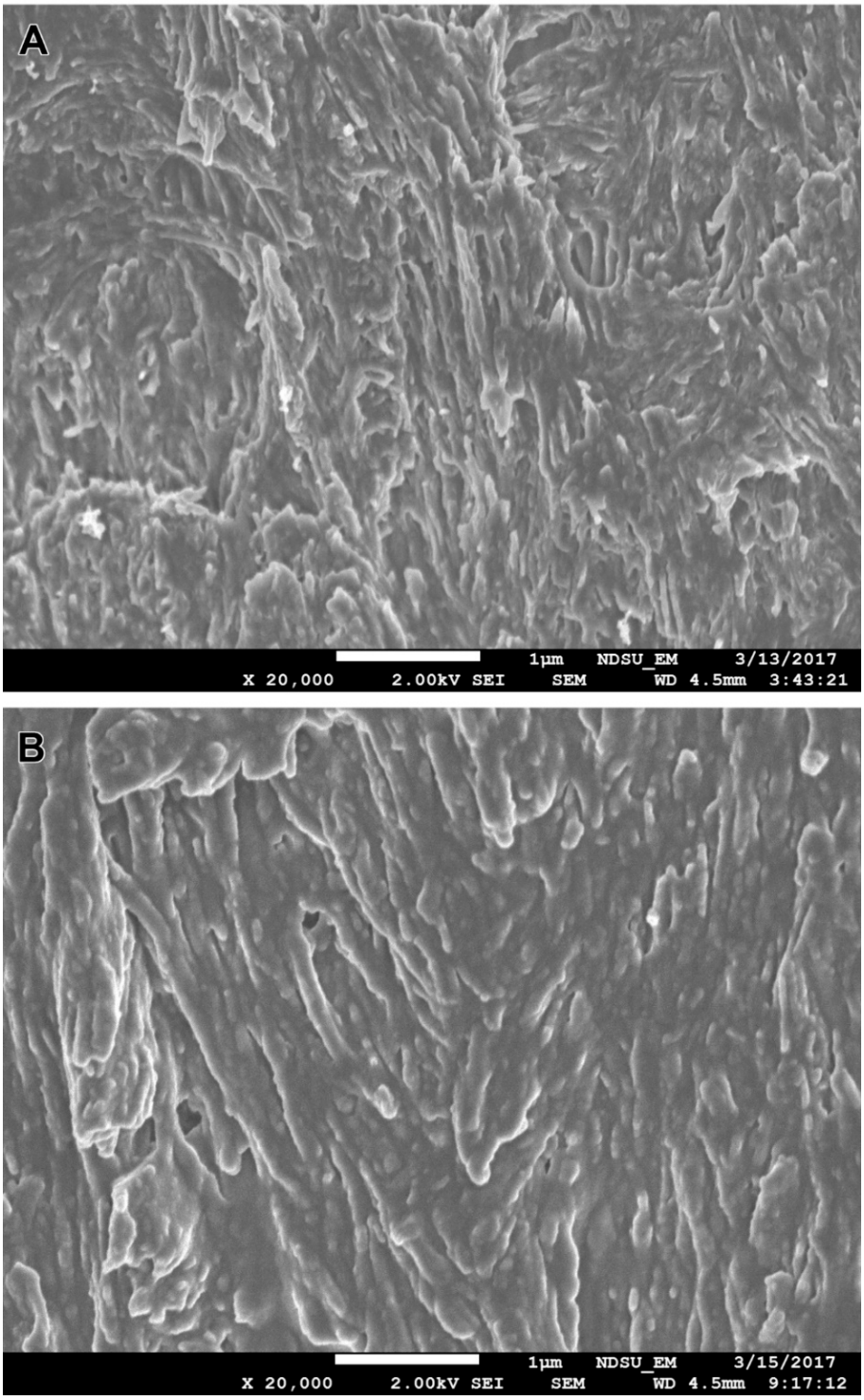

Figure E.4. FESEM secondary electron image of longitudinal sections of human bone (x20,000 original magnification). (A) healthy. (B) osteogenesis imperfecta.

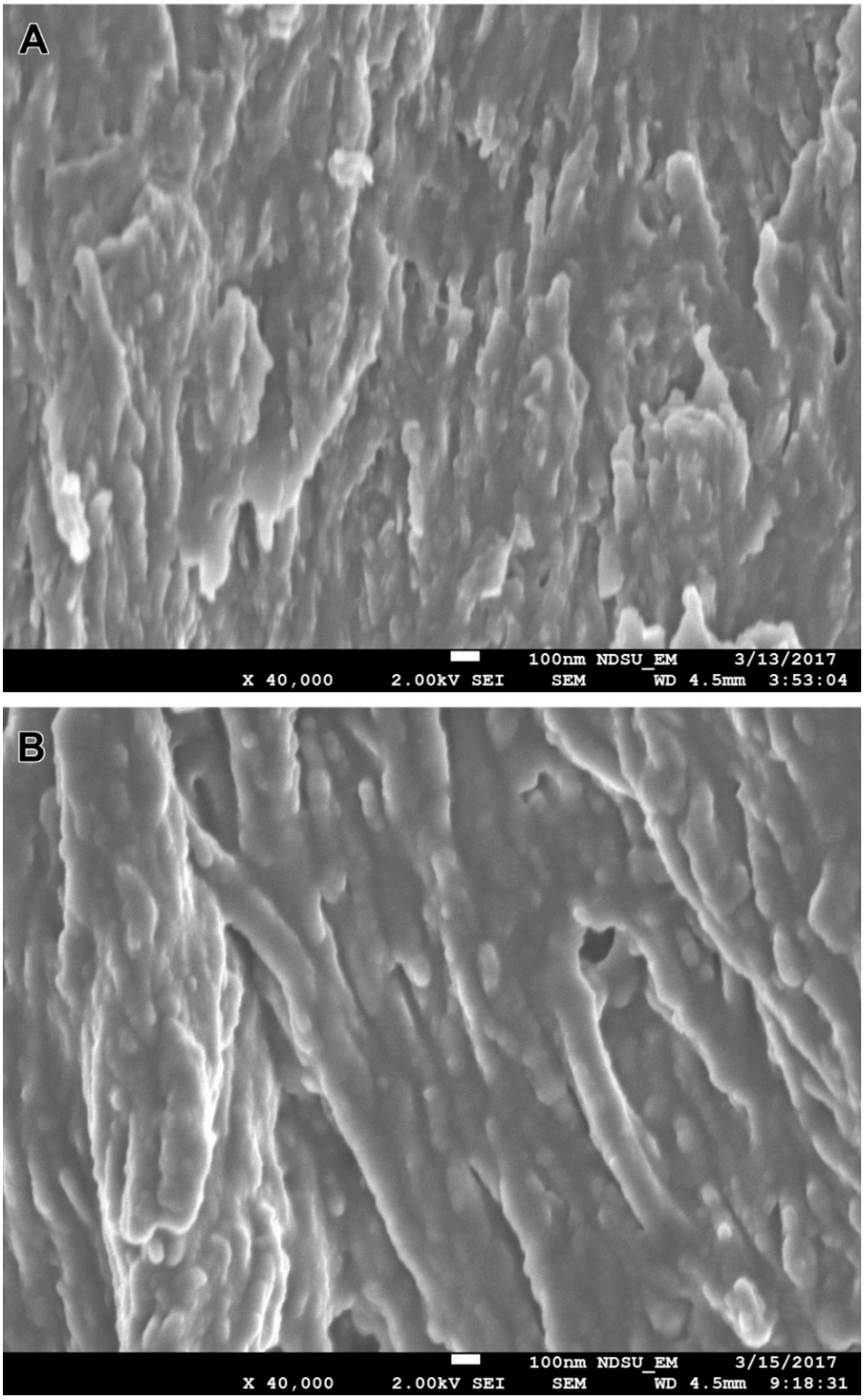

Figure E.5. FESEM secondary electron image of longitudinal sections of human bone (x40,000 original magnification). (A) healthy. (B) osteogenesis imperfecta.

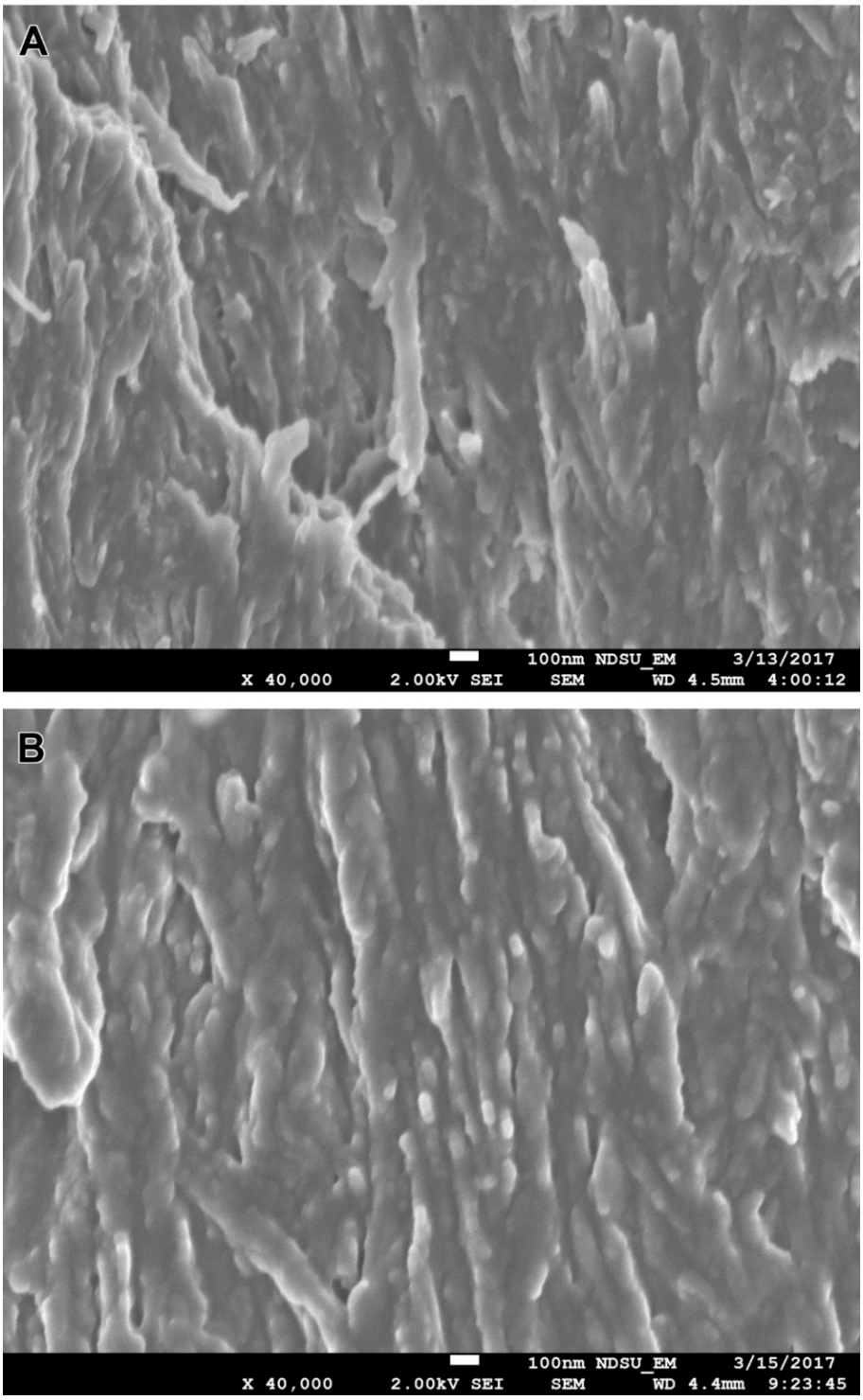

Figure E.6. FESEM secondary electron image of longitudinal sections of human bone (x40,000 original magnification). (A) healthy. (B) osteogenesis imperfecta.

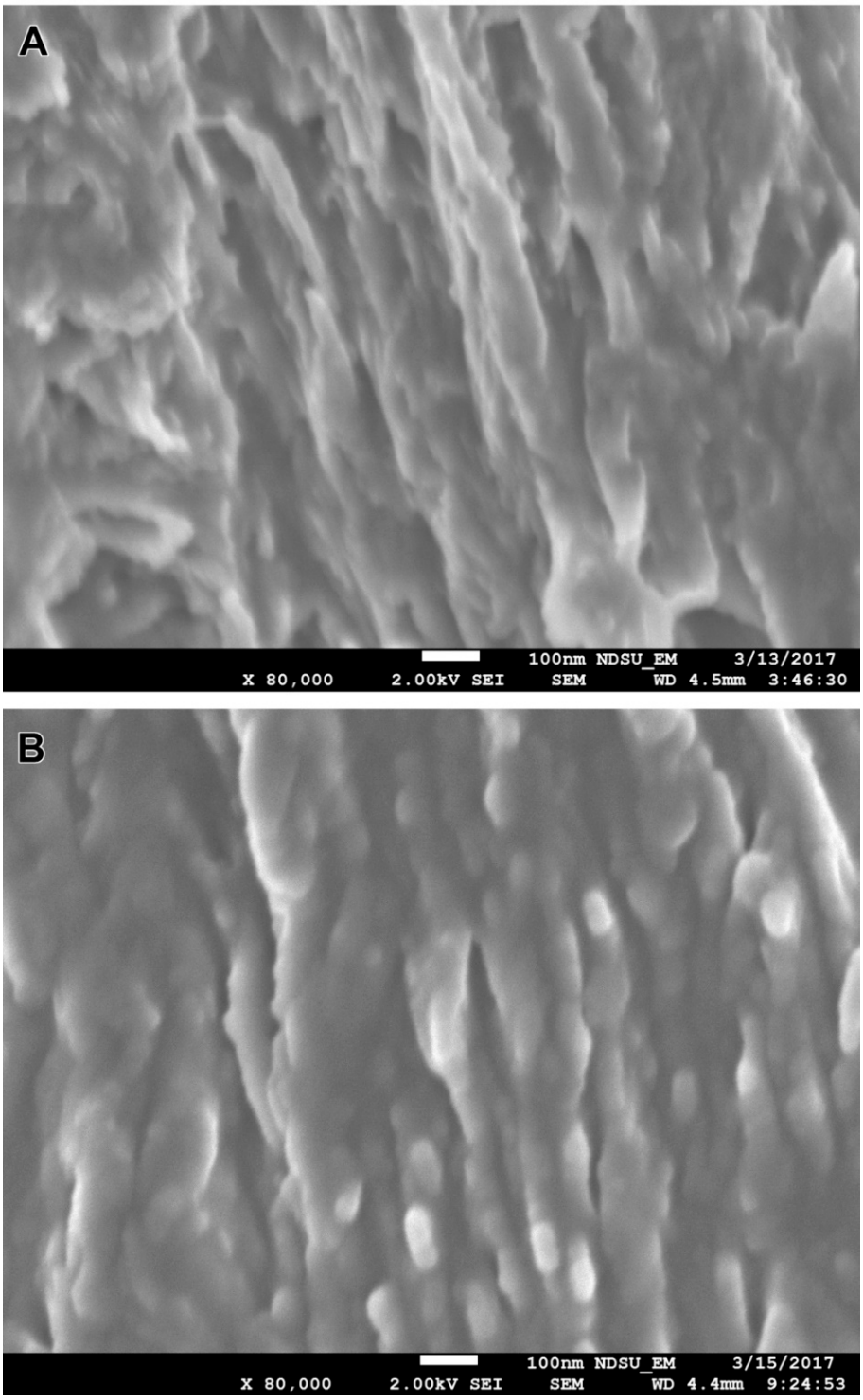

Figure E.7. FESEM secondary electron image of longitudinal sections of human bone (x80,000 original magnification). (A) healthy. (B) osteogenesis imperfecta.

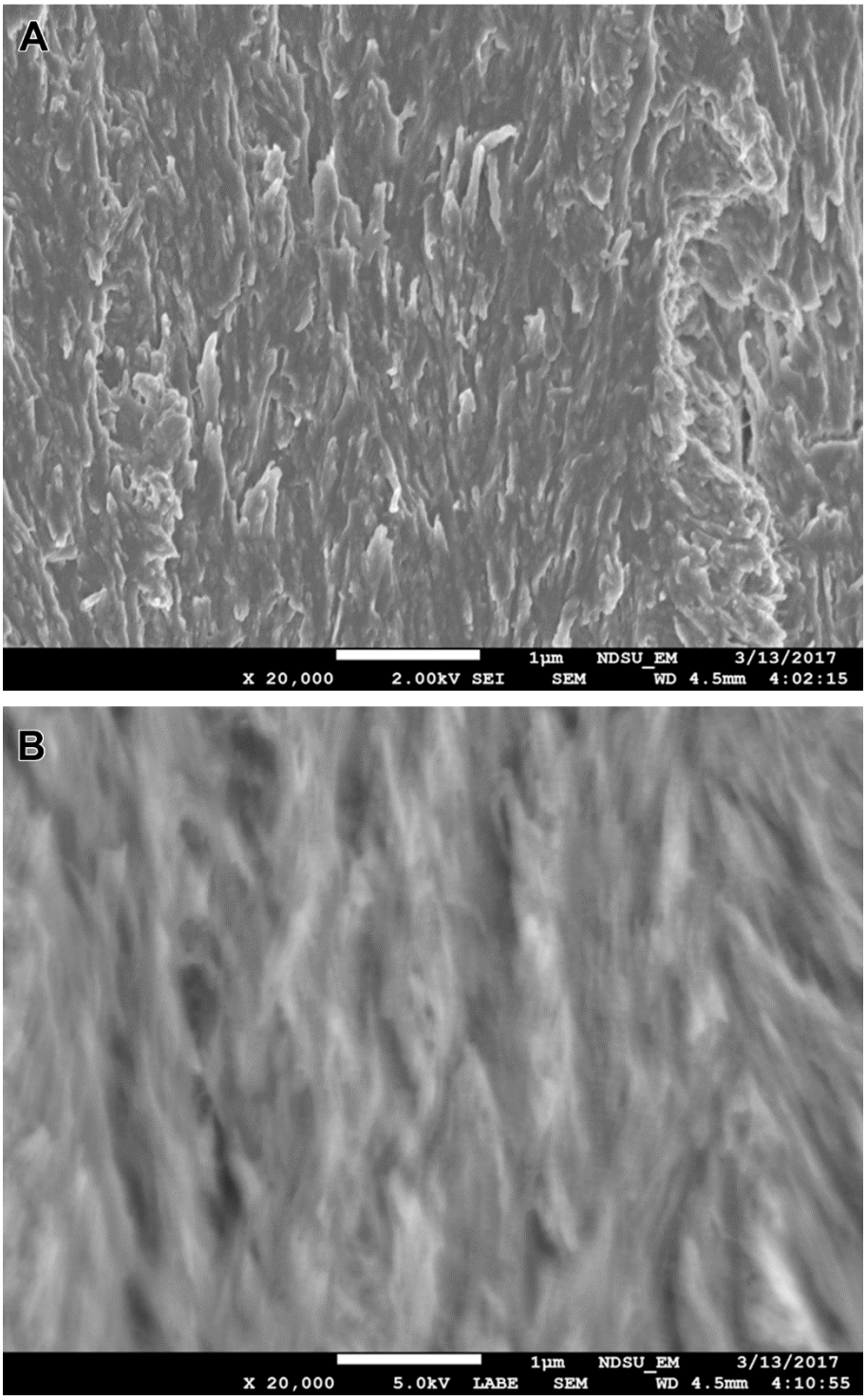

Figure E.8. Comparison of secondary and low-angle backscattered electron images for identical areas of healthy longitudinal bone (x20,000 original magnification). (A) secondary electron image. (B) low-angle backscattered electron image.

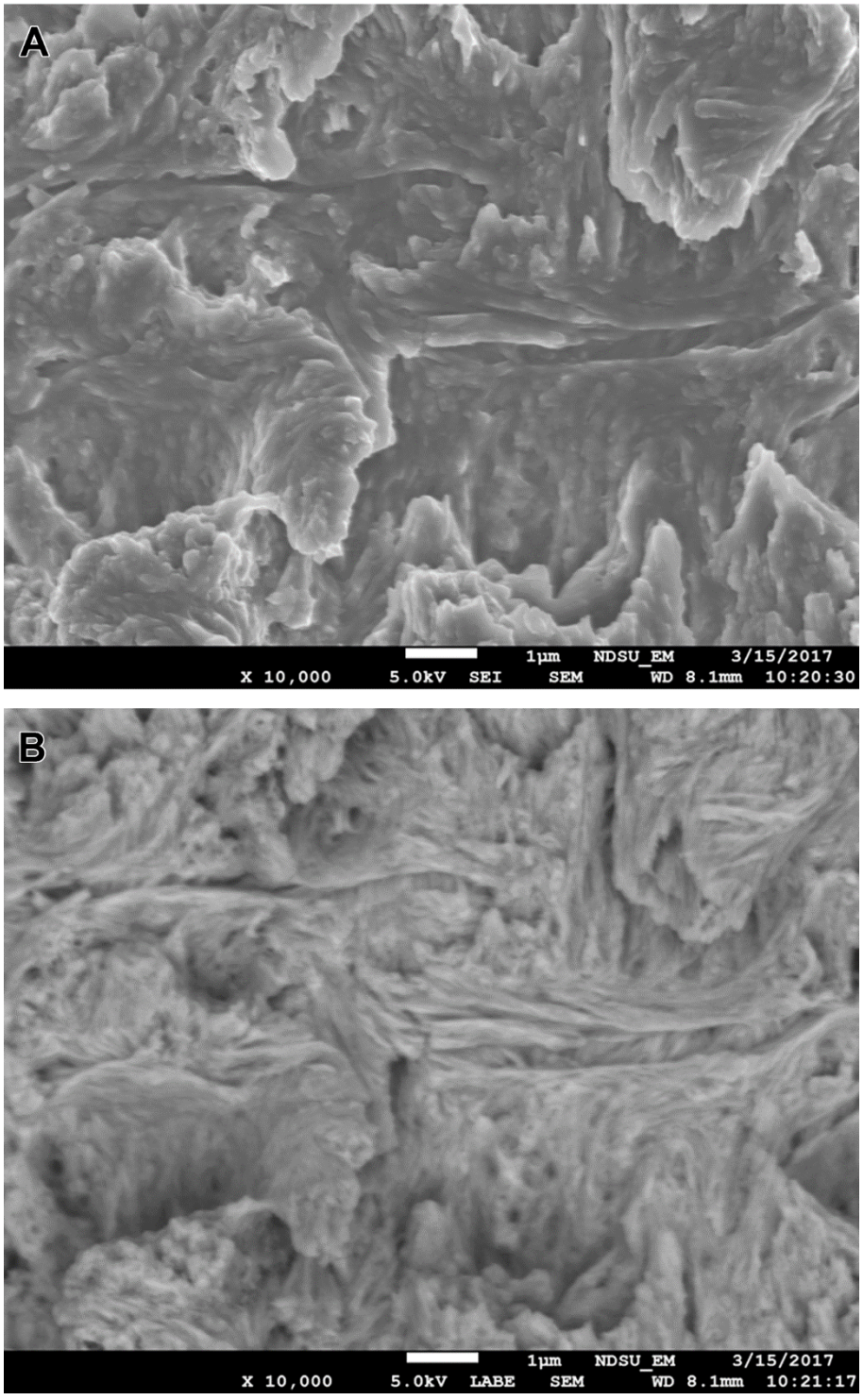

Figure E.9. Comparison of secondary and low-angle backscattered electron images for identical areas of osteogenesis imperfecta longitudinal bone (x10,000 original magnification). (A) secondary electron image. (B) low-angle backscattered electron image.

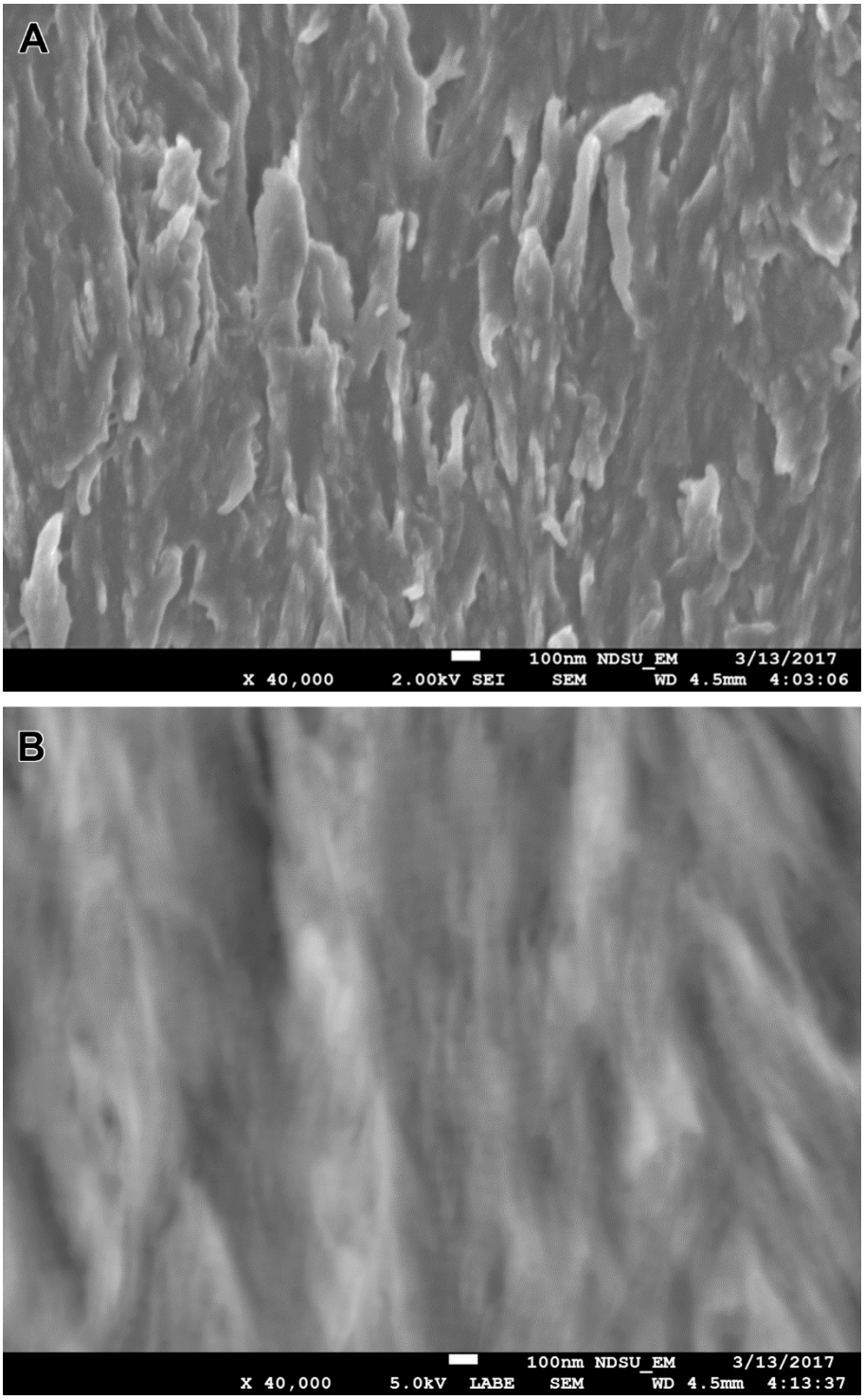

Figure E.10. Comparison of secondary and low-angle backscattered electron images for identical areas of healthy longitudinal bone (x40,000 original magnification). (A) secondary electron image. (B) low-angle backscattered electron image.

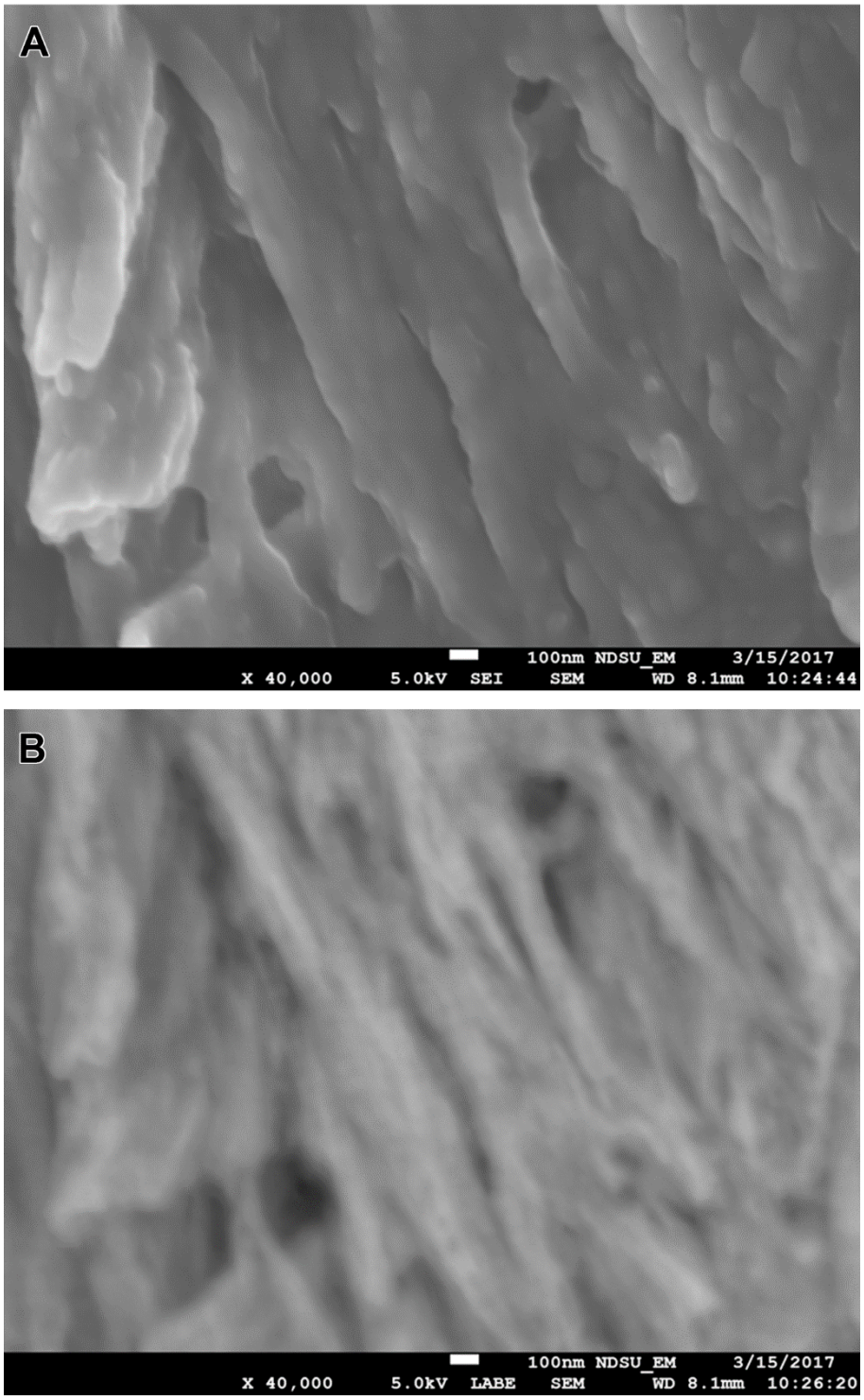

Figure E.11. Comparison of secondary and low-angle backscattered electron images for identical areas of osteogenesis imperfecta longitudinal bone (x40,000 original magnification). (A) secondary electron image. (B) low-angle backscattered electron image.

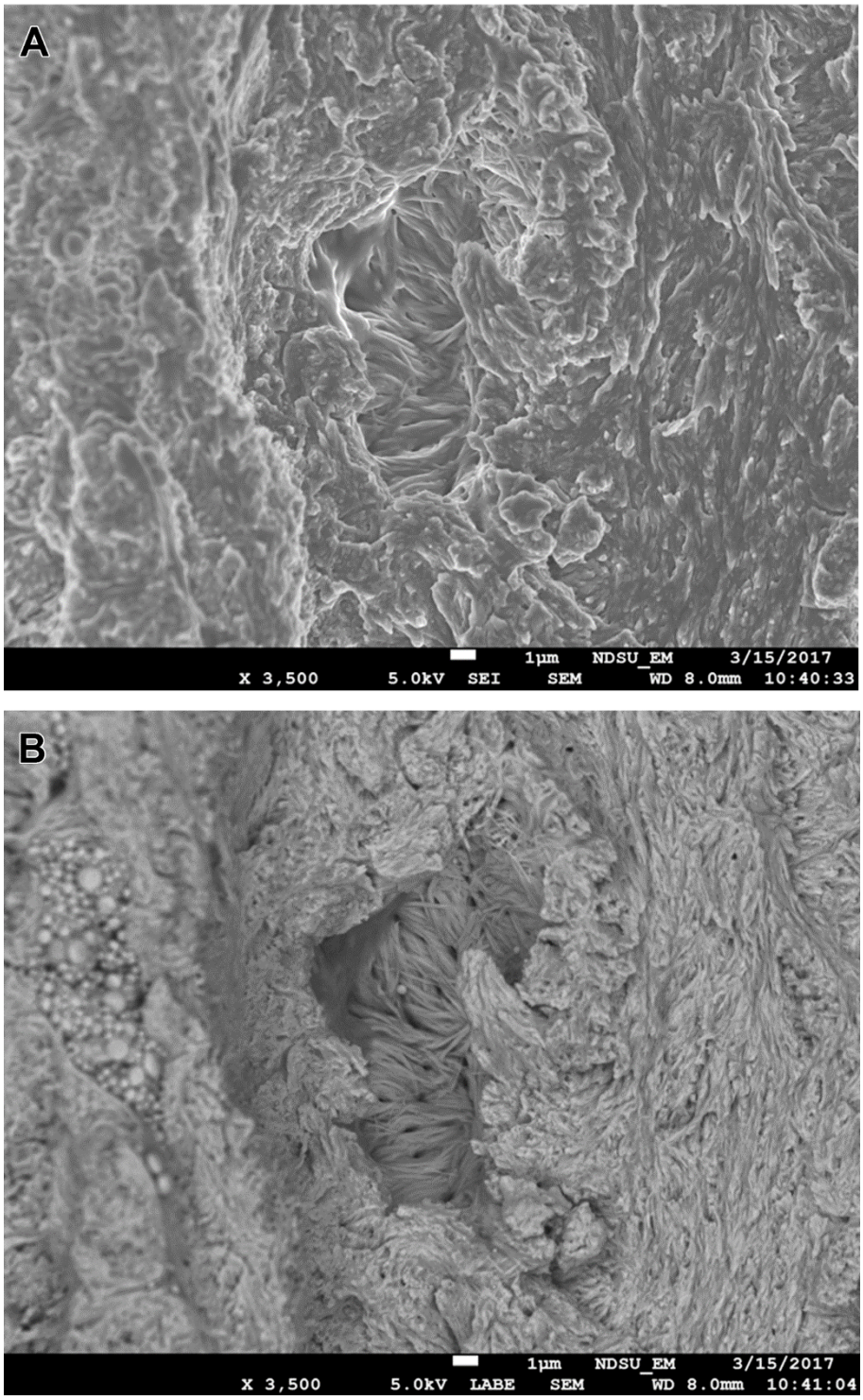

Figure E.12. Comparison of secondary and low-angle backscattered electron images for identical areas of osteogenesis imperfecta longitudinal bone (x3,500 original magnification). (A) secondary electron image. (B) low-angle backscattered electron image.

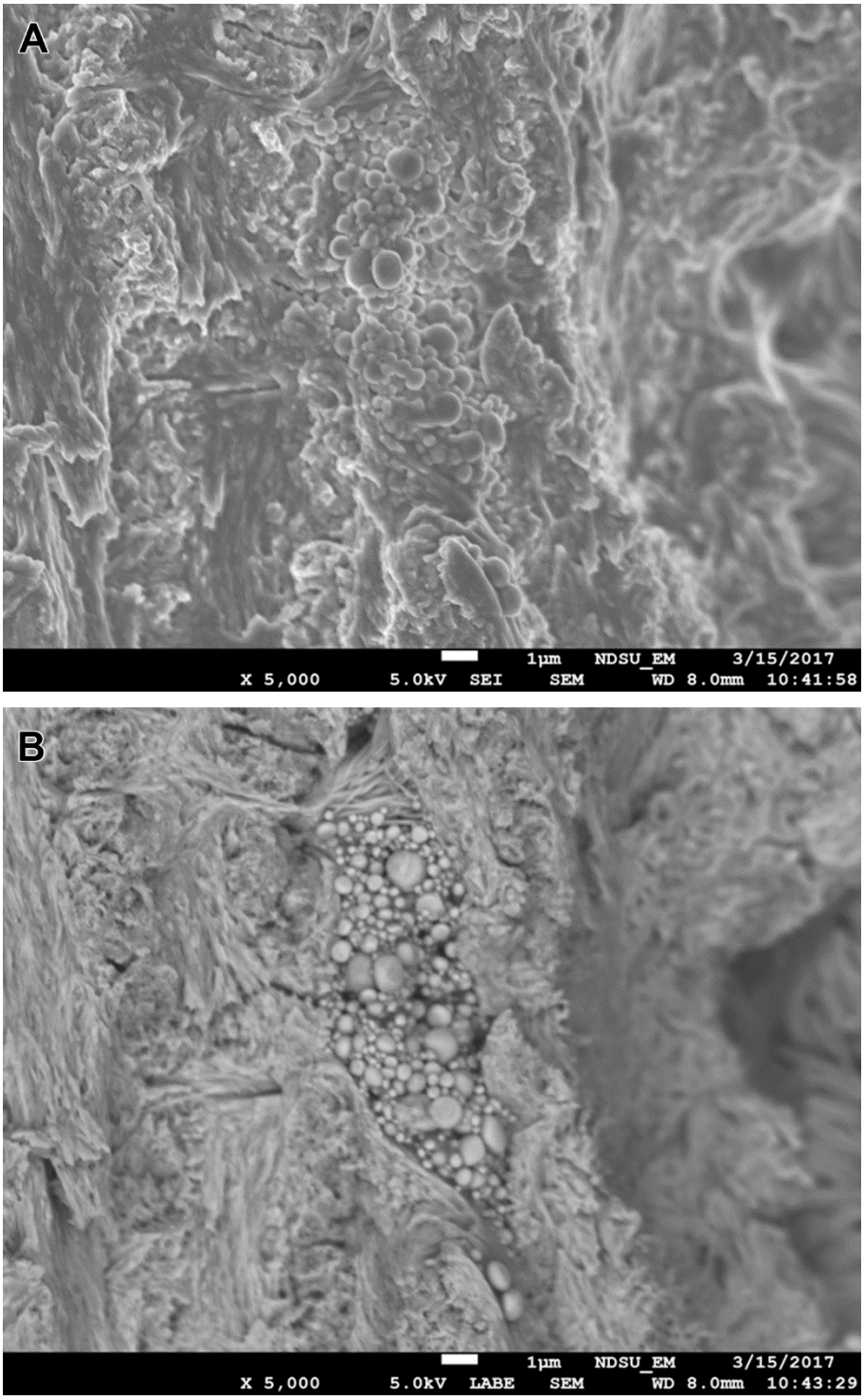

Figure E.13. Comparison of secondary and low-angle backscattered electron images for identical areas of osteogenesis imperfecta longitudinal bone (x5,000 original magnification). (A) secondary electron image. (B) low-angle backscattered electron image.

E.1.2. Transverse section

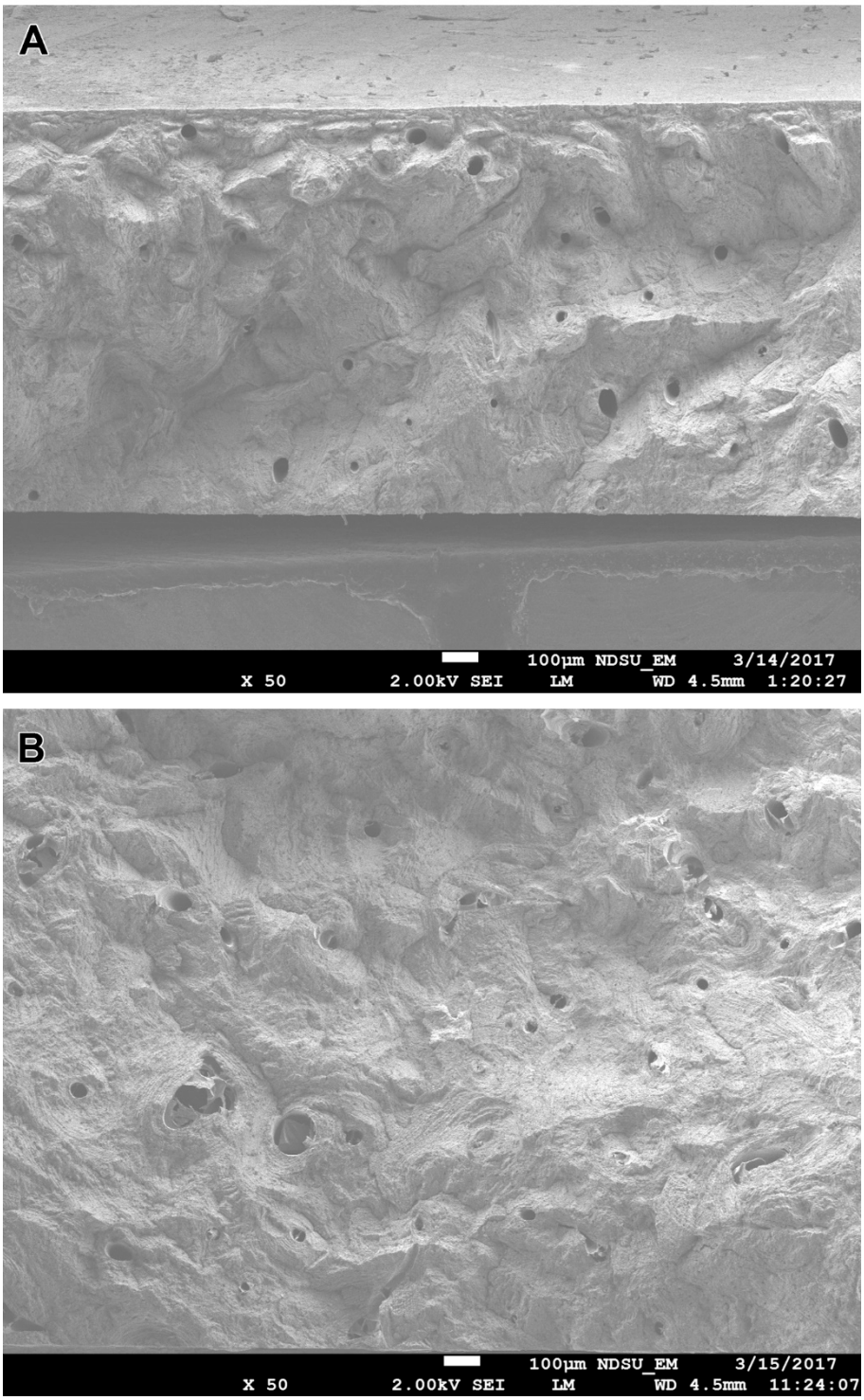

Figure E.14. FESEM secondary electron image of transverse sections of human bone (x50 original magnification). (A) healthy. (B) osteogenesis imperfecta.

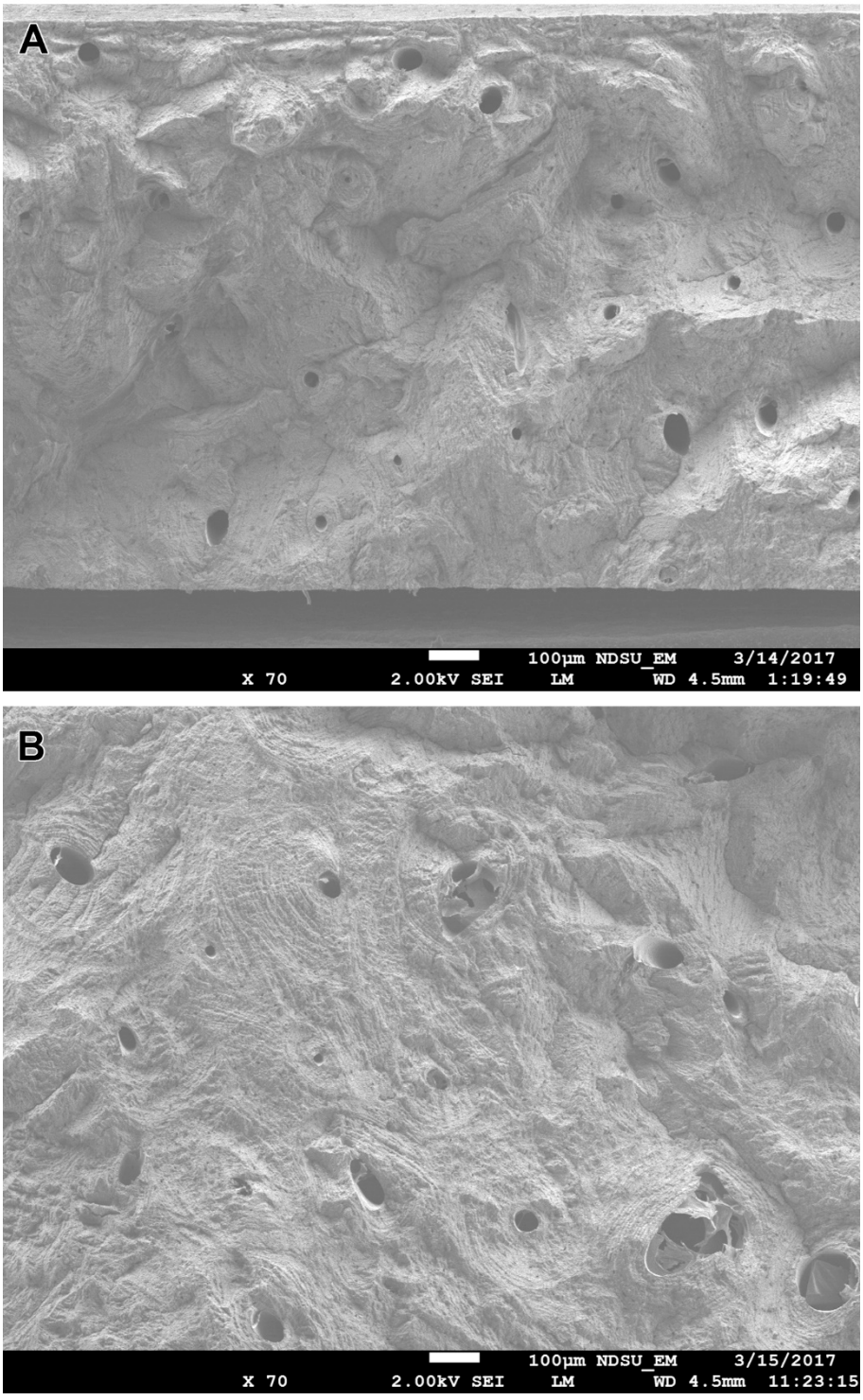

Figure E.15. FESEM secondary electron image of transverse sections of human bone (x70 original magnification). (A) healthy. (B) osteogenesis imperfecta.

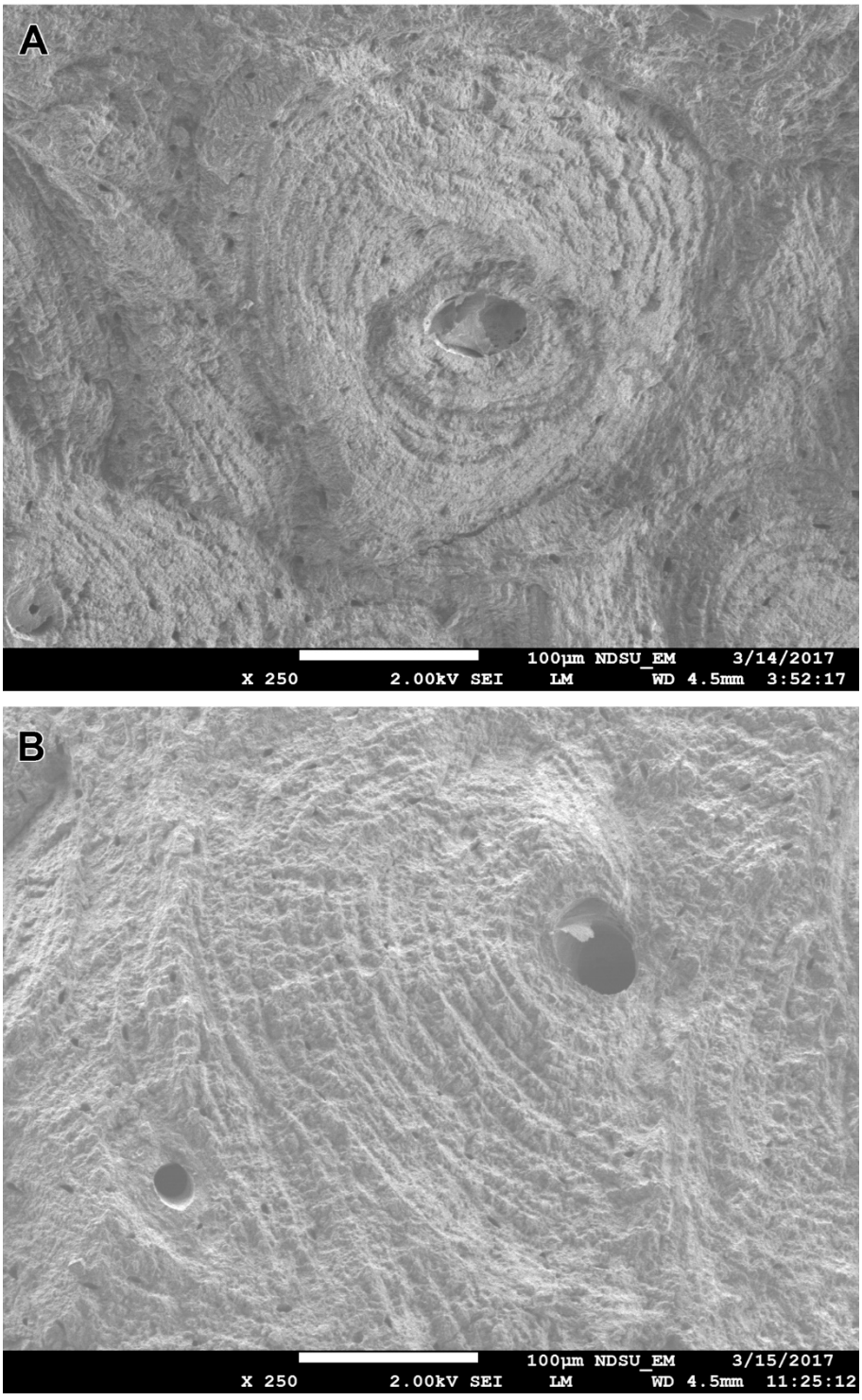

Figure E.16. FESEM secondary electron image of transverse sections of human bone (x250 original magnification). (A) healthy. (B) osteogenesis imperfecta.

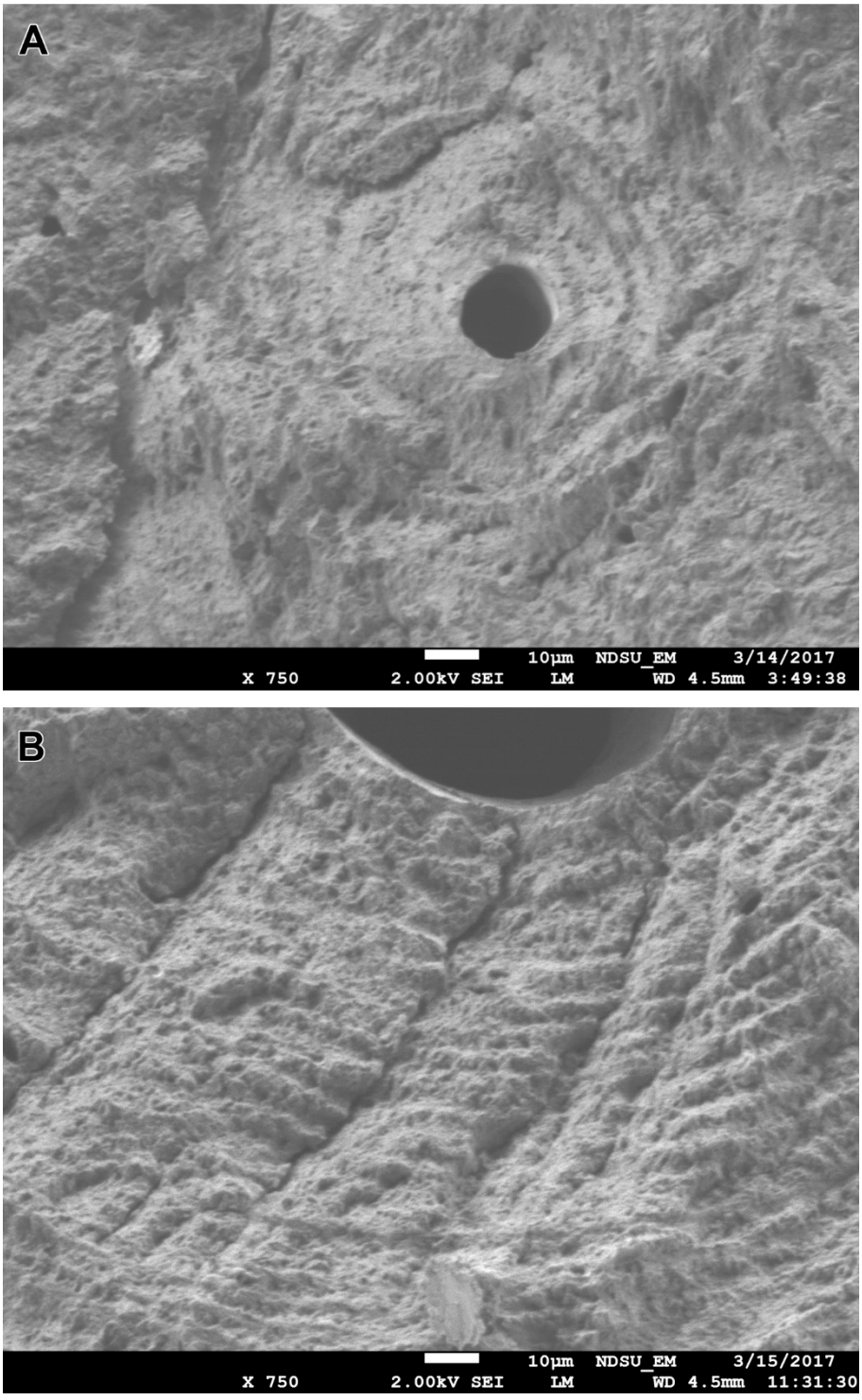

Figure E.17. FESEM secondary electron image of transverse sections of human bone (x750 original magnification). (A) healthy. (B) osteogenesis imperfecta.

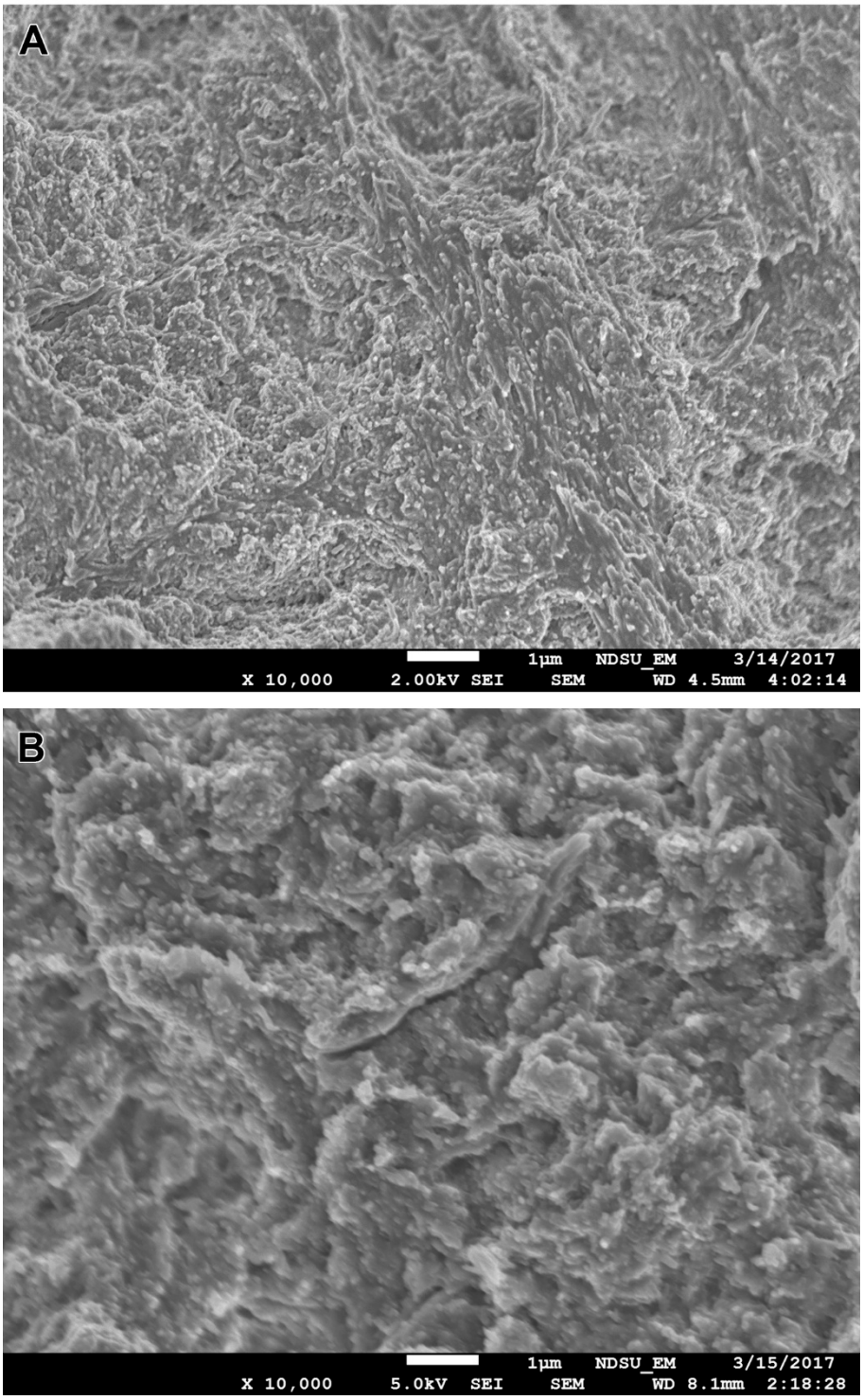

Figure E.18. FESEM secondary electron image of transverse sections of human bone (x10,000 original magnification). (A) healthy. (B) osteogenesis imperfecta.

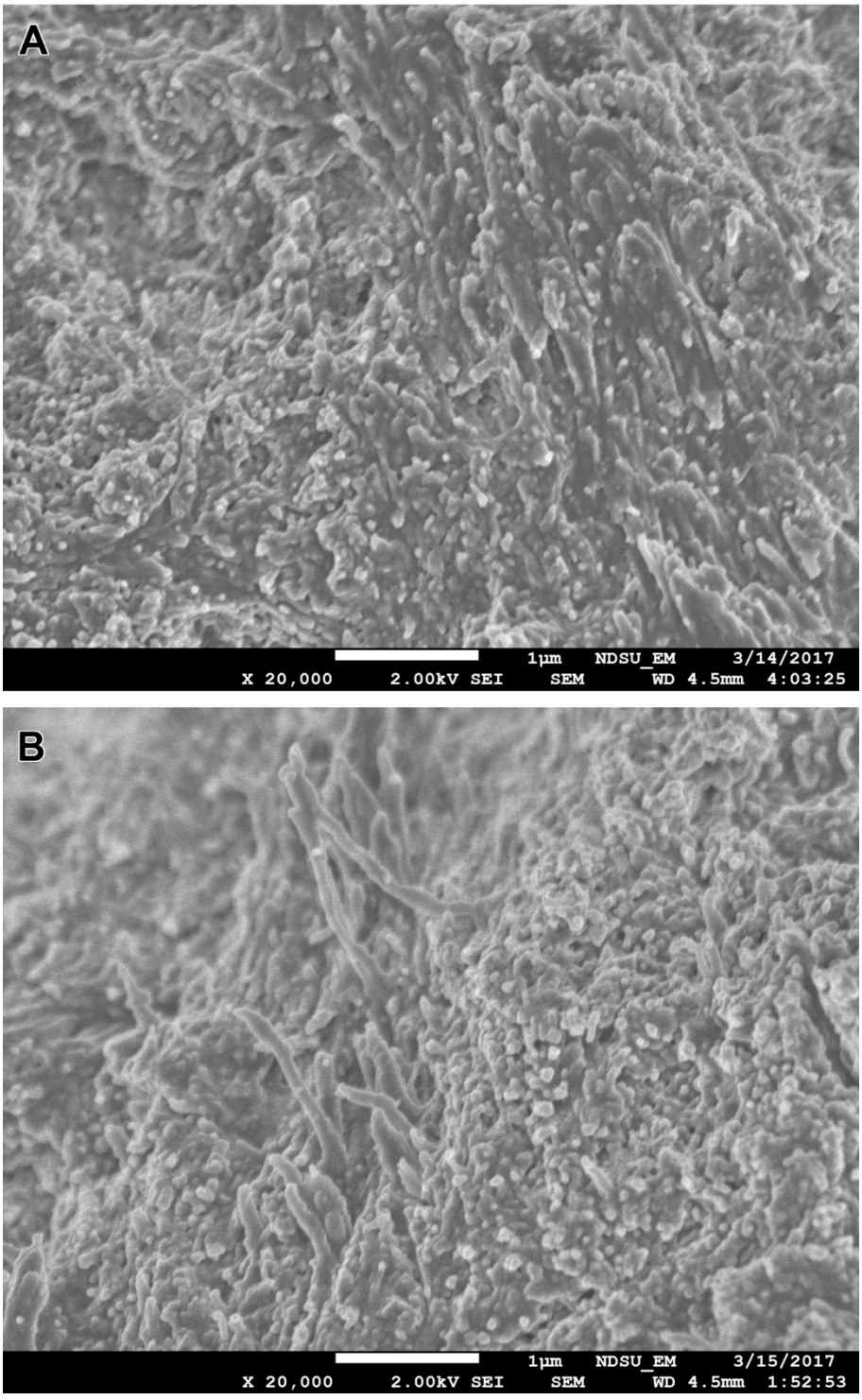

Figure E.19. FESEM secondary electron image of transverse sections of human bone (x20,000 original magnification). (A) healthy. (B) osteogenesis imperfecta.

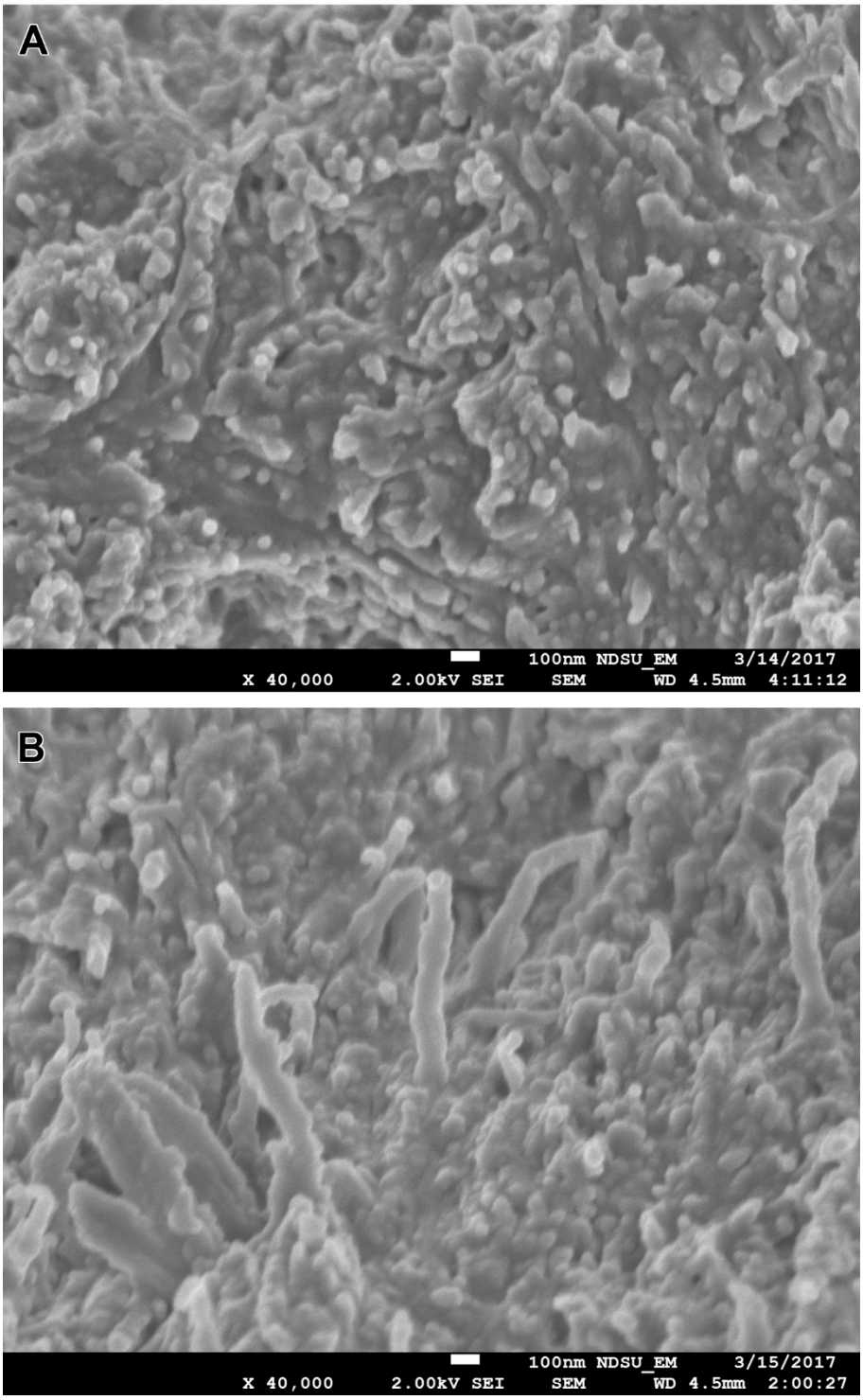

Figure E.20. FESEM secondary electron image of transverse sections of human bone (x40,000 original magnification). (A) healthy. (B) osteogenesis imperfecta.

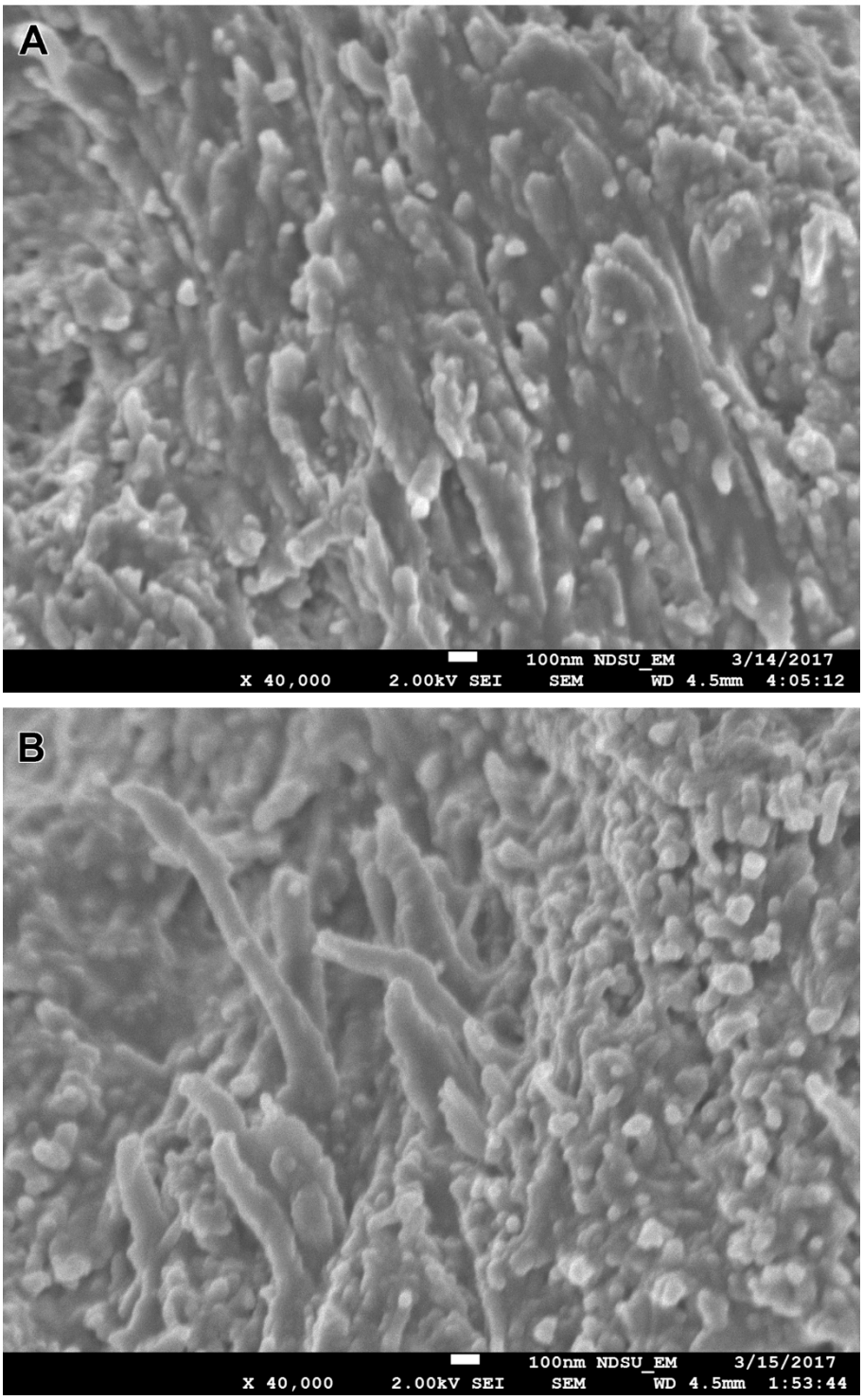

Figure E.21. FESEM secondary electron image of transverse sections of human bone (x40,000 original magnification). (A) healthy. (B) osteogenesis imperfecta.

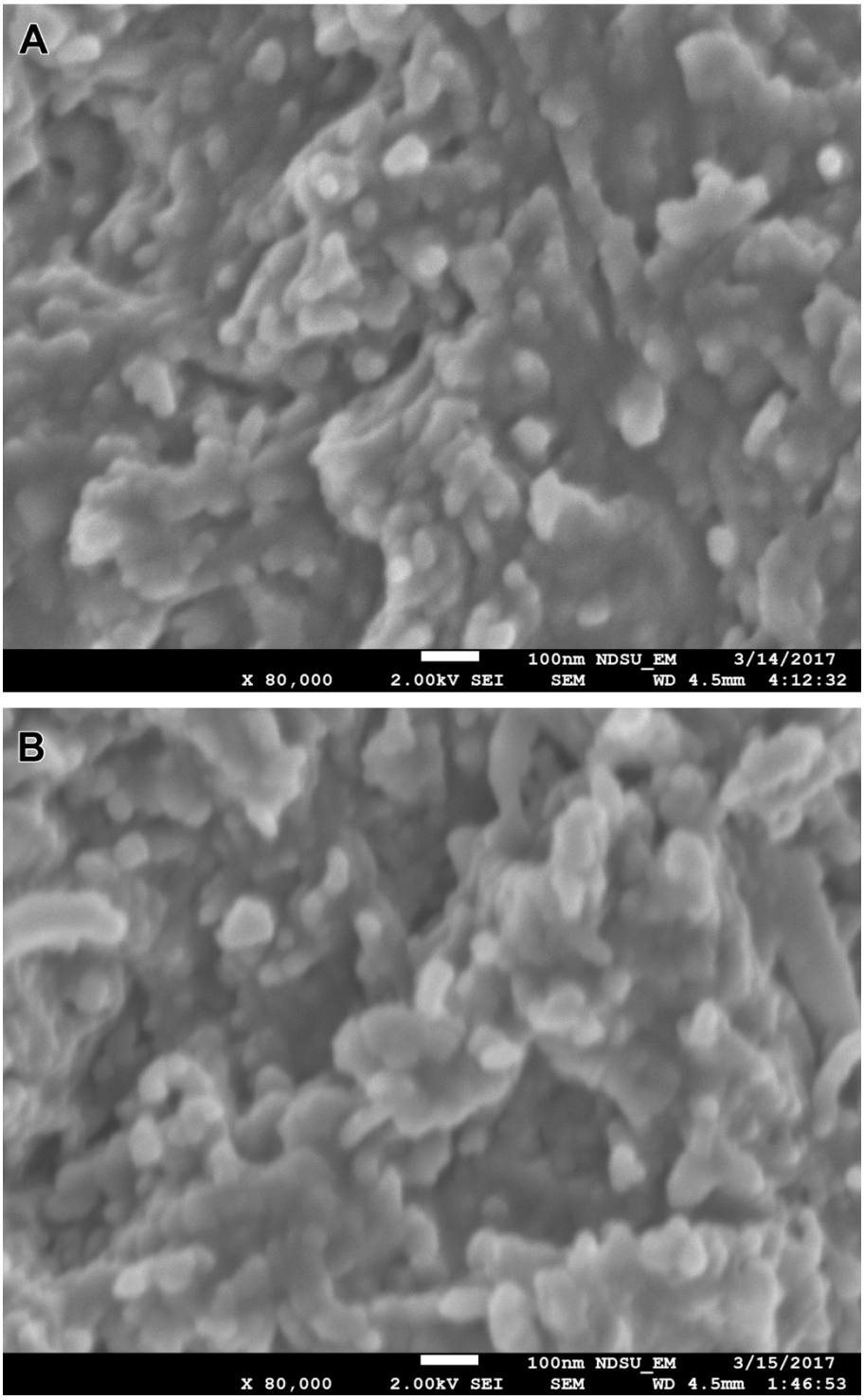

Figure E.22. FESEM secondary electron image of transverse sections of human bone (x80,000 original magnification). (A) healthy. (B) osteogenesis imperfecta.

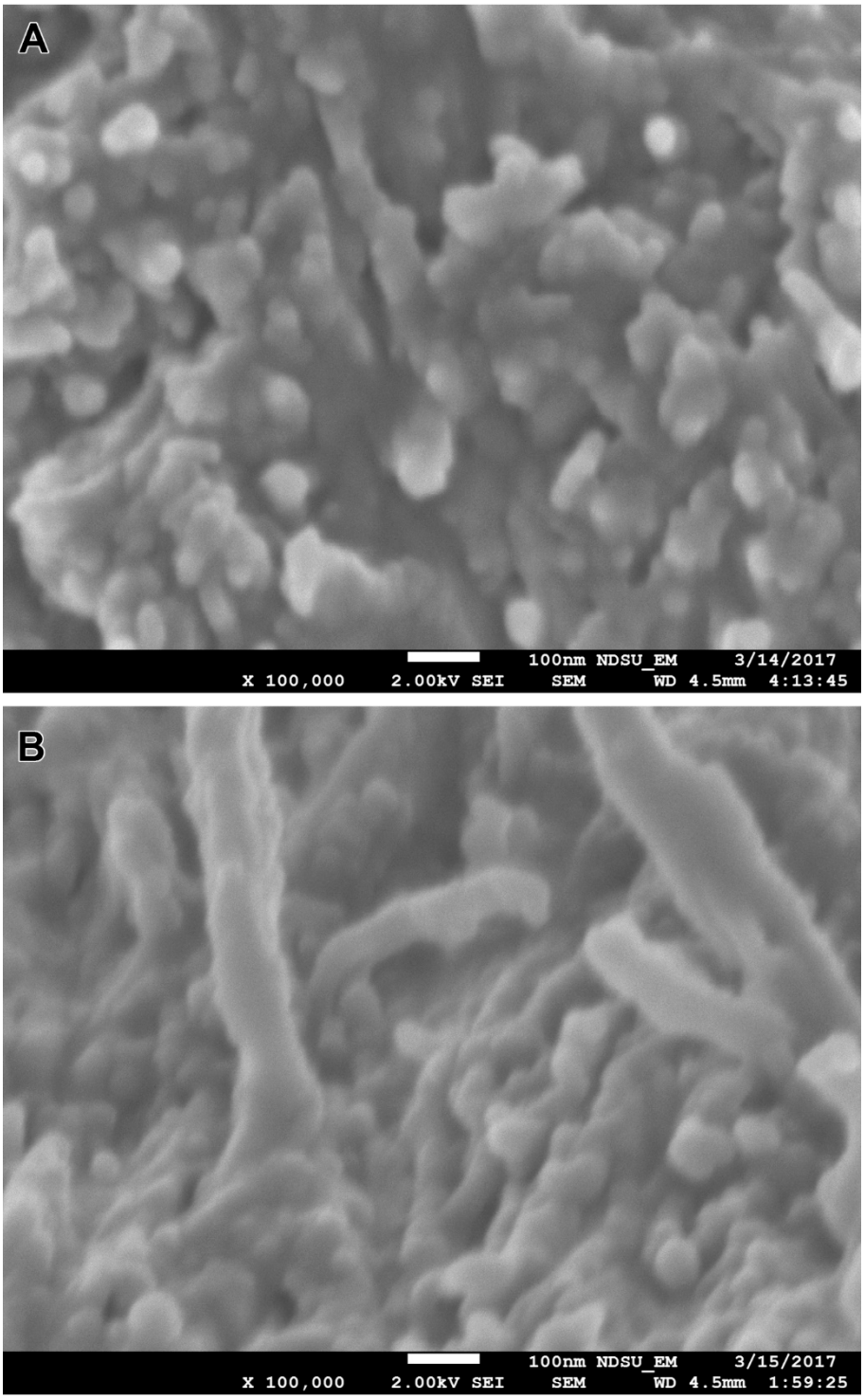

Figure E.23. FESEM secondary electron image of transverse sections of human bone (x100,000 original magnification). (A) healthy. (B) osteogenesis imperfecta.

APPENDIX F. SELECTED TEM IMAGES OF UNMODIFIED CLAY, MODIFIED CLAY, HAP, IN-SITU HAPCLAY AND β-TCP

F.1. Unmodified clay

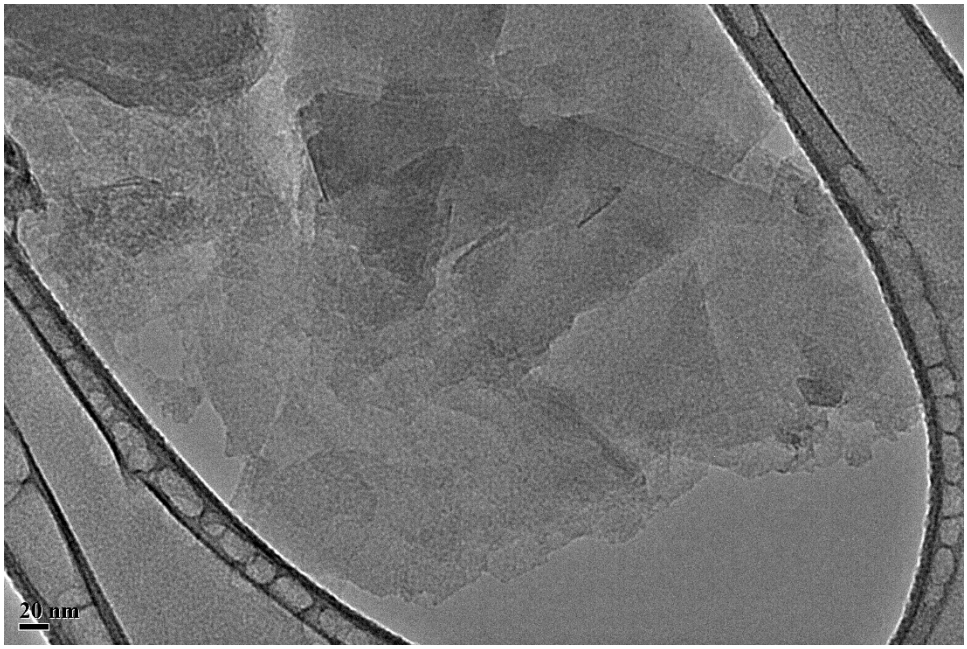

Figure F.1. TEM image of unmodified clay (x40,000 original magnification) showing clay sheets.

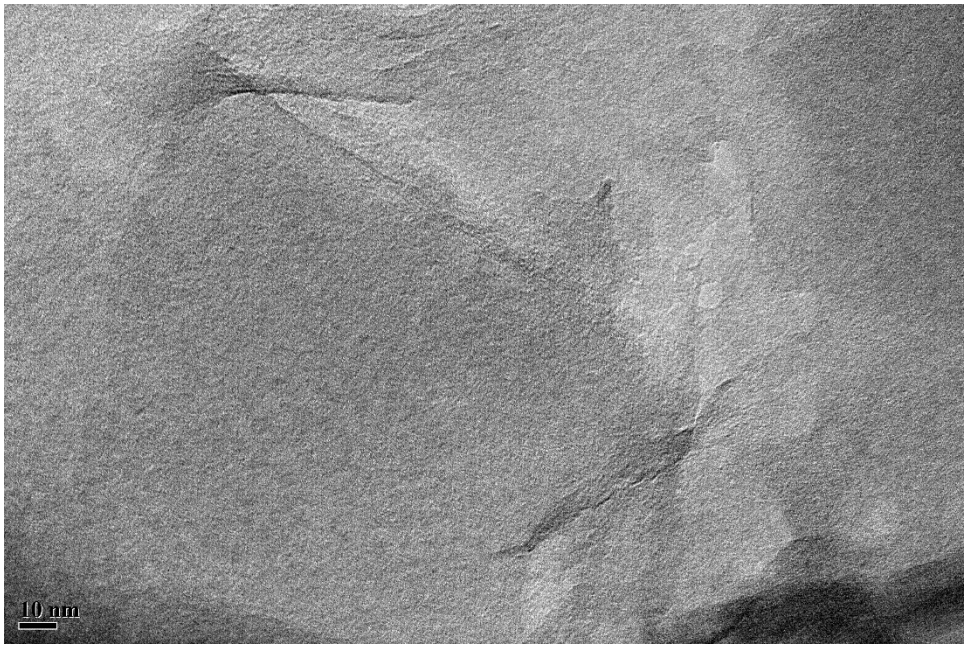

Figure F.2. TEM image of unmodified clay (x100,000 original magnification).

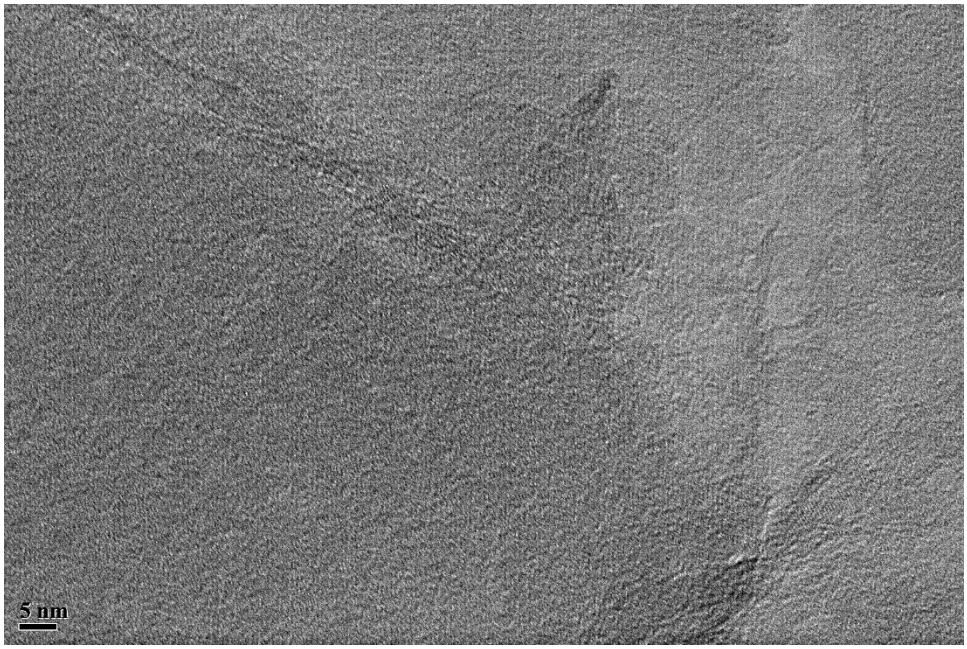

Figure F.3. TEM image of unmodified clay (x200,000 original magnification).

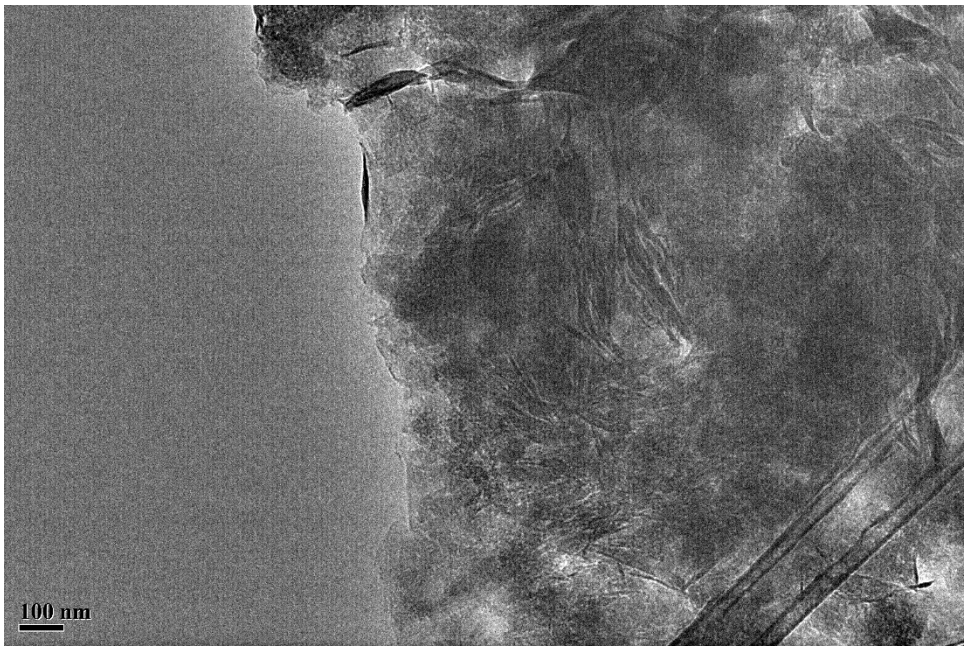

Figure F.4. TEM image of unmodified clay (x12,000 original magnification).

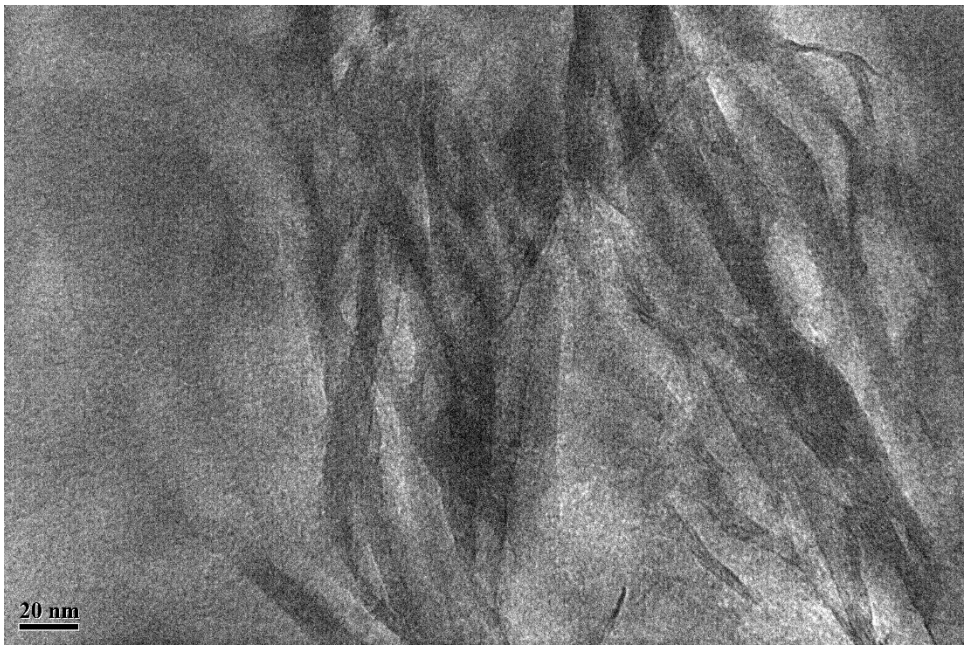

Figure F.5. TEM image of unmodified clay (x80,000 original magnification).

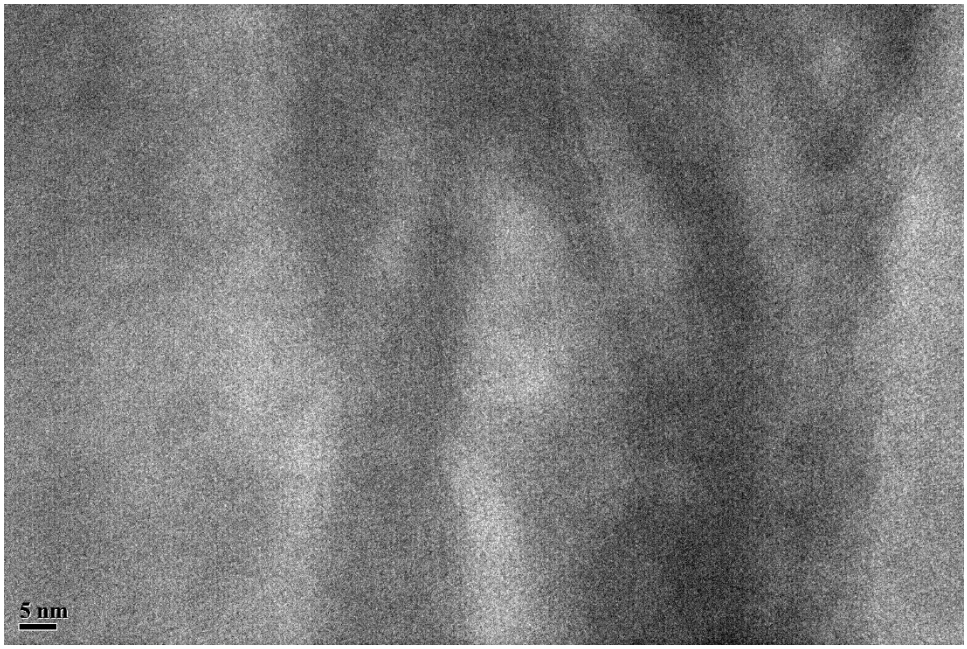

Figure F.6. TEM image of unmodified clay (x200,000 original magnification).

F.2. Modified clay

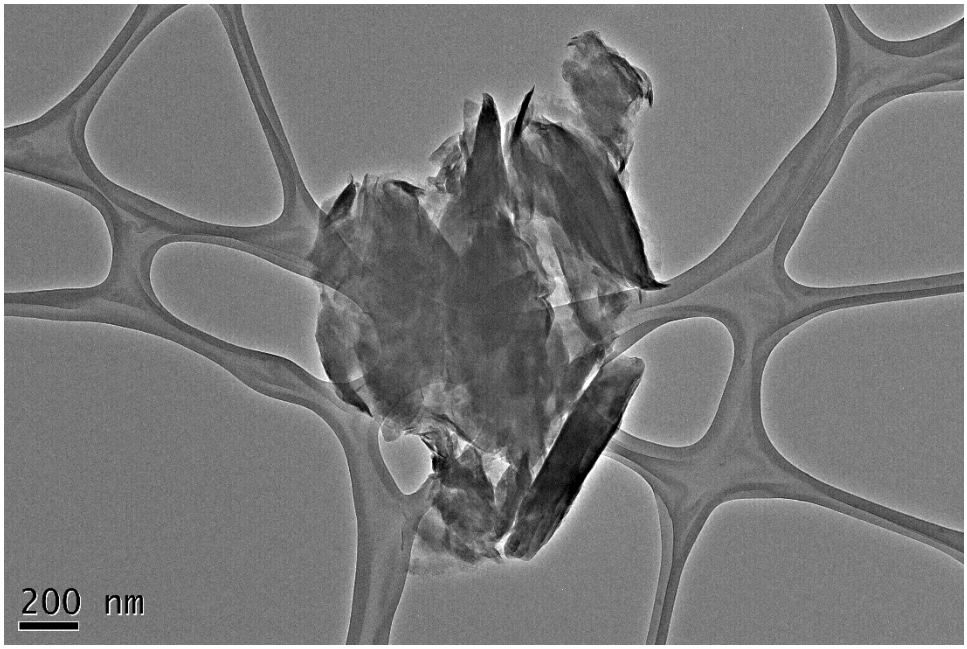

Figure F.7. TEM image of modified clay (x8,000 original magnification).

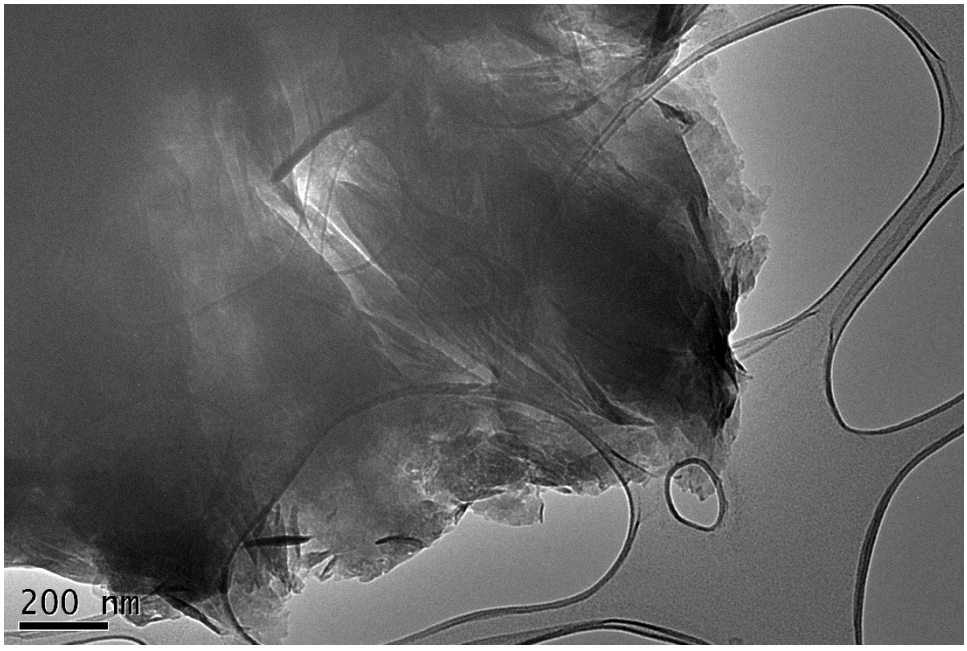

Figure F.8. TEM image of modified clay (x12,000 original magnification).

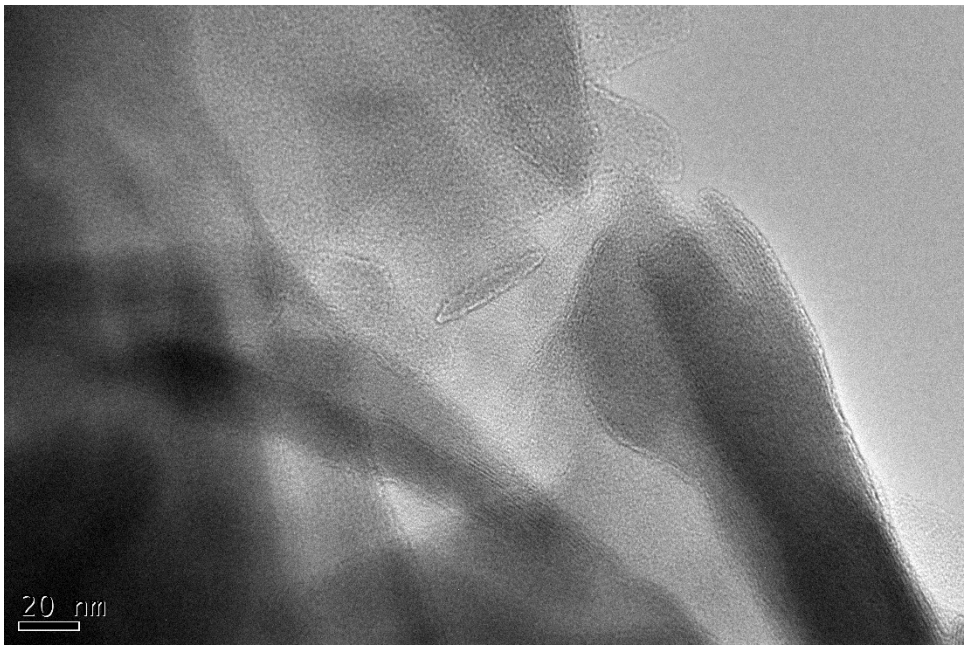

Figure F.9. TEM image of modified clay (x80,000 original magnification).

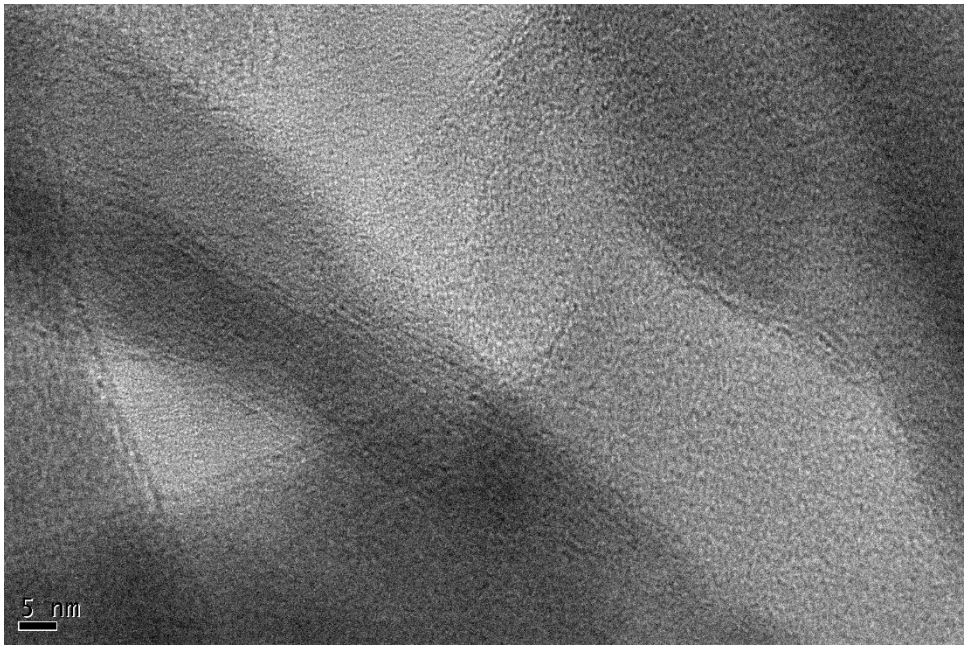

Figure F.10. TEM image of modified clay (x200,000 original magnification).

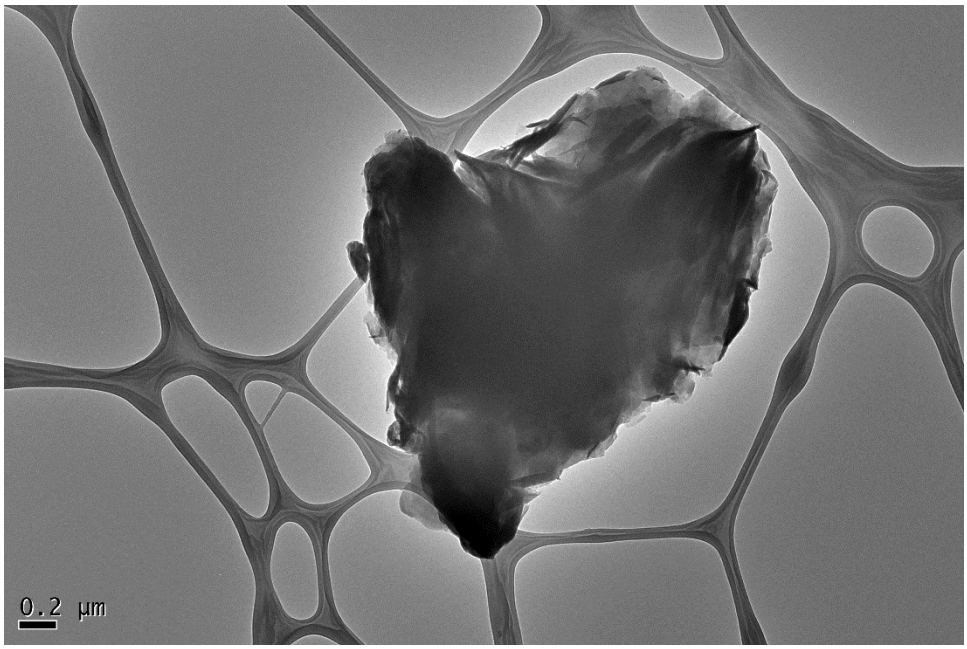

Figure F.11. TEM image of modified clay (x5,000 original magnification).

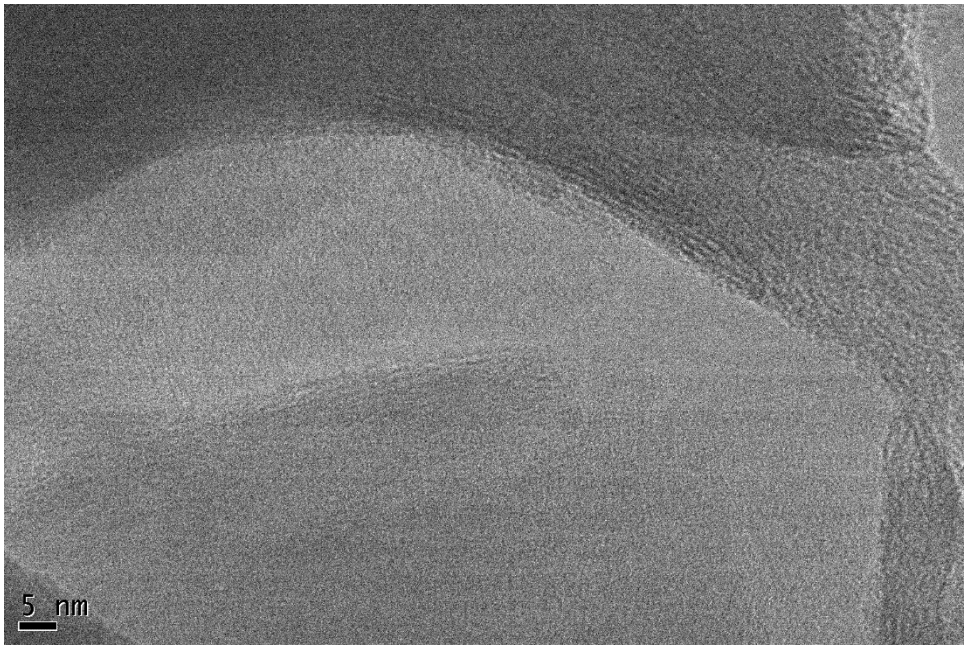

Figure F.12. TEM image of modified clay (x200,000 original magnification).

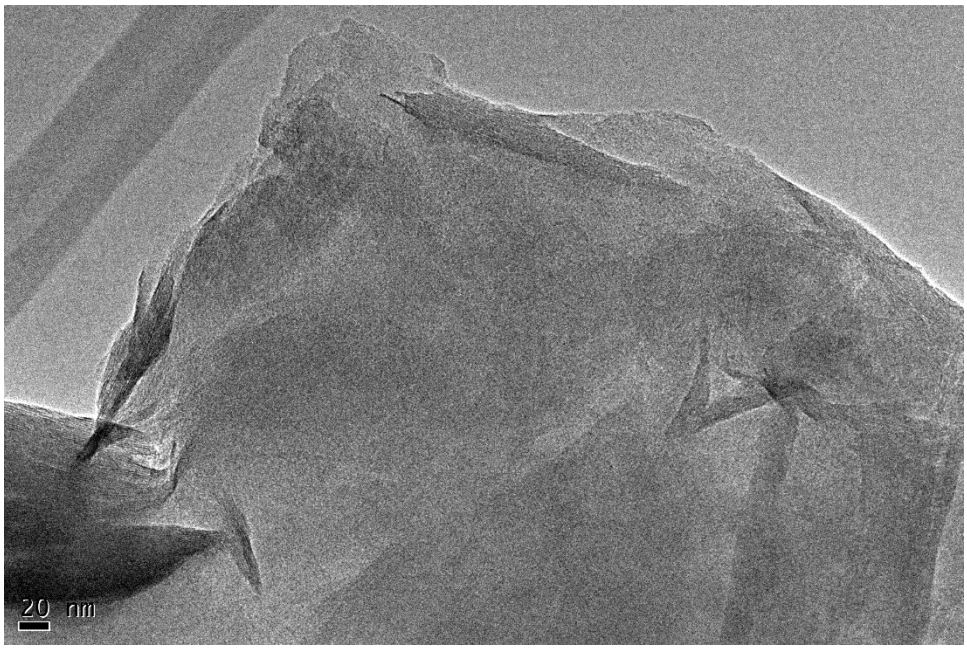

Figure F.13. TEM image of modified clay (x40,000 original magnification).

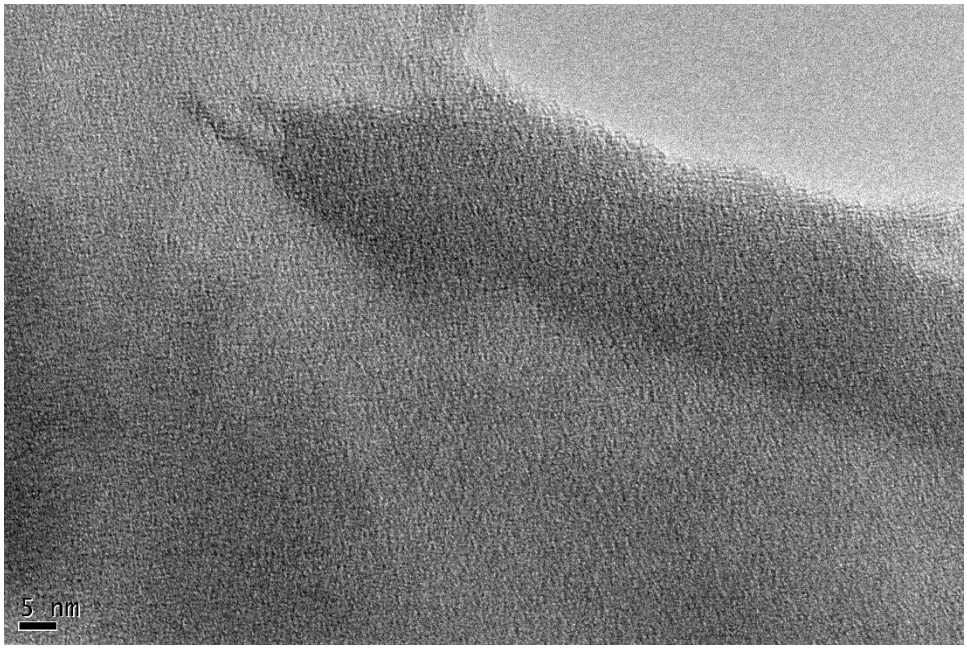

Figure F.14. TEM image of modified clay (x200,000 original magnification).

F.3. HAP

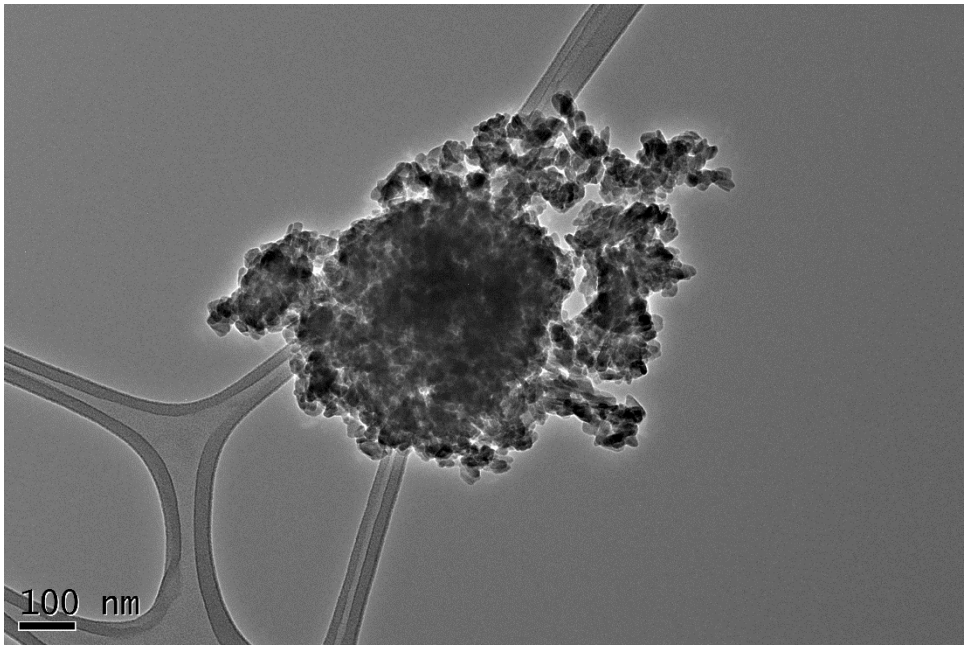

Figure F.15. TEM image of HAP (x15,000 original magnification).

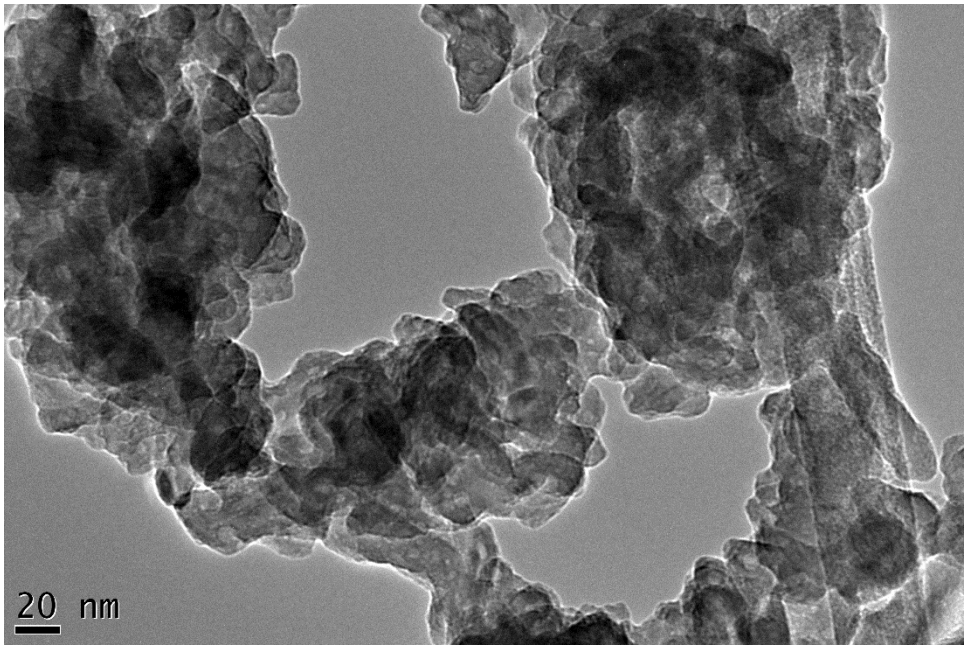

Figure F.16. TEM image of HAP (x15,000 original magnification).

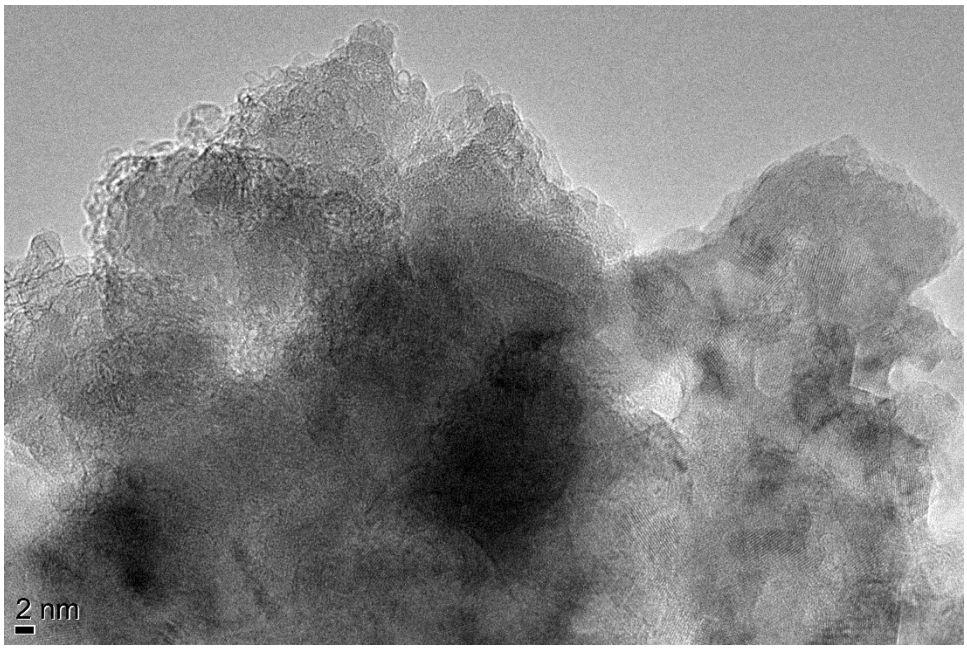

Figure F.17. TEM image of HAP showing lattice structure (x250,000 original magnification).

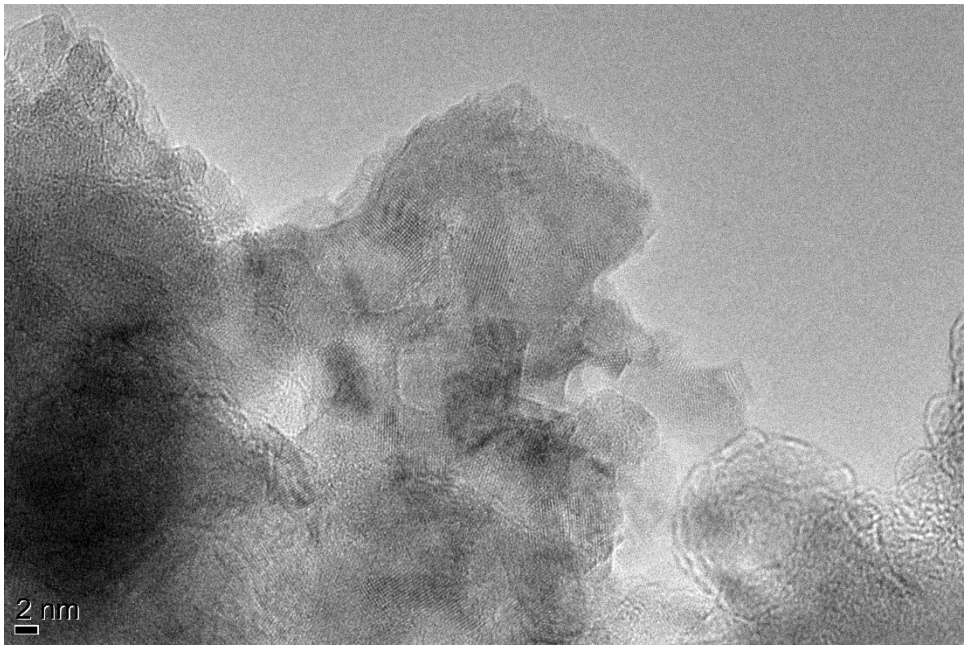

Figure F.18. TEM image of HAP showing lattice structure (x300,000 original magnification).

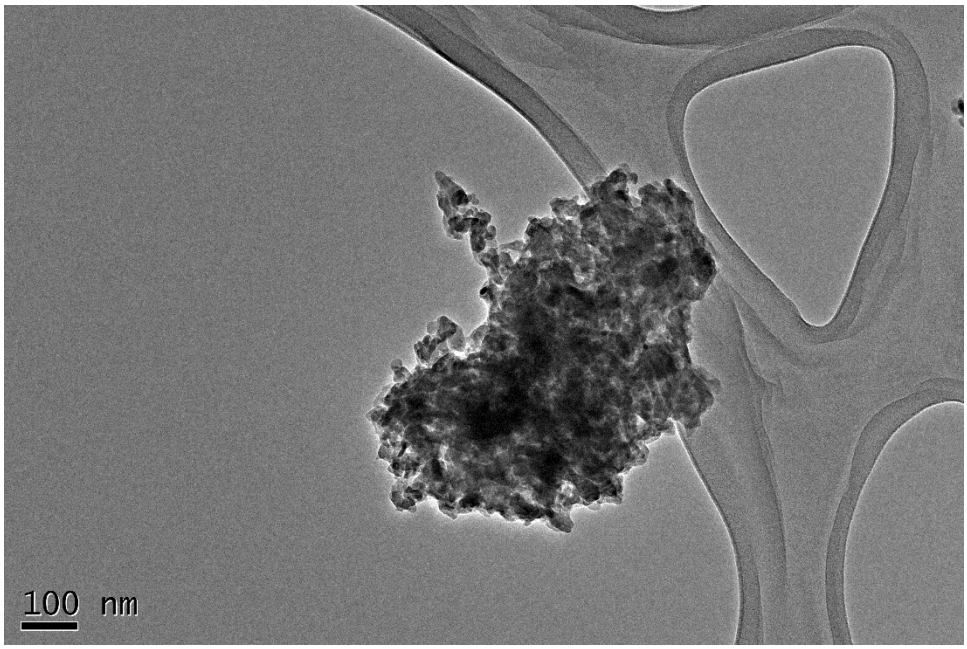

Figure F.19. TEM image of HAP (x15,000 original magnification).

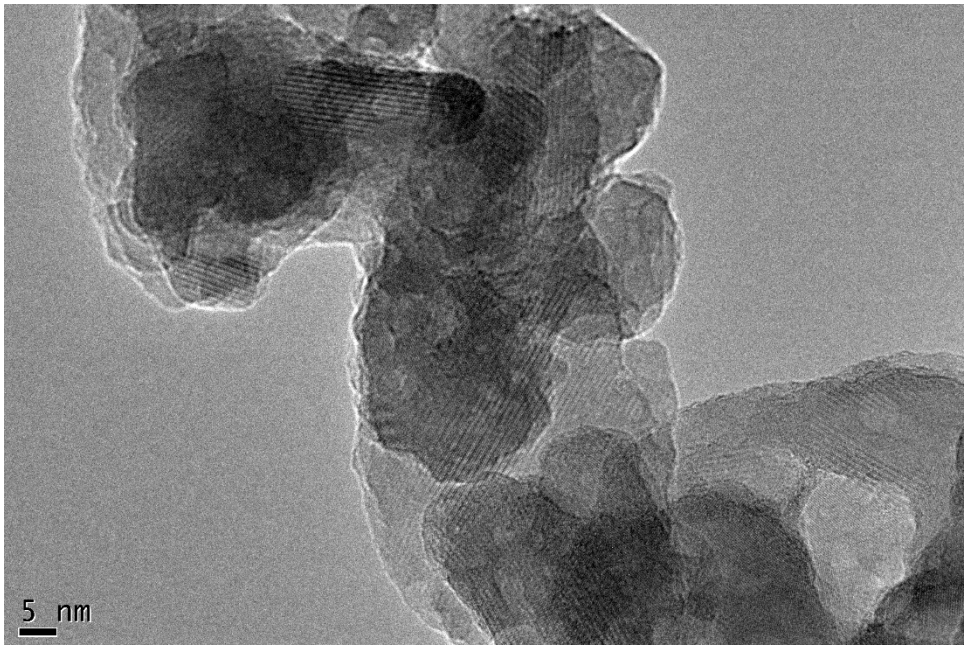

Figure F.20. TEM image of HAP showing lattice structure (x200,000 original magnification).

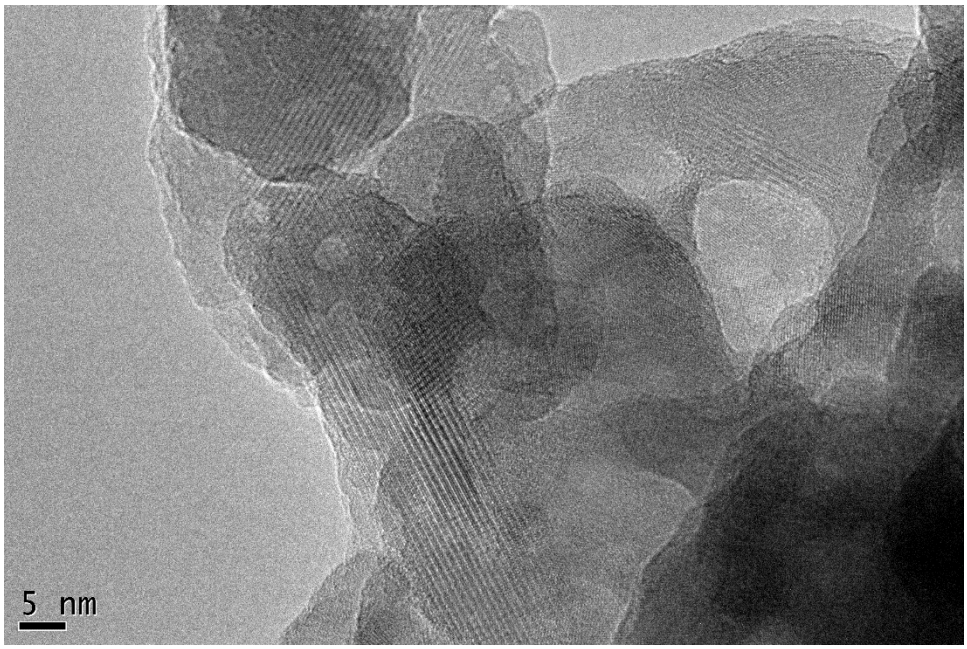

Figure F.21. TEM image of HAP showing lattice structure (x200,000 original magnification).

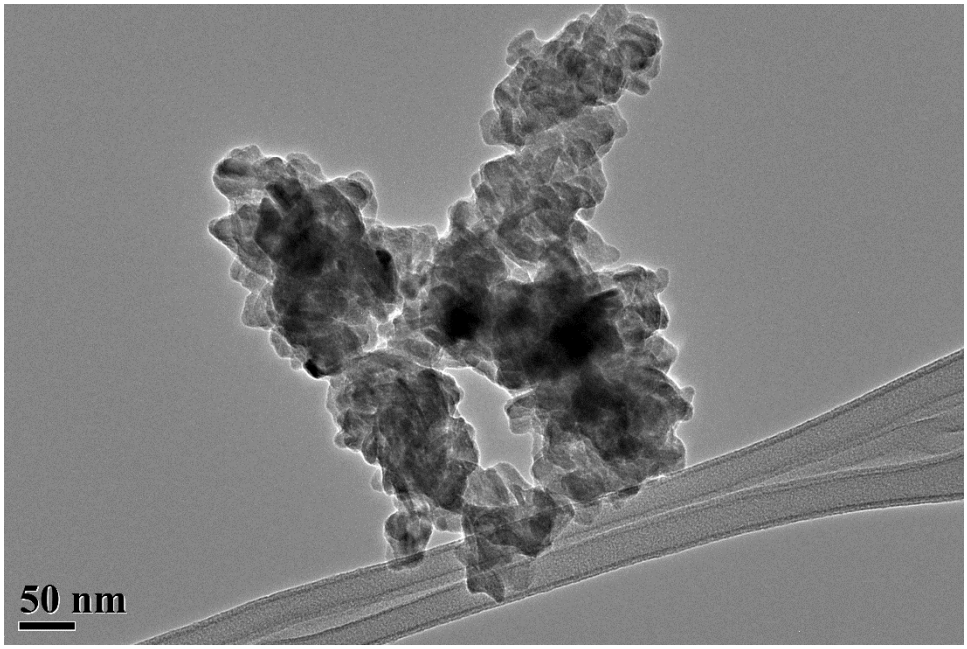

Figure F.22. TEM image of HAP (x30,000 original magnification).

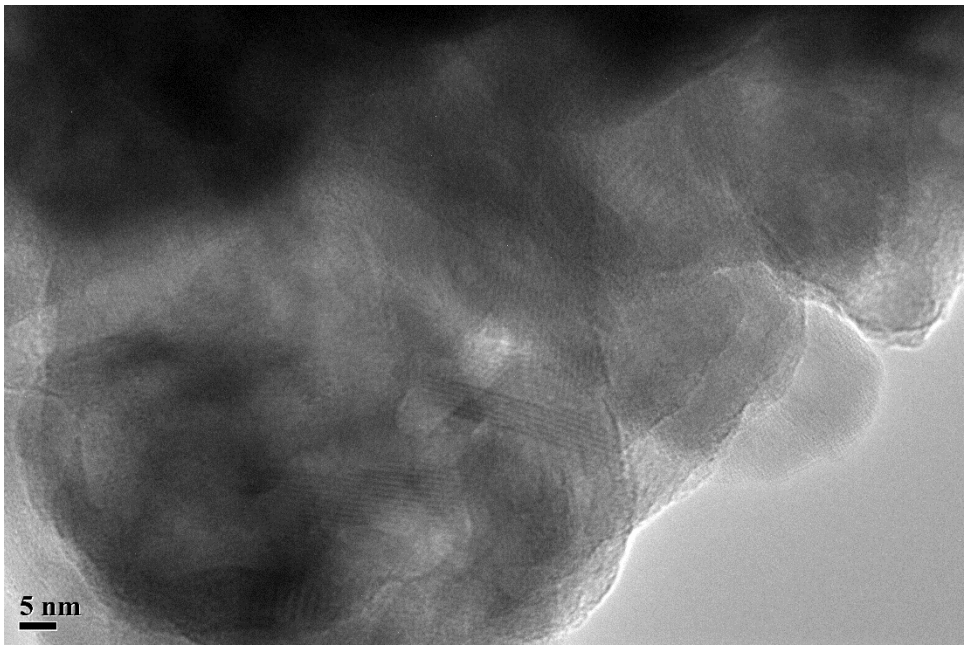

Figure F.23. TEM image of HAP showing lattice structure (x200,000 original magnification).

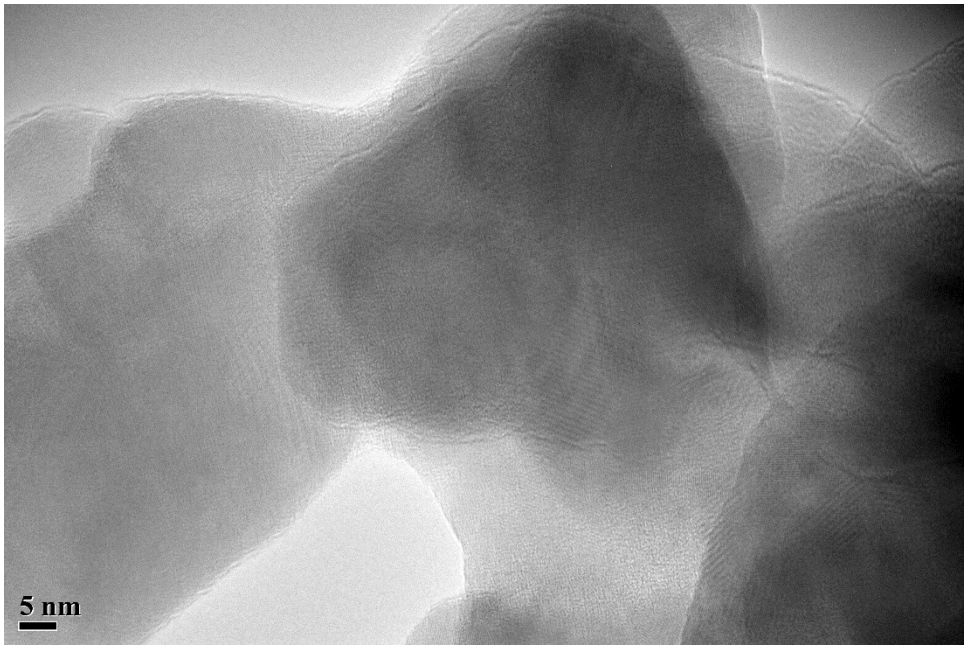

Figure F.24. TEM image of HAP showing lattice structure (x200,000 original magnification).

F.4. In-situ HAPclay

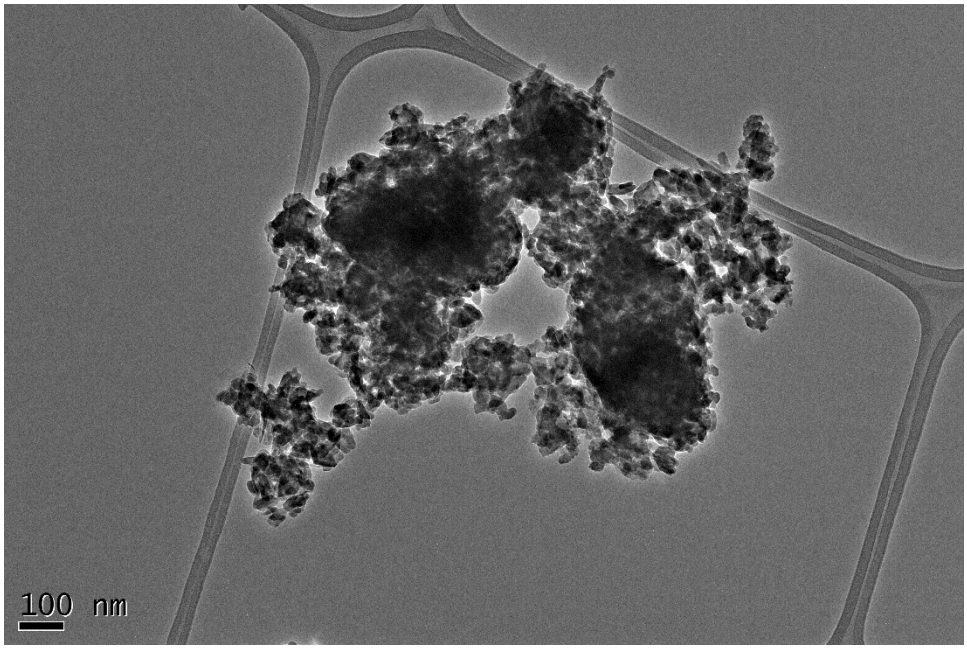

Figure F.25. TEM image of in-situ HAPclay (x15,000 original magnification).

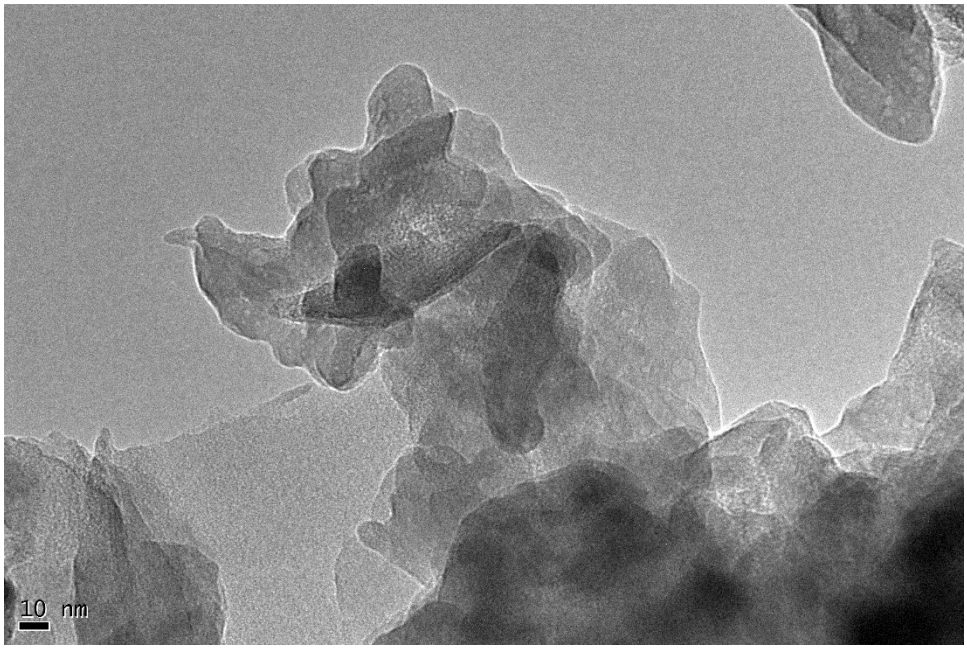

Figure F.26. TEM image of in-situ HAPclay (x80,000 original magnification).

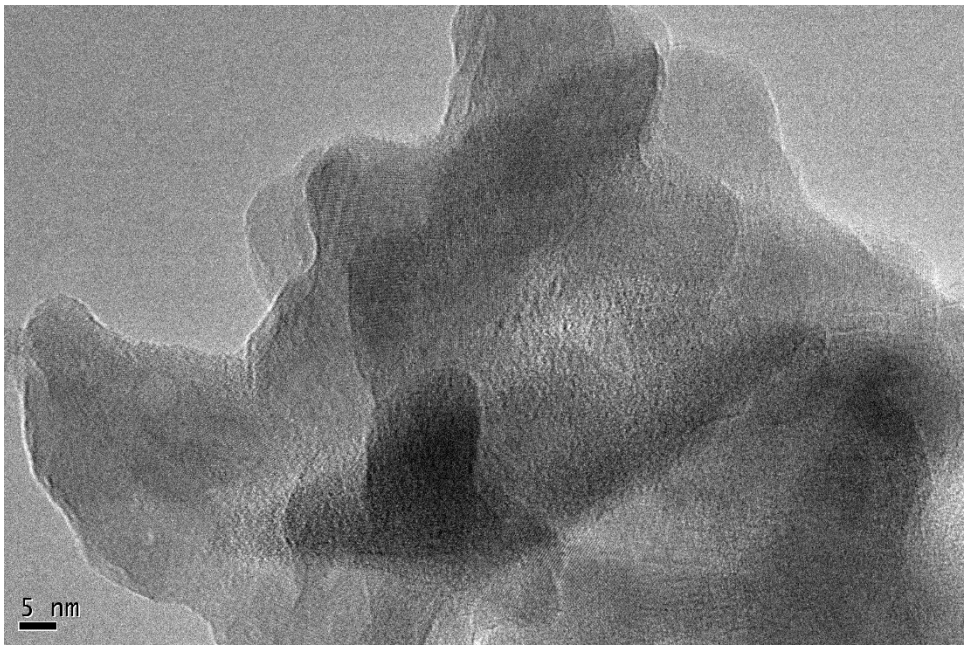

Figure F.27. TEM image of in-situ HAPclay showing lattice structure (x200,000 original magnification).

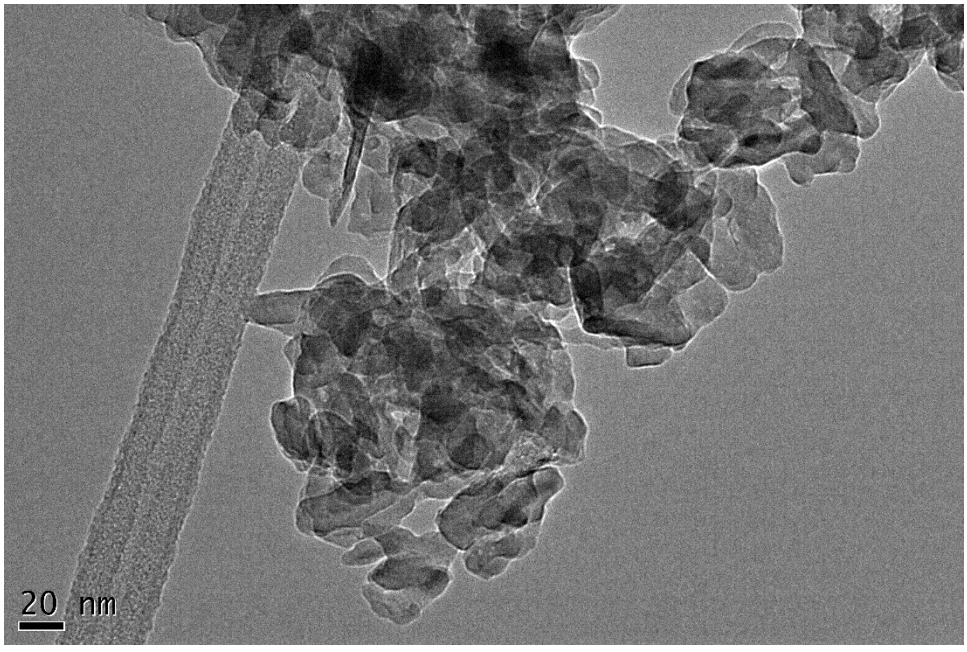

Figure F.28. TEM image of in-situ HAPclay (x20,000 original magnification).

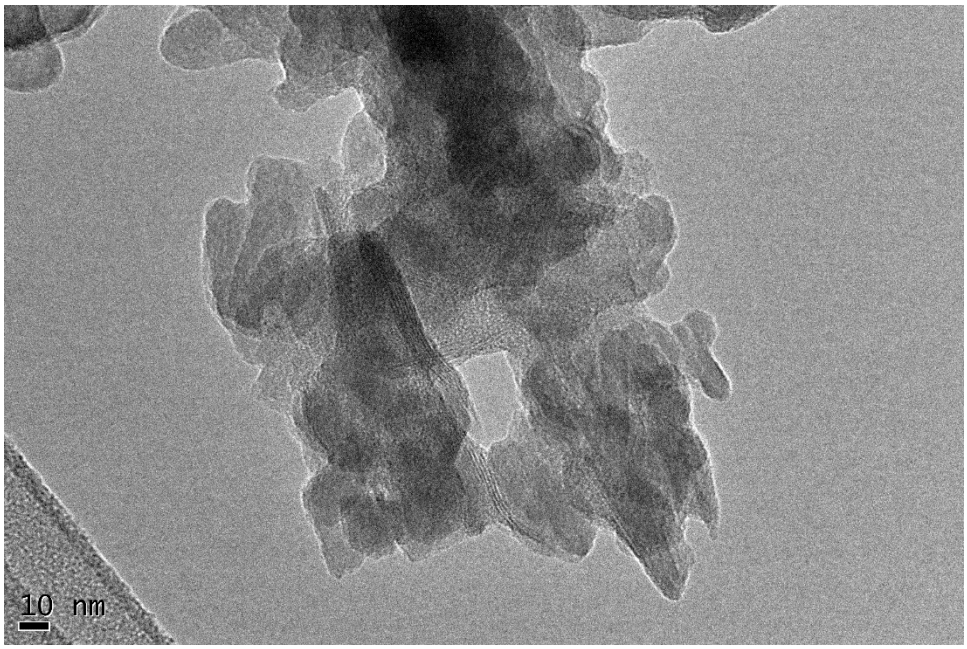

Figure F.29. TEM image of in-situ HAPclay (x80,000 original magnification).

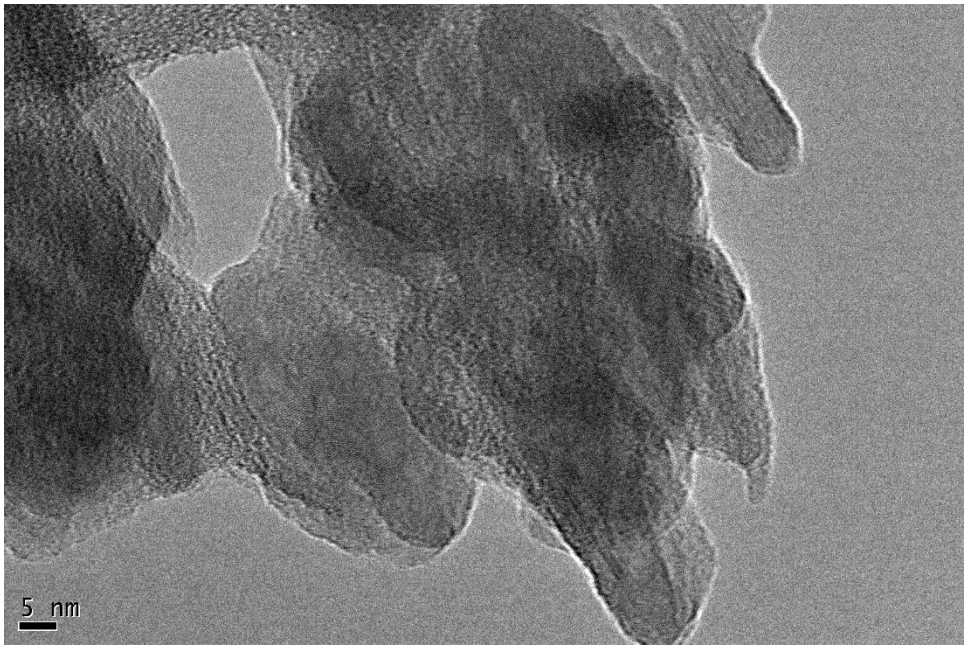

Figure F.30. TEM image of in-situ HAPclay showing lattice structure (x200,000 original magnification).

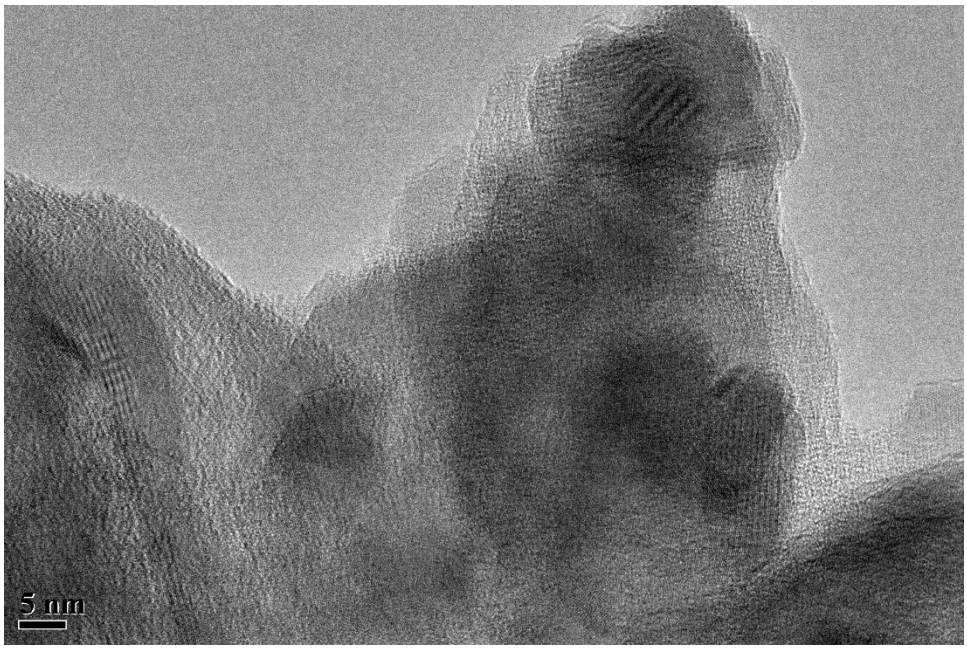

Figure F.31. TEM image of in-situ HAPclay showing lattice structure (x200,000 original magnification)

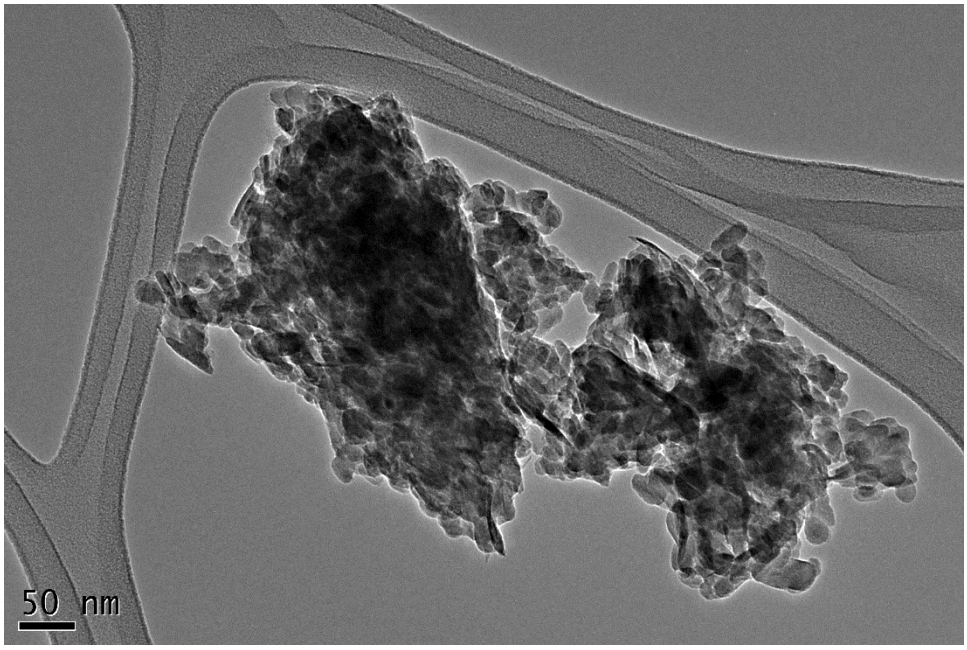

Figure F.32. TEM image of in-situ HAPclay (x30,000 original magnification).

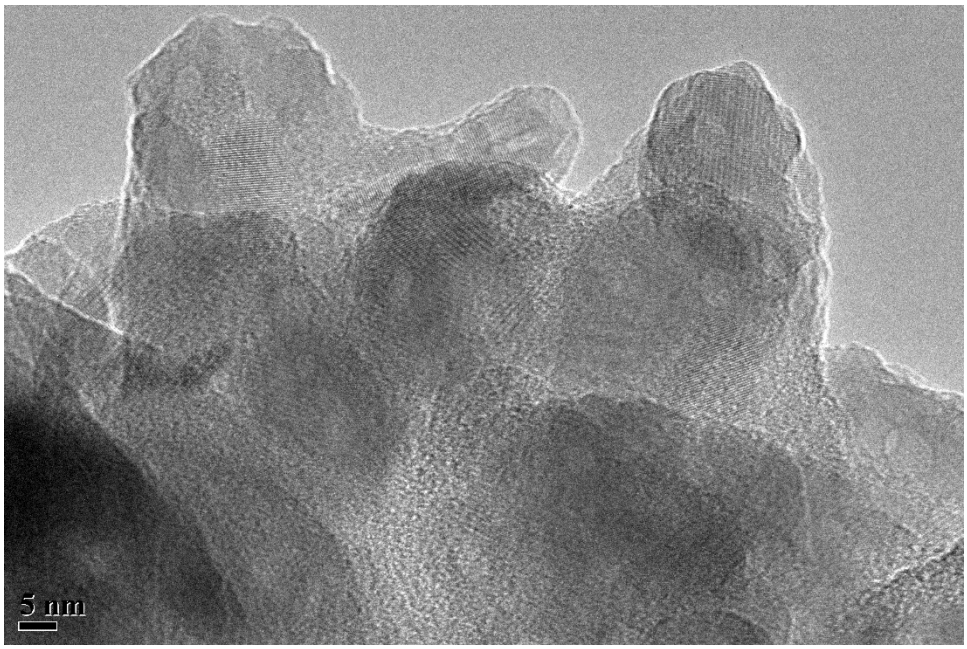

Figure F.33. TEM image of in-situ HAPclay showing lattice structure (x200,000 original magnification).

Figure F.34. TEM image of in-situ HAPclay showing lattice structure (x200,000 original magnification).

F.5. β-TCP

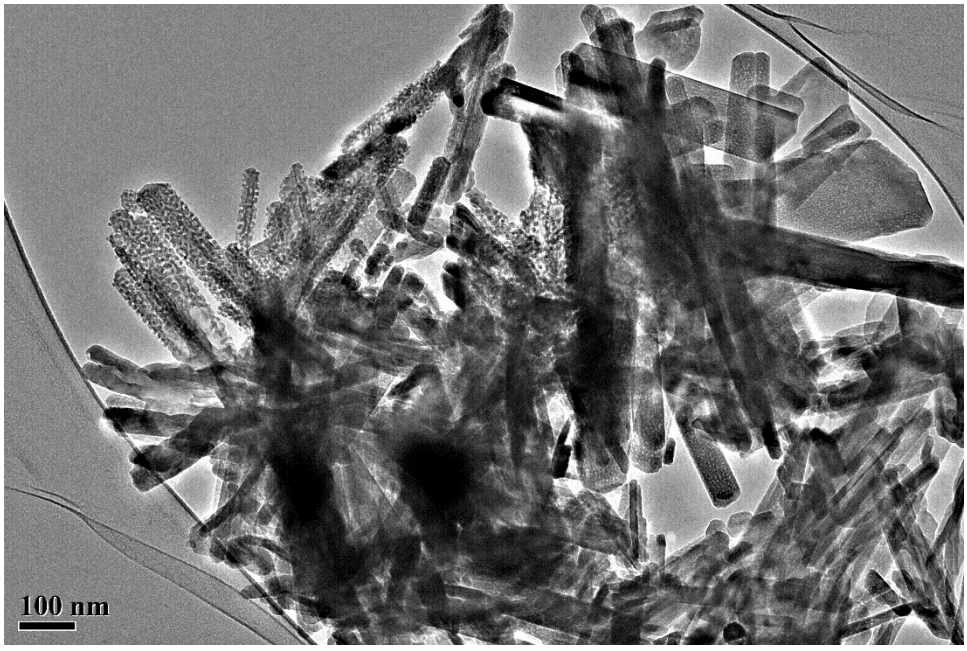

Figure F.35. TEM image of β-TCP (x15,000 original magnification).

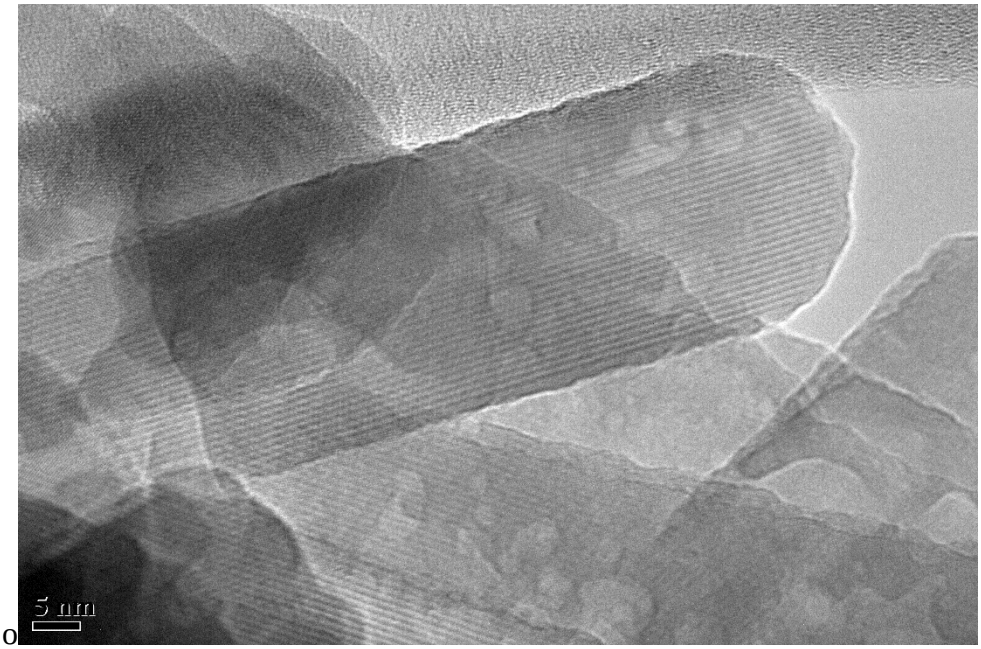

Figure F.36. TEM image of β-TCP showing lattice structure (x200,000 original magnification).

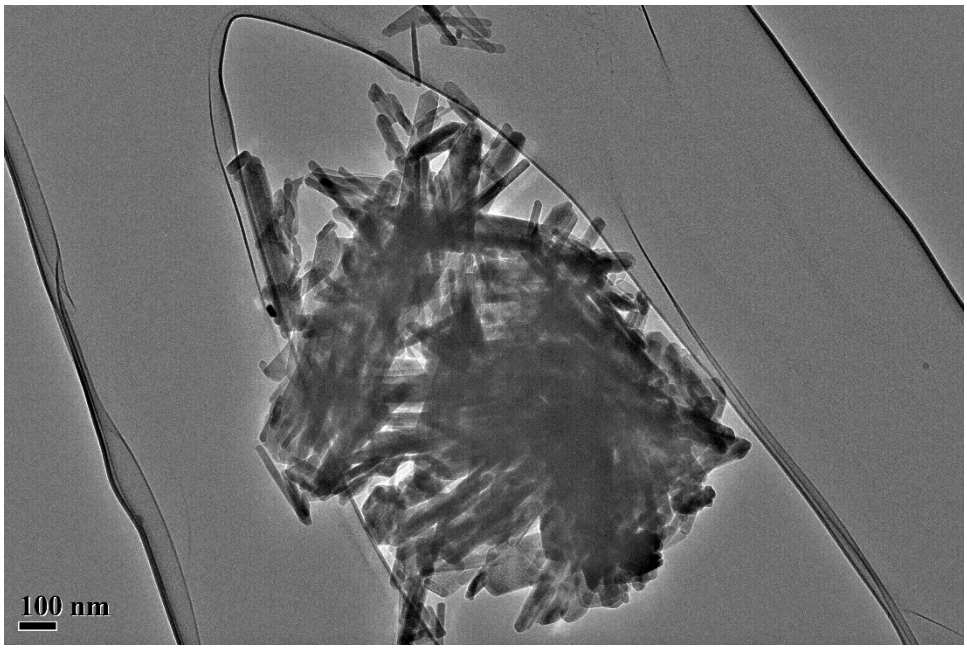

Figure F.37. TEM image of β-TCP (x10,000 original magnification).

Figure F.38. TEM image of β-TCP showing lattice structure (x200,000 original magnification).

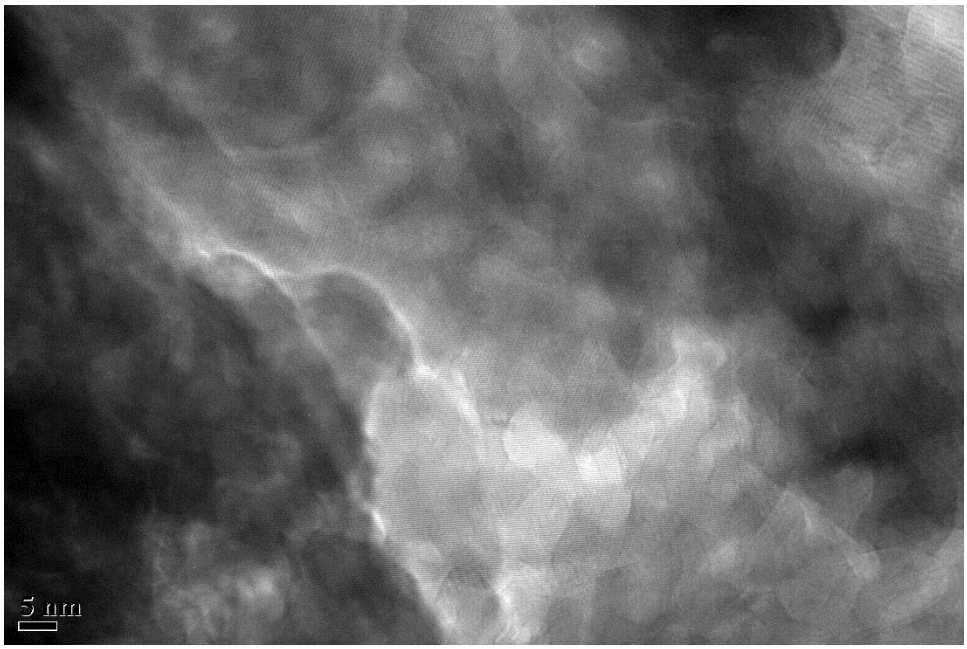

Figure F.39. TEM image of β-TCP showing lattice structure (x200,000 original magnification).

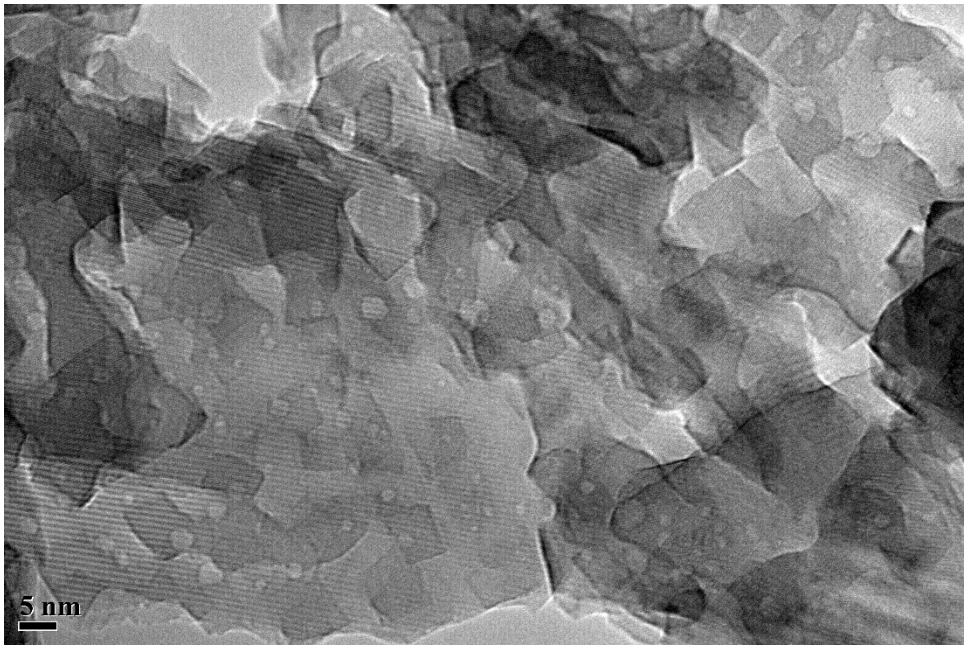

Figure F.40. TEM image of β-TCP showing lattice structure (x200,000 original magnification).

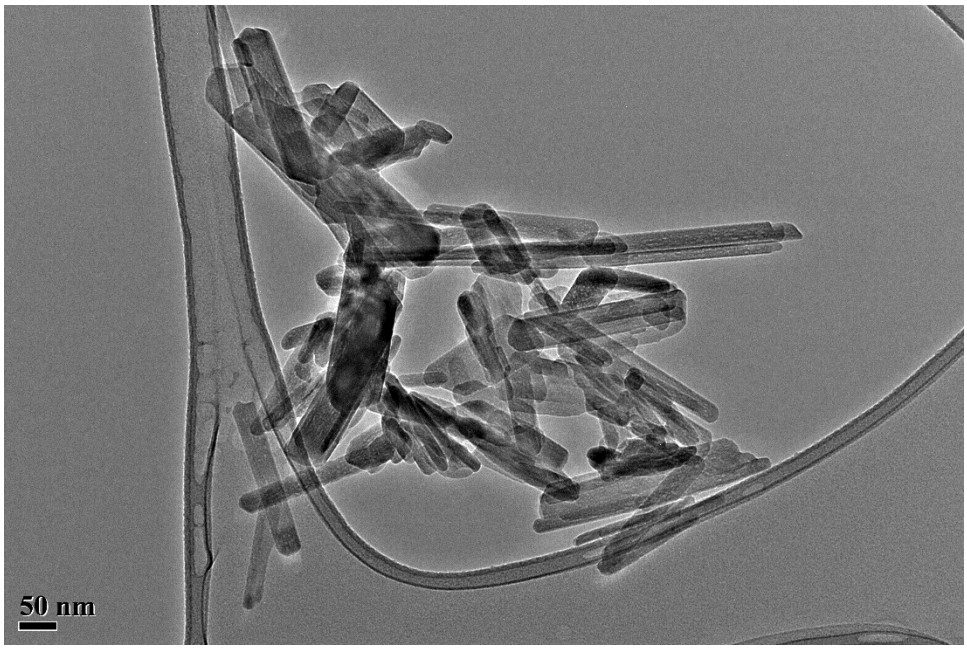

Figure F.41. TEM image of β-TCP (x20,000 original magnification).

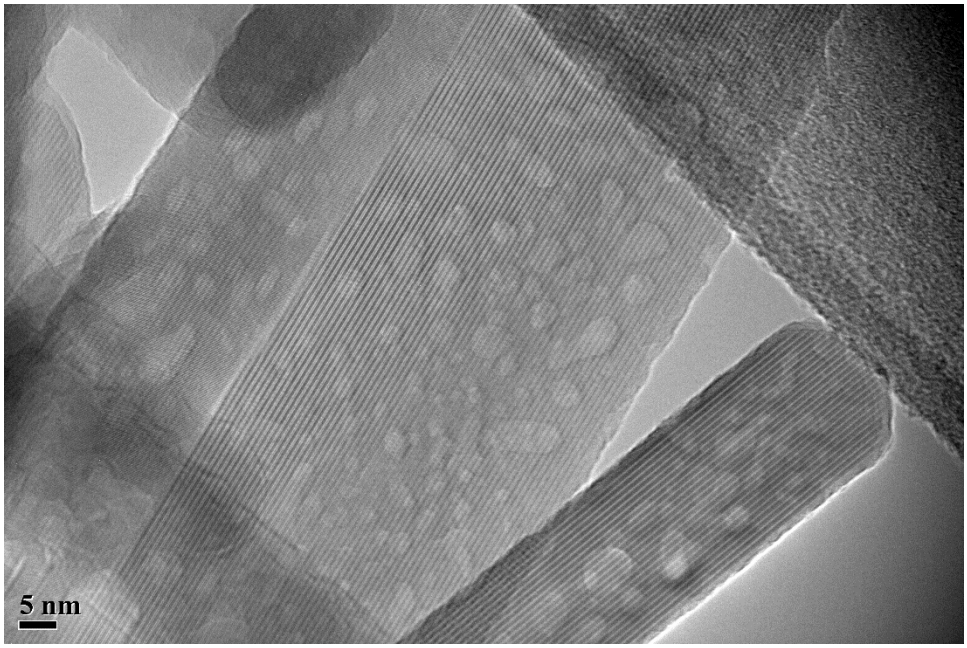

Figure F.42. TEM image of β-TCP showing lattice structure (x200,000 original magnification).

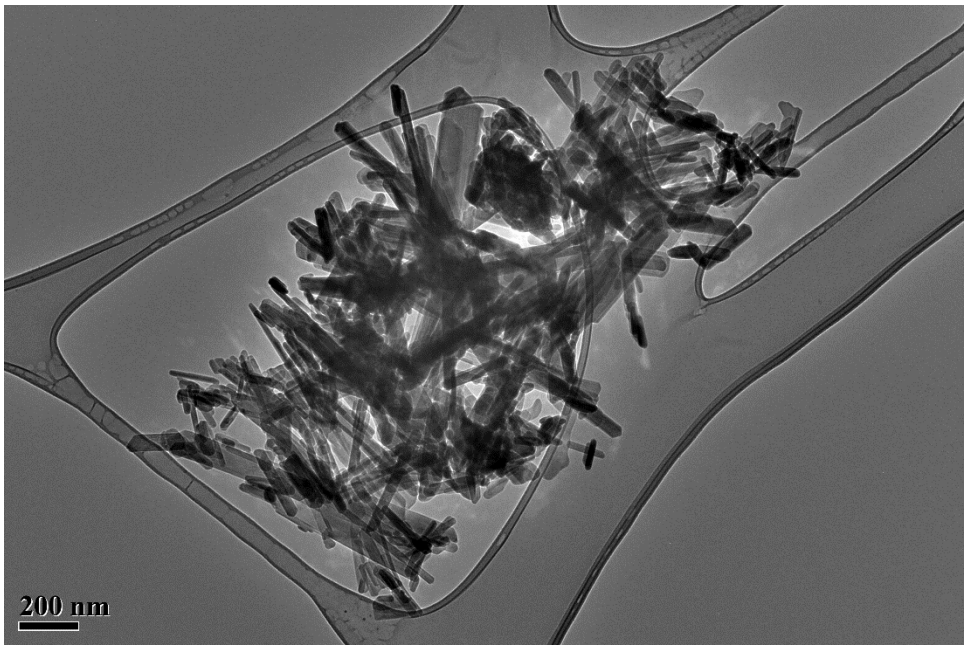

Figure F.43. TEM image of β-TCP (x80,000 original magnification).

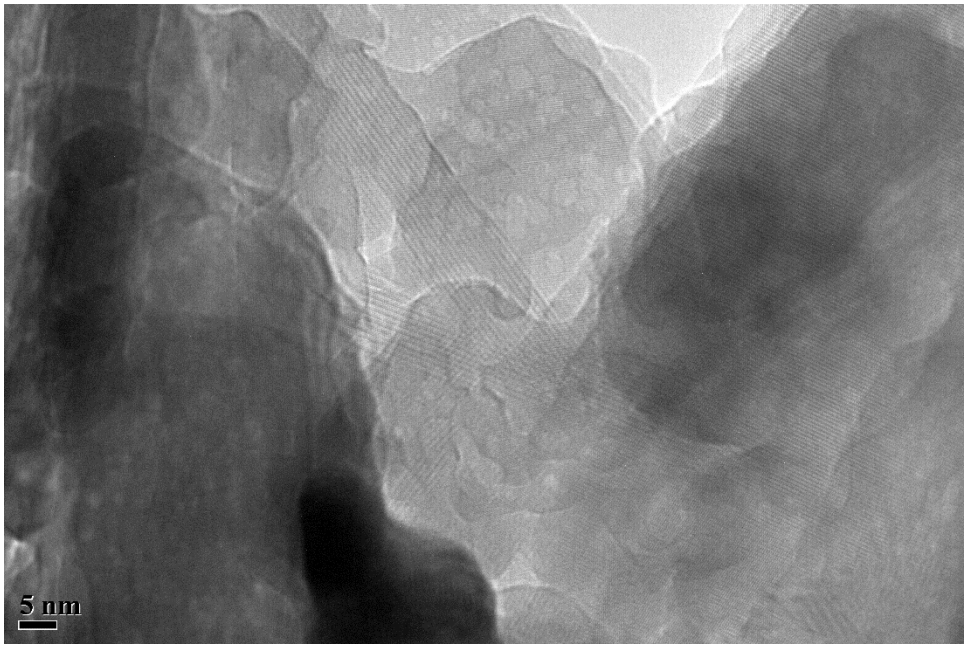

Figure F.44. TEM image of β-TCP showing lattice structure (x200,000 original magnification).

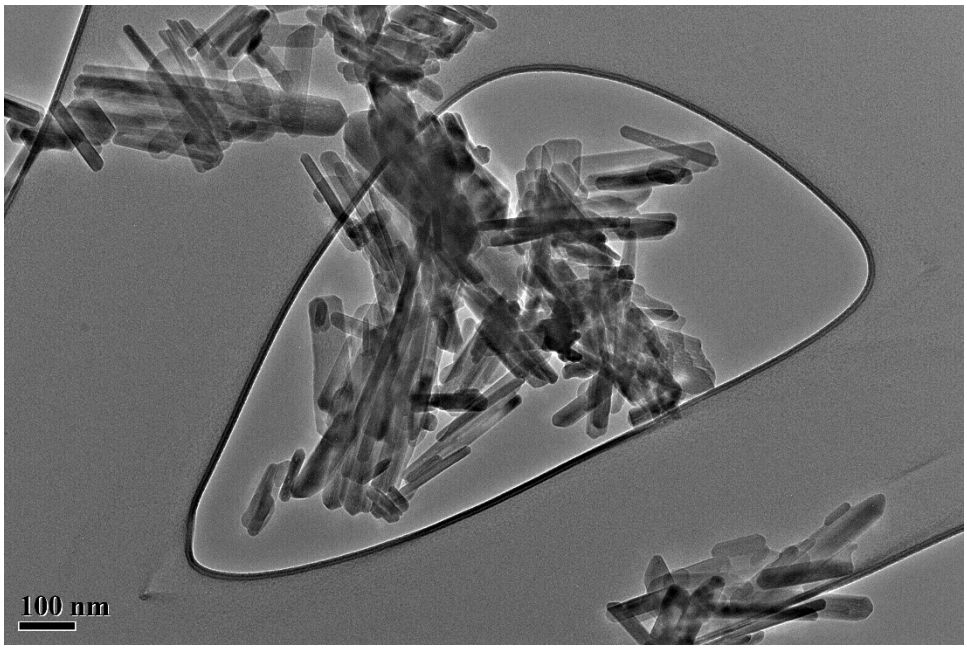

Figure F.45. TEM image of β-TCP (x15,000 original magnification).

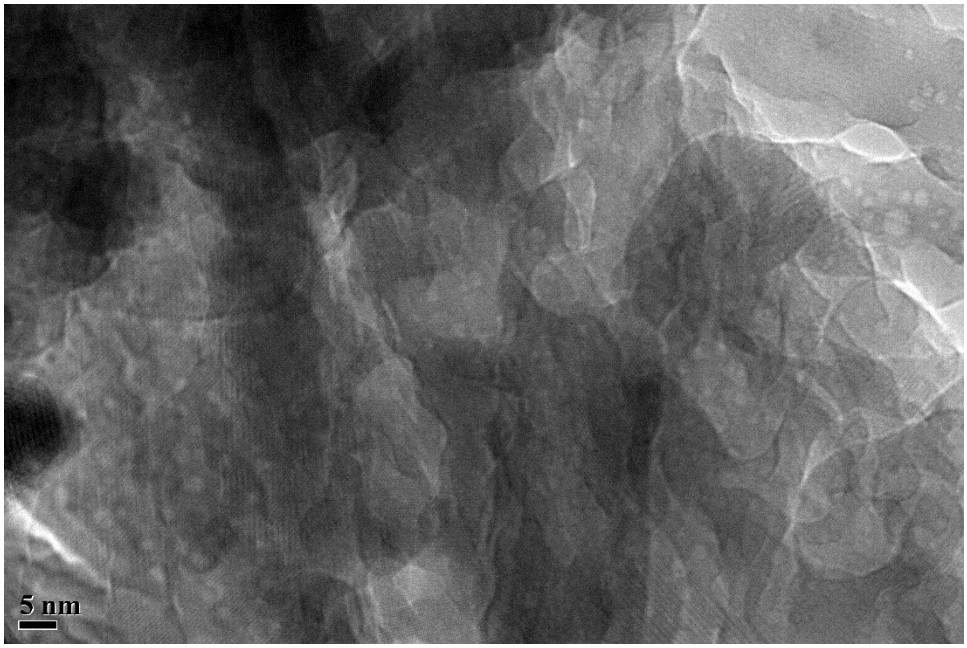

Figure F.46. TEM image of β-TCP showing lattice structure (x200,000 original magnification).

APPENDIX G. COMPARISON OF REPRESENTATIVE TEM IMAGES OF THE ACQUISITION AREAS OF EELS SPECTRA FROM HUMAN BONE

G.1. TEM images of healthy and OI diseased human bone where EELS spectra were acquired, longitudinal sections

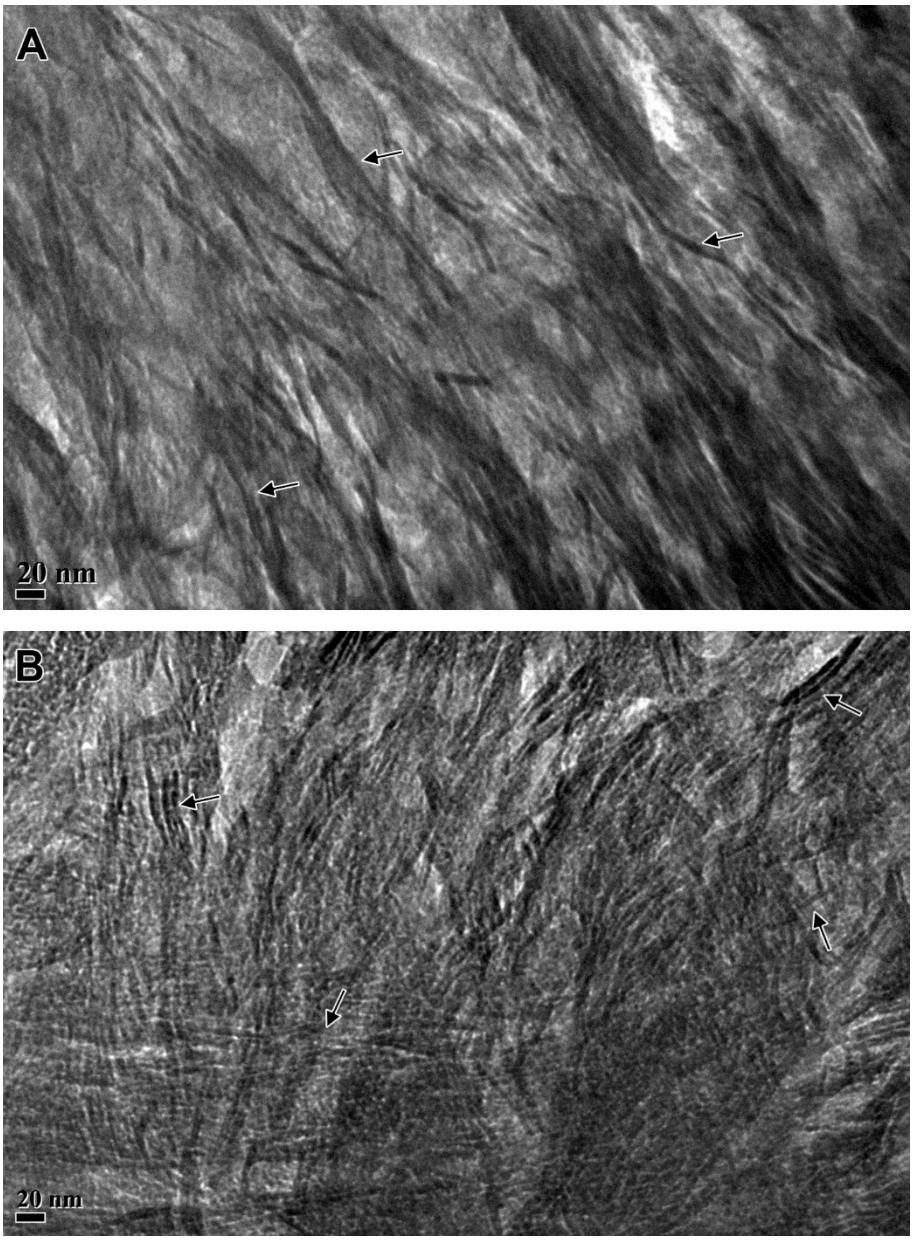

Figure G.1. TEM image of longitudinal section of human bone (x40,000 original magnification). (A) healthy and (B) osteogenesis imperfecta. Arrows denote collagen fibrils.

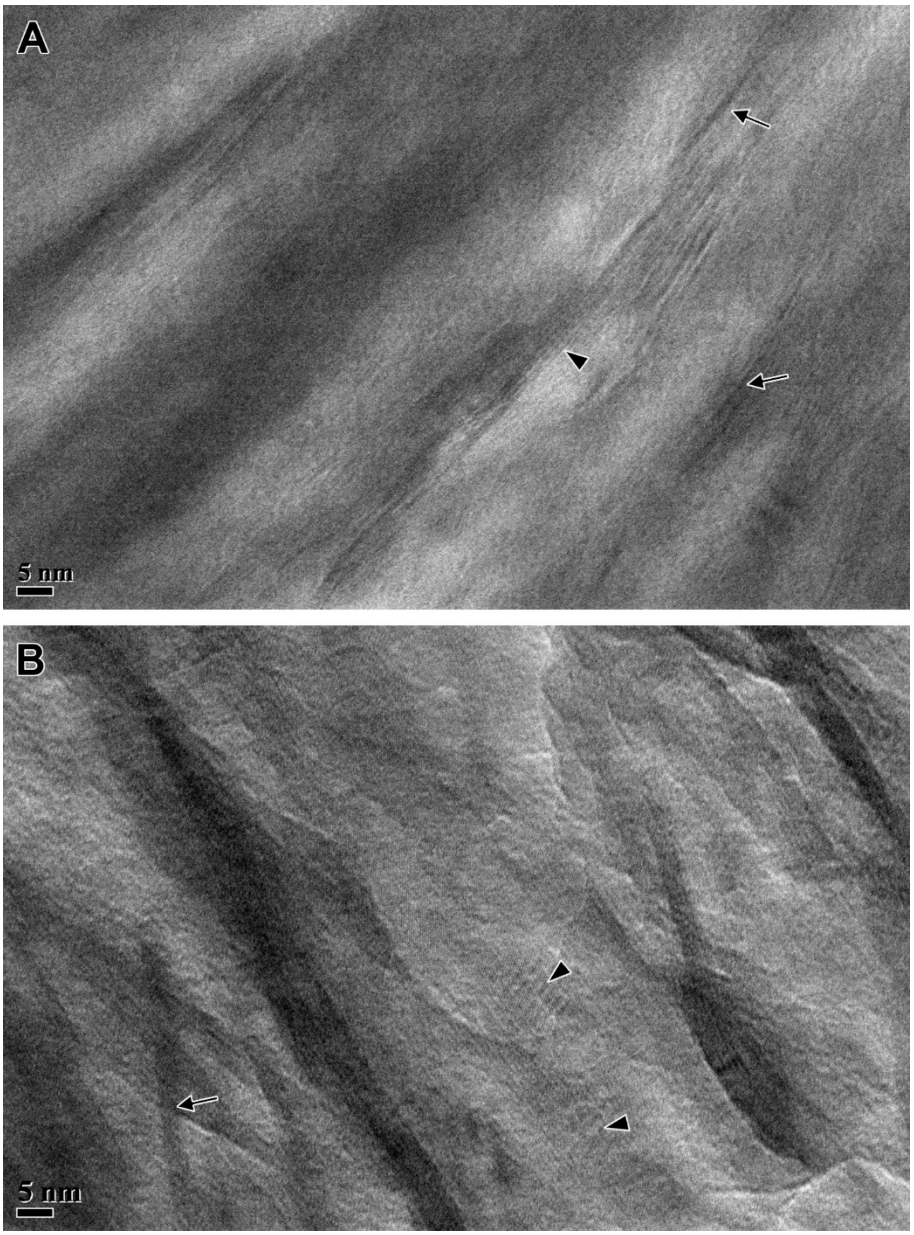

Figure G.2. TEM image of longitudinal section of human bone (x200,000 original magnification). (A) healthy and (B) osteogenesis imperfecta. Arrows denote collagen fibrils and arrowheads denote HAP crystal lattice.

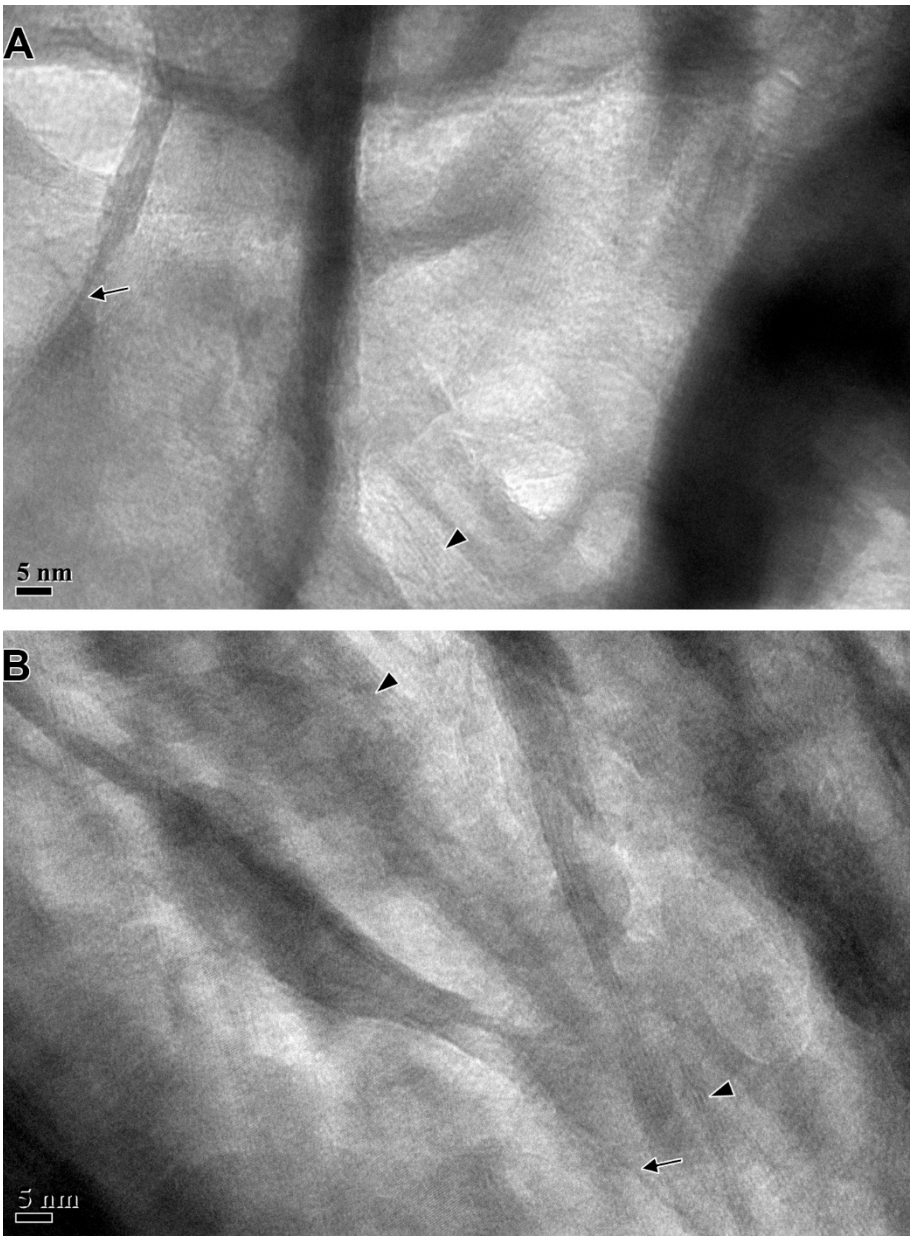

Figure G.3. TEM image of longitudinal section of human bone (x200,000 original magnification). (A) healthy and (B) osteogenesis imperfecta. Arrows denote collagen fibrils and arrowheads denote HAP crystal lattice.

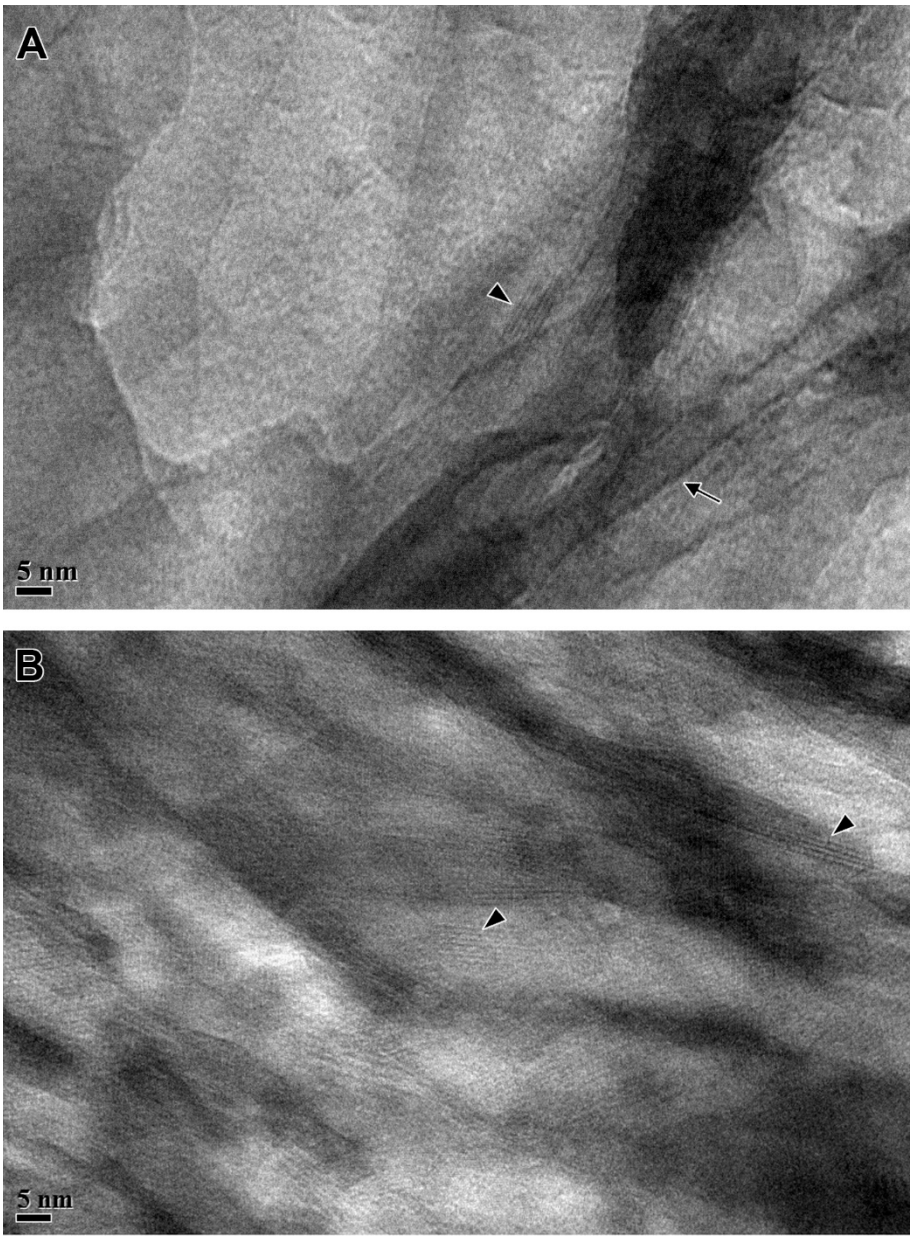

Figure G.4. TEM image of longitudinal section of human bone (x200,000 original magnification). (A) healthy and (B) osteogenesis imperfecta. Arrows denote collagen fibrils and arrowheads denote HAP crystal lattice.

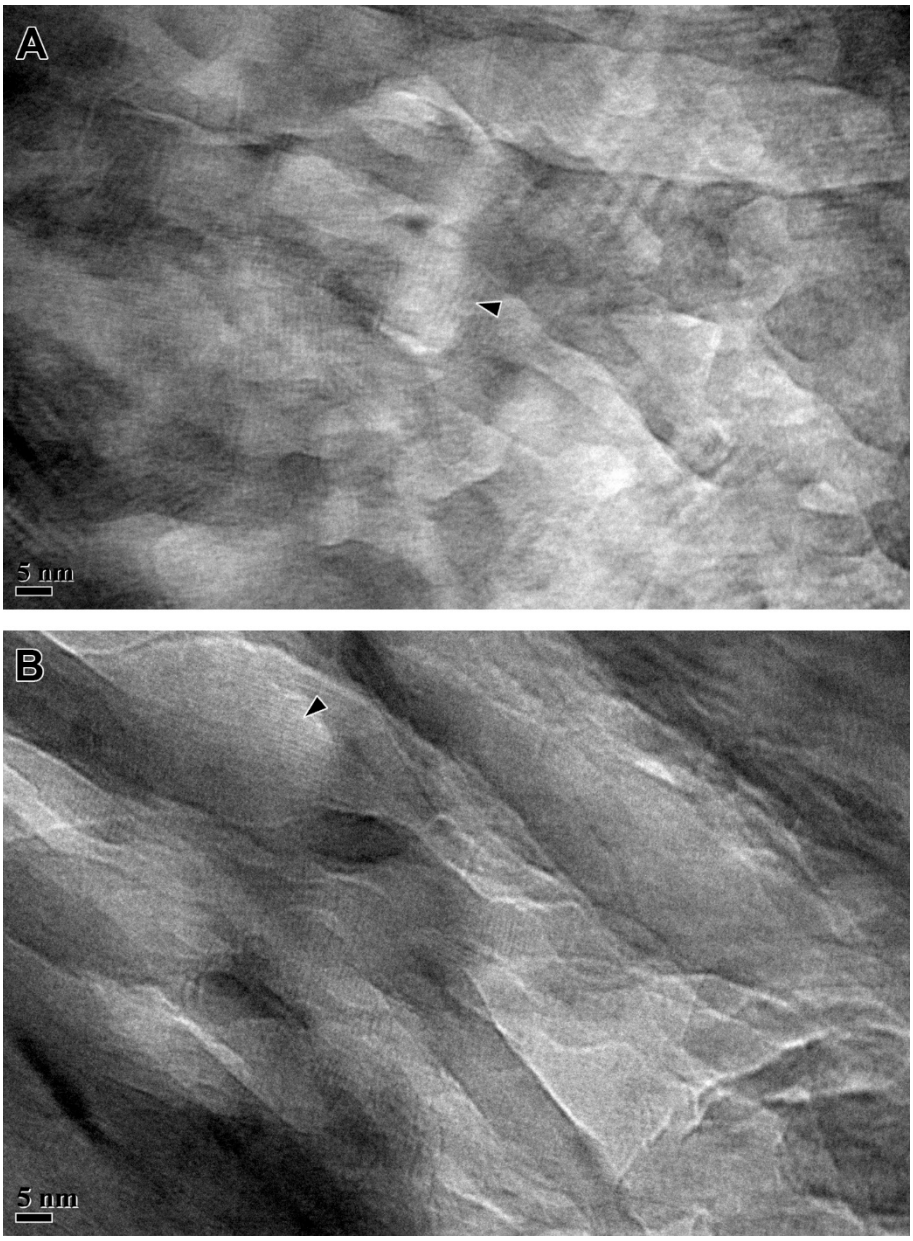

Figure G.5. TEM image of longitudinal section of human bone (x200,000 original magnification). (A) healthy and (B) osteogenesis imperfecta. Arrowheads denote HAP crystal lattice.

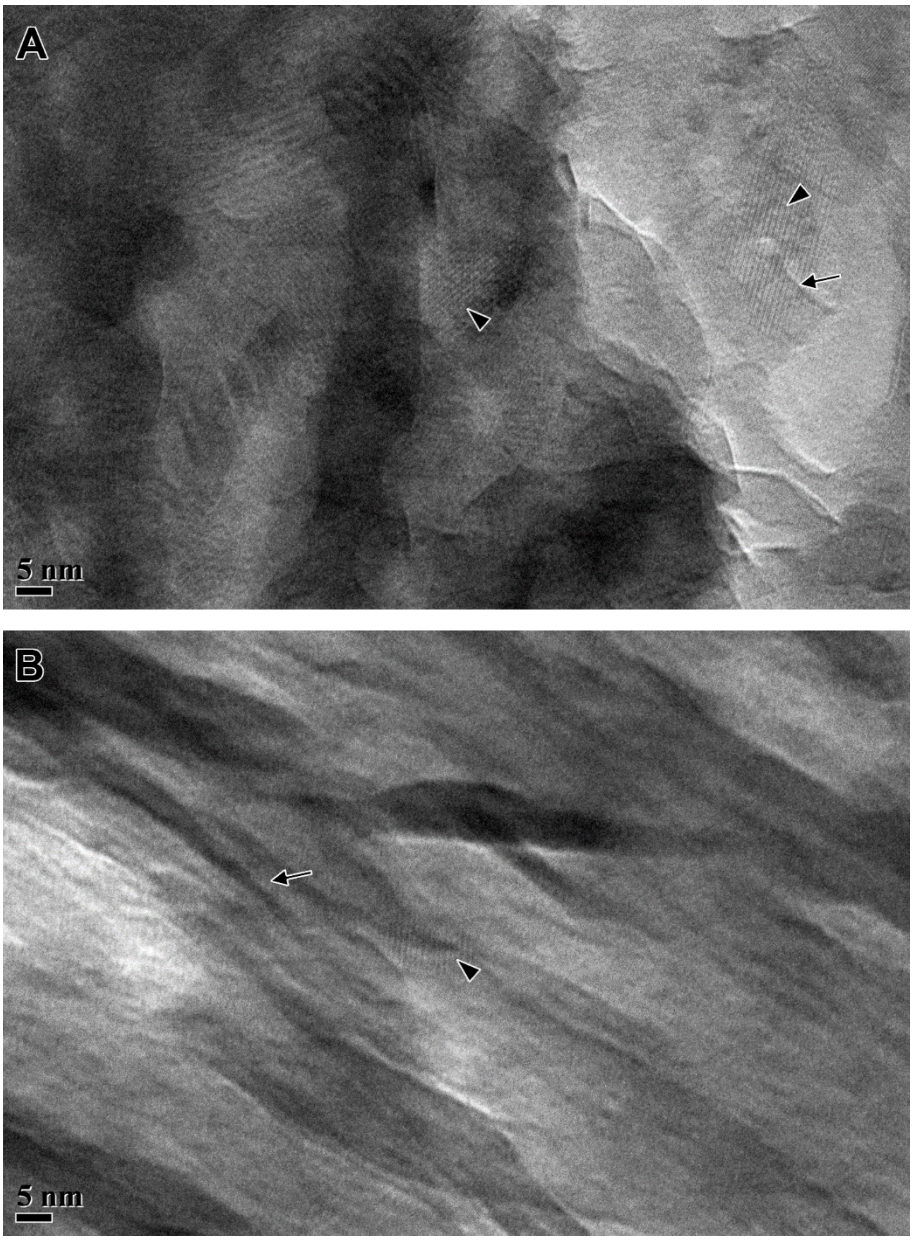

Figure G.6. TEM image of longitudinal section of human bone (x200,000 original magnification). (A) healthy and (B) osteogenesis imperfecta. Arrows denote collagen fibrils and arrowheads denote HAP crystal lattice.

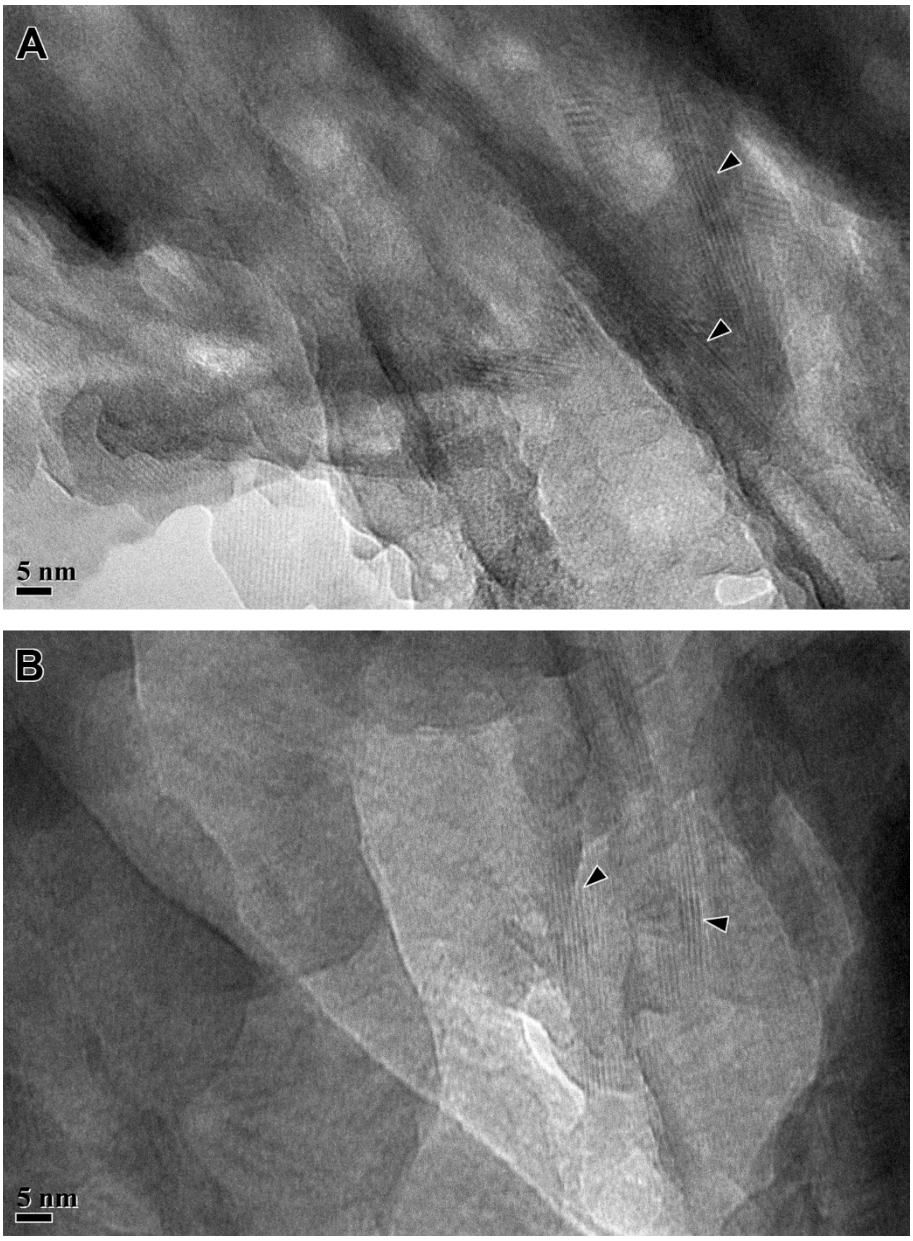

Figure G.7. TEM image of longitudinal section of human bone (x200,000 original magnification). (A) healthy and (B) osteogenesis imperfecta. Arrowheads denote HAP crystal lattice.

G.2. TEM images of healthy and OI diseased human bone where EELS spectra were acquired, transverse sections

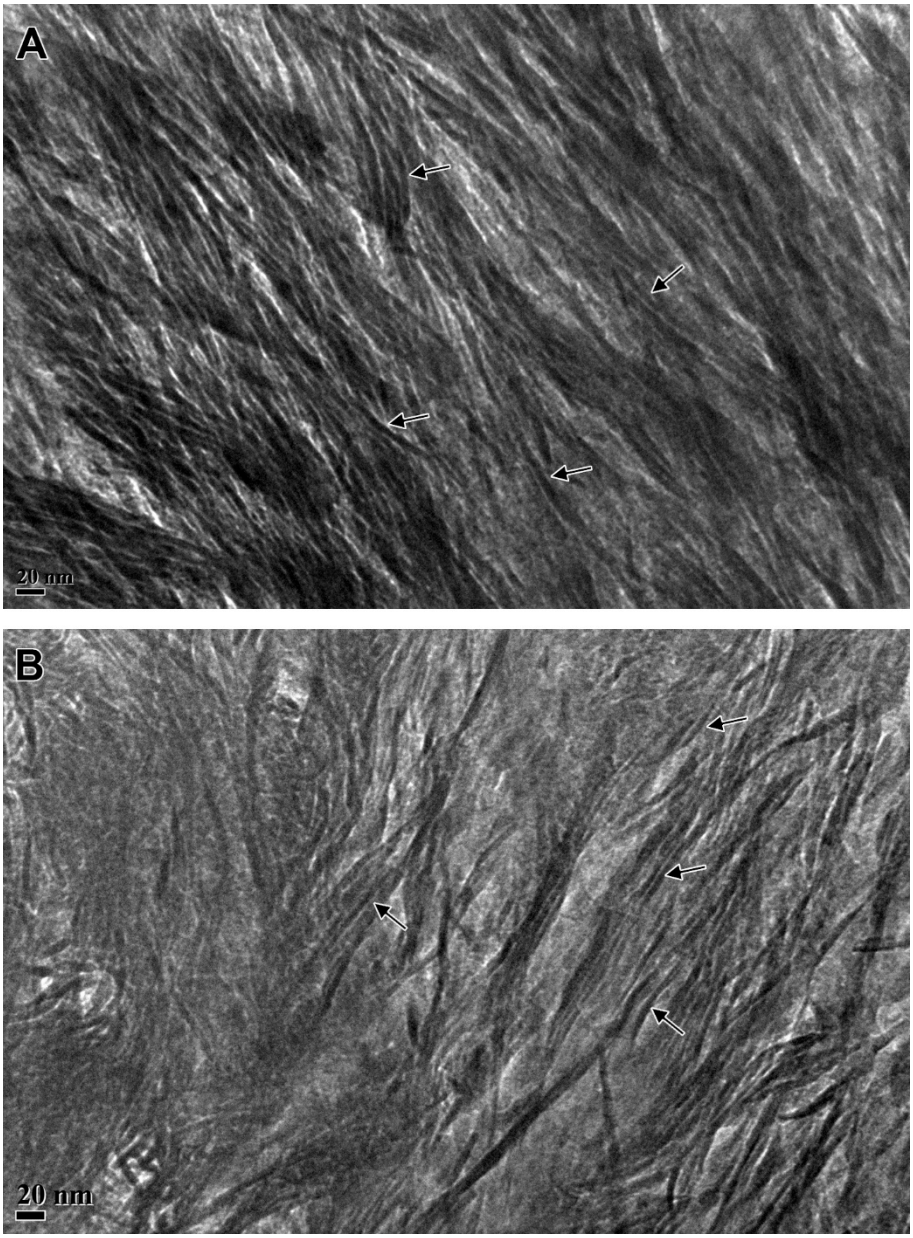

Figure G.8. TEM image of transverse section of human bone (x40,000 original magnification). (A) healthy and (B) osteogenesis imperfecta. Arrows denote collagen fibrils.

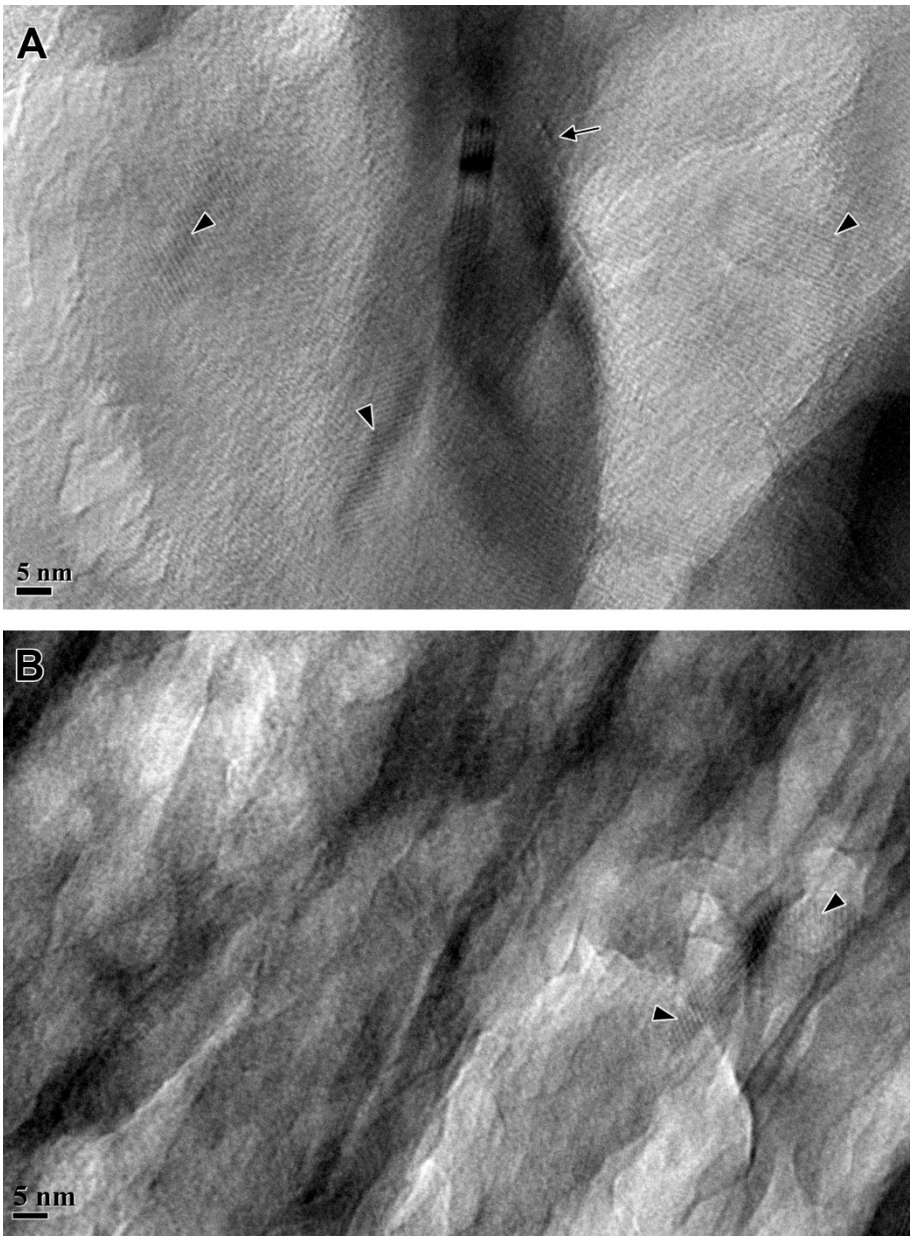

Figure G.9. TEM image of transverse section of human bone (x200,000 original magnification). (A) healthy and (B) osteogenesis imperfecta. Arrows denote collagen fibrils and arrowheads denote HAP crystal lattice.

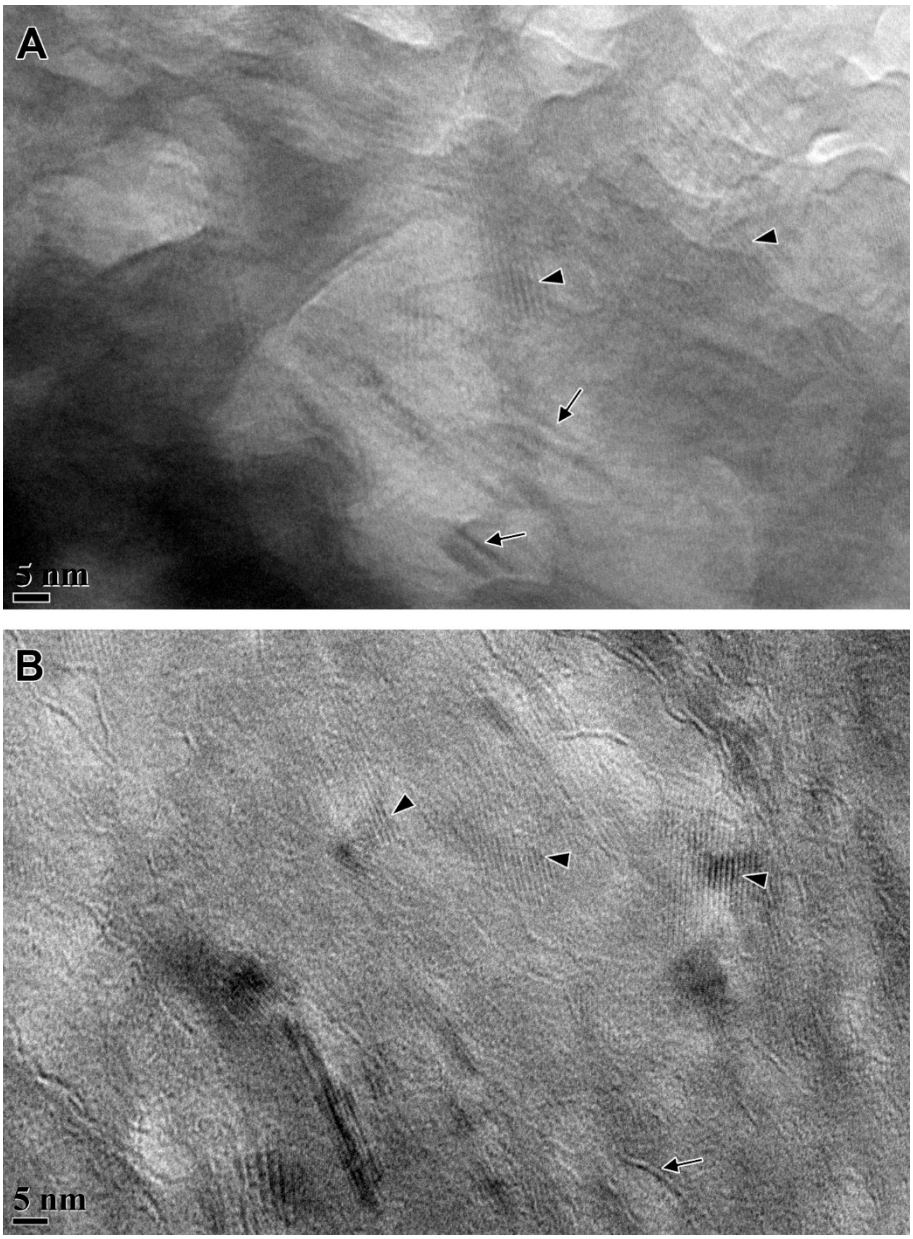

Figure G.10. TEM image of transverse section of human bone (x200,000 original magnification). (A) healthy and (B) osteogenesis imperfecta. Arrows denote collagen fibrils and arrowheads denote HAP crystal lattice.

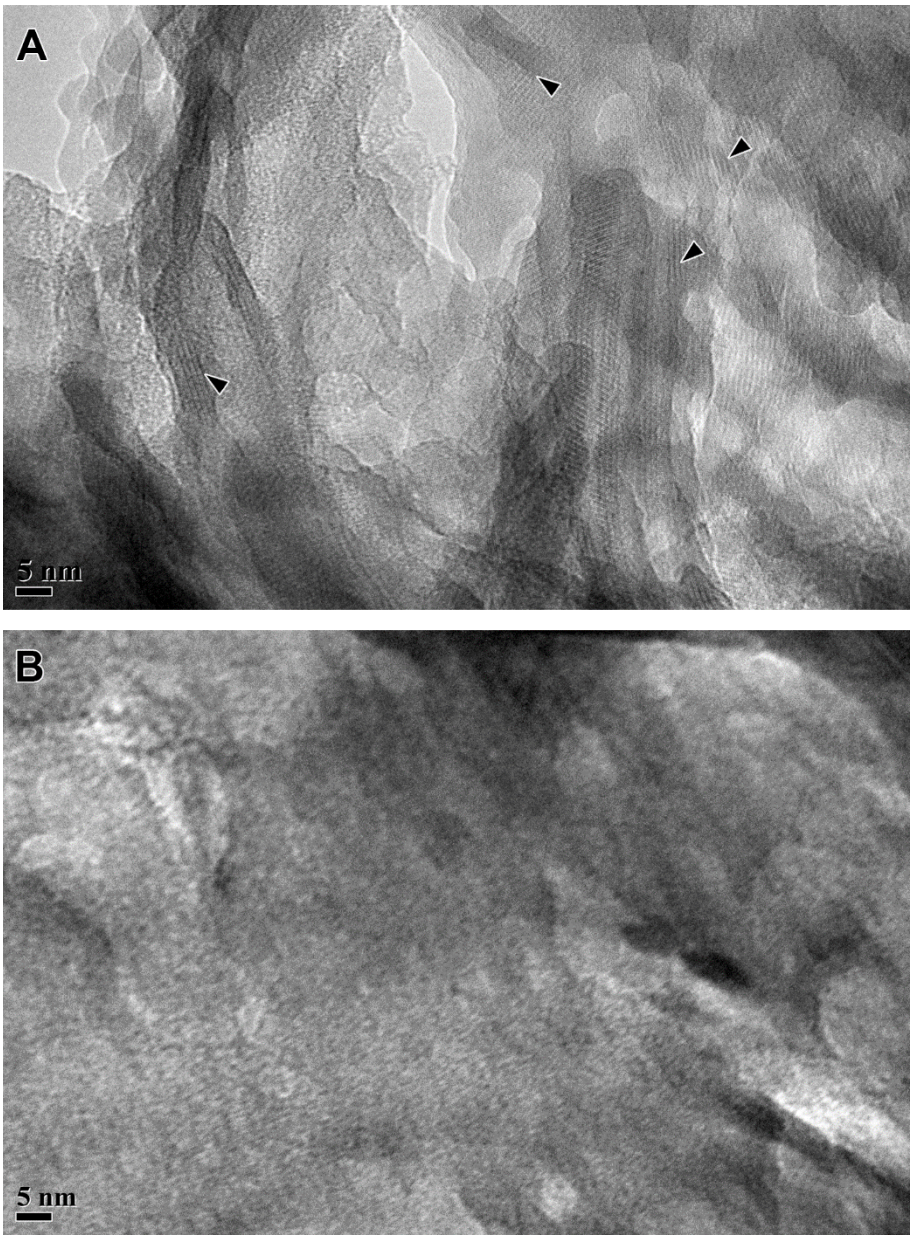

Figure G.11. TEM image of transverse section of human bone (x200,000 original magnification). (A) healthy and (B) osteogenesis imperfecta. Arrowheads denote HAP crystal lattice.

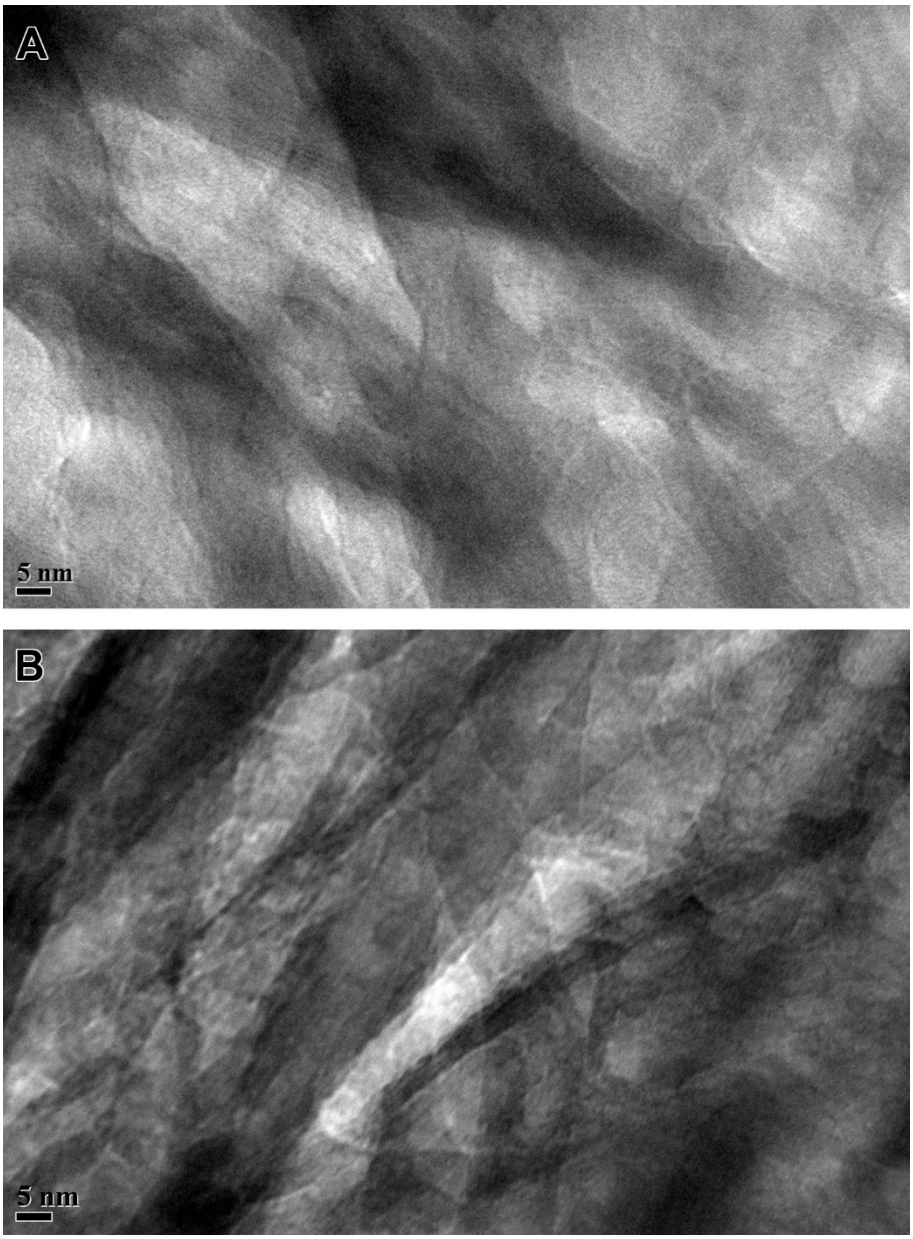

Figure G.12. TEM image of transverse section of human bone (x200,000 original magnification). (A) healthy and (B) osteogenesis imperfecta.

APPENDIX H. TEM IMAGES SHOWING BANDING IN HUMAN BONE, LONGITUDINAL SECTION

H.1. TEM images of banding in healthy and osteogenesis imperfecta diseased human bone

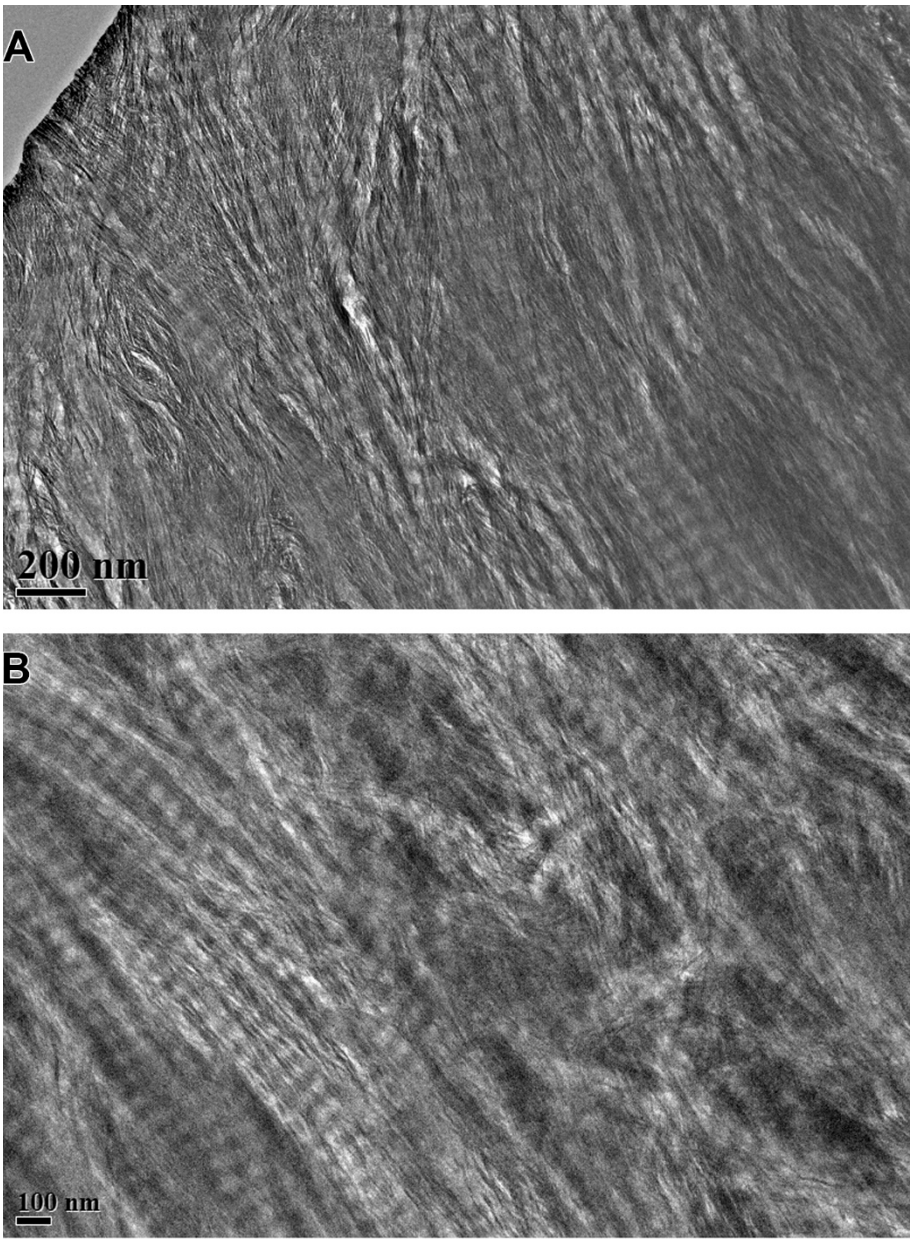

Figure H.1. TEM images showing banding in longitudinal sections of human bone (x10,000 original magnification). (A) healthy. (B) osteogenesis imperfecta.

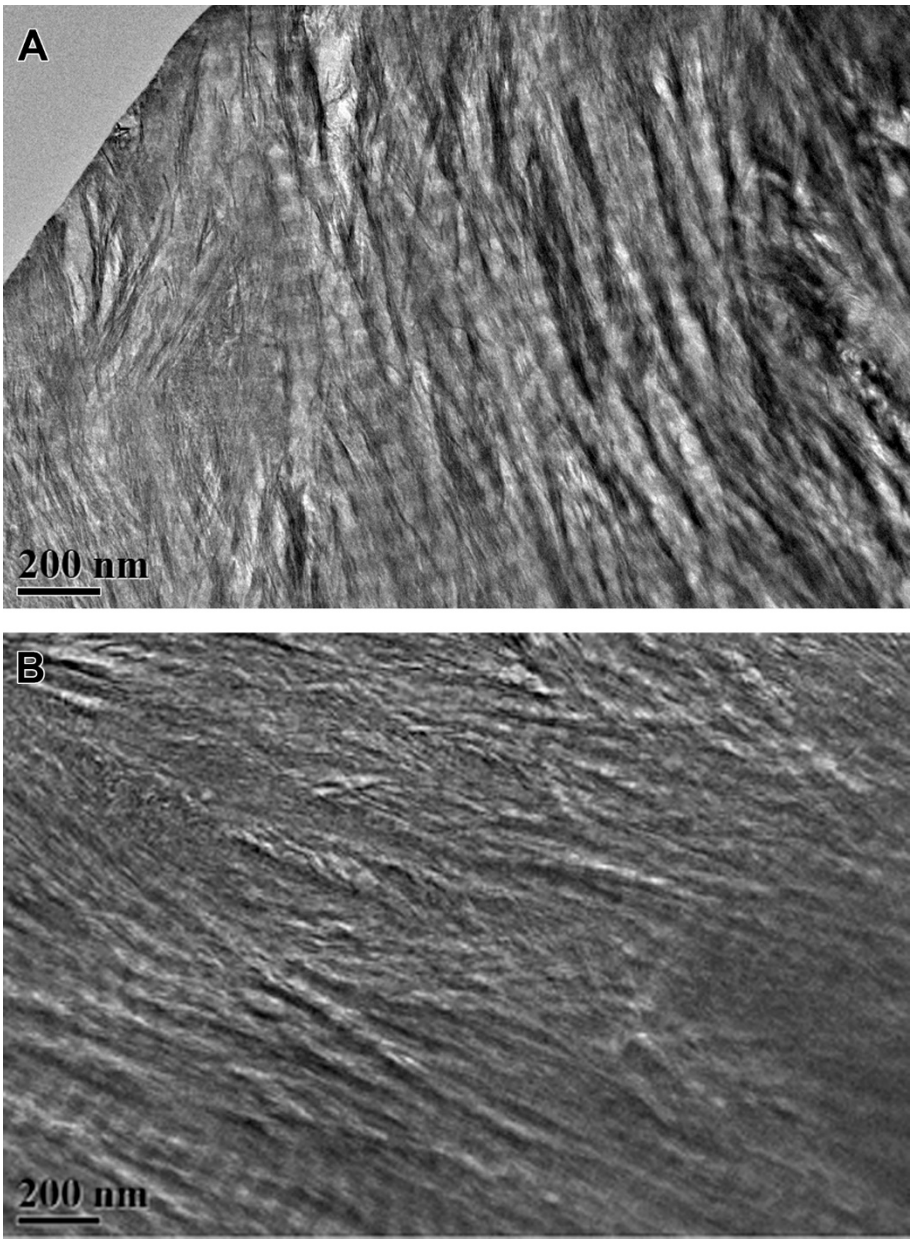

Figure H.2. TEM images showing banding in longitudinal sections of human bone (x12,000 original magnification). (A) healthy. (B) osteogenesis imperfecta.

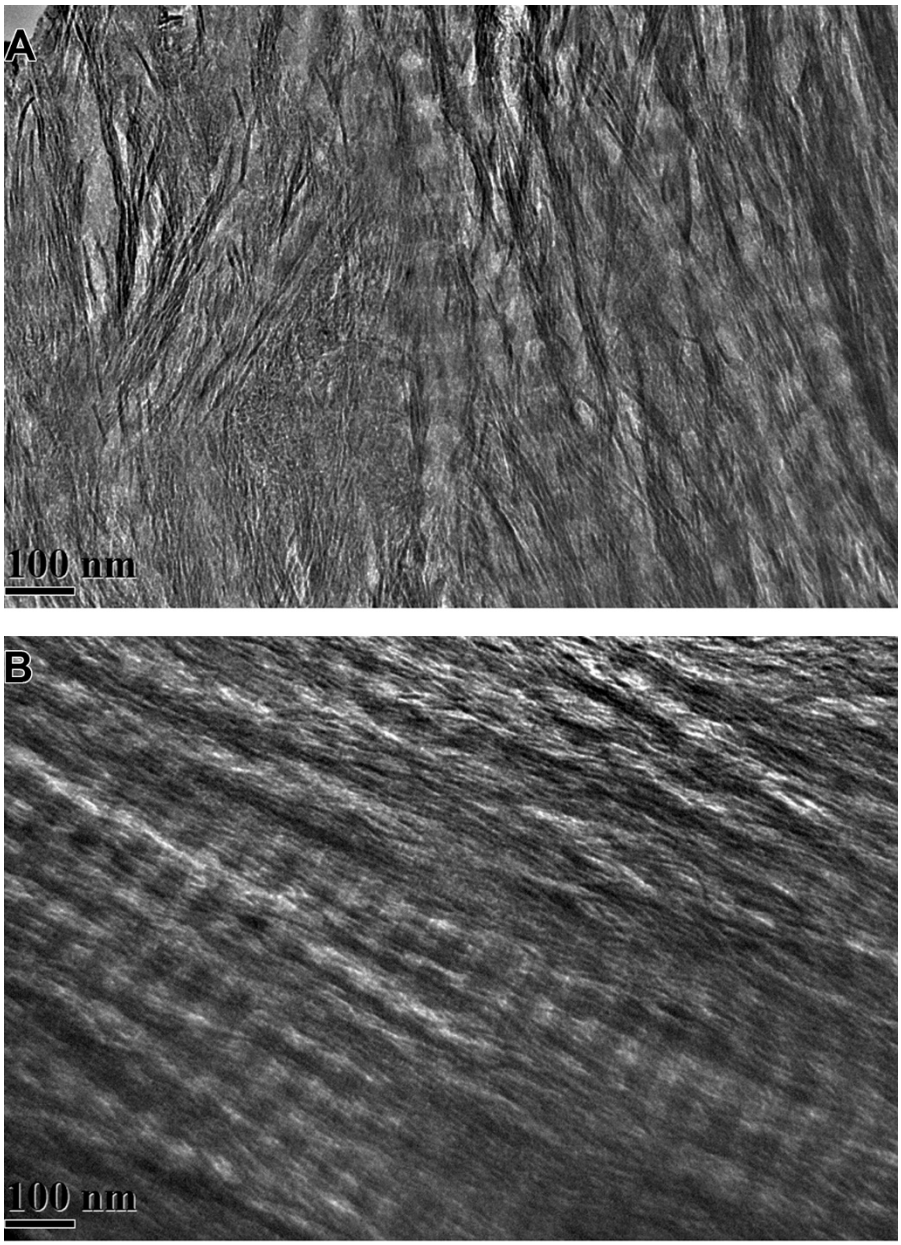

Figure H.3. TEM images showing banding in longitudinal sections of human bone (x20,000 original magnification). (A) healthy. (B) osteogenesis imperfecta.

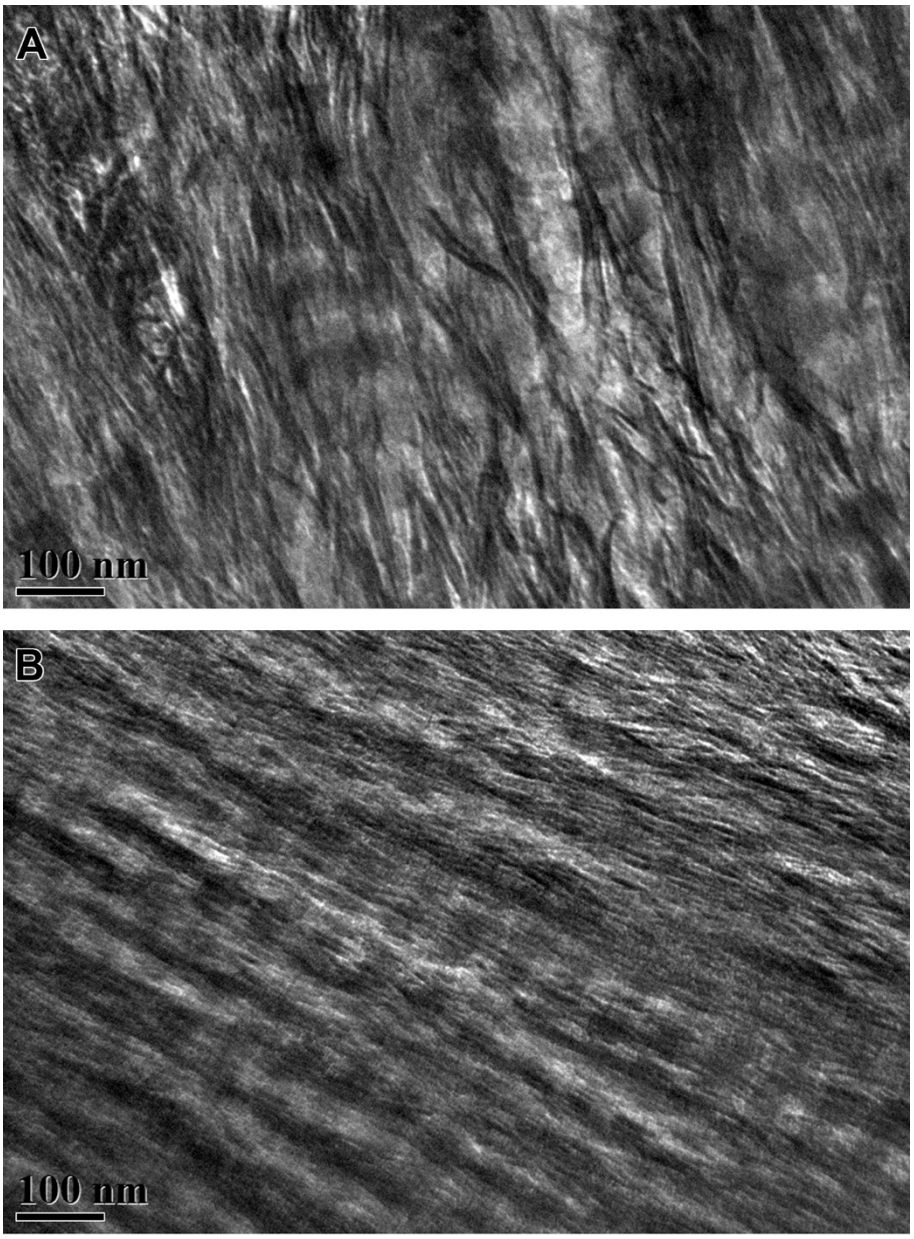

Figure H.4. TEM images showing banding in longitudinal sections of human bone (x25,000 original magnification). (A) healthy. (B) osteogenesis imperfecta.

APPENDIX I. SELECTED OVERLAYS OF EELS SPECTRA

I.1. Overlays of ε_1 spectra

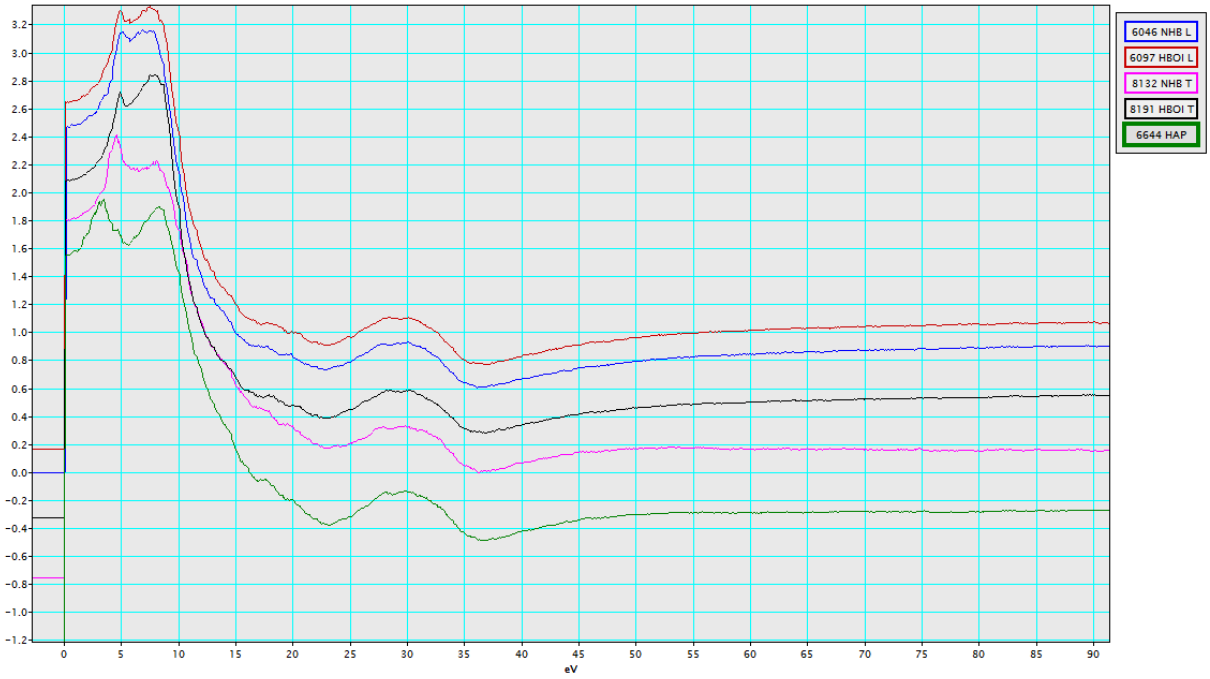

Figure I.1. ε_1 spectra overlays of healthy human bone (longitudinal and transverse), osteogenesis imperfecta diseased human bone (longitudinal and transverse) and HAP.

I.2. Overlays of ε_2 spectra

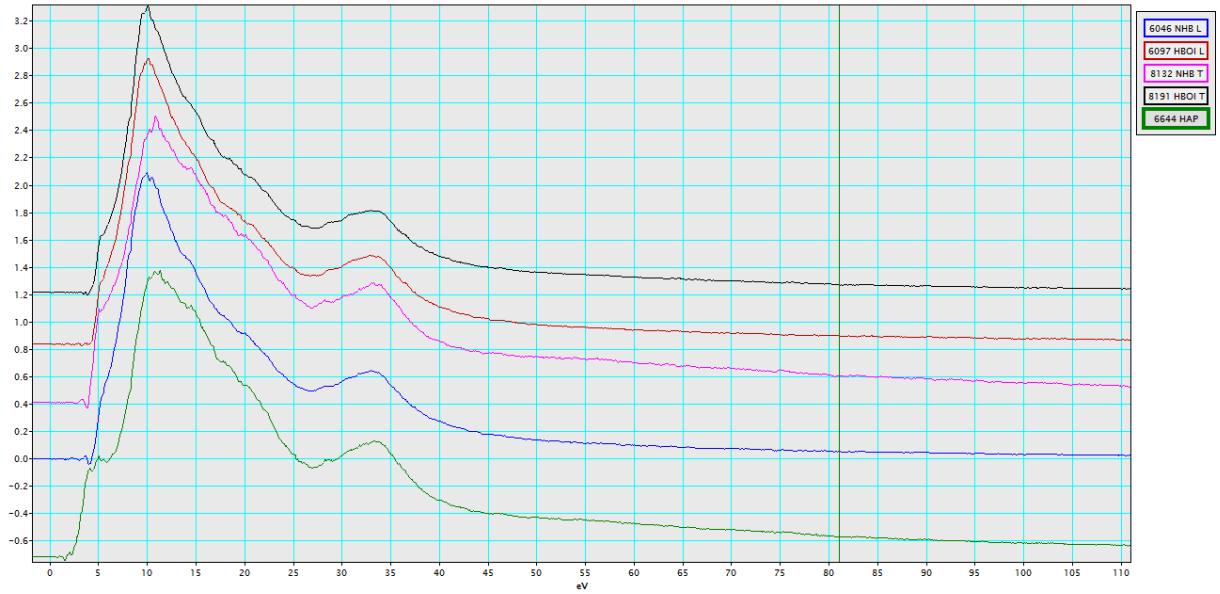

Figure I.2. ε_2 spectra overlays of healthy human bone (longitudinal and transverse), osteogenesis imperfecta diseased human bone (longitudinal and transverse) and HAP.

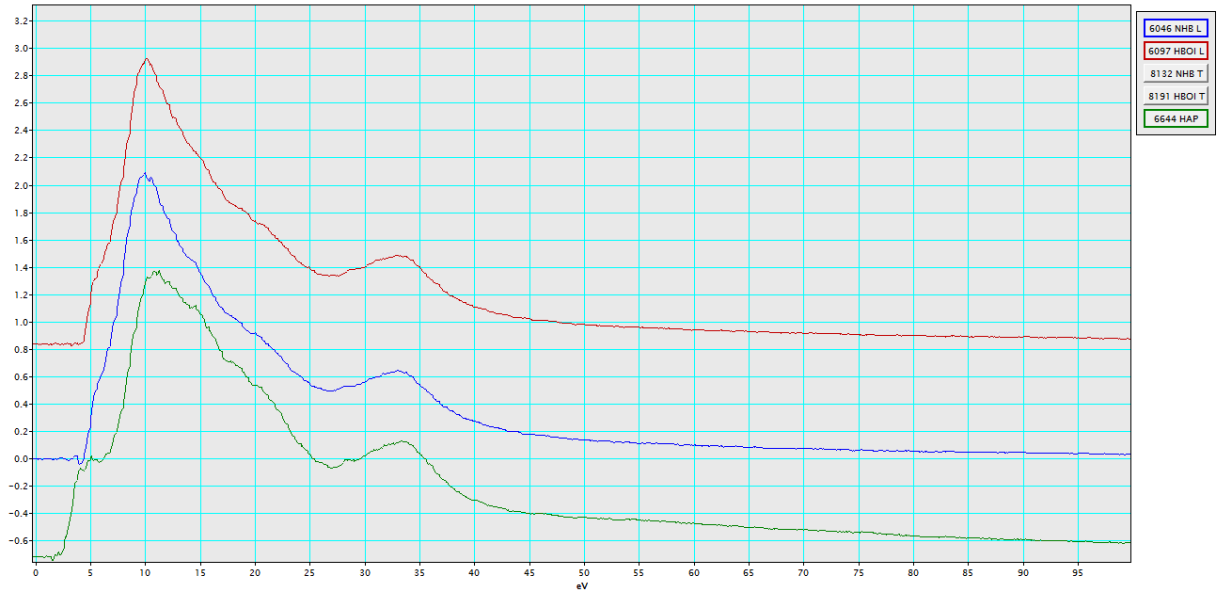

Figure I.3. ε_2 spectra overlays of longitudinal healthy human bone, longitudinal osteogenesis imperfecta diseased human bone and HAP.

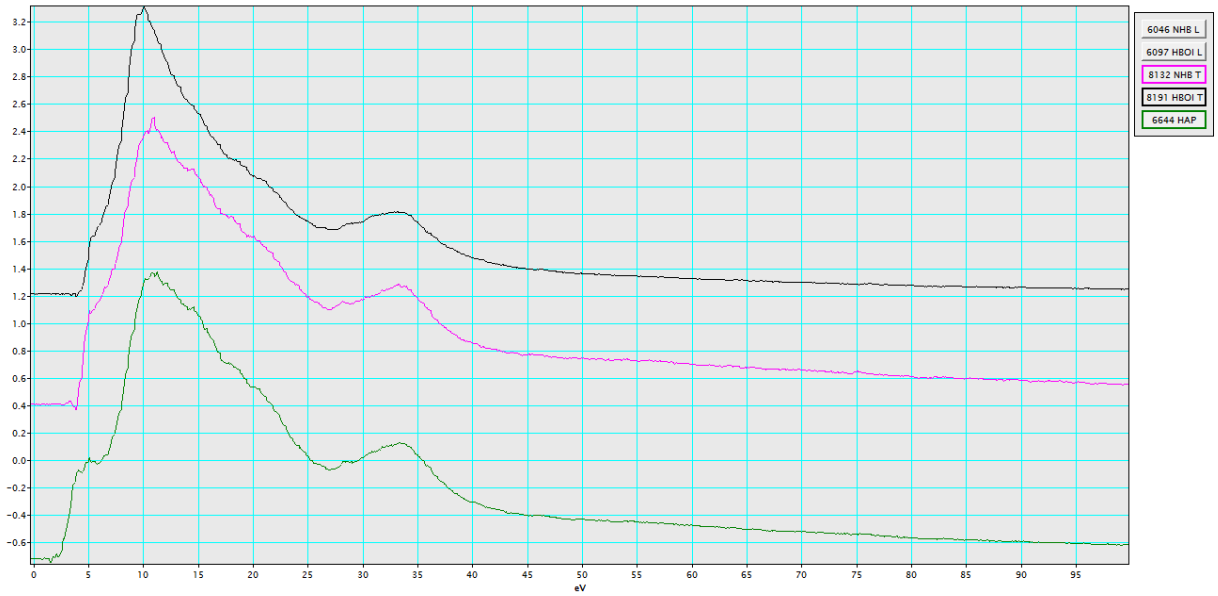

Figure I.4. ε_2 spectra overlays of transverse healthy human bone, transverse osteogenesis imperfecta diseased human bone and HAP.

I.3. Overlays of ELF spectra

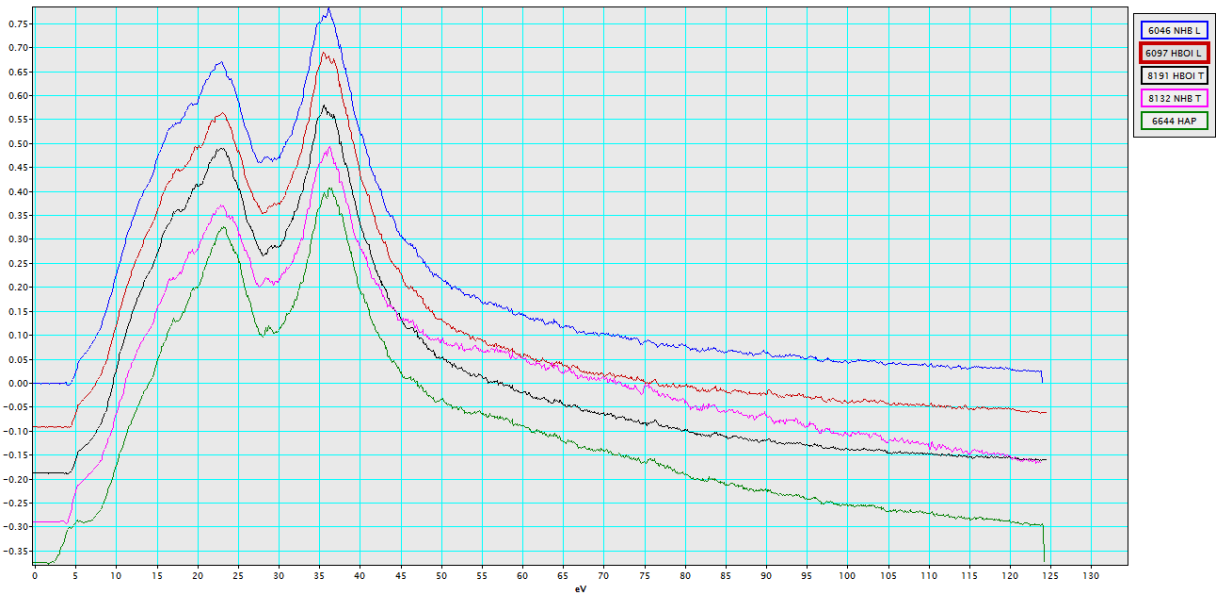

Figure I.5. ELF spectra overlays of healthy human bone (longitudinal and transverse), osteogenesis imperfecta diseased human bone (longitudinal and transverse) and HAP.

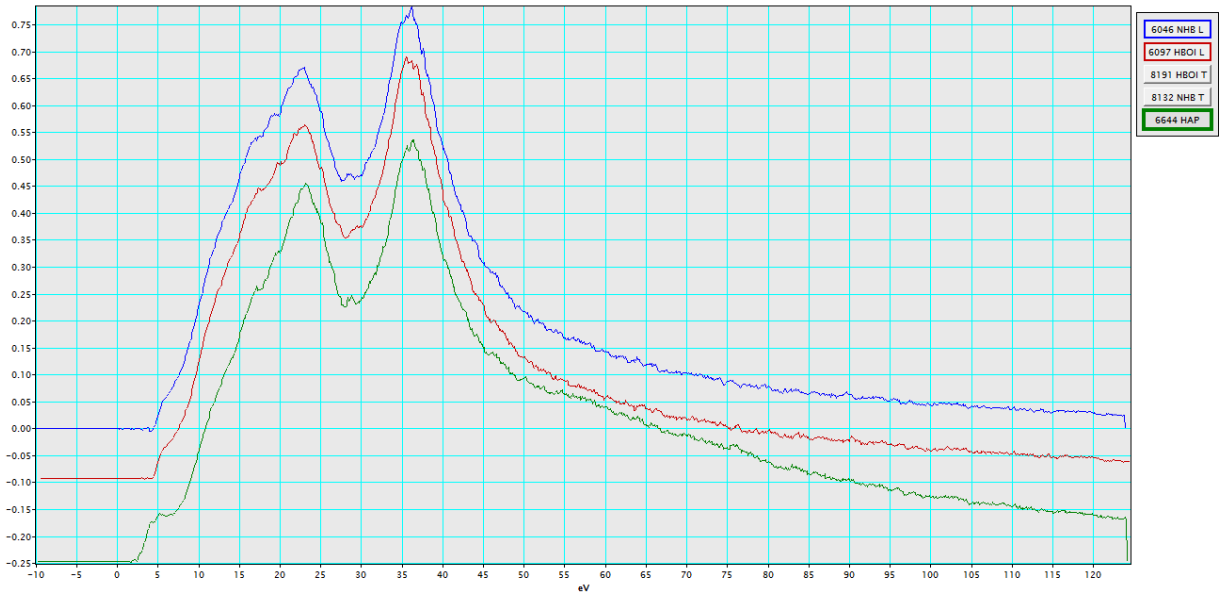

Figure I.6. ELF spectra overlays of longitudinal healthy human bone, longitudinal osteogenesis imperfecta diseased human bone and HAP.

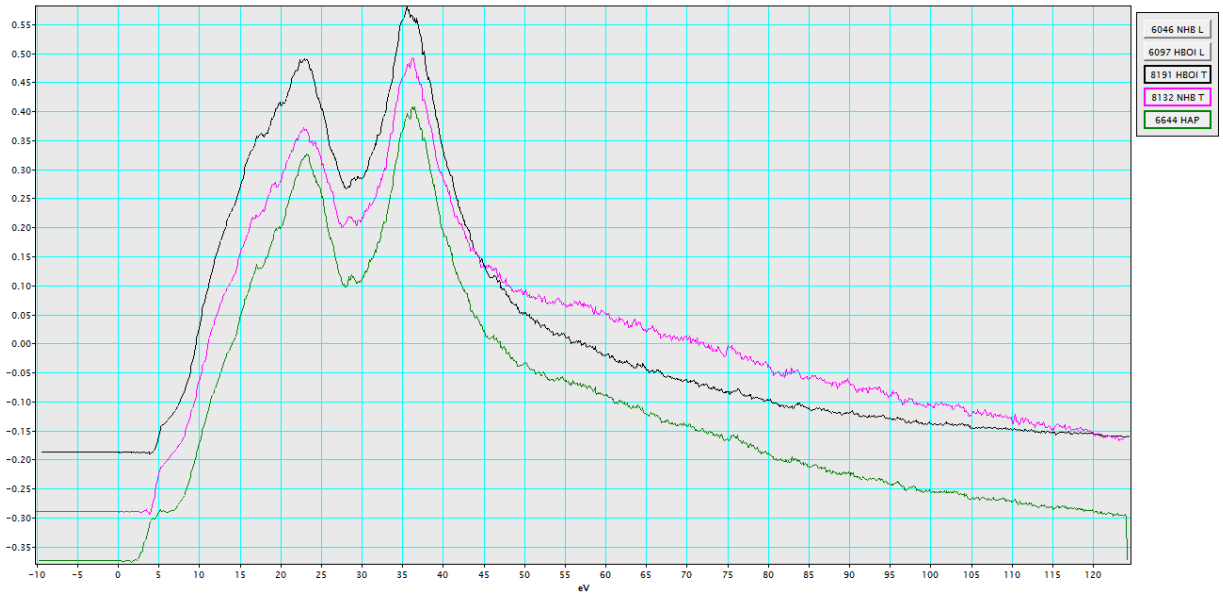

Figure I.7. ELF spectra overlays of transverse healthy human bone, transverse osteogenesis imperfecta diseased human bone and HAP.

I.4. Overlays of P-$L_{2,3}$ spectra

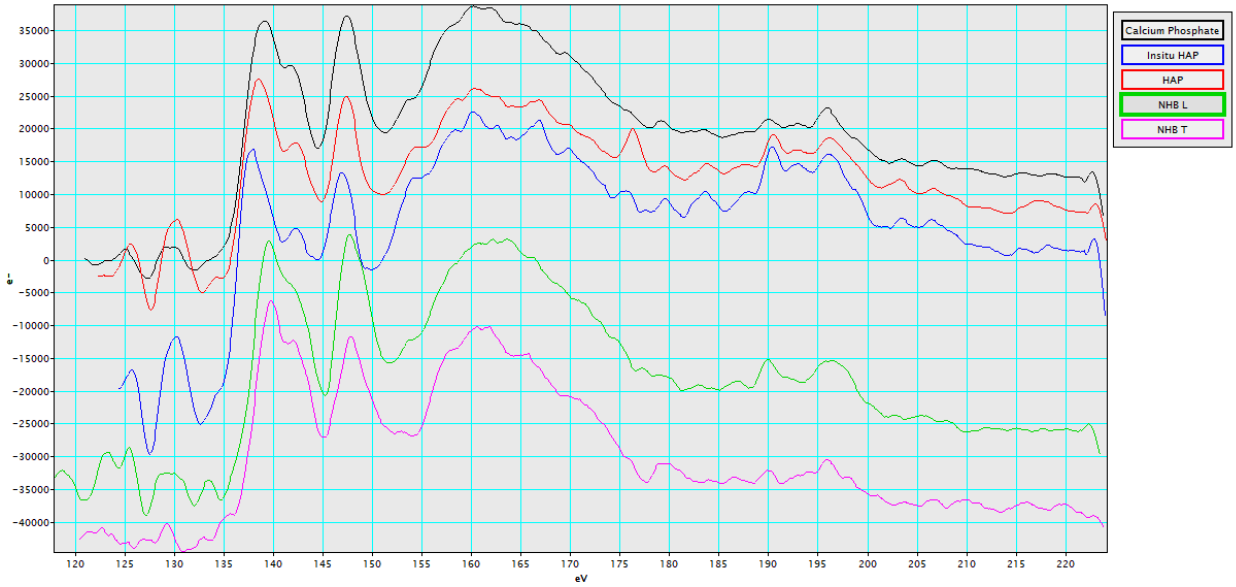

Figure I.8. P-$L_{2,3}$ spectra overlays of healthy human bone (longitudinal and transverse), osteogenesis imperfecta diseased human bone (longitudinal and transverse) and HAP.

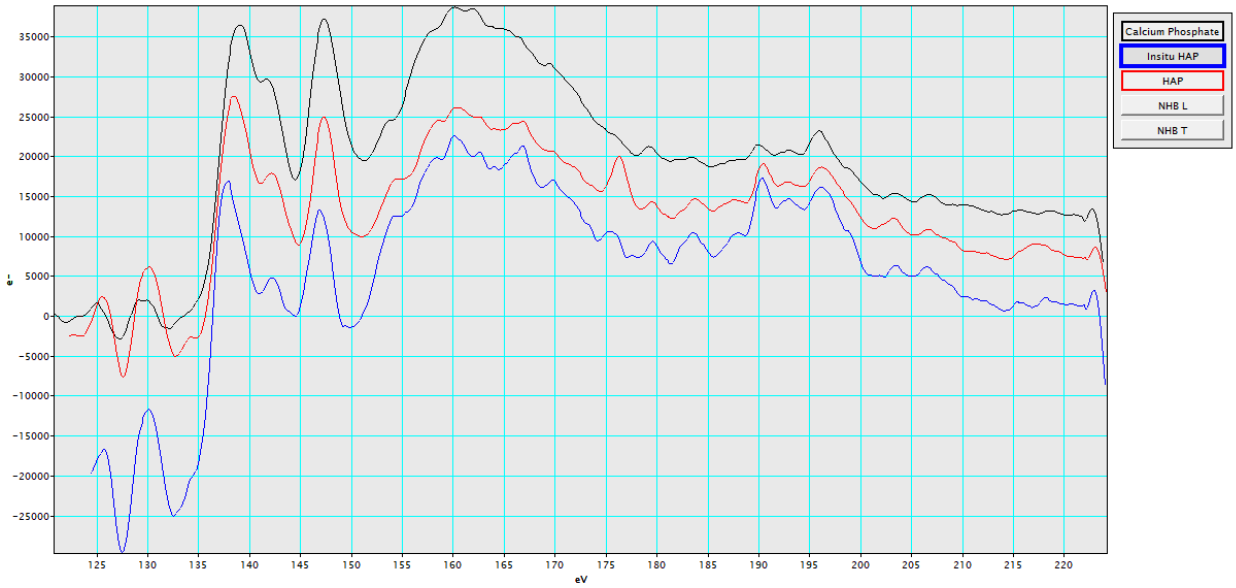

Figure I.9. P-$L_{2,3}$ spectra overlays of β-TCP, in-situ HAPclay, and HAP.